Mathematical Modeling of Solid Oxide Fuel Cells using Hydrocarbon Fuels

by

Won Yong Lee

B.S., Mechanical Engineering
Seoul National University, 2001

S.M., Mechanical Engineering
Massachusetts Institute of Technology, 2006

Submitted to the Department of Mechanical Engineering in Partial Fulfillment of the Requirements for the Degree of

Doctor of Philosophy in Mechanical Engineering

at the

MASSACHUSETTS INSTITUTE OF TECHNOLOGY

JUNE 2012

Signature of Author .....
Department of Mechanical Engineering
June 1, 2012

Certified by.....
Ahmed F. Ghoniem
Ronald C. Crane (1972) Professor
Thesis Supervisor

Accepted by.....
David E. Hardt
Chairman, Department Committee on Graduate Students

Mathematical Modeling of Solid Oxide Fuel Cells using Hydrocarbon Fuels

By

Won Yong Lee

Submitted to the Department of Mechanical Engineering
on 1 June 2012, in Partial Fulfillment of the Requirements
for the Degree of Doctor of Philosophy in Mechanical Engineering

Abstract

Solid oxide fuel cells (SOFCs) are high efficiency conversion devices that use hydrogen or light hydrocarbon (HC) fuels in stationary applications to produce quiet and clean power. While successful, HC-fueled SOFCs face several challenges, the most significant being performance degradation due to carbon deposition and the need of external reforming when using heavier HC. Modeling these devices faces these as well as other complexities such as the presence of multiple electrochemistry pathways including those of H_2 and CO. The goals of this thesis are to: (1) improve the thermodynamic analysis of carbon deposition, (2) develop a multi-step CO electrochemistry mechanism, and (3) apply the CO along with the H_2 electrochemistry mechanisms to predict the cell performance when using syngas.

Two carbon deposition mechanisms have been identified: homogeneously formed soot and catalytically grown carbon fiber. All previous thermodynamic analyses have used graphite to represent the properties of the deposited carbon regardless of the formation mechanism. However, the energetic and entropic properties of these two types of carbon are different from those of graphite. A new thermodynamic analysis is proposed that: (1) uses experimentally measured data for carbon fiber if the anode includes Ni catalyst; and (2) uses soot precursors such as CH_3 and C_2H_2 to predict soot formation. The new approach improves the prediction of the onset of carbon deposition where previous analyses failed.

A new multi-step CO electrochemistry model is proposed in which CO is directly involved in the charge-transfer steps. The model structure, with a single set of kinetic parameters at each temperature, succeeds in reproducing the characteristics of the EIS data of patterned anodes including the inductive loop at high activation overpotential. The model successfully predicts the steady-state Tafel plots, and explains the positive dependence of the exchange current density on p_{CO_2}.

Finally, a membrane-electrode-assembly (MEA) model is developed incorporating multi-species transport through the porous structure, detailed elementary heterogeneous reactions on the Ni surface, and for the first time, detailed electrochemistry models for H_2 and CO. The model successfully reproduces the performance of SOFCs using pure H_2 or CO. The MEA model can isolate/distinguish between the roles/contributions of the reforming chemistry and CO electrochemistry in SOFCs using syngas. Adding reforming thermochemistry improves the agreement with experiments at lower current densities, and raises the limiting current density by

providing more H_2 via the water-gas shift reaction. Adding CO electrochemistry improves the prediction at high current densities by the additional current generated by the CO electrochemical oxidation. The current from CO becomes comparable to that from H_2 as the CO content at the TPB increases.

Thesis Supervisor: Ahmed F. Ghoniem
Title: Ronald C. Crane (1972) Professor

Acknowledgements

First and foremost, I would like to thank my advisor, Professor Ahmed Ghoniem, for his exceptional guidance, expertise and patience over the years. It has truly been an honor and great pleasure to work with him. I am also grateful to my thesis committee members, Prof. Harry Tuller, Prof. Martin Bazant, Prof. Alexander Mitsos and Prof. Yang Shao-Horn for their critical advice and encouraging comments.

I appreciate the Samsung Scholarship Foundation as well as King Abdullah University of Science and Technology for financial support on my thesis research. I was able to explore new ideas thanks to them.

I would like to extend my gratitude to many talented people in the Reacting Gas Dynamics group. Dr. Jeff Hanna thoroughly reviewed the thesis and provided valuable comments. Dr. Daehyun Wee helped me to settle in the group. Dr. Fabrice Schlegel, Dr. Murat Altay, Dr. Simcha Singer and Kushal Kedia are great companions. I also had memorable time with Korean lab-mates, Seung-Hyuck and Jongsup.

I cannot imagine how I would have survived throughout the years without my great friends in Cambridge. It is a great pleasure to thank my Cambridge family: Sangwon, Sang-il, Seon-Joo, Kyung-ryeol, Hakyung, Jinho, Sangmok, Jaejeen, Inyong, Sewoong and Kyung-eun. I cannot believe how much they have done for me throughout my time here. I am grateful to have the wonderful companions in social gatherings: Wonyoung, Taeho, Hongchul, Jooeun, Jaewon, Wonjae, Sungjune, and Hajong. Hanging out with them has been the most enjoyable and rejuvenating moments. I am blessed to have awesome seniors: Dongkun, Chiwon, Sangjin, Jin-Oh, Jaemyung, Sungjoong, Kang-Hyun, Yeonwoo, Kitae, Heejin and Yongjin. They shared their wisdom and experience with me. My thanks also go to Wonjung, Jungpyo, Sanha, Hyunglae, Kimin, Sungho, Hansohl, Yun-seog, Wonjoon, Jong-ho, Kwangmin, Kyoo-chul, Hyungryul, Gyu-Boong, Sungmin and Jessie for embracing me like a real brother.

I am indebted to many of my friends outside of Boston to support me: in Korea, Kumhee, Hyunmin, Jae, Byungwoon, Soo-Hwan, Suhan, Yonghyun, Sanghoon, Juntae, and Beom-Kyu; in the U.S., Seungho, Jinwoo, Hojung and Bokyung. Their occasional visits, packages, emails and calls helped me to soothe homesickness.

Last but most importantly, none of this would have been possible without the love of my family - my parents and sister. Their life-long support and encouragement has contributed so much to making me who I am, and I simply cannot thank them enough for everything they have done for me.

I dedicate this work to my parents.

Page left intentionally blank

Contents

List of Figures

List of Tables

Page left intentionally blank

Chapter 1

General Introduction

Early fuel cells were designed to use hydrogen because it is easy to convert electrochemically. In addition, the only product from a hydrogen fuel cell is water, making them environmentally friendly energy conversion devices. However, the production of hydrogen using environmentally friendly and economic methods has not yet been achieved. According to the National Renewable Energy Laboratory [1, 2], almost all of the hydrogen in the U.S. today is produced by steam reforming of natural gas, and for the near term this method of production will continue to dominate. Hydrogen can also be produced using renewable energy sources or nuclear energy. However, the infrastructure to store and deliver hydrogen is another challenging problem. Furthermore the overall life cycle efficiency of hydrogen economy is low. Our dependence on hydrocarbon fuels as the primary source of energy will continue for several decades, given the current infrastructure and the costs associated with changing it.

A major advantage of a solid oxide fuel cell (SOFC) system for highly efficient electric power generation lies in its potential for direct use of hydrocarbon fuels, without the requirement for upstream fuel preparation, such as reforming. The fuel flexibility of a SOFC arises from the fact that O^{2-} anions, not protons, are the charged species transported from the cathode to the anode across the electrolyte. This allows SOFCs, in principle, to electrochemically oxidize traditional hydrocarbon fuels (as opposed to being chemically oxidized in a combustion process) [1]. Hence, significant research is focused on the development of solid oxide fuel cells that use hydrocarbon fuels. In recent years, researchers have rigorously investigated SOFC performance

operating on different fuels, including hydrogen, hydrocarbons, and syngas, and with various material and support structures. Table 1.1 shows selected examples of cell performance from recent studies, which provides a representation of the state-of-the-art research and development status of SOFCs fueled operating on hydrogen, hydrocarbon, or syngas.

Table 1.1. Comparison of peak power densities for SOFCs operating on H_2, CO, or hydrocarbon fuels

Group	Material	Temperature (°C)	Fuel (vol %)	Peak power density (W/cm^2)	Note
Jiang and Virkar [2], 2001	Ni-YSZ/YSZ/LSM	800	Pure H_2 Pure CH_3OH (50% C_2H_5OH + 50% H_2O)	1.7 1.3 0.8	
		650	Pure CH_3OH (50% C_2H_5OH + 50% H_2O)	0.6 0.3	
Jiang and Virakr [3], 2003	Ni-YSZ/ YSZ+SDC/LSC+SDC	800C	Pure H_2 Pure CO	1.7 0.7	
Murray et al. [4], 1999	(Ni-YSZ/YDC)/YSZ/YDC+LSM	550 - 650	97% CH_4 + 3% H_2O	0.13 (550°C) 0.25 (600°C) 0.37 (650°C)	Barnett Group
Liu and Barnett [5], 2003	Ni-YSZ/YSZ/LSM+YSZ	600 - 800	97% CH_4 + 3% H_2O	0.96 (800°C) 0.65 (750°C) 0.3 (700°C) 0.2 (650°C) 0.13 (600°C)	Barnett Group
Lin et al. [6], 2005	Ni-YSZ/YSZ/(GDC-LSCF/LSCF)	600 -800	97% H_2 + 3% H_2O	1.44 (800°C) 0.7 (700°C)	Barnett Group
			97% CH_4 + 3% H_2O	1.27 (800°C) 0.52 (700°C)	
Lin et al. [7], 2006	(PSZ-CeO2/Ni-YSZ)/YSZ/LSCF-GDC	750-800	97% CH_4 + 3% H_2O	1.23 (800°C) 0.9 (750°C)	Barnett Group
Zhan and Barnett [8], 2005	(Ru-CeO2/PSZ/Ni-YSZ)/YSZ/LSCF-GDC	500-750	Pure H_2	1.37 (750°C) 0.9 (700°C) 0.5 (650°C) 0.3 (600°C) 0.2 (550°C) 0.1 (500°C)	Barnett Group (Catalyst layer & partial oxidation)
		575-825	10.7% C_3H_8 + 18.7% O_2 + 70.6% Ar	0.48 (825°C) 0.45 (750°C) 0.35 (700°C) 0.29 (665°C) 0.2 (620°C)	

				0.12 (575°C)	
Zhan and Barnett [9], 2006	(Ru-CeO2/Ni-SDC)/SDC/LSCF-SDC	590	6% iso-octane – 94% air	0.6	Barnett Group (Catalyst layer & partial oxidation)
Park et al. [10], 2000	Cu-CeO2/YSZ/LSM-YSZ	700 – 800	Pure H_2	0.31 (800°C) 0.22 (700°C)	Gorte Group
			Pure n-butane (C_4H_{10})	0.18 (800°C) 0.12 (700°C)	
Kim et al. [11], 2001	Cu-CeO2/YSZ/LSM-YSZ	700	(40 wt % Decane + 60 wt% N_2) (40 wt % Toluene + 60 wt% N_2) (40 wt% Diesel + 60 wt% N_2)	0.1* 0.1* 0.1*	Gorte Group * Stable operation (Not peak power)
Hibino et al. [12], 2003	3 wt% Ru-Ni-GDC/GDC/Sm0.5Sr0.5CoO3 (SSC)	600	97.1% H_2 + 2.9% H_2O Pure CH_4 Pure C_2H_6 Pure C_3H_8	0.769 0.750 0.716 0.648	Ru Catalyst addition to the anode
Shao et al. [13]	Ni-SDC/SDC/SDC-BSCF	787	18.8 CH_4 + 16.2% O_2 + 65 % H_2	0.76	a single-chamber cell

1.1. Operation

In the context of SOFCs, the reforming of hydrocarbon fuels may, in general, take place externally in a separate process, or internally inside the hot stack. When an external reformer is used, a well-established steam-reforming technology can be utilized. However, internal reforming of hydrocarbon fuels in SOFC systems has many advantages: (i) it increases the system efficiency by recuperating waste heat from the stack into the fuel supply; (ii) it reduces the complexity and cost of the system by eliminating the need for the external reformer and associated heating arrangements, and by reduction in the stack cooling air requirement and associated equipment [3]. There are various alternatives for internal reforming of hydrocarbons,

including steam reforming, dry reforming, partial oxidation, and autothermal reforming. Because of some drawbacks associated with the internal reforming processes, additional interest has been given to direct conversion of dry hydrocarbon fuels. Direct conversion of a hydrocarbon means conversion in the SOFC without pre-mixing the fuel gas with steam or CO_2, and without processing the fuel before it enters the stack. The two most widely accepted internal reforming processes in the SOFC, steam reforming and partial oxidation, and the direct conversion of dry hydrocarbon fuel are discussed below.

1.1.1. Steam reforming

Steam reforming (SR), sometimes called steam-methane reforming (SMR), is a process in which high-temperature steam is used to produce a mixture of hydrogen and CO (i.e., syngas) from methane, ethanol, propane, or even gasoline. The lighter hydrocarbons react with hot water vapor in the presence of a catalyst to produce hydrogen, carbon monoxide, and a relatively small amount of carbon dioxide. Steam reforming is extremely endothermic, and therefore requires an external source of heat but can sometimes utilize recycled heat from exothermic processes depending on system configuration. The reforming process is generally followed by the water-gas shift (WGS) reaction (mildly exothermic), where the carbon monoxide can further react with steam to produce more hydrogen. The SR and WGS reactions are, respectively,

$$C_xH_y + xH_2O \leftrightarrow xCO + \left(x + \frac{y}{2}\right)H_2$$

$$CO + H_2O \leftrightarrow CO_2 + H_2$$

However, steam reforming poses several problems.

(a) Steam reforming requires considerable amount of water in the fuel channel, with a typical steam-to-carbon molar ratio (S:C) of about two, which results in a diluted fuel. This has a negative effect on the electrochemical efficiency.

(b) High steam partial pressure can cause sintering of the nickel anode particles, resulting in a significant reduction in the catalytic activity of the anode and a loss in cell performance

(c) Steam reforming is an extremely endothermic process. Internal steam reforming directly on the anode may cause large thermal gradients that can damage the cell

(d) Extra costs are involved in heat exchange and additional equipment for steam separation or recycling of the anode exhaust

Because of the drawbacks of the steam reforming processes, recent research has been focused more on the partial oxidation and the direct utilization of hydrocarbon fuels.

1.1.2. Partial oxidation

Partial oxidation (POx) is a chemical reaction between the hydrocarbon and oxygen (generally from air because of its convenience and cost) in a substoichiometric ratio, hence the name "partial oxidation." Catalytic partial oxidation (CPOx) reduces the required reforming temperature from around 1200°C to 800-900°C through the use of a catalyst (e.g., nickel). For cost reasons, supported nickel catalysts are generally preferred, although highly dispersed platinum and rhodium catalysts are also commonly used because of their greater activity and resistance to carbon deposition. Recent work has shown that nickel-based anode can have excellent selectivity for the partial oxidation of methane with minimal carbon deposition.

$$CH_4 + \frac{1}{2}O_2 \rightarrow CO + 2H_2$$

$$C_nH_{2n+2} + \frac{n}{2}O_2 \rightarrow nCO + (n+1)H_2$$

Barnett et al [4-7] have demonstrated the feasibility of using partial oxidation in SOFCs running on natural gas, propane, and iso-octane. Using oxygen, or even air, this is a much simpler, more convenient and less costly process in terms of system configuration compared with the internal steam reforming [3]. However, when air is used, it dilutes the fuel with nitrogen and can decrease the overall efficiency. Even when oxygen is fed with the fuel, this leads to a lower electrical efficiency due to the energy loss in oxidizing the hydrocarbon. Partial oxidation is an exothermic reaction, in contrast to the strongly endothermic steam reforming reaction.

Self-sustaining internal steam reforming is precluded during start-up and operation at low power levels because the strongly endothermic nature requires high temperatures. Because partial oxidation is an exothermic process, if offers the potential for start-up and self-sustaining operation of internally reforming SOFCs running on natural gas and other hydrocarbons at low power. It is likely that a combination of partial oxidation and steam reforming will be used as the basis for operation from zero power through low power loads to operation at full load [14].

1.1.3. Direct utilization

Because of some drawbacks associated with the internal steam reforming and partial oxidation processes, researchers have been trying to develop a SOFC that directly uses hydrocarbon fuels without any reforming or partial oxidation. Murray et al. [8] and Park et al. [9] reported power densities of 0.37 W/cm^2 and 0.12 W/cm^2 for a SOFC operating with dry natural gas at temperatures of 700°C and 900°C, respectively. They claimed that direct electrochemical oxidation is achieved within the SOFCs. Mogensen and Kammer [15] provided a comprehensive review of the direct conversion of hydrocarbons in SOFCs, and were critical of the likelihood of

single-step electrochemical oxidation of a hydrocarbon fuel, even in the case of the simplest hydrocarbon, CH_4. Instead, they suggested that the reactions may proceed via the following elementary reaction steps:

$$CH_4 + O^{2-} \leftrightarrow CH_3OH + 2e^-$$
$$CH_3OH + 2O^{2-} \leftrightarrow HCOOH + H_2O + 4e^-$$
$$HCOOH + O^{2-} \leftrightarrow CO_2 + H_2O + 2e^-$$

Alternatively, cracking of methane followed by electrochemical oxidation of the cracking products likely follows a path given by [15]

$$CH_4 \leftrightarrow C + 2H_2$$
$$C + 2O^{2-} \leftrightarrow CO_2 + 4e^-$$
$$H_2 + 2O^{2-} \leftrightarrow H_2O + 2e^-$$

1.2. Physical processes in SOFC using HCs

The membrane-electrode-assembly (MEA) is the heart of any fuel cell. In a SOFC, the MEA consists of a dense oxygen-ion-conducting electrolyte sandwiched between two porous cermet electrodes. When the fuel is hydrogen, H_2 molecules in the fuel channel are transported through the porous structure to electrochemically reactive sites known as triple- or three-phase boundaries (TPBs). It is generally accepted that current-producing charge-transfer reactions only occur at or very near the TPB, where the electron conductor (metal), ion conductor (oxide), and the necessary gas-phase reactants (in the pore space) come together. When H_2 reaches the TPB, it is oxidized by O^{2-} ion to produce H_2O, which is transported out of the porous anode to the fuel channel. Similarly, O_2 molecules are transported to the TPB on the cathode side and reduced to O^{2-} ions, which are conducted from the cathode to the anode through the dense nonporous electrolyte. The electrons generated on the anode are harvested and utilized through an external

circuit and moved back to the cathode. When the fuel is switched from H_2 to a hydrocarbon source, additional physical processes must take place in the anode, while the physical processes in the cathode and the electrolyte remain the same.

1.2.1. Thermochemistry and carbon deposition

Typical operating temperatures of SOFCs are high enough that homogeneous gas-phase chemistry within the anode and fuel channel should be considered when using hydrocarbon fuels. Moreover, because the most common anode metal is nickel, there are abundant catalytic activity to promote thermo-chemical reactions via heterogeneous chemistry. Both homogeneous and heterogeneous chemistry play key roles in reforming a hydrocarbon fuel into a hydrogen- and CO-rich fuel as shown in Figure 1-1.

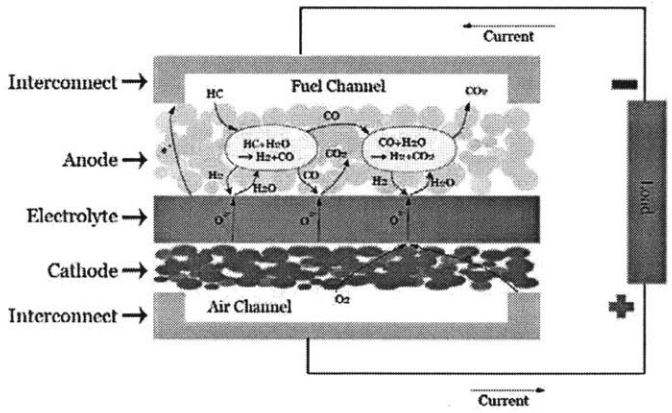

Figure 1-1. A schematic of physical processes in the MEA of a SOFC

A significant concern during reforming processes is the formation of solid carbon through undesired side reactions. Amongst other deleterious effects, solid carbon formed in the anode can block the pores and increase transport resistance for gas species trying to reach the TPB, and/or prevent reforming reactions by covering the catalyst particles. At typical SOFC operating

temperatures with hydrocarbon or syngas fuels, the extent of carbon formation depends on factors such as the steam-to-carbon ratio, operating conditions (e.g., temperature, pressure, current density), and anode catalyst. Although it is possible to minimize carbon deposition on traditional Ni-YSZ anodes by providing sufficient H_2O in the fuel stream, the amounts required are generally excessive, diluting the fuel and reducing the overall efficiency, in addition to creating device- and systems-scale complexity because of the need for water management solutions. In this light, analysis of carbon deposition in the SOFC anode—including the deposition and growth mechanisms, and material tolerances—is absolutely necessary if SOFCs are to be a viable and economical option for efficiently utilizing carbon-containing fuels.

1.2.2. Multiple electrochemical pathways

Solid oxide fuel cells (SOFCs) can operate on various fuels, including hydrogen, carbon monoxide, methane and other hydrocarbons [4–6,9,10,16,17]. However, there is no consensus on which species are electrochemically oxidized at the anode triple phase boundary (TPB) when carbon-containing fuels are used. Because hydrocarbon (HC) fuels are partially or completely reformed to other species, such as hydrogen and carbon monoxide, while flowing through a porous nickel anode, determining the composition of the fuel when it is electrochemically oxidized is a challenge.

Fast direct electrochemical oxidation of hydrocarbons in SOFCs has been suggested by two groups: the Barnett group [4] at Northwestern University, and the Gorte group [10,18,19] at the University of Pennsylvania. Both groups used dry hydrocarbons to exclude possible reforming reactions. However, Mogensen and Kammer [15] suspect that hydrocarbon conversion proceeds by pathways other than direct oxidation, e.g., by cracking and reforming followed by

electrochemical oxidation of the fuel fragments and reforming products. This is because the measured open circuit voltages (OCVs) are much lower than those predicted by the Nernst equations when based on the direct conversion of the original fuel. It is still being debated whether hydrocarbon fuels directly participate in charge-transfer reactions without being reformed to H_2 and/or CO, which are subsequently involved in the electrochemical reactions. Even though multiple possible electrochemical oxidation pathways have been suggested for various species, these pathways remain much less studied than H_2 electrochemical oxidation.

For example, carbon monoxide almost always exists when a hydrocarbon fuel is supplied because the hydrocarbon fuel is reformed or pyrolyzed internally or externally. However, based on the following two arguments, CO electrochemistry has been ignored in many MEA models [21,22]:

(i) CO electrochemical oxidation rate is slower than that of H_2,

(ii) CO is reformed to H_2 via the water-gas shift reaction at the anode prior to reaching the TPB.

When pure CO is supplied to a porous Ni-YSZ anode, Jiang and Virkar [3] reported that the maximum power density reaches only about 40% of that obtained using pure H_2. Similarly, according to experimental results using a nickel-patterned anode on YSZ by Sukeshini et al. [20], the maximum power density using CO is about 50% of that obtained when using H_2 only. Though not at the same level as H_2, CO electrochemistry is certainly not negligible in these cases.

The water-gas-shift (WGS) reaction can convert CO to H_2 only when there is sufficient H_2O. Depending on the type of fuels and the technologies of gasification or reforming, the composition of the syngas may vary widely and H_2O produced from oxidation of H_2 may or may not be used to convert CO via the WGS. Generally, methane-derived syngas via reforming is H_2-

rich while coal-derived syngas via gasification is CO-rich. When CO is the dominant species in the fuel composition, the assumption that H_2 electrochemistry is still dominant and CO electrochemistry can be safely neglected must be retracted. The extreme and obvious case is a pure stream of CO, which would produce zero current under the usual assumption. Therefore, the two arguments used to support the idea that CO electrochemistry can be ignored are not always valid. Among multiple electrochemical oxidation pathways, CO electrochemistry needs to be included in MEA models for systems in which CO is expected to be relevant, and the assumption that it is negligible must be verified if CO is present but expected to be of little significance.

1.3. Thesis outline

Because carbon deposition can cause the degradation of SOFCs using hydrocarbon fuels, it is necessary to predict whether carbon may form. We begin our study with a thermodynamic analysis of solid carbon formation in the Ni anode of SOFCs, discussed in Chapter 2. Two carbon deposition mechanisms are examined: homogeneously formed soot and catalytically grown carbon fiber. We are critical of the assumption made by previous researchers that the thermodynamic properties of graphite can represent those of the deposited carbon regardless of its structure, and propose a new thermodynamic analysis approach: (1) to use experimentally measured data for carbon fiber if the anode includes Ni catalysts; (2) to use soot precursors such as CH_3 and C_2H_2 to predict soot formation. A multiphase equilibrium solver is developed based on the Villar-Cruise-Smith (VCS) algorithm and is used to revisit cases where previous calculations based on the properties of graphite failed to explain experimental observations.

CO electrochemistry needs to be included in the MEA model. However, a CO electrochemistry model as good as H_2 electrochemistry model has not been developed. In

Chapter 3, a new multi-step CO electrochemistry model is developed based on a pattern-anode geometry where the effects of transport and thermochemistry can be minimized. The mechanism is fitted to impedance measurements and validated using steady-state data of current-voltage. The characteristic features of the measured electrochemical impedance spectroscopy (EIS), such as the two suppressed semi-circles and the low frequency inductance loop, are discussed. The kinetic mechanism for CO electrochemical oxidation is then applied within an MEA model in Chapter 4.

In order to predict the performance of SOFCs using hydrocarbon fuels, an MEA model should incorporate the complex coupling of the muti-physic processes. In Chapter 4, we develop a membrane-electrode-assembly (MEA) model incorporating multi-species transport through the porous structure, detailed elementary heterogeneous reactions on the Ni surface, and for the first time, detailed electrochemistry models for H_2 and CO. The model results are compared with the performance of SOFCs using pure H_2, CO, syngas. The role of reforming chemistry and CO electrochemistry and the contribution of H_2 and CO electrochemical oxidation to the total current are investigated.

1.4. References

[1] S. McIntosh and R. J. Gorte, "Direct hydrocarbon solid oxide fuel cells.," *Chemical reviews*, vol. 104, no. 10, pp. 4845-65, Oct. 2004.

[2] Y. Jiang and A. V. Virkar, "A High Performance, Anode-Supported Solid Oxide Fuel Cell Operating on Direct Alcohol," *Journal of The Electrochemical Society*, vol. 148, no. 7, p. A706, 2001.

[3] Y. Jiang and A. V. Virkar, "Fuel composition and diluent effect on gas transport and performance of anode-supported SOFCs," *Journal of the Electrochemical Society*, vol. 150, no. 7, pp. 942-951, 2003.

[4] E. P. Murray, T. Tsai, and S. A. Barnett, "A direct-methane fuel cell with a ceria-based anode," *Nature*, vol. 400, no. 6745, pp. 649–651, 1999.

[5] J. Liu and S. A. Barnett, "Operation of anode-supported solid oxide fuel cells on methane and natural gas," *Solid State Ionics*, vol. 158, no. 1, pp. 11–16, Feb. 2003.

[6] Y. Lin, Z. Zhan, J. Liu, and S. A. Barnett, "Direct operation of solid oxide fuel cells with methane fuel," *Solid State Ionics*, vol. 176, no. 23–24, pp. 1827-1835, Jul. 2005.

[7] Y. Lin, Z. Zhan, and S. A. Barnett, "Improving the stability of direct-methane solid oxide fuel cells using anode barrier layers," *Journal of Power Sources*, vol. 158, no. 2, pp. 1313-1316, 2006.

[8] Z. Zhan and S. Barnett, "Use of a catalyst layer for propane partial oxidation in solid oxide fuel cells," *Solid State Ionics*, vol. 176, no. 9–10, pp. 871-879, Mar. 2005.

[9] Z. Zhan and S. A. Barnett, "Operation of ceria-electrolyte solid oxide fuel cells on iso-octane–air fuel mixtures," *Journal of Power Sources*, vol. 157, no. 1, pp. 422-429, 2006.

[10] S. Park, J. Vohs, and R. J. Gorte, "Direct oxidation of hydrocarbons in a solid-oxide fuel cell," *Nature*, vol. 404, no. 6775, pp. 265-7, Mar. 2000.

[11] H. Kim, S. Park, J. M. Vohs, and R. J. Gorte, "Direct Oxidation of Liquid Fuels in a Solid Oxide Fuel Cell," *Journal of The Electrochemical Society*, vol. 148, no. 7, p. A693, 2001.

[12] T. Hibino, A. Hashimoto, M. Yano, M. Suzuki, and M. Sano, "Ru-catalyzed anode materials for direct hydrocarbon SOFCs," *Electrochimica Acta*, vol. 48, no. 17, pp. 2531-2537, Jul. 2003.

[13] Z. Shao, J. Mederos, W. C. Chueh, and S. M. Haile, "High power-density single-chamber fuel cells operated on methane," *Journal of Power Sources*, vol. 162, no. 1, pp. 589-596, Nov. 2006.

[14] S. C. Singhal and K. Kendall, *High-temperature Solid Oxide Fuel Cells: Fundamentals, Design and Applications*. Elsevier Science, 2003, p. 406.

[15] M. Mogensen and K. Kammer, "Conversion of Hydrocarbons in Solid Oxide Fuel Cells," *Annual Review of Materials Research*, no. 13, 2003.

[16] Z. Zhan, J. Liu, and S. A. Barnett, "Operation of anode-supported solid oxide fuel cells on propane–air fuel mixtures," *Applied Catalysis A: General*, vol. 262, no. 2, pp. 255-259, May 2004.

[17] Z. Zhan and S. A. Barnett, "Solid oxide fuel cells operated by internal partial oxidation reforming of iso-octane," *Journal of Power Sources*, vol. 155, no. 2, pp. 353-357, 2006.

[18] S. Park, R. Craciun, J. M. Vohs, and R. J. Gorte, "Direct oxidation of hydrocarbons in a solid oxide fuel cell. I. Methane oxidation," *Journal of the Electrochemical Society*, vol. vol, pp. 146pp3603-3605, 1999.

[19] R. J. Gorte, S. Park, J. M. Vohs, and C. Wang, "Anodes for direct oxidation of dry hydrocarbons in a solid-oxide fuel cell," *Advanced Materials*, vol. 12, no. 19, pp. 1465-1469, 2000.

[20] A. M. Sukeshini, B. Habibzadeh, B. P. Becker, C. A. Stoltz, B. W. Eichhorn, and G. S. Jackson, "Electrochemical Oxidation of H2, CO, and CO/H2 Mixtures on Patterned Ni Anodes on YSZ Electrolytes," *Journal of The Electrochemical Society*, vol. 153, no. 4, p. A705, 2006.

[21] H. Zhu, R. J. Kee, V. M. Janardhanan, O. Deutschmann, and D. G. Goodwin, "Modeling elementary heterogeneous chemistry and electrochemistry in solid-oxide fuel cells," *Journal of the Electrochemical Society*, vol. 152, no. 12, p. A2427-A2440, 2005.

[22] V. M. Janardhanan and O. Deutschmann, "Numerical study of mass and heat transport in solid-oxide fuel cells running on humidified methane," *Chemical Engineering Science*, vol. 62, no. 18–20, pp. 5473-5486, Sep. 2007.

Chapter 2

Thermodynamics analysis of deposited carbon on a Ni anode of SOFCs

Abstract

Two carbon deposition mechanisms have been identified: homogeneously formed soot and catalytically grown carbon fiber. All previous thermodynamic analyses have used graphite to represent the properties of the deposited carbon regardless of the formation mechanism. However, the energetic and entropic properties of these two types of carbon are different from those of graphite. We propose a new thermodynamic analysis in which we: (1) use experimentally measured data for carbon fiber if the anode includes Ni catalyst; and (2) use soot precursors such as CH_3 and C_2H_2 to predict soot formation. The new approach improves the prediction of the onset of carbon deposition where previous analyses failed.

Nomenclature

Symbol	Meaning	Common Units
$\mathbf{A}$	formula matrix	
$\mathbf{A_C}$	Sub-matrix corresponding to the component species in the formula matrix	
$\mathbf{A_R}$	Sub-matrix corresponding to the remaining species in the formula matrix	
a_i	Activity of species i, $a_i = \exp\left(\frac{\mu_i(T,P,x) - \mu_i^0(T,P)}{\Re T}\right)$	
a_{ki}	the number of kth element in the molecular formula of species i = the entry of the formula matrix	
b_k	number of moles of the kth element in the system	
$\mathbf{b}$	element-abundance vector	
C	rank(**A**)	
G	Gibbs Free Energy	[J/mol]
$\nabla \mathbf{G} = \frac{\partial G}{\partial \xi}$	the gradient vector of G	
$\frac{\partial^2 G}{\partial \xi^2}$	Hessian matrix of G	[J/K]
$\mathbf{I_R}$	R × R identity matrix	
J_c	Critical Current Density	[A/cm^2]
K	Equilibrium Constant	
Min	minimize	
M	number of elements	
N	number of species	
$\mathbf{N}$	stoichiometric matrix	
n_i	Number of moles of species i	
$\mathbf{n}$	species-abundance vector with entries n_i	

p	Pressure	[Bar]
$\Re$	Ideal Gas Constants	8.31 [J/mol K]
R	Maximum number of linearly independent chemical equations; (=N-C)	
T	Temperature	[K]

Greek Symbol	**Meaning**	**Common Units**
α, β	Driving force for carbon deposition	
α	an index for a phase	
ν_j	stoichiometric vector of reaction j	
ν_{ij}	stoichiometric coefficient of the i th species in the j th stoichiometric vector	
ξ_j	the extent of reaction j	
$\boldsymbol{\xi}$	Extent of reaction vector with entries ξ_j	
μ_i	chemical potential of species i	
$\boldsymbol{\mu}$	chemical potential vector with entries μ_i	
δ	Change in (a quantity)	
$\delta^*_{k,\alpha}$	1 if species k is in any multispecies phase α ; zero otherwise	
$\delta_{k,\alpha}$	1 if species k is in the particular phase α ; zero otherwise	
π_m	number of multi-species phases	
ω	step-size parameter	

Subscript	**Meaning**
c	Critical

Superscript	**Meaning**
0	Initial value
m	An iteration index
T	Transpose of a vector or a matrix

2.1. Introduction

One of the biggest challenge to operating SOFCs on HC fuels directly is the performance degradation caused by carbon deposition [1–26]. Deposited carbon can (1) block the pores of the anode and inhibit gas transport, (2) prevent reforming reactions by covering or breaking the metal catalyst, or (3) stop current generation by blocking the triple phase boundary (TPB). At typical SOFC operating temperatures using hydrocarbon or syngas fuels, the extent of carbon formation depends on factors such as the steam/carbon ratio, the operating conditions, e.g., the temperature, pressure, and current density, as well as the anode design including the porosity of the structure and the anode catalyst. Although it is possible to minimize carbon deposition on traditional Ni-YSZ anodes by providing sufficient H_2O in the fuel stream, the amounts required are generally excessive, diluting the fuel and reducing the overall efficiency. In addition, this creates device- and system-scale complexity because of the need for water management solutions. In light of this, the analysis of carbon deposition in the SOFC anode is necessary.

Under typical SOFC operating conditions, there are two dominant carbon formation mechanisms [27]; (1) homogeneously formed soot consisting of polycyclic aromatic hydrocarbons (PAHs), and (2) heterogeneously formed carbon fiber on the catalyst surface. These mechanisms have been studied extensively in applications such as reforming [28,29], carbon nano-fiber production [30–33], and combustion [34–36]. However, previous thermodynamic analyses of carbon formation [12,14,21–24,37] has been based on the assumption that thermodynamic properties of graphite can represent those of carbon deposits even though the thermodynamic properties of carbon deposits have been reported to be different

from those of graphite [4,5,38–40]. Previous thermodynamic analyses failed to explain many experimental observations [5,13,14,41]. Thus, the goal of the present study is to improve the prediction of carbon deposition by incorporating more accurate representation of carbon deposition mechanisms while using experimentally measured carbon fiber properties instead of graphite as a surrogate for carbon deposits. Moreover, soot precursors are used to predict the formation of homogeneously deposited carbon.

The mechanisms of the two types of carbon deposition are examined in Section 2.2. Experimental results and analysis of carbon deposition in SOFCs are reviewed and an improved thermodynamic analysis approach is proposed in Section 2.3. A multiphase equilibrium solver is developed in Section 2.4, and is used to predict general trends in Section 2.5. Cases that previous thermodynamic analyses failed to explain are revisited in Section 2.6 using the proposed approach. Results are discussed and conclusions are presented in Section 2.7 and 2.8, respectively.

2.2. Carbon Deposition Mechanisms

Carbon deposition mechanisms have been studied extensively in the reforming industry [28,29], in carbon nano-fiber (CNF) formation [30–33], and in combustion [34–36], but not as much in SOFCs. Three types of carbons: carbon fiber, encapsulating polymers, and pyrolytic carbon, have been identified in deposited carbon in these applications. For each, the formation characteristics and resulting impact on the catalyst are summarized in Table 2.1.

Table 2.1. Types of deposited carbon and their characteristics (Taken from [29])

	Whisker carbon	Encapsulating polymers	Pyrolytic cabon
Formation mechanism	▪ Diffusion of C though Ni-crystal ▪ Nucleation and whisker growth with Ni crystal at top	▪ Slow polymerization of C_nH_m radicals on Ni surface, into encapsulating film	▪ thermal cracking of hydrocarbon ▪ deposition of C-precursors on catalyst
Effects	▪ No deactivation of Ni-surface ▪ Break-down of catalyst and increasing pressure drop	▪ Progressive deactivation	▪ Encapsulation of catalyst particle ▪ Deactivation and increasing pressure drop
Temperature	> 720K	< 770K	> 870K
Critical parameters to promote carbon formation	▪ High temperature ▪ Low H2O/ C_nH_m ▪ Low activity aromatic feed ▪ No enhanced H2O adsorption	▪ Low temperature ▪ Low H_2O/C_nH_m ▪ Low H_2/C_nH_m ▪ Aromatic feed	▪ High temperature ▪ High void fraction ▪ Low H_2O/C_nH_m ▪ High pressure ▪ Activity of catalyst

The type of deposited carbon depends on the temperature, pressure, porosity, and fuel composition. Encapsulating carbon is known to form by slow polymerization of C_nH_m radicals on the Ni surface, most often at temperatures lower than 500°C. Because the operating temperatures of SOFCs are typically well above this value, it is not of much concern in this application. Hence, we will focus on the other two carbon deposition mechanisms: (1) homogeneously formed carbon, often called soot formation, and (2) heterogeneously formed carbon on a catalyst surface, often called carbon nano-fiber because its shape is fibrous. In this

section, the formation mechanism, effect of the deposited carbon on the catalyst performance, and its thermodynamic properties are reviewed for each type.

2.2.1. Homogeneously formed carbon: Soot

2.2.1.1. Soot formation mechanism

Models of soot formation and oxidation have been studied in combustion, and are reviewed by Kennedy [34]. Soot is mostly carbon; but other elements such as hydrogen and oxygen are usually present. It is produced during high temperature pyrolysis or combustion of hydrocarbons typically on the rich side of diffusion flames. The soot formation mechanism has been described as follows: (1) as the hydrocarbon pyrolyzes, it produces smaller hydrocarbons, in particular acetylene(C_2H_2) [34] and methyl radicals (CH_3) [1,2]; (2) CH_3 recombines as the first step toward molecular-weight growth [1,2] up to the first aromatic species by H-abstraction-C_2H_2-addition (HACA) [35] as shown in Figure 2-1; (3) the aromatics species grow by the addition of other aromatic species to form larger polycyclic aromatic hydrocarbons (PAHs) as shown in Figure 2-2. The detailed kinetics model of soot formation is comprised of two main parts: (1) gas-phase chemistry, which includes the pyrolysis of the primary hydrocarbon and the formation of higher hycrocarbons up to pyrene, and (2) the soot particle growth. Figure 2-2 describes the evolution of the soot particle by collisional coagulation and surface growth.

$$CH_3 + CH_3 \rightarrow C_2H_6 \xrightarrow{H-Abstraction} C_2H_5 \xrightarrow{\beta-scission} C_2H_4 \xrightarrow[\beta-scission]{H-Abstraction}$$
$$C_2H_2 \xrightarrow{+CH_3} C_3H_5 \xrightarrow{H-Abstraction} C_3H_4 \xrightarrow{C_2H_2} C_5H_8$$

Figure 2-1. Gas phase chemistry leading to cyclopentene (C_5H_8) by H-abstraction-C_2H_2-addition (HACA)

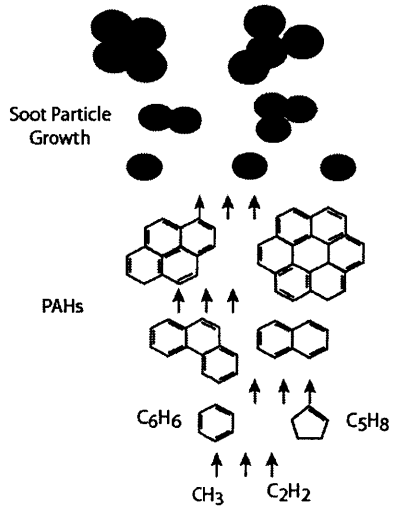

Figure 2-2. Schematics describing the aromatic species growth to polycyclic aromatic hydrocarbons (PAHs) and soot particle dynamics such as surface growth and collisional coagulation.

Appel et al. [35] developed a kinetics model for soot formation incorporating detailed chemistry and physics. The gas-phase chemistry is based on the Wang and Frenklach mechanism [42] consisting of 99 chemical species and 531 reactions. It includes the pyrolysis, formation of linear hydrocarbons up to C6 species, the formation of benzene (C_6H_6) and further reactions leading to pyrene ($C_{16}H_{10}$), as well as the oxidation pathways of the aromatic species. The soot particle dynamics model describes the growth of polycyclic aromatic hydrocarbons (PAHs) beyond pyrene considering PAH coagulation, aggregation and surface growth. For their simulation of nine laminar premixed flames, the temperature profiles were taken from the experimental data. Their numerical simulation was compared to the experimental results and the agreement between the model predictions and experimental data was reported to be within a factor of 3. This level of agreement was reported to be very encouraging, considering the current uncertainty in the thermodynamics and kinetics of aromatics and soot chemistry.

Lindstedt and co-workers have developed soot nucleation and growth models for laminar and turbulent diffusion flames under the assumption that acetylene is primarily responsible for the nucleation and growth of the soot particles. The mechanism has been extended and improved on since then. A detailed review of the mechanism can be found in [34].

2.2.1.2. Effect of soot on catalysts performance

Pyrolytic carbon is normally found as dense shale on reactor walls during pyrolysis of HC. The carbon deposits encapsulate and deactivate the catalyst particles, eventually filling out the void between the particles [29,43]. Bae and co-workers studied the homogenously formed carbon deposits in diesel auto-thermal reformer [44,45] and in the SOFC anode [46]. They reported rapid degradation of performance of the reformer/SOFCs. The homogeneously formed carbon deposits deactivate the catalyst particles and blocks the pores of the porous catalyst.

2.2.2. Heterogeneously formed carbon deposition: CNF

2.2.2.1. CNF formation mechanism

Carbon deposition from methane in the presence of Ni catalyst has been extensively studied in the methane reforming industry [29,30,43,47,48]. This knowledge can be utilized in SOFCs because the SOFC anode environment is similar to that in the methane reforming reactor in two ways: (1) the gas temperature ranges from 800-1050K; (2) The microstructure of the reforming catalyst is almost identical to that of the SOFC anode in that the Ni catalyst is dispersed in the supporting material, Al_2O_3 for reforming and YSZ in an SOFC.

Carbon forms on catalysts such as Ni, Fe, and Co in a fiber-like shape, called carbon nano-fiber (CNF) [29,30,47,49]. To study CNF growth mechanism, the catalysts, Ni, Fe, and Co,

have been used either as bulk particles (size typically 100 nm) or as supported particles (10-50 nm). All of these metals can dissolve carbon and form metal carbide. Typically, methane, carbon monoxide, syngas, ethyne and ethane are employed to provide the carbon atoms [30].

The mechanism of formation of CNF [27,29,50,51] that has generally been accepted includes (1) hydrocarbon adsorption on the surface, (2) conversion of the adsorbed hydrocarbon to adsorbed surface carbon via surface reactions, (3) subsequent segregation of suface carbon into layers near the surface, (4) diffusion of carbon through Ni, and (5) the precipitation on the rear side of the Ni particle. These series of processes lead to the formation of CNF.

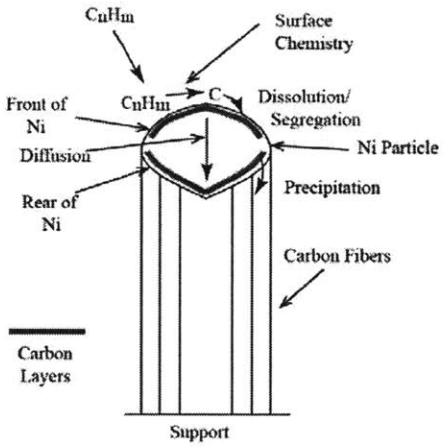

Figure 2-3. Schematic representation of the catalytic growth of a CNF using a gaseous carbon-containing gas. Step 1: decomposition of carbon-containing gases on the metal surface. Step 2: carbon atoms dissolve in and diffuse through the bulk of the metal. Step 3: precipitation of carbon in the form of a CNF consisting of graphite.

De Chen extended the microkinetic model [52] for CH_4 reforming on Ni to include the CNF formation processes as follows [53,54].

$$\text{Dissolution/segregation: } C(Ni) \leftrightarrow C_{Ni,f} + (Ni)$$

Diffusion of carbon through Ni: $C_{Ni,f} \leftrightarrow C_{Ni,r}$

Precipitation/dissolution of carbon: $C_{Ni,r} \leftrightarrow C_f$

Encapsulating carbon formation: $3C(Ni) \rightarrow 3C_{encap}$

where $C_{Ni,f}$ is the carbon dissolved in Ni at the front of the particle,; $C_{Ni,r}$ is the carbon dissolved in Ni at the rear of the particle (support side); C_f is carbon fiber; $C_{encapsulating}$ represents the encapsulating carbon formation on the Ni surface, which deactivates the catalyst.

The properties of carbon on the front side of Ni and the carbon fiber on the rear side are different. The different chemical potentials of these carbon materials result in different solubility in the front and rear side of the Ni crystal, thus creating a driving force for the diffusion of carbon through Ni [53,54]. Carbon filaments do not deactivate the catalyst as encapsulating carbon does. The encapsulating carbon deactivates the catalysts by decreasing the total number of active sites on Ni. The filamentous carbon growth rate is determined by diffusion under the assumption that the dissolution, segregation and precipitation are fast and in equilibrium. Knowledge on encapsulating carbon formation is limited and the formation step of encapsulating carbon is assumed to be irreversible. De Chen's mechanism is the only available kinetic mechanism of filamentous carbon formation. Moreover, the equilibrium assumption and the corresponding properties related to the dissolution, segregation and precipitation steps need to be improved and the irreversibility of the encapsulating carbon has not been confirmed.

2.2.2.2. The effect of CNF on catalyst performance

As shown in Figure 2-3, the filamentous carbon grows with the nickel catalyst at the top of the carbon fiber. The catalyst particle is destroyed when the carbon fiber hits the pore wall.

Carbon fibers may also result in increasing the pressure drop by blocking the gas passage [29,43]. In some cases, the catalyst is not deactivated and large amount of carbon can accumulate [29]. Thus, CNF formation may lead to a stable operation with gradual degradation of performance.

2.2.2.3. Thermodynamic properties of CNF

Researchers studied carbon formation resulting from the decomposition of CO and CH_4 on a Ni catalyst for more than 75 years [40]. Many reported that the thermodynamic properties of the deposited filamentous carbon are different from those of graphite [38–40].

The thermodynamic properties of carbon deposited on Ni have been measured for the following two reactions.

$$CH_4 \leftrightarrow C + 2H_2 \quad \text{(R. 1) Methane cracking reaction}$$

$$2CO \leftrightarrow C + CO_2 \quad \text{(R. 2) Boudouard Reaction}$$

By measuring the equilibrium concentration of the gas species, the Gibbs free energy of the deposited carbon can be retrieved. Rostrup-Nielson [38] and De Bokx et al. [39] measured the difference between the Gibbs free energy of the deposited carbon and that of graphite using the following equation.

$$\Delta G = G_{CNF} - G_{graphite} = -RT \ln\left(\frac{K_{CNF}}{K_{graphite}}\right)$$

where $K_{graphite}$ is the equilibrium constant computed using graphite properties; K_{CNF} is the equilibrium constants calculated using the measured gas pressures in the experiments and assuming that the activity of the deposited solid carbon is unity as follows:

$$K_{CNF} = \frac{P_{H_2}^2}{P_{CH_4}} \text{ for (R. 1)}$$

$$K_{CNF} = \frac{P_{CO_2}}{P_{CO}^2} \text{ for (R. 2)}$$

Figure 2-4 and Figure 2-5 show the equilibrium constants measured by Rostrup-Nielson [38] and De Bokx et al. [39] in comparison with the equilibrium constants computed using the graphite properties. It is clearly shown that the measured equilibrium constants are different from the values computed using graphite, which implies that the deposited carbon has different thermodynamic properties than graphite.

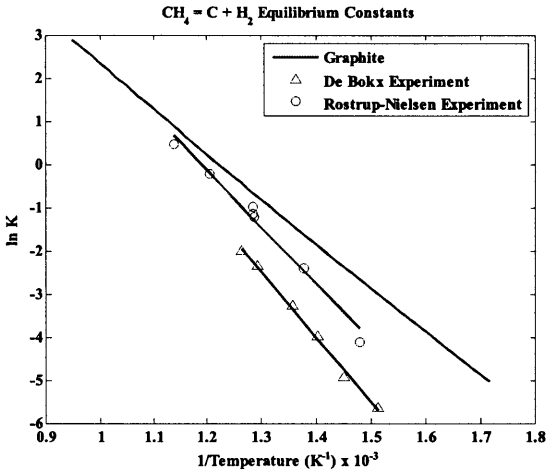

Figure 2-4. Measured equilibrium constants for CH_4 decomposition: triangles for De Bokx et al's measurement over 50 wt% Ni/SiO2; circles for Rostrup-Nielsen over 25 wt% Ni/MgO. The equilibrium constants based on graphite data are also included. Reproduced from Alstrup [40]

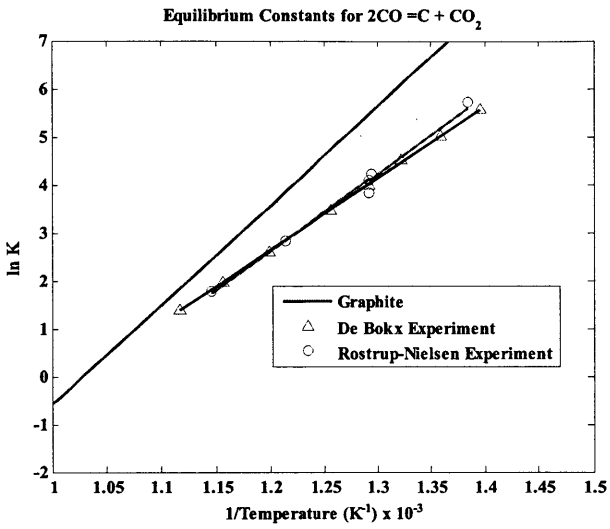

Figure 2-5. Measured equilibrium constants for the Boudouard reaction: triangles for De Bokx et al's measurement over 50 wt% Ni/SiO2; circles for Rostrup-Nielsen over 25 wt% Ni/MgO. The equilibrium constants based on graphite data are also included. Reproduced from Alstrup [40]

The discrepancy between the thermodynamic properties of deposited carbon and those of graphite was attributed to: (a) the additional energy needed to form the deposited carbon or (b) an intermediate phase forming at the interface between the Ni catalyst and the deposited carbon.

Rostrup-Nielsen [38] suggested that the difference can be explained by the contribution of the surface energy and the disordered structure of the filament. He concluded that the intermediate Ni_3C is unstable between 400°C and 1600°C and it would not change the equilibrium constant. Later, Alstrup [40] improved Rostrup-Nielsen model by adding the bending energy derived by Tibbetts [55] to explain the difference between graphite and the carbon fiber. While Rostrup-Nielsen [38] introduced the effect of the disordered structure energy term without a mathematical expression, Nolan et al. [56] provided the expressions for the graphite stacking misalignment enthalpy and entropy.

Manning et al. [57] proposed that the observed difference is due to the formation of an intermediate meta-stable carbide phase(Ni_3C) at 700K, as shown in (R. 3) and (R. 4) below, which is less important at higher temperatures. De Bokx et al. [39] supported Manning's argument by refuting Rostrup-Nielsen's explanation based on the fact that the experimentally measured difference in the Gibbs energy is comparable to the Ni_3C formation Gibbs free energy and is higher than the value obtained from the surface energy and the energy of structural disorder.

$$CH_4 + 3Ni \leftrightarrow Ni_3C + 2H_2 \qquad \text{(R. 3)}$$

$$3\,Ni + 2CO \leftrightarrow Ni_3C + CO_2 \qquad \text{(R. 4)}$$

Alstrup [40] proposed a new model combining the additional energy and the intermediate phase approaches to explain carbon filament growth. His model is essentially similar to that used in the additional energy approach, and the difference lies in that the intermediate Ni_3C phase provides the driving force for the migration of the carbon atoms through the nickel particle by maintaining a high carbon concentration at the front of the Ni particle.

Depending on the structure of the deposited carbon, the relevant explanation may differ. If the carbon encapsulating the Ni catalyst is prevalent, the interface energy would be dominant. On the other hand, if the deposited carbon has a form of carbon nano-fiber, the interface occupies only a fraction of the entire structure. The difference can be dictated by the additional energy required to create the structure such as the surface energy, the bending energy and the disordered entropy.

2.2.2.4. Summary

Homogeneously formed soot has the chemical structure of polycyclic aromatic hydrocarbons, whose thermodynamic properties are different from those of graphite. Once soot is formed, it encapsulates and deactivates the catalyst particles, eventually filling out the void between the particles. Soot formation and deposition is usually accompanied by rapid degradation of the catalyst performance. Heterogeneously grown carbon nano-fiber on catalysts has the same chemical composition as graphite. However, its thermodynamic properties have experimentally been shown to differ from those of graphite. Carbon fiber does not deactivate the catalyst particles and instead leads to gradual degradation of the catalyst performance.

2.3. Literature Review on SOFCs

Since SOFCs have been shown to operate directly on hydrocarbon fuels, there has been research on carbon deposition on their anodes under different conditions [1–26]. Gorte and co-workers [3–5,7–10] used Cu-based anodes and pure YSZ anodes, which do not catalyze carbon fiber formation. Hence, in their case, the deposited carbon should be homogeneously formed soot. On the other hand, Barnett and co-workers [11–18] utilized conventional Ni-based anodes, which promote homogeneously and heterogeneously formed carbon deposits. In this section, both experimental findings and analytical approaches to model carbon deposition in SOFC anodes are reviewed. An improved thermodynamic analysis is proposed considering both carbon deposition mechanisms, soot and CNF.

2.3.1. Experimental results on homogeneous carbon formation

Gorte and co-workers focused on Cu-based anodes in SOFCs using HC fuels [3–5,7–10]. McIntosh et al. [3] observed an improvement in the performance of SOFCs with Cu-ceria-YSZ anodes at 700°C when undiluted CH_4, propane, or n-butane were fed to the cell. Toluene and decane were also used but as 75% mixture in N_2. Large increases in the power density were observed during operation with H_2 after the anode had been exposed to any of the hydrocarbons except methane. The performance enhancement was shown to be due to improved connectivity in the electron-conducting phase by the carbon deposited while the cell operated on a HC. The improved performance is completely reversible after the anode is re-oxidized. The deposited carbon was not graphitic because the deposits react at 400°C while graphite does not react until T> 700°C. McIntosh et al. [4] further investigated carbon deposition on Cu-YSZ anodes and confirmed that carbon layers play an important role in providing electronic conductivity near the TPB. The carbon deposits were dissolved in toluene and analyzed by gas chromatography-mass spectrometry (GC-MS). Compounds identified by the GC-MS analysis are aromatic, most with multiple, conjugated aromatic rings. They compared carbon deposits on Cu-based cermet and Ni-based cermet, and reported that the type and formation mechanism of deposited carbon on Cu-based cermet are very different from what is observed on Ni-based cermet. Because Cu is known not to catalyze carbon formation, as opposed to Ni, the carbon deposit on Cu-based anodes must have formed homogeneously; that is, it was soot. Kim et al. [5] increased the operating temperature to 800°C and observed the deactivation of the SOFCs at temperatures above 700°C. The cause of the deactivation was the filling of the pores with polyaromatic compounds formed by gas-phase, free-radical reactions. Formation of these compounds occurs at a negligible rate

below 700°C but increases rapidly above 700°C.

To study gas-phase kinetics within the anode channel, Sheng and Dean [19] conducted experiments with (50% n-C_4H_{10}+50% H_2O) and (50% n-C_4H_{10}/50% N_2) at p=0.8atm, residence time of 5 sec, and T=500-800°C in a quartz reactor. When the reactor temperature was raised to 700°C and above, carbon deposits were observed on the inner walls of the quarts reactor. Note that there was no catalyst; thus, the carbon formed was homogeneously formed soot.

Gupta et al. [20] conducted experiments to study fuel conversion and carbon formation of butane and ethanol under SOFC conditions. Butane and ethanol were fed into a quartz reactor where an YSZ disk was placed at the end of the reactor. Experiments were performed at 700, 750 and 800°C. Carbon deposits formed in all cases except for ethanol at T=700°C. Butane is found to be more prone to carbon deposition than ethanol. Because there is no catalyst in their study and pyrolysis occurs at 700°C for butane [5][4], the observed carbon should be formed via pyrolysis. The carbon deposits from pyrolysis are composed of polycyclic aromatic hydrocarbons (PAHs).

2.3.2. Experimental results on catalytically grown carbon

Barnett and co-workers focused on Ni-based anodes in SOFCs using HC fuels such as methane [11,12,14,18], propane [13,15], iso-octane [16,17]. In their experiments [11,12,14,18], methane was supplied as pure or slightly humidified (3%). Note that in steam reforming reactions, high steam/carbon (S/C) ratios, typically over 2, are used to suppress carbon deposition [23,58]). It was shown that SOFCs with Ni-based anodes can operate with methane at temperatures < 700°C [11,12,14]. At temperature higher than 700°C, carbon deposition can be

mitigated and eventually avoided as the current density increases. Lin et al. [14] defined a critical current density (J_c) above which SOFCs is free from performance degradation. The measured J_c is listed in Table 2.2. J_c increased with increasing temperature. Up to 700°C, gradual degradation was observed only at very low currents (< 0.1 A/cm^2). However, when T>700°C, rapid cell deactivation was observed at current densities below the critical current densities.

Table 2.2. Critical current density measured for methane fuel by Lin et al. [14]

Temperature (°C)	Critical current density (A/cm^2)
650	$0 < J_c < 0.1$
700	$0 < J_c < 0.1$
750	$0.8 < J_c < 1.2$
800	$1.4 < J_c < 1.8$

For a methane-fueled SOFC producing 1 mA/cm^2 at 700°C, cross-sectional SEM micrographs and X-ray diffraction (EXD) spectra confirmed that carbon was deposited on the anode surface facing the anode channel [14]. However, the anode surface facing the electrolyte appeared to be free from carbon. It was suspected that the reaction products at the TPB, H_2O and CO_2, may suppress carbon deposition. Similarly, in the anode of a SOFC using iso-octane/air fuel mixtures at 590°C, carbon was detected only on the anode surface facing the fuel channel [16]. In order to mitigate carbon deposition near the anode channel, Barnett and co-workers introduced a catalyst layer of Ru-CeO_2 when using propane [15] and iso-octane [16,17]. Furthermore, adding an inert barrier layer consisting of partially stabilized zirconia (PZO) and

CeO_2, both of which are resistant to coking, reduced J_c to less than 0.6 A/cm^2 from 1.8A/cm^2 for a methane-fueled SOFC at 800°C. Although some performance was sacrificed because of the additional diffusion layer, carbon deposition was mitigated. Because neither the catalyst nor the barrier layer is an electronic conductor, current was collected at the side of the anode.

Takeguchi et al. [23] experimentally investigated carbon deposition on Ni-YSZ cermet anode and the effect of adding alkaline earth metals (Mg, Ca, and Sr) to a Ni-YSZ cermet anode on carbon deposition. The addition of the alkaline earth metals retarded the carbon deposition rates. Among them, the CaO addition was effective in suppressing carbon deposition and promoting CH_4 reforming. However, the electrochemical activity of the anode slightly deteriorated. From SEM images of deposited carbon on Ni-YSZ cermet with CH_4 at 1000°C, bulky carbon fibers were observed, the diameter of which was far different from that observed in supported Ni catalyst in steam reforming. Nano-sized fiber could be grown from supported Ni catalyst while the diameter of the carbon fiber on Ni-YSZ cermet was on the order of micron. The Ni-YSZ cermet preparation method leads to larger Ni catalyst, which was suspected to be responsible for the larger carbon fiber.

2.3.3. Carbon deposition analysis

There have been mainly three approaches to predict carbon deposition in SOFCs: (1) thermodynamic analysis using Boudouard and methane cracking reactions only, (2) full equilibrium calculation with all possible reactions, and (3) kinetics analysis.

Armor [58] reported that the two major pathways for carbon formation at high operating temperature are the Boudouard reaction (R. 2) and the methane cracking reaction (R. 1). Based

on these two reactions, Klein et al. [26] defined two parameters representing the driving force for carbon deposition. The two parameters, α and β, are defined as:

$$\alpha = \frac{p_{CO_2} a_{carbon}}{p_{CO_2}^2 K_{Boudouard}} \tag{0.1}$$

$$\beta = \frac{p_{H_2}^2 a_{carbon}}{p_{CH_4} K_{cracking}} \tag{0.2}$$

where a_{carbon} represents carbon activity which was taken to be 1. p_i is the partial pressure of a gas species i. $K_{\text{Boudouard}}$ and K_{cracking} are the equilibrium constants of the Boudouard and the methane cracking reactions, respectively.

For each reaction, if α or β<1, the system is not at equilibrium and the reaction proceeds towards the right. In this case carbon deposition is thermodynamically favored. Equilibrium is reached when α or β=1. On the other hand, for α or β>1, carbon formation is thermodynamically impossible and the reaction proceeds towards the left. The same approach was applied by Vakouftsi et al. [25]. This approach was adopted in multi-dimensional CFD analysis [25,26] to reduce the complexity of the calculation. However, it should be noted that the two reactions can occur simultaneously, and when α<1 and β>1 or vice versa, this approach fails to provide a decisive thermodynamic prediction.

Most of carbon deposition equilibrium analysis in SOFCs [12,14,21–24,37] has been performed by minimizing the total Gibbs free energy of the system subject to element balance. This is equivalent to considering all possible reactions including the Boudouard and methane cracking reactions. This equilibrium approach can provide a thermodynamically accurate

prediction when there are many possible reactions that can lead to carbon formation. It is important to mentioned that all previous analyses assumed that graphite can be used to represent the properties of the carbon deposits [12,14,21–24,37].

Soot formation kinetics in SOFCs have been studied by Dean and co-workers for dry natural gas [1,59], butane [19], JP-8 [2], and ethanol and butane [20]. In their research, only gas phase chemistry was considered, without soot particle dynamics. The most recent mechanism involved 350 species and 3450 reactions [59], representing oxidation and pyrolysis kinetics for hydrocarbons up to C6 species. It also included the molecular-weight growth reactions leading to PAH formation. When soot formation kinetics was coupled with the membrane-electrode assembly (MEA) model, the full soot formation mechanism was reduced to 37 species and 150 reactions to reduce the computational complexity. By adding the reduced soot formation mechanism, their computational time increased from 5 minute to 5 hours. Note that in the soot formation simulation, the temperature profile in the calculation domain is usually taken from experiments [19,35] or assumed to be uniform [2] to eliminate the computational time required for solving the energy equation. Because the actual soot is neither defined nor included in the model, the propensity to form PAH deposits was characterized by the sum of mole fractions of all the product species that contain five or more carbon atoms, designated as C5+. After comparing their simulation to experiments using butane in quarts tubes [19], a mole fraction of 10^{-3} for C5+ was suggested as an approximate threshold for deposit formation.

There has been no attempts to implement the catalytic growth mechanism of carbon fiber on Ni because the only available kinetics mechanism proposed by de Chen [53,54] needs to be

improved further before it can be applied for quantitative prediction.

2.3.4. Summary and Improvement

In Cu-based and pure-YSZ anodes, soot consisting of PAHs [4] homogeneously forms at temperatures above 700°C. Below this temperature, soot formation is negligible and kinetically limited [3,5,19,20]. Soot deactivates the SOFCs by covering the catalysts and filling the pores. In Ni-based anodes, carbon fibers were observed [23] and products forming as a result of current generation mitigated performance degradation [14]. The critical current densities required to avoid performance degradation increased rapidly as the temperature was raised above 700°C [14], which is consistent with the characteristics of soot formation. Regardless of the presence of Ni in the SOFC anodes, soot formation is anticipated when T>700°C. Catalytically grown carbon fiber is expected when SOFC anodes contain catalysts such as Ni, Fe, or Co.

With regard to the kinetics analysis of carbon deposition, only gas phase reactions up to C5+ species were implemented [1,2,19,20,59] without incorporating the growth mechanism to PAHs and the subsequent soot particle dynamics. Implementing a reduced soot formation mechanism increased the computational time from 5 minutes to 5 hours. Any attempts to include the carbon fiber growth mechanism have not been made. Most of the carbon deposition prediction studies in SOFCs utilized thermodynamic analyses [12,14,21–24,37], all of which assumed that graphite can represent carbon deposits regardless of its formation mechanism. There are several cases [5,13,14,41] where thermodynamic calculation cannot explain experimental observation. Those cases were used to conclude that carbon formation is kinetically controlled.

It has been clearly shown that the deposited carbon, either in carbon fiber form or in soot form, has different thermodynamic properties from graphite. For catalytically grown carbon fiber, the Gibbs free energy was measured and reported [38,39]. However, this value has never been utilized in the thermodynamic analysis of carbon deposition. For the homogeneously grown soot, only concentration of precursors such as C5+ species, not the actual soot concentration, were used to predict soot formation because working with full soot formation mechanism requires very large computational time.

In this work, we propose the following approach to predict carbon deposition based on the experimental findings and the current analysis methods.

(1) Soot forms homogeneously at T>700°C regardless of the presence of Ni, Fe, or Co. The prediction of soot formation will be examined using soot precursors such as CH_3 and C_2H_2 instead of graphite. It is assumed that it is impossible to form soot at T<700°C.

(2) Catalytically grown carbon fiber has different Gibbs free energy from that of graphite. The amount of carbon fiber is calculated using the experimentally measured Gibbs free energy.

After developing a multiphase equilibrium solver in Section 2.4, this approach is applied to the analysis in Section 2.5. The cases where previous thermodynamic analysis failed to explain experimental observations are revisited in Section 2.6.

2.4. Thermodynamic analysis method

The equilibrium state of a mixture can be calculated by minimizing the total Gibbs free energy of the mixture while applying the constraint of element conservation. The element

conservation constraints can be incorporated in two ways [60–62] :

(1) non-stoichiometric formulation: the element conservation equations are given as constraints. The resulting equilibrium problem is a constrained optimization problem.

(2) stoichiometric formulation: the element conservation equations are incorporated by means of stoichiometric equations and the extent of reactions. The equilibrium problem becomes an (essentially) unconstrained optimization problem.

The two approaches are mathematically equivalent [60]. The Brinkley-NASA-RAND (BNR) algorithm and the Villars-Cruise-Smith (VCS) algorithm are the most advanced algorithms in non-stoichiometric and stoichiometric approaches, respectively. The VCS algorithm is known to be better in handling multiphase problems, especially those involving single-species phases[60–62] such as the solid phase including only carbon species in the present analysis. In this section, the VCS algorithm is described and the equilibrium code based on VCS is developed.

2.4.1. Stoichiometric formulation

Element conservation Equations can be expressed as follows:

$$\sum_{i=1}^{N} a_{ki} n_i = b_k; \qquad k = 1,2,...,M \tag{2.1}$$

where a_{ki} is the number of the kth element in the molecular formula of species i; n_i is the number of moles of i; b_k is the fixed number of moles of the k^{th} element in the system; M is the number of elements; and N is the number of species.

The nomenclature and notations in [60–62] will be followed here. The element

conservation equations are referred to as the element-abundance equations in the equilibrium calculation. In vector-matrix form, the element-abundance equations in (2.1) are

$$\mathbf{An} = \mathbf{b} \tag{2.2}$$

where **A** is the formula matrix whose entries are a_{ki}, **n** is the species-abundance vector whose entries are n_i, and **b** is the element-abundance vector whose entries are b_k.

The stoichiometric vector, ν_j, is defined as

$$\mathbf{A}\nu_j = \mathbf{0}; \qquad (\nu_j \neq \mathbf{0}) \qquad j = 1,2,...,R \tag{2.3}$$

where R is the number of linearly independent solutions of equation (2.3). R corresponds to the number of possible reactions among the given species. The quantity R is given by

$$R = N - C \tag{2.4}$$

where C=rank(**A**).

Equation (2.3) can also be written as

$$\sum_{i=1}^{N} a_{ki}\nu_{ij} = 0; \qquad k = 1,2,...,M; \qquad j = 1,2,...,R \tag{2.5}$$

where ν_{ij} is called the stoichiometric coefficient of the i th species in the j th stoichiometric vector.

The general solution of equation (2.1) or (2.2), a set of M equations in N unknowns, is

$$\mathbf{n} = \mathbf{n}^{\circ} + \sum_{j=1}^{R} \nu_j \xi_j \tag{2.6}$$

where $\mathbf{n}^{\circ}$ is an initial composition and the quantities ξ_j are a set of real parameters, corresponds to the extent of reaction.

The stoichiometric matrix **N** is defined as a collection of the stoichiometric vectors as

$$\mathbf{N}=\left(\mathbf{v}_1,\mathbf{v}_2,...,\mathbf{v}_R\right) \tag{2.7}$$

Component species are defined as a set of C species, whose set of formula vectors $\{\mathbf{a}_1,\mathbf{a}_2,...,\mathbf{a}_C\}$ satisfies $rank(\mathbf{a}_1,\mathbf{a}_2,...,\mathbf{a}_C)=C$ where $C=rank(A)$. When we arrange the formula matrix with the order of the C component species followed by the remaining R (=N-C) species as follows

$$\mathbf{A}=\left(\mathbf{A}_C,\mathbf{A}_R\right) \tag{2.8}$$

where $\mathbf{A}_C$ is the column vectors corresponding to the component species, $\mathbf{A}_R$ is the column vectors corresponding to the remaining species

then, the stoichiometric matrix can be derived through algebraic manipulation in [60] as follows,

$$\mathbf{N}=\begin{pmatrix}-\mathbf{A}_C^{-1}\mathbf{A}_R\\ \mathbf{I}_R\end{pmatrix} \tag{2.9}$$

where $\mathbf{I}_R$ is R × R identity matrix.

The mole numbers in (2.6) can be written as

$$\mathbf{n}=\mathbf{n}^o+\mathbf{N}\xi \tag{2.10}$$

where $\xi=\left(\xi_1,\xi_2,...,\xi_R\right)$

Once existing species are presumed, an equilibrium composition can be expressed in terms of the extents of reactions using (2.10), which satisfies the element conservation constraints.

2.4.2. Formulations of the equilibrium conditions

At fixed temperature (T) and pressure (P), the total Gibbs free energy of the system (G) should be at a minimum for the system to be at equilibrium. That is,

$$\min_{\mathbf{n}} G(\mathbf{n}) \tag{2.11}$$

subject to

$$\mathbf{An} = \mathbf{b} \tag{2.2}$$

and

$$\mathbf{n} \geq \mathbf{0} \tag{2.12}$$

where $G(\mathbf{n}) = \mathbf{n}^{\mathrm{T}}\boldsymbol{\mu}(T,P,\mathbf{n})$ and $\boldsymbol{\mu}(T,P,\mathbf{n})$ is the chemical potential vector with entries μ_i

When the stoichiometric formulation is applied, the equation (2.11) becomes

$$\min_{\xi} G(\xi) \tag{2.13}$$

such that

$$\mathbf{n} = \mathbf{n}^{\mathbf{0}} + \mathbf{N}\xi \geq \mathbf{0} \tag{2.14}$$

where $G(\xi) = \left(\mathbf{n}^{\mathbf{0}} + \mathbf{N}\xi\right)^{\mathrm{T}} \boldsymbol{\mu}\left(T,P,\mathbf{n}^{\mathbf{0}} + \mathbf{N}\xi\right)$

Without the non-negativity constraint (2.14), the constrained optimization problem becomes the unconstrained optimization problem. The number of unknown parameters is reduced to R (=N-C) from N+M (N unknown mole numbers and M Largrange multiplier for the constraints) in the constrained optimization approach.

The necessary condition that $G(\xi)$ be a minimum with respect to ξ is

$$\nabla G_j \equiv \left.\frac{\partial G}{\partial \xi_j}\right|_{T,P} = \sum_{i=1}^{N} \left.\frac{\partial G}{\partial n_i}\right|_{T,P} \frac{\partial n_i}{\partial \xi_j} = \sum_{i=1}^{N} \nu_{ij}\mu_i = 0 \qquad j = 1,2,...,R \tag{2.15}$$

where ∇G_j is the j-th element of the vector $\nabla \mathbf{G}$, which is defined as the gradient vector of G with respect to the extent of reaction vector ξ.

In vector-matrix form, equation (2.15) can be written as

$$\nabla \mathbf{G} \equiv \frac{\partial G}{\partial \xi} = \mathbf{0} \tag{2.16}$$

Equation (2.15) and (2.16) is the classical chemical formulation of the equilibrium condition that the sum of Gibbs free energy of reactants should be same with the sum of Gibbs free energy of products.

During iteration of the minimization calculation, the changes in the mole numbers $\boldsymbol{\delta n}^{(m)}$ from the m-th estimate $\mathbf{n}^{(m)}$ satisfying the element-abundance constraints are related to reaction-extent vector ξ by

$$\delta \mathbf{n} = \mathbf{N}\delta\xi \tag{2.17}$$

2.4.3. VCS algorithm

The minimization direction can be obtained by approximating the total Gibbs free energy by a quadratic function in vector-matrix form as

$$G = G_0 + \left(\left.\frac{\partial G}{\partial \xi}\right|_{T,P}\right)_0^T \delta\xi + \frac{1}{2}\delta\xi^T \left(\left.\frac{\partial^2 G}{\partial \xi^2}\right|_{T,P}\right)_0 \delta\xi \tag{2.18}$$

where 0 stands for the current iteration composition, $\left.\frac{\partial^2 G}{\partial \xi^2}\right|_{T,P}$ is Hessian matrix of G with respect to ξ, whose (i,j) element is defined as

$$\left.\frac{\partial^2 G}{\partial \xi_i \partial \xi_j}\right|_{T,P} = \frac{\partial}{\partial \xi_j}\left(\sum_{k=1}^{N} v_{ki}\mu_k\right)\Bigg|_{T,P} = \sum_{k=1}^{N}\left(v_{ki}\sum_{l=1}^{N}\left.\frac{\partial \mu_k}{\partial n_l}\right|_{T,P}\frac{\partial n_l}{\partial \xi_j}\right) = \sum_{k=1}^{N}\sum_{l=1}^{N} v_{ki}v_{lj}\left.\frac{\partial \mu_k}{\partial n_l}\right|_{T,P} \tag{2.19}$$

By applying the necessary condition, equation (2.16), to equation (2.18), $\delta\xi$ can be obtained as

$$\delta\xi^{(m)} = -\left(\frac{\partial^2 G}{\partial \xi^2}\right)^{-1}_{\mathbf{n}^{(m)}}\left(\frac{\partial G}{\partial \xi}\right)_{\mathbf{n}^{(m)}} \tag{2.20}$$

where m is an iteration index.

The inverse of Hessian matrix needs to be computed at every iteration. The VCS algorithm is based on this second-order minimization scheme and approximates the inverse of Hessian matrix directly without using the inverse of matrix operation. The approximation requires the component species in the formula matrix **A** in equation (2.8) should be those with the largest mole numbers. In other words, the entries of the formula matrix **A** are numbering the component species from 1 to M and the non-component species from (M+1) to N. In case of an ideal multiphase system, the chemical potential is defined as

$$\mu_{i,\alpha}\left(T,P,n_{i,\alpha}\right) = \mu_i^o\left(T,P\right) + \Re T \ln\frac{n_{i,\alpha}}{n_{t,\alpha}} \tag{2.21}$$

where $n_{i,\alpha}$ is the number of moles of species i in the phase α and $n_{t,\alpha}$ is the total number of moles in the phase α.

$\delta\boldsymbol{\xi}$ is derived in the VCS algorithm as follows [60]:

$$\delta\xi_j^{(m)} = -\frac{1}{\Re T}\left(\frac{\delta^*_{j+M,\alpha}}{n^{(m)}_{j+M}} + \sum_{k=1}^{M}\frac{\nu_{kj}^2\delta^*_{k,\alpha}}{n_k^{(m)}} - \sum_{\alpha=1}^{\pi_m}\sum_{k=1}^{N}\frac{\left(\nu_{ki}\delta_{k,\alpha}\right)^2}{n^{(m)}_{t,\alpha}}\right)^{-1}\nabla G_j^{(m)} \qquad \left(j=1,2,...,R\right) \qquad (2.22)$$

Here, α denotes a phase. $\delta^*_{k,\alpha}=1$ if species k is in any multispecies phase α and is zero otherwise. $\delta_{k,\alpha}=1$ if species k is in the particular phase α and is zero otherwise. $n_{t,\alpha}$ is the total number of moles in the particular phase α . π_m is the number of multi-species phases. $\Re$ is the ideal gas constant. T is temperature [K].

When the Hessian matrix in (2.22) becomes singular, $\delta\xi_j^{(m)}$ is determined using the first-order minimization scheme as

$$\delta\xi_j^{(m)} = -\frac{1}{\Re T}\nabla G_j^{(m)} \qquad (2.23)$$

2.4.3.1. Step-size parameter

Smith and Missen [62] reported that the introduction of step-size parameter, ω, which determines the distance between successive iterations in the direction defined by $\delta\boldsymbol{\xi}^{(m)}$, improved the convergence. The mole number change $\delta\mathbf{n}$ is multiplied by the scalar step-size parameter as

$$\mathbf{n}^{(m+1)} = \mathbf{n}^{(m)} + \omega^{(m)}\delta\mathbf{n}^{(m)} \qquad (2.24)$$

Determination of the optimal step-size is equivalent to the one-dimensional optimization problem

$$\min_{\omega>0} G\left(\mathbf{n}^{(m)} + \omega\delta\mathbf{n}^{(m)}\right) \qquad (2.25)$$

Many techniques are available for determining the step-size parameter such as interval

halving, golden-section search, and Fibonacci search. Smith and Missen [62] noted that too much computation time should not be spent for the exact minimizing ω. Usually it is preferable to determine ω only approximately and then proceed to the next iteration. A very simple procedure is proposed by Smith and Missen [62]. First, the value of

$$\left(\frac{dG}{d\omega}\right)_{\omega=1} = \sum_{i=1}^{N}\left(\frac{\partial G}{\partial n_i}\right)_{\mathbf{n}=\mathbf{n}^{(m)}+\delta\mathbf{n}^{(m)}} \delta n_i^{(m)} \tag{2.26}$$

is calculated. If this quantity is negative or zero, it is assumed that G has not passed the minimizing value of ω, then $\omega^{(m)} = 1$. If the quantity in (2.26) is positive, then

$$\omega^{(m)} = \frac{\left(dG/d\omega\right)_{\omega=0}}{\left(dG/d\omega\right)_{\omega=0} - \left(dG/d\omega\right)_{\omega=1}} \tag{2.27}$$

where

$$\left(\frac{dG}{d\omega}\right)_{\omega=0} = \sum_{i=1}^{N}\left(\frac{\partial G}{\partial n_i}\right)_{\mathbf{n}=\mathbf{n}^{(m)}} \delta n_i^{(m)} \tag{2.28}$$

The step-size parameter is further adjusted using the interval-halving method to satisfy the non-negativity constraints

$$\mathbf{n}^{(m+1)} = \mathbf{n}^{(m)} + \omega^{(m)}\boldsymbol{\delta}\mathbf{n}^{(m)} \geq \mathbf{0} \tag{2.29}$$

2.4.3.2. Special Features

The chemical equilibrium problem in general has special features [60,61] that make it atypical of many numerical problems, and these features must be accounted for: (1) Numerical difficulties, (2) single-species phase, and (3) initial composition

Numerical difficulties

There are often variations of many orders of magnitude in the values of the equilibrium mole numbers, which causes a severe scaling problem. When a species in a multispecies phase is present in a very small amount, the step-size parameter ω in equation (2.29) may be forced to be very small, to satisfy the non-negativity constraints. This would cause the VCS algorithm to be slow. Also, the chemical potential of a species approaches negatively infinite values as its amount approaches zero. This causes numerical difficulties for species present in very small amounts [61]. In order to avoid these numerical difficulties, the VCS algorithm adopted the following measure [60–62]. When species attain a concentration of less than a fraction 10^{-5} of the least abundant component species, they are removed from the main calculation and determined separately using equilibrium conditions in connection with component species. The mole number of minor species, which has been removed from main calculations, are determined by

$$n_{i,\alpha}^{(m+1)} = n_{t,\alpha}^{m} \exp\frac{\nabla G_j^*}{\Re T}; \qquad (i = j + C) \tag{2.30}$$

where α is the multispecies phase including species i.

Here,

$$\nabla G_j^* = \mu_i^* + \sum_{k=1}^{C} \nu_{kj} \mu_k \tag{2.31}$$

where μ_i^* is the chemical potential of species i excluding the logarithmic terms involving the mole numbers as follows

$$\mu_i = \mu_i^* + \Re T \ln\left(\frac{n_{i,\alpha}}{n_{t,\alpha}}\right) \tag{2.32}$$

Combination of equations (2.30) and (2.31) is equivalent to the necessary condition of the thermodynamic equilibrium in equation (2.15).

Single-species phases

The stoichiometric algorithm is ideally suited to problems involving single-species phase [60]. If n_i for a single-species phase tends to become negative during the course of the calculation, it is set to zero. On each subsequent iteration, ∇G_j for the stoichiometric equation forming one mole of the species is examined, where ∇G_j is given by

$$\nabla G_j = \mu_i + \sum_{k=1}^{C} \nu_{kj} \mu_k; \qquad (j = i - C) \tag{2.33}$$

If ∇G_j<0, the species is reintroduced into the calculation. By this means, single-species phases may readily enter and leave the main calculation during the course of the iterative procedure.

Initial composition

The mole number of species i, n_i, in a multi-species phase, is zero if, and only if, all species in the phase also have zero mole numbers [60]. In other words, if a multi-species phase is present, all species in the phase should have positive mole numbers, not zero. Hence, initial estimate including zero entries cannot be used. If n_i is zero, replace the value with 10^{-10} times the minimum value among the initial positive mole numbers.

2.4.4. Simulation procedures

The simulation procedures are as follows:

(1) Define possible species, their initial composition and the operating conditions (T, P).

(2) Read NASA Glenn coefficients [63] of the species and calculate their enthalpy and entropy. The Gibbs free energy of ideal gas species is calculated as

$$\mu_{i,\alpha}\left(T,P,n_{i,\alpha}\right)=\mu_i^o\left(T\right)+\Re T\ln P+\Re T\ln\frac{n_{i,\alpha}}{n_{t,\alpha}} \tag{2.34}$$

(3) Determine the component species such that their mole numbers are the largest ones in order to approximate the inverse of Hessian matrix as explained in Section 2.4.3. Construct the formula matrix **A** in equation (2.8) and calculate the stoichiometric matrix **N** in equation (2.9).

$$\mathbf{A}=\left(\mathbf{A_C},\mathbf{A_R}\right) \tag{2.8}$$

$$\mathbf{N}=\begin{pmatrix}-\mathbf{A_C^{-1}A_R}\\ \mathbf{I_R}\end{pmatrix} \tag{2.9}$$

(4) Determine the major and minor species: major species are the species involved in the main calculation and their number of moles should be larger than 10^{-5} of that of the least amount of component species; the minor species are the remaining species.

(5) Determine the existence of the single-species phase, solid carbon, using equation (2.33)

$$\nabla G_j=\mu_i+\sum_{k=1}^{C}\nu_{kj}\mu_k;\qquad\left(j=i-C\right) \tag{2.33}$$

where j is the species index for solid carbon phase

(6) Depending on the steps (4) and (5), update the formula matrix.

(7) Calculate $\delta\xi$ using equations (2.22) and (2.23)

$$\delta\xi_j^{(m)} = -\frac{1}{\Re T}\left(\frac{\delta^*_{j+M,\alpha}}{n^{(m)}_{j+M}} + \sum_{k=1}^{M}\frac{v_{kj}^2\delta^*_{k,\alpha}}{n_k^{(m)}} - \sum_{\alpha=1}^{\pi_m}\sum_{k=1}^{N}\frac{\left(v_{ki}\delta_{k,\alpha}\right)^2}{n_{t,\alpha}^{(m)}}\right)^{-1}\nabla G_j^{(m)} \qquad (j=1,2,...,R) \qquad (2.22)$$

$$\delta\xi_j^{(m)} = -\frac{1}{\Re T}\nabla G_j^{(m)} \qquad (2.23)$$

(8) Determine the step-size parameter ω using equations (2.27) and (2.29), and update the mole numbers $\mathbf{n}^{(m+1)}$

$$\omega^{(m)} = \frac{\left(dG/d\omega\right)_{\omega=0}}{\left(dG/d\omega\right)_{\omega=0} - \left(dG/d\omega\right)_{\omega=1}} \qquad (2.27)$$

$$\mathbf{n}^{(m+1)} = \mathbf{n}^{(m)} + \omega^{(m)}\boldsymbol{\delta}\mathbf{n}^{(m)} \geq \mathbf{0} \qquad (2.29)$$

(9) Update the minor species mole numbers using equation (2.30).

$$n_{i,\alpha}^{(m+1)} = n_{t,\alpha}^{m}\exp\frac{\nabla G_j^*}{\Re T}; \qquad (i = j + C) \qquad (2.30)$$

(10) compute ∇G_j with the updated mole numbers using equation (2.15).

$$\nabla G_j = \sum_{i=1}^{N} v_{ij}\mu_i \qquad j = 1,2,...,R \qquad (2.15)$$

(11) Check the convergence using the necessary condition for equilibrium as

$$\max\left|\nabla\mathbf{G}\right| < 0.5\times10^{-5}\left[J\right] \qquad (2.35)$$

(12) If the solution has converged, then stop. Otherwise, the whole calculation is iterated from the step (3)

The overall procedure is shown in Figure 2-6. The equilibrium calculation in our analysis is always converged. For an ideal multiphase system, the total Gibbs free energy is a convex

function [60]. Thus, the converged solution is a global minimum.

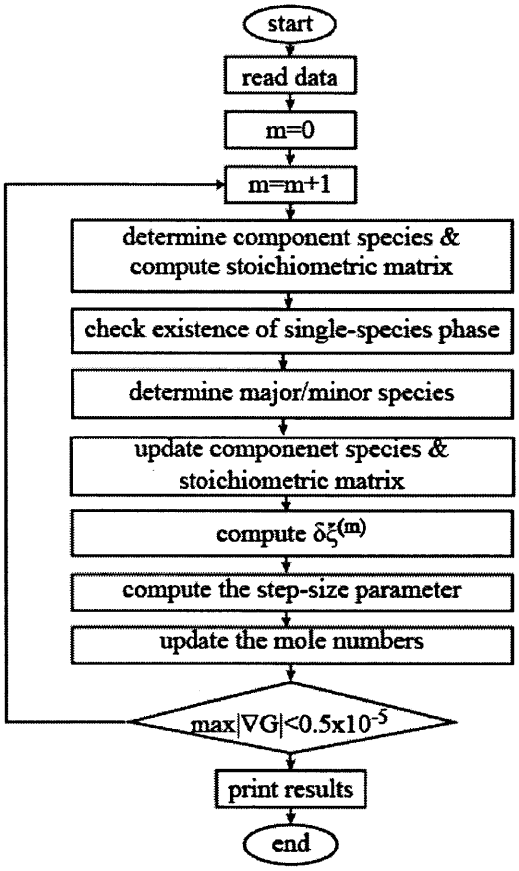

Figure 2-6. Flow chart of VCS algorithm simulation procedure

2.5. Simulation Results (I): General trend

The equilibrium composition depends not only on the fuel mixture but also on the temperature. The analysis results are presented either by (1) fixing the fuel composition and changing the temperature or (2) fixing the temperature and changing the compositions while displaying the results using a ternary diagram. Most of the results calculated are shown as the

number of moles rather than partial pressures because the partial pressure cannot be defined for solid phases, i.e., solid carbon in this study.

For the thermodynamic calculation, the following 34 species consisting of carbon, hydrogen and/or oxygen, are considered: C(solid), CH_4, H_2O, H_2, CO, CO_2, C_2H, C_2H_2, C_2H_3, C_2H_4, C_2H_5, C_2H_6, C_3H_7, C_3H_8, n-C_4H_{10}, nC_5H_{12}, n-C_8H_{18}, iso-C_8H_{18}, CH, CH_2, CH_2CO, CH_3, CH_3CHO, CH_3O, CH_3OH, C_2H_5OH, H, H_2O_2, HCCO, HCO, HO_2, O, O_2, and OH. All the thermodynamic properties are calculated using NASA Glenn coefficients [63]. The thermodynamic properties of solid carbon are taken from either De Bokx et al.'s data, which we call "De Bokx carbon" for short, or graphite, depending on the assumption. Figure 2-7 compares the Gibbs free energy of graphite and the catalytically grown carbon fiber measured by De Bokx et al. based on the Boudouard reaction [40].

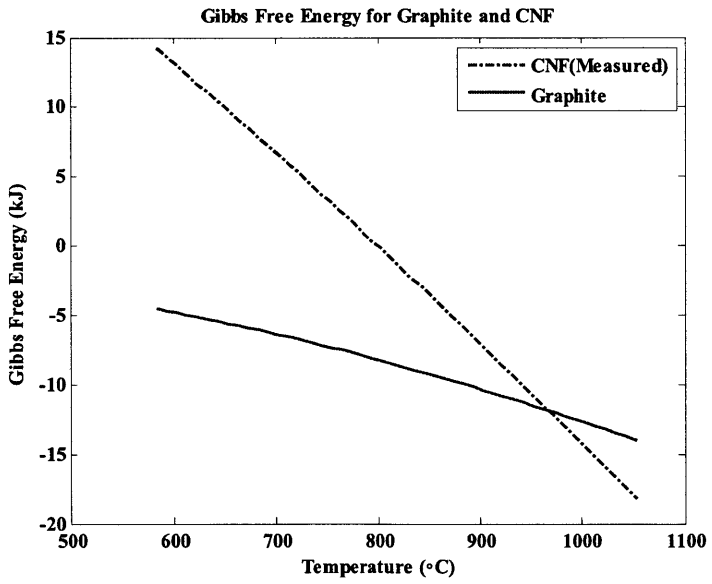

Figure 2-7. The Gibbs free energy computed from the measured equilibrium constants by De Bokx et al. [40] and the Gibbs free energy of graphite.

2.5.1. Results for different fuels

For a given fuel composition, the equilibrium composition of the products can be determined as a function of temperature. In the following, two fuels, methane and methanol, are examined for different steam-to-carbon ratios (S/C) at temperatures between 100 and 1000°C. Sasaki and Teraoka [21] pointed out that carbon deposition at temperatures lower than the typical SOFC operating temperatures of 600°C-800°C needs to be examined because the fuel experiences temperatures ranging from the room temperature to the SOFC operating temperatures during preheating and pretreatment processes. All the calculations are based on 1 mole of carbon. In the following, the simulation results based on De Bokx et al's experimental measurement will be referred to as 'the De Bokx'; the simulation results based on graphite thermodynamic properties will be referred to as 'graphite'.

2.5.1.1. Methane

Among hydrocarbons, methane is one of the most stable fuels and it is the major component of natural gas. Figure 2-8 to 2-10 show the equilibrium products of methane at temperatures between 100 and 1000°C when the steam-to-carbon ratios (S/C) is 0, 1, and 1.5. In these figures, the results in (a) are based on the measured Gibbs free energy of deposited carbon by De Bokx et al. [39], called the De Bokx carbon; while the results in (b) are based on the assumption that the deposited carbon is graphite.

Figure 2-8 shows the equilibrium product composition when S/C=0. Because there is no H_2O, the only possible reaction is methane cracking, which is endothermic at standard temperature and pressure (STP).

$$CH_4 \leftrightarrow C + 2H_2 \qquad \Delta H_R = 74.6\ kJ/mol \qquad \text{(R. 1)}$$

Figure 2-8 shows that CH_4(g) is stable at lower temperatures, while it decomposes to form H_2(g) and carbon at higher temperatures because of the endothermic nature of the methane cracking reaction. The amount of solid carbon formed increases with temperature. Because CNF has a higher Gibbs free energy than graphite, it requires more energy to form, and the amount of carbon formed is less than when graphite is assumed to be the deposited carbon until it reaches saturation at 700°C.

When S/C=1, methane reforms to CO and CO_2 and there is an additional reaction involving solid carbon, the Boudouard reaction, which is exothermic.

$$2CO \leftrightarrow C + CO_2 \qquad \Delta H_R = -172\ kJ/mol \qquad \text{(R. 2)}$$

Solid carbon is formed and consumed by the methane cracking reaction and the Boudouard reaction, respectively. As the temperature increases, carbon is formed at an intermediate temperature window by methane cracking and it disappears by the Boudouard reaction (gasification) at higher temperatures, as shown in Figure 2-9. The temperature window is between 650 and 800°C for the graphite as shown in (b). It is shifted toward higher temperatures for the De Bokx carbon. Within the corresponding windows, less carbon is formed when assuming De Bokx carbon. The stable species at high temperatures are H_2 and CO.

No solid carbon is expected at the S/C of 1.5, as can be seen in Figure 2-10. There is no difference between the results using De Bokx carbon and graphite because solid carbon is not favorable at S/C=1.5, for either cases. At lower temperatures, CH_4 and H_2O are the stable species, while H_2 and CO become the dominant species at high temperatures. At intermediate

temperatures 300-550°C, there are more CO_2 and CO.

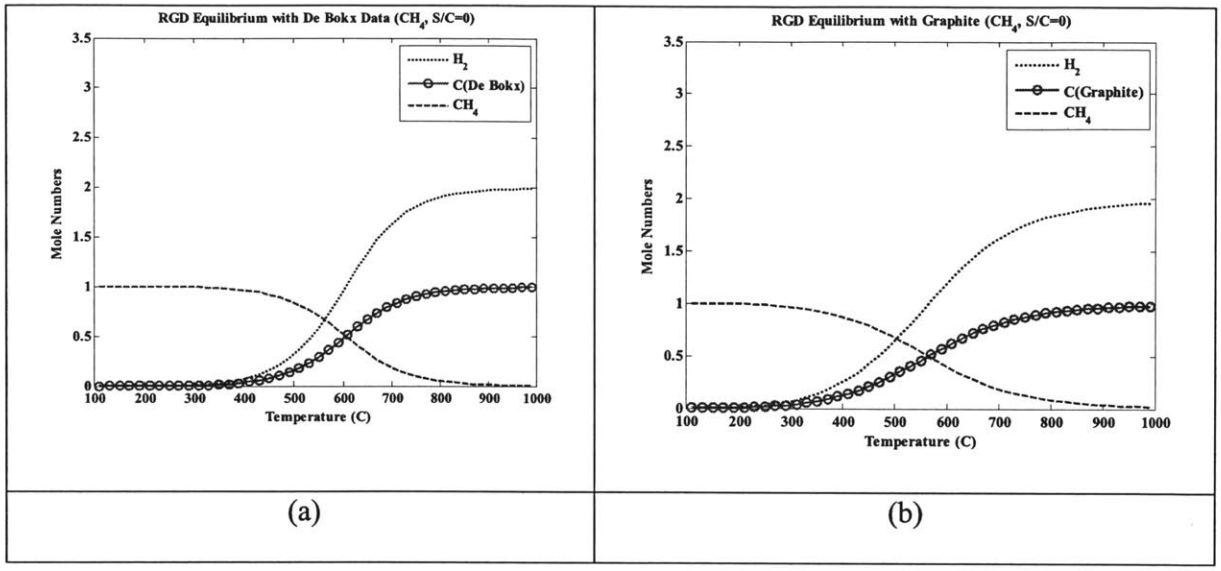

Figure 2-8. Equilibrium products from methane when steam-to-carbon ratio (S/C)=0. The Gibbs free energy of the carbon deposited is represented by (a) de Bokx experimental measurements and (b) graphite.

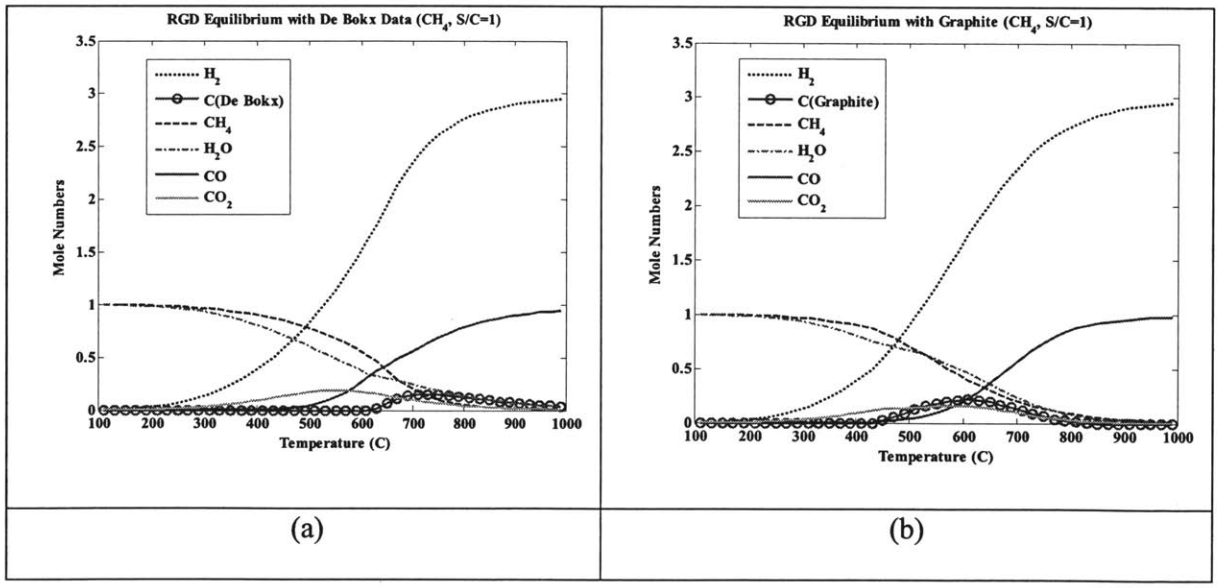

Figure 2-9. Equilibrium products from methane when steam-to-carbon ratio (S/C)=1. The Gibbs free energy of the carbon deposited is represented by (a) de Bokx experimental measurements and (b) graphite.

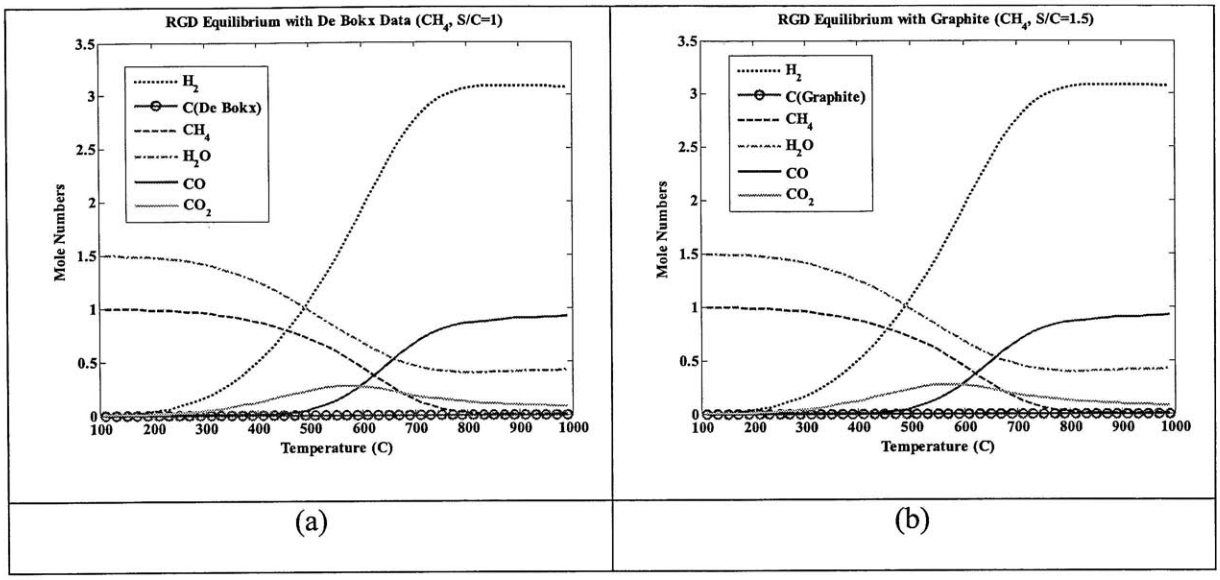

Figure 2-10. Equilibrium products from methane when steam-to-carbon ratio (S/C)=1.5. The Gibbs free energy of the carbon deposited is represented by (a) de Bokx experimental measurements and (b) graphite.

2.5.1.2. Methanol

Methanol (CH_3OH) is easily produced from natural gas and is easy to handle. For SOFCs, direct-methanol fuel cell operation has been demonstrated by Jiang and Virakr [41]. Figure 2-11 to 2-13 show the equilibrium products of methanol decomposition or reforming at S/C=0, 1, and 1.5, respectively. Results in (a) are based on the measured Gibbs free energy of the deposited carbon by De Bokx et al. [39]; results in (b) are based on the assumption that the deposited carbon is graphite.

There are noticeable differences in the predictions between the De Bokx carbon and graphite at S/C=0. For graphite, carbon deposition occurs at any temperatures below 900°C, while for De Bokx carbon solid carbon ocurs between 550 and 900°C only. The amount of carbon predicted using the properties of the De Bokx carbon is less than when using those of

graphite. Jiang and Virkar [41] reported that no carbon was observed when the fuel was pure methanol at T= 650°C and 800 °C. Even though the amount of solid carbon is greatly reduced when assuming the De Bokx carbon, solid carbon still forms. It should be noted that De Bokx et al's thermodynamic data [39] was measured on a supported Ni catalyst where the mean Ni catalyst particle size was 5.4 nm. Takeguchi et al. [23] showed that the diameter of carbon fiber formed in Ni-YSZ anode is much larger than that formed on a supported Ni catalyst. This may explain the difference between our prediction and the Jiang and Virakr's observation.

When S/C=0, the carbon deposition window for methanol lies at lower temperatures, as shown in Figure 2-11b, while that for methane lies at high temperatures. Note that there is almost no methanol in the products in Figure 2-11 to 2-13. The presence of methanol is thermodynamically unfavorable at any temperature; it decomposes to CH_4, H_2O, and C at low temperatures. At high temperatures, carbon is removed by the Boudouard gasification reaction, and CH_4 is cracked to produce H_2. When S/C=1 or 1.5, the only difference between predictions using the De Bokx carbon and graphite is that carbon is expected to form at around 100°C for graphite, while it is not favored at any temperature when using the properties of the De Bokx carbon. The amount of water formed in the case of methanol is much higher than that formed in methane. This is reasonable as alcohol could be regarded as hydrated hydrocarbons [21]. Therefore, less H_2O is needed to prevent carbon deposition in methanol compared with methane.

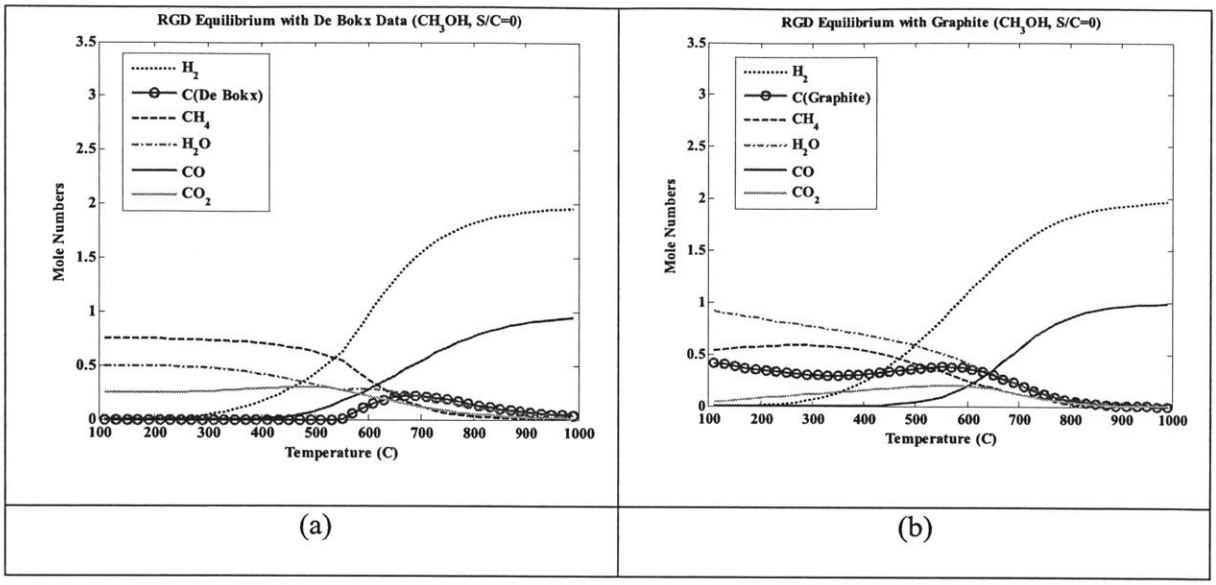

Figure 2-11. Equilibrium products from methanol when steam-to-carbon ratio (S/C)=0. The Gibbs free energy of the carbon deposited is represented by (a) de Bokx experimental measurements and (b) graphite.

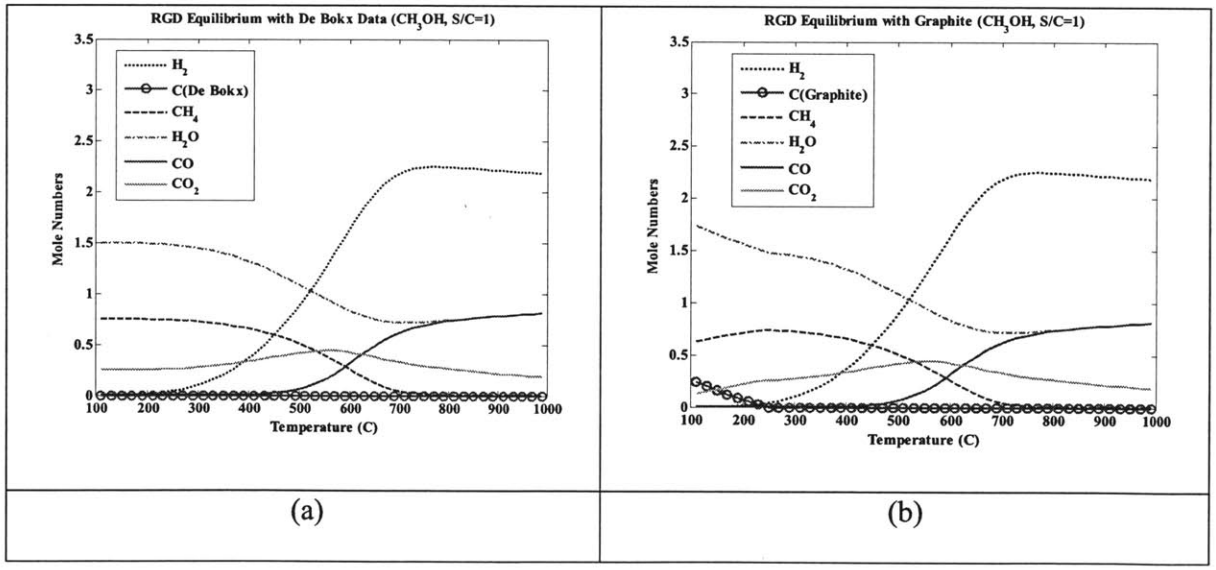

Figure 2-12. Equilibrium products from methanol when steam-to-carbon ratio (S/C)=1. The Gibbs free energy of the carbon deposited is represented by (a) de Bokx experimental measurements and (b) graphite.

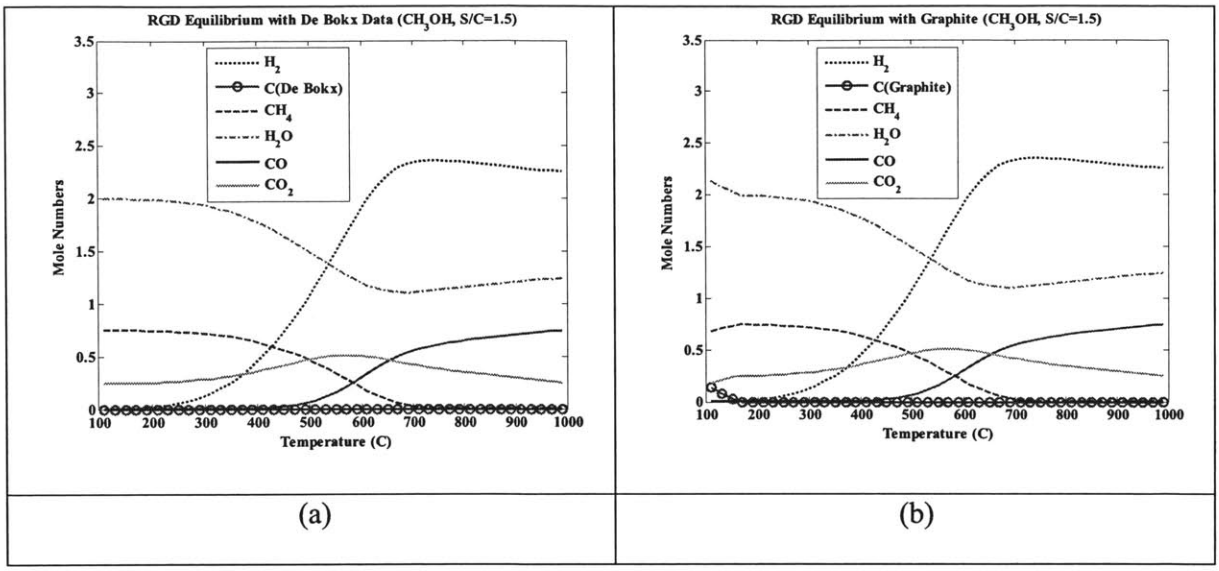

Figure 2-13. Equilibrium products from methanol when steam-to-carbon ratio (S/C)=1.5. The Gibbs free energy of the carbon deposited is represented by (a) de Bokx experimental measurements and (b) graphite.

2.5.2. Impact of fuel mixture composition

Ternary diagrams

Under conditions of thermodynamic equilibrium, the mixture composition is solely determined by the fraction of C, H, and O in the fuel mixture at a given T and P. For a given C-H-O ratio, the equilibrium composition is independent of the "original" hydrocarbon molecules [21]. Thus, given the C-H-O ratio, a mixture can be presented on a C-H-O ternary diagram.

A ternary diagram is a triangle, with each of its three sides or axes representing the mole fraction of one of the three elements: C, H, and O in the mixture where the sum of mole fractions is constrained by $X_C+X_H+X_O=1$. The mole fraction for each element increases from 0 to 1 along its corresponding axis in a counter-clockwise direction around the diagram. A mixture consisting of these three elements is represented by a point within this triangular coordinate system. Lines

of constant mole fraction for each element in the mixture are shown in Figure 2-14 (a), (b), and (c) for C, H, and O, respectively. To guide reading and interpretation of the composition, these lines are extended across the corresponding axis for all three elements. Figure 2-14 (d) is the overlay of panels (a)-(c). To illustrate an example of a specific composition, the red circle in panel (d) corresponds to C:H:O=0.5:0.3:0.2, which is where each of the three mole fraction lines intersect. For a resolution (i.e., mole fraction increment) of 0.1 along each axis, only 66 mixtures can be represented by the diagram because there are only 66 such intersections. In general, for a resolution of Δx, the number of mixtures is $\frac{(1/\Delta x+1)(1/\Delta x+2)}{2}$.

In order to draw the contour lines of the number of moles of a particular species, the equilibrium composition needs to be computed at every point in the ternary diagram. For our analysis, a resolution of 1/150 is chosen for each element, which corresponds to 11,476 intersection points. For a given temperature and pressure, an initial mixture is set according to the three element mole fractions for a single point, then equilibrated using the method described in Section 2.4. In the equilibrium calculation, only 34 species are allowed to exist, so that the amount of C, H and O are conserved and divided amongst the 34 species. The result of the calculation at each point is an equilibrium mixture defined by a specific composition. Contour lines for any species in the mixture among the 34 considered (e.g. H_2O, CH_4, O_2, C) can be drawn after the calculation is repeated for all 11,476 points. Contour lines of the number of moles of carbon, partial pressure of oxygen, and the corresponding open circuit voltage are shown in the ternary diagrams in the following sections.

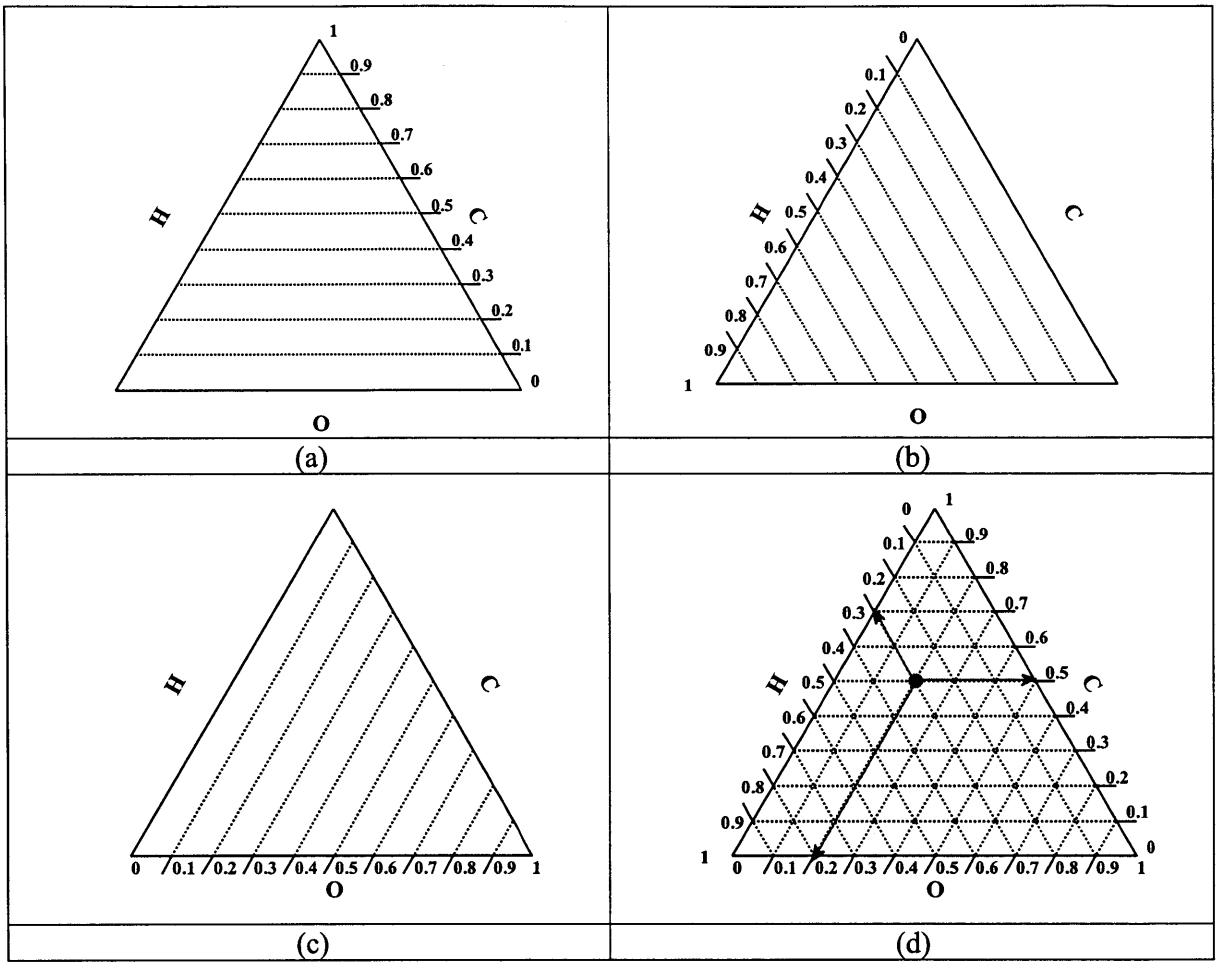

Figure 2-14. Reading of a ternary diagram (a) lines of constant mole fraction of C (b) lines of constant mole fraction of H (c) lines of constant mole fraction of O (d) the composition of a given mixture indicated by a red circle is C:H:O=0.5:0.3:0.2.

2.5.2.1. Carbon

Figure 2-15 shows the constant-temperature contour lines corresponding to a carbon mole number of 10^{-6}, which is defined as the carbon deposition demarcation line. 10^{-6} is chosen arbitrarily as the demarcation line for carbon deposition because Matlab failed to draw a contour line of zero mole of carbon. A mixture whose composition lies below this line has an equilibrium composition with less than 10^{-6} moles of carbon. The lines obtained for carbon mole numbers

between 10^{-3} and 10^{-9}, instead of 10^{-6}, nearly coincided, in agreement with Sasaki and Teraoka [22]. Demarcation lines are plotted for different mixture temperatures between 200 and 1000°C. In Figure 2-15 carbon deposition occurs when the composition of the fuel mixture lies on the carbon rich side of the demarcation lines. The difference between the predictions when using graphite and the De Bokx carbon is negligible at T=800°C and 1000°C because the Gibbs free energy difference between these carbons is small as shown in Figure 2-7. At these high temperatures, the carbon deposition demarcation lines connect H_2 and CO, which means that the dominant species are H_2 and CO when carbon starts to deposit. No carbon deposition is expected if the carbon-to-oxygen ratio is less than unity. CH_3OH lies close to these lines; thus, the addition of a small amount of H_2O or O_2 can prevent carbon deposition in methanol as compared to CH_4, as discussed in section 2.5.1.2.

When using graphite to represent the properties of deposited carbon, as the temperature decreases, (i) the carbon deposition region expands into what was the carbon free region, and (ii) the carbon demarcation lines move from the lines connecting H_2 and CO to the lines connecting CH_4 and CO_2. The first result, (i), indicates that a higher steam-to-carbon ratio (S/C) or a higher O_2-to-carbon ratio is needed to prevent carbon deposition at lower temperatures. The addition of CO_2 reduces carbon deposition at high temperatures (due to gasification or Boudouard reactions). The addition of CO_2 is not as effective at lower temperatures. In general, the amount of H_2O, O_2, or CO_2 needed to suppress carbon deposition increases at lower temperature. The second results, (ii), indicates that CH_4 and CO_2 are stable species at lower temperatures, while H_2 and CO are the dominant species at higher temperatures because of methane cracking and the

Boudouard reaction, as discussed in the section 2.5.1.

For the De Bokx carbon, the second result, (ii), stays the same: that is, at high temperature, the stable species are H_2 and CO, while at lower temperature CH_4 and CO_2 are the stable species. However, the penetration of the carbon-formation region into the carbon-free region is weaker because the measured Gibbs free energy is larger than that of graphite and carbon formation requires more energy.

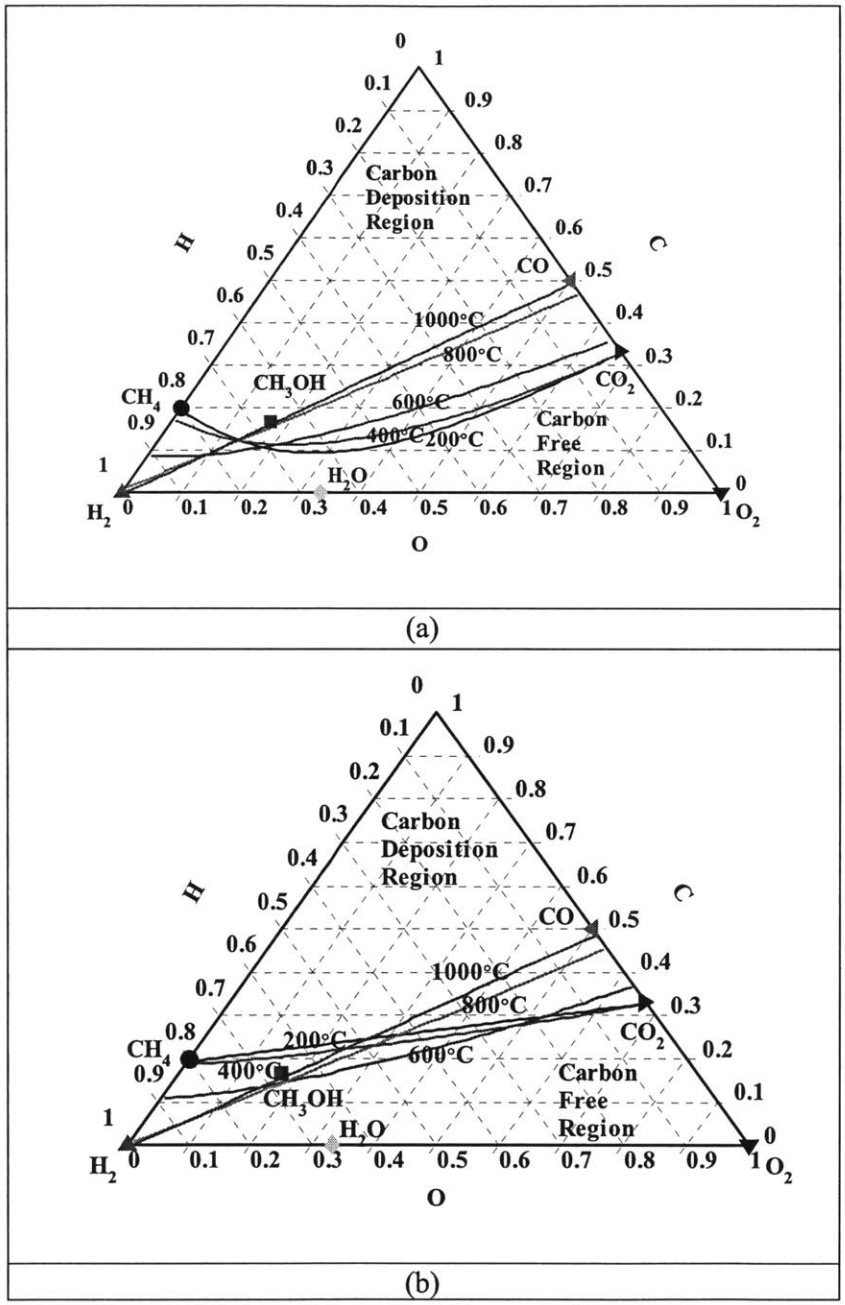

Figure 2-15. Carbon deposition demarcation lines evaluated at constant temperatures in the C-H-O ternary diagram at temperatures between 200 °C and 1000 °C. (a) the deposited carbon is assumed to be graphite; (b) De Bokx et al's measurement are used to characterize the carbon deposit. Region below the line represents mixtures whose equilibrium composition at this temperature has less than 10^{-6} moles of carbon and hence considered as free of carbon.

2.5.3. OCV

Figure 2-16 shows the contour lines of the oxygen partial pressures at T=600°C using the De Bokx et al's data for the solid carbon thermodynamic properties. These lines show the oxygen partial pressure at equilibrium for a fuel mixture whose composition is located along the corresponding line. The demarcation line for carbon deposition is also shown. The contour lines are often shown as $\log\left(p_{O_2} / bar\right)$ [22,23] because the oxygen partial pressure spans the range of $O(10^{-22})$ and $O(10^{-32})$ when the OCV is ~1V. In the carbon deposition region, the contour lines of p_{O_2} connect the pure solid carbon vertex and the carbon deposition demarcation line. The same trend has been reported by Sasaki and Teraoka [22] and Takeguchi et al. [23]. This is because additional carbon in the carbon deposition region does not change the activity of solid carbon, which is always 1, and the gas partial pressures are not affected by the amount of solid carbon. Adding carbon to a mixture on the carbon demarcation line moves the mixture composition location along the line connecting the pure solid carbon vertex and the carbon demarcation line. Thus, these lines are contour lines of partial pressure of other gaseous species in the equilibrium mixture.

Within the carbon deposition region, the oxygen partial pressure decreases as the hydrogen-to-oxygen ratio increases. In the carbon-free region, the p_{O_2} contour lines approach the line connecting the location of H_2O and that of CO_2 as the oxygen-to-hydrogen or oxygen-to-carbon ratio increases. The line connecting the points corresponding to pure H_2O and CO_2 represents cases where products consist only of H_2O and CO_2, which can be considered the

complete oxidation line.

Figure 2-17 shows the corresponding open circuit voltage (OCV) assuming that the cathode side is supplied with air (p_{O_2} =0.21 bar). The OCV is evaluated using the following equation

$$OCV = \frac{\Re T}{4F} \ln\left(\frac{p_{O_2,c}}{p_{O_2,a}}\right)$$

When the composition crosses the complete oxidation line, the oxygen partial pressure increases drastically; accordingly, the OCV drops significantly to 0.4V. Considering the contributions of the different overpotentials at finite current, that is, the activation, concentration and ohmic overpotentials of an operating cell, an OCV for a fuel mixture whose composition is located below the complete oxidation line is too low to be practical. Therefore, the composition of the fuel mixture to be used for an operating SOFC with a reasonable finite current and voltage should lie in the trapezoidal region between the carbon deposition line and the complete oxidation line.

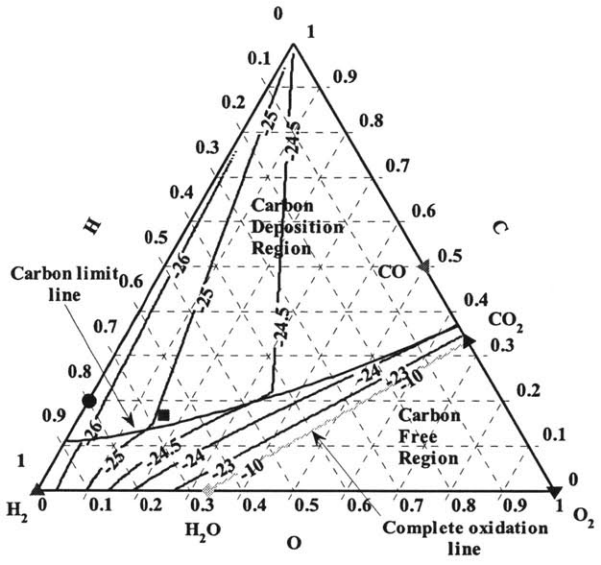

Figure 2-16. The oxygen partial pressure contour lines, shown as $\log\left(p_{O_2} / bar\right)$ at T=600°C. The De Bokx et al's data is used for the deposited solid carbon. The lines correspond to the fuel mixture whose equilibrium composition at T=600°C contains the shown value of oxygen partial pressure. Also shown are the carbon deposition demarcation line and the complete oxidation line.

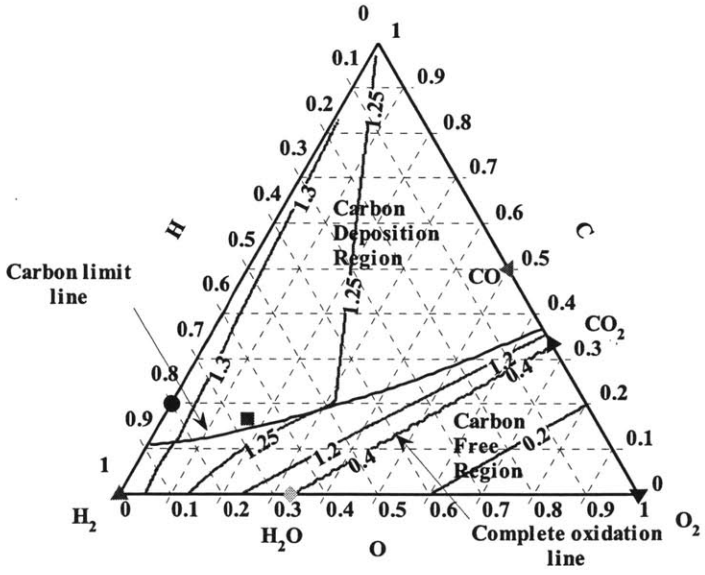

Figure 2-17. The open Circuit Voltage (OCV) [V] contour lines at T=600°C and the De Bokx et al's data is used for the deposited solid carbon.

Comparison with Experiments

Liu and Barnett [12] measured the OCV as a function of temperature for H_2 and CH_4 diluted with 3% H_2O. Figure 2-18 compares the measurements of Liu and Barnett [12] for 97% H_2 and 3% H_2O and the computed OCV using our equilibrium calculation. The difference between the measurement and calculation is about 0.03V, which is about 3% of the measured OCV. This difference can be accounted for by the measurement error or oxygen leakage. Figure 2-19 compares the OCV measured by Liu and Barnett [12] for 97% CH_4 and 3% H_2O and the computed values using one of three different assumptions: (1) no solid carbon, which is represented by a dot-dot line; (2) the solid carbon is graphite, which is shown by a dash-dash line; (3) De Bokx et al's measurement are used to represent the thermodynamic properties of carbon deposits, which is indicated by a dash-dot line. The computed OCV without the solid carbon shows a significant discrepancy of 0.2-0.4V. By adding solid carbon in either form, graphite or the De Bokx carbon, the agreement between the computed OCV and the measurement is significantly improved. The error is on the same order of O(0.03V) as in the case of H_2. The OCV measurement indicates that solid carbon should exist on the fuel side.

The difference in the computed OCV when using graphite and the De Bokx carbon is not that noticeable in Figure 2-19. The different Gibbs free energies result in changes in the mole numbers of the major species, as shown in Figure 2-21; the amount of methane decomposition is reduced when using the properties of the De Bokx carbon, resulting in higher CH_4 and lower H_2 and solid carbon, as compared to when using the properties of graphite. However, the oxygen partial pressures span between $O(10^{-22})$ and $O(10^{-32})$ as shown in Figure 2-20 and they do not

depend significantly on the type of carbon.

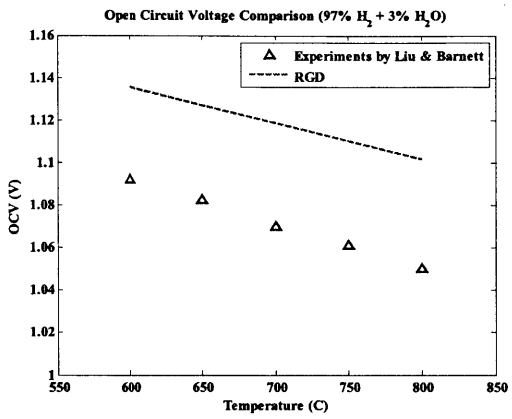

Figure 2-18. Temperature dependence of the OCV for 97% H_2 and 3% H_2O. Triangles are the experimentally measured OCV by Liu and Barnett [12]; the dashed line is calculated from equilibrium.

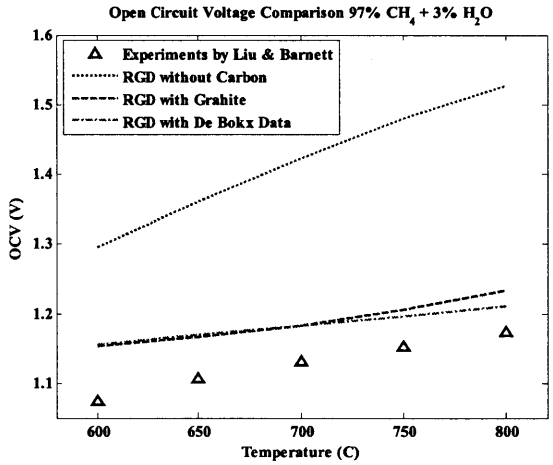

Figure 2-19. Temperature dependence of the OCV for 97% CH_4 and 3% H_2O. Triangles are the experimentally measured OCV by Liu and Barnett [12]; the dashed line is calculated from equilibrium.

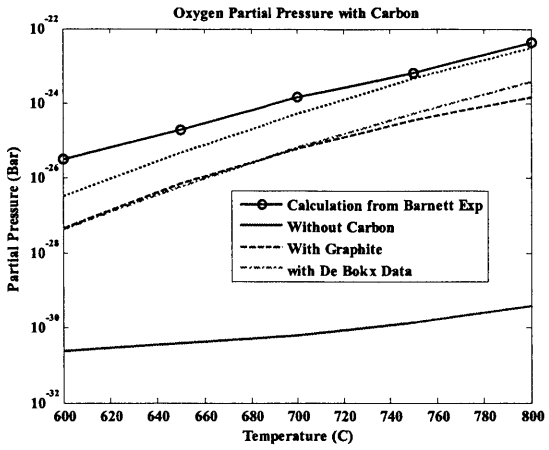

Figure 2-20. The equilibrium oxygen partial pressure on the anode side for 97% CH_4 and 3% H_2O: open circles represents p_{O_2} calculated from Liu and Barnett OCV measurement[12]; p_{O_2} computed from equilibrium without solid carbon is shown in the solid line; p_{O_2} computed from equilibrium with graphite is shown in the dashed line; p_{O_2} computed from equilibrium with De Bokx et al's data is shown in dot-dot line.

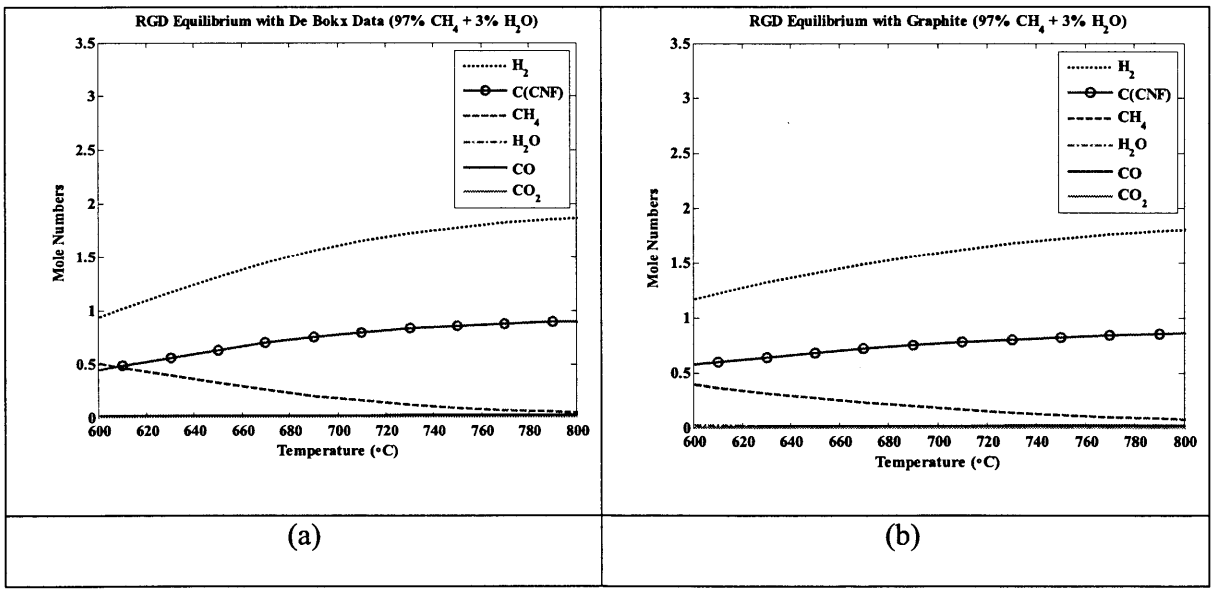

Figure 2-21. Equilibrium products for 97% CH_4 and 3% H_2O. The Gibbs free energy of the carbon deposited is represented by (a) De Bokx experimental measurements and (b) graphite.

Summary

In this section, the following general trend has been shown for fuel mixtures of methane or methanol combined with steam at different S/C ratios: (1) as S/C is raised, carbon deposition is mitigated; (2) less amount of steam is needed to avoid carbon deposition for methanol; and (3) at lower temperatures CH_4 and H_2O are stable, while H_2 and CO become the dominant species at high temperatures. When the fuel is pure methanol, the prediction of carbon deposition is improved when De Bokx et al's data is used.

The C-H-O ternary diagram is utilized to display the carbon deposition boundary, the p_{O_2} contours and the corresponding OCVs. Suitable fuel compositions for an SOFC have been suggested based on the carbon demarcation line and the complete oxidation line. When De Bokx et al's data is used for the deposited carbon, the penetration of the carbon formation region into the carbon free region is weak because the measured Gibbs free energy is larger than that of graphite and carbon formation requires more energy. By adding solid carbon in either form of graphite or the De Bokx carbon, the agreement between the computed OCV and the measurement is significantly improved.

2.6. Simulation Results (II): Special cases

In the previous sections, the general trends for carbon deposition are discussed and the result using De Bokx et al.'s data are shown to improve the prediction of carbon deposition for pure methanol. In this section, we will examine three more cases where previous attempts at using thermodynamic predictions failed to explain the experimental observations. We show that

we can improve the prediction and explain the trends better by discarding the assumption that the deposited carbon is graphite. Instead, we use: (1) De Bokx et al.'s data for the carbon fiber if the anode includes Ni catalysts, and (2) the partial pressures of soot precursors, CH_3 and C_2H_2, to predict soot formation.

2.6.1. Effect of CNF thermodynamic property

Zhan et al. [13] studied the performance of SOFCs operating on propane-air mixtures. They measured the anode exhaust gas composition as a function of temperature for a C_3H_8(10.7%)-O_2(18.7%)-Ar(70.6%) fuel mixture over a Ni-YSZ anode at open circuit conditions. No carbon was detected on the anode side under any of the conditions tested at temperatures between 550°C and 800°C. However, their equilibrium calculation using graphite properties for the deposited carbon predicted a large amount of carbon. They used this result to support their conclusion that carbon deposition was kinetically controlled. We show next that much less carbon is deposited when using De Bokx et al.'s data.

Figure 2-22 shows the equilibrium product composition as a function of temperature for the mixture of C_3H_8(0.36 moles) + moles O_2(0.64 moles). Their total partial pressure of this mixtue is 0.294 bar which corresponds to the Zhan et al.'s fuel composition [13]. Note that the inert species does not need to be included in the equilibrium calculation. Large amount of carbon is predicted at temperatures below 700°C as shown in Figure 2-22a when the carbon is assumed to be graphite. However, the amount of deposited carbon is greatly reduced when carbon is modeled using De Bokx et al.'s data [39], as shown in Figure 2-22b. This is because in the De Bokx et al.'s data, the deposited carbon has higher Gibbs energy than graphite. This result is also

consistent with the results obtained for pure methanol in the section 2.5.1.2, where the amount of deposited carbon was also greatly reduced when switching from graphite to the De Bokx carbon. The amount of carbon predicted by our model still does not match the measurement. As discussed in the previous section, the Gibbs energy measured by De Bokx et al. [39] is for carbon deposited on a supported Ni catalyst. The carbon fiber formed on a Ni-YSZ anode has different structure and may have different Gibbs free energy. Therefore, using measurements of the Gibbs free energy for the carbon fiber on Ni-YSZ anode may further improve the prediction further.

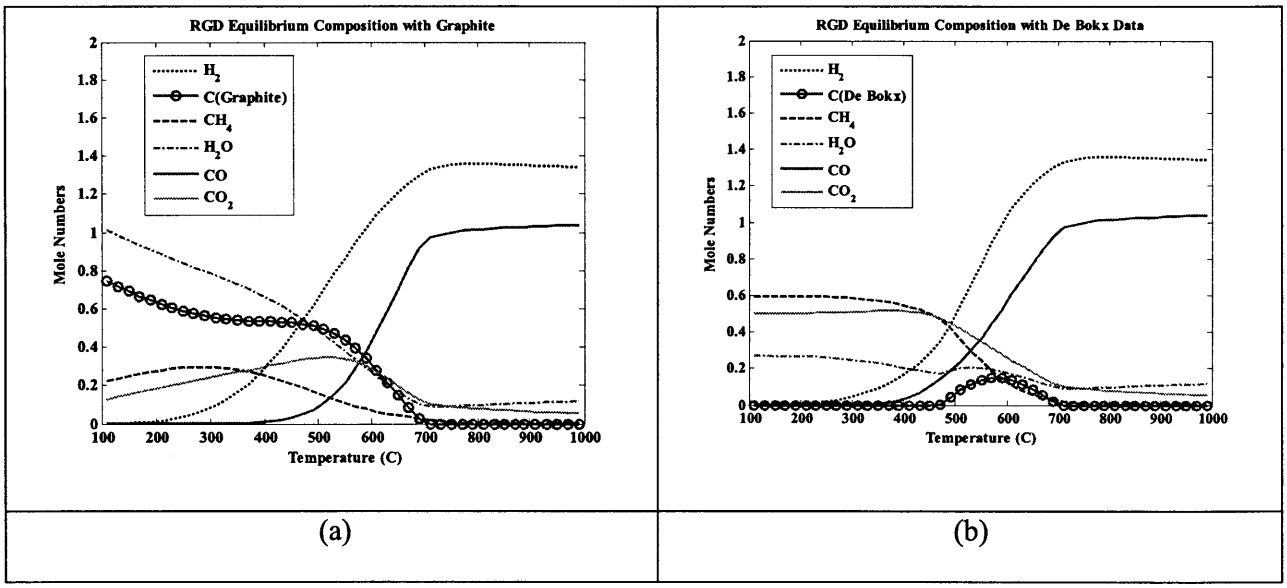

Figure 2-22. Equilibrium product distribution as a function of temperature for a C_3H_8(10.7%)-O_2(18.7%)-Ar(70.6%) fuel mixture. (a) solid carbon is modeled as graphite; (b) solid carbon is modeled using De Bokx et al's data.

2.6.2. Concentrations of soot formation precursors

Kim et al. [5] measured the weight change of a YSZ slab exposed to n-butane in a quartz-tube reactor with S/C=1.5 after 4 h. Their measurements showed that the weight began to change at T>680°C and rapidly increases at T>750°C. Based on the fact that forming graphite is not

thermodynamically favorable under this experimental condition, they concluded that thermodynamic equilibrium calculations cannot be used to predict carbon formation. Note that there is no catalyst in their study unless YSZ by itself catalyzes carbon deposits; thus, the observed carbon should be formed from gas phase pyrolysis of butane. The deposited carbon from pyrolysis is composed of polycyclic aromatic hydrocarbons (PAHs).

Figure 2-23 shows the equilibrium products as a function of temperature. The initial composition of the mixture is 1 mole of C_4H_{10} and 6 moles of H_2O, which corresponds to Kim et al. [5] experimental condition (S/C=1.5). The equilibrium calculation is done with the De Bokx's data for solid carbon. Results show that the equilibrium solid carbon is zero, contrary to the experimental observation. However, this form of solid carbon cannot be used to model PAH's or soot.

In the detailed soot formation kinetics analysis by Dean and co-workers [1,2,19,20], the propensity of homogeneous carbon soot formation was determined using the concentrations of C5+, which is likely to be responsible for the soot formation. In their analysis, the threshold value of C5+ concentrations for soot formation was fitted to agree with experimental observations.

Here, and similar to the approach used in the kinetics analysis to determine the threshold for soot carbon formation, the equilibrium concentrations of species that precede soot formation is examined. From the literature review, CH_3 and C_2H_2 are known to be the main precursors for the pyrolytic carbon formation. Because the 29 species specified in Section 2.5 does not include n-Butane (C_4H_{10}), additional species are included for the equilibrium calculation: n-C_4H_{10}, n-

C_5H_{12}, n-C_8H_{18}, iso-C_8H_{18}, and C_2H_5OH. Figure 2-24 shows the calculated partial pressure (bar) of CH_3 and C_2H_2 for the case shown in Figure 2-23. Their partial pressures (bar) are 6×10^{-10} and 1.6×10^{-10}, respectively, and CH_3 partial pressures increases rapidly at 680°C. The partial pressures of CH_3 and C_2H_2 exceeds $O(1\times10^{-9})$ and $O(1.6\times10^{-10})$ at 750°C when the weight change of a YSZ slab increased rapidly in Kim et al.'s experiments [5].

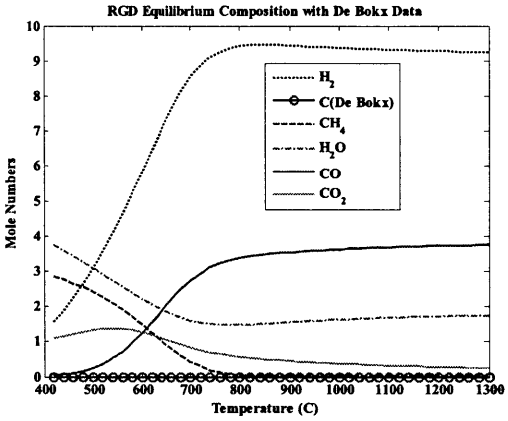

Figure 2-23. Equilibrium products profiles as a function of temperature when the fuel is butane with S/C=1.5.

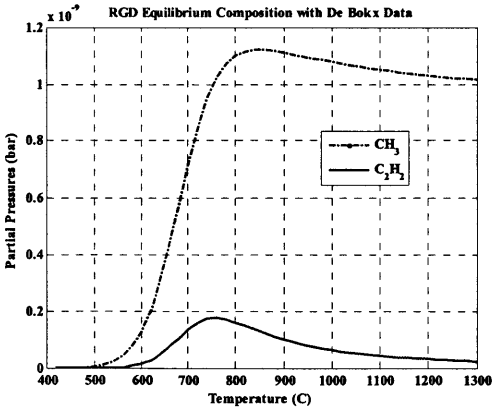

Figure 2-24. Equilibrium concentrations of CH_3 and C_2H_2, the indispensable soot forming species, as a function of temperature when the fuel is butane with S/C=1.5.

Lin et al. [14] studied Ni-YSZ supported SOFCs operating on slightly humidified methane fuel (97% CH_4 + 3% H_2O) at 650, 700, 750 and 800°C. They measured the cell voltage versus time at various constant currents. They found that the voltage was stable, and the cell showed no performance degradation when the current exceeded a certain value, which was defined as the critical current density (J_c). In other words, the SOFC was free from performance degradation above the critical current density. The measured J_c is listed in Table 2.2. J_c increases with temperatures. In their measurements, at zero current there was a slight voltage drop initially and the voltage became stable and constant at 650°C. At 700°C, the OCV was continuously declining. A rapid voltage drop was recorded at values below the critical current densities; thus, the OCV could not be measured at 750 and 800°C. Through the literature review, we found that the catalytically grown carbon may lead to a gradual degradation of the catalyst performance. On the other hand, soot formation deactivates the catalyst and fills out the pores, resulting in rapid performance degradation. It is thus suspected that the performance degradation at T>700°C is more related to the soot formation rather than catalytically grown carbon fiber. This hypothesis is examined next using our equilibrium calculations.

Figure 2-25 shows the equilibrium products versus temperatures in a fuel of 97% CH_4 and 3% H_2O. These results show that at temperatures above 500°C, carbon fiber is expected. As mentioned in the literature review, carbon fiber does not cause performance degradation until it reaches the pore walls and break the catalyst at the top. The formation of carbon fiber cannot provide a definitive prediction on performance degradation. Since the rapid voltage drop may be associated with soot formation, we need to examine the partial pressures of soot precursors, CH_3

and C_2H_2.

Figure 2-26 shows the partial pressures (bar) of CH_3 and C_2H_2 and they are 2×10^{-9} and 5×10^{-10}, respectively, at 700°C.

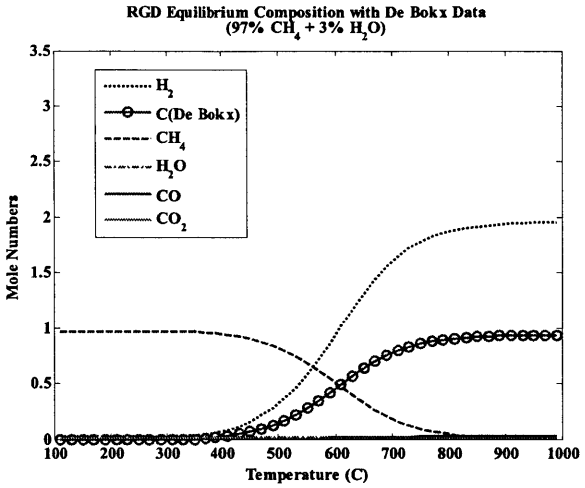

Figure 2-25. Equilibrium product profile as a function of temperature when the initial composition is 97% CH_4 and 3% H_2O. De Bokx et al's data [39] is used for the solid carbon properties.

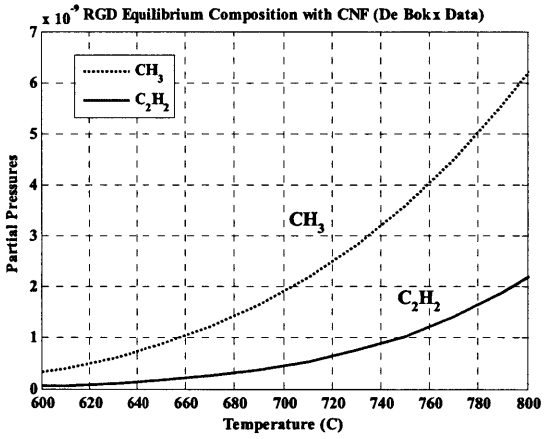

Figure 2-26. Partial pressure (bar) of soot precursors, CH_3 and C_2H_2, as a function of temperature when the initial composition is 97% CH_4 and 3% H_2O.

The calculated partial pressures of CH_3 and C_2H_2, typical soot precursors, are found to be

$O(10^{-9})$ and $O(10^{-10})$ bar, respectively when rapid soot formation is predicted for the two cases: (1) n-butane in with S/C=1.5 [5] and (2) 97% CH_4 and 3% H_2O [14]. The threshold value for rapid soot formation, being in the same range, can be utilized to determine whether further kinetics analysis of soot formation is necessary. However, more cases need to be examined whether the same range of threshold values can be found when the rapid soot formation occurs.

2.7. Discussion

In our analysis, we applied De Bokx et al.'s data for deposited carbon regardless of the catalyst structure such as the Ni particle size or the supporting material. However, the growth rate of carbon fiber is reported to depend on the Ni particle size and the supporting material [33,50]. By applying De Bokx et al's data instead of those of graphite, we are able to improve the prediction for the cases when no carbon was observed [13,41]. Previous thermodynamic analysis using graphite data, which predicted large amount of solid carbon, failed to explain the experimental observations. Our results show that a small amount of solid carbon is predicted when we use the De Bokx carbon. It is noted that the carbon fiber formed on Ni-YSZ has different structure from that grown on a supported Ni catalyst, as is the case of De Bokx et al [39]. Therefore, the carbon fiber formed on Ni-YSZ may have different Gibbs free energy from De Bokx et al's data. Measurement of the Gibbs free energy of carbon fiber in the Ni-YSZ anode has never been performed. Results of such measurement may be able to further improve the prediction of carbon deposition. Analytical expressions for the Gibbs energy difference have been proposed and they are dependent on the inner and outer radii of the carbon filament

[38,40,50,56]. The radii depends on the size of the Ni catalyst particle [38,50]. However, how the radii are determined is still under investigation [32,55]. Once the expression is developed further, it can be incorporated in our analysis because the developed code allows thermodynamic properties to depend not only on temperature but also on other parameters.

The partial pressures of CH_3 and C_2H_2, typical soot precursors, are found to be $O(10^{-9})$ bar and $O(10^{-10})$ bar, respectively when rapid soot formation is observed. It is worthwhile to examine whether the same threshold can be applicable to various cases. The propensity of rapid soot formation can be estimated by using the partial pressures of the soot precursors, instead of graphite.

2.8. Conclusion

Two dominant carbon deposition mechanisms have been identified: homogeneously formed soot and catalytically grown carbon fiber. The thermodynamic properties of these two types of carbon are different from graphite because of the different chemical composition and structure of soot and the carbon fiber. All previous thermodynamic analyses were based on the assumption that graphite can represent the deposited carbon regardless of its formation mechanism. A new thermodynamic analysis approach has been proposed in which we use: (1) De Bokx et al.'s data for carbon fiber if the anode includes Ni catalysts, and (2) partial pressures of soot precursors, CH_3 and C_2H_2, instead of graphite, to predict soot formation. The new approach improved the prediction of carbon fibers and soot formation in the cases where previous thermodynamic analysis failed to predict.

2.9. References

[1] K. M. Walters, A. M. Dean, H. Zhu, and R. J. Kee, "Homogeneous kinetics and equilibrium predictions of coking propensity in the anode channels of direct oxidation solid-oxide fuel cells using dry natural gas," *Journal of power sources*, vol. 123, no. 2, pp. 182-189, Sep. 2003.

[2] G. K. Gupta, J. R. Marda, A. M. Dean, A. M. Colclasure, H. Zhu, and R. J. Kee, "Performance predictions of a tubular SOFC operating on a partially reformed JP-8 surrogate," *Journal of Power Sources*, vol. 162, no. 1, pp. 553-562, Nov. 2006.

[3] S. McIntosh, J. M. Vohs, and R. J. Gorte, "Role of Hydrocarbon Deposits in the Enhanced Performance of Direct-Oxidation SOFCs," *Journal of The Electrochemical Society*, vol. 150, no. 4, p. A470, 2003.

[4] S. McIntosh, H. He, S.-I. Lee, O. Costa-Nunes, V. V. Krishnan, J. M. Vohs, and R. J. Gorte, "An Examination of Carbonaceous Deposits in Direct-Utilization SOFC Anodes," *Journal of The Electrochemical Society*, vol. 151, no. 4, p. A604, 2004.

[5] T. Kim, G. Liu, M. Boaro, S.-I. Lee, J. M. Vohs, R. J. Gorte, O. H. Al-Madhi, and B. O. Dabbousi, "A study of carbon formation and prevention in hydrocarbon-fueled SOFC," *Journal of Power Sources*, vol. 155, no. 2, pp. 231-238, Apr. 2006.

[6] X. Wang and R. J. Gorte, "Steam reforming of n-butane on Pd / ceria," *Catalysis Letters*, vol. 73, no. 1, pp. 15-19, 2001.

[7] R. J. Gorte, H. Kim, and J. M. Vohs, "Novel SOFC anodes for the direct electrochemical oxidation of hydrocarbon," *Journal of Power Sources*, vol. 106, pp. 10-15, 2002.

[8] S. Park, R. Craciun, J. M. Vohs, and R. J. Gorte, "Direct oxidation of hydrocarbons in a solid oxide fuel cell. I. Methane oxidation," *Journal of the Electrochemical Society*, vol. vol, pp. 146pp3603-3605, 1999.

[9] H. Kim, C. Lu, W. L. Worrell, J. M. Vohs, and R. J. Gorte, "Cu-Ni Cermet Anodes for Direct Oxidation of Methane in Solid-Oxide Fuel Cells," *Journal of The Electrochemical Society*, vol. 149, no. 3, p. A247, 2002.

[10] H. Kim, S. Park, J. M. Vohs, and R. J. Gorte, "Direct Oxidation of Liquid Fuels in a Solid Oxide Fuel Cell," *Journal of The Electrochemical Society*, vol. 148, no. 7, p. A693, 2001.

[11] E. P. Murray, T. Tsai, and S. A. Barnett, "A direct-methane fuel cell with a ceria-based anode," *Nature*, vol. 400, no. 6745, pp. 649–651, 1999.

[12] J. Liu and S. A. Barnett, "Operation of anode-supported solid oxide fuel cells on methane and natural gas," *Solid State Ionics*, vol. 158, no. 1, pp. 11–16, Feb. 2003.

[13] Z. Zhan, J. Liu, and S. A. Barnett, "Operation of anode-supported solid oxide fuel cells on propane–air fuel mixtures," *Applied Catalysis A: General*, vol. 262, no. 2, pp. 255-259, May 2004.

[14] Y. Lin, Z. Zhan, J. Liu, and S. A. Barnett, "Direct operation of solid oxide fuel cells with methane fuel," *Solid State Ionics*, vol. 176, no. 23–24, pp. 1827-1835, Jul. 2005.

[15] Z. Zhan and S. Barnett, "Use of a catalyst layer for propane partial oxidation in solid oxide fuel cells," *Solid State Ionics*, vol. 176, no. 9–10, pp. 871-879, Mar. 2005.

[16] Z. Zhan and S. A. Barnett, "Operation of ceria-electrolyte solid oxide fuel cells on iso-octane–air fuel mixtures," *Journal of Power Sources*, vol. 157, no. 1, pp. 422-429, 2006.

[17] Z. Zhan and S. A. Barnett, "Solid oxide fuel cells operated by internal partial oxidation reforming of iso-octane," *Journal of Power Sources*, vol. 155, no. 2, pp. 353-357, 2006.

[18] Y. Lin, Z. Zhan, and S. A. Barnett, "Improving the stability of direct-methane solid oxide fuel cells using anode barrier layers," *Journal of Power Sources*, vol. 158, no. 2, pp. 1313-1316, 2006.

[19] C. Y. Sheng and A. M. Dean, "Importance of Gas-Phase Kinetics within the Anode Channel of a Solid-Oxide Fuel Cell," *The Journal of Physical Chemistry A*, vol. 108, no. 17, pp. 3772-3783, Apr. 2004.

[20] G. K. Gupta, A. M. Dean, K. Ahn, and R. J. Gorte, "Comparison of conversion and deposit formation of ethanol and butane under SOFC conditions," *Journal of Power Sources*, vol. 158, no. 1, pp. 497-503, Jul. 2006.

[21] K. Sasaki and Y. Teraoka, "Equilibria in Fuel Cell Gases I. Equilibrium Compositions and Reforming Conditions," *Journal of The Electrochemical Society*, vol. 150, no. 7, p. A878, 2003.

[22] K. Sasaki and Y. Teraoka, "Equilibria in Fuel Cell Gases: II. The C-H-O Ternary Diagrams," *Journal of The Electrochemical Society*, vol. 150, no. 7, p. A885, Jul. 2003.

[23] T. Takeguchi, Y. Kani, T. Yano, R. Kikuchi, K. Eguchi, K. Tsujimoto, Y. Uchida, A.

Ueno, K. Omoshiki, and M. Aizawa, "Study on steam reforming of CH4 and C2 hydrocarbons and carbon deposition on Ni-YSZ cermets," *Journal of Power Sources*, vol. 112, no. 2, pp. 588-595, Nov. 2002.

[24] J.-H. Koh, B.-S. Kang, H. C. Lim, and Y.-S. Yoo, "Thermodynamic Analysis of Carbon Deposition and Electrochemical Oxidation of Methane for SOFC Anodes," *Electrochemical and Solid-State Letters*, vol. 4, no. 2, p. A12, 2001.

[25] E. Vakouftsi, G. E. Marnellos, C. Athanasiou, and F. Coutelieris, "CFD modeling of a biogas fuelled SOFC," *Solid State Ionics*, vol. 192, no. 1, pp. 458-463, Jun. 2011.

[26] J. Klein, Y. Bultel, S. Georges, and M. Pons, "Modeling of a SOFC fuelled by methane: From direct internal reforming to gradual internal reforming," *Chemical Engineering Science*, vol. 62, no. 6, pp. 1636-1649, Mar. 2007.

[27] S. McIntosh and R. J. Gorte, "Direct hydrocarbon solid oxide fuel cells.," *Chemical reviews*, vol. 104, no. 10, pp. 4845-65, Oct. 2004.

[28] J. Rostrup-Nielsen, J. Sehested, and J. Norskov, "Hydrogen and synthesis gas by steam- and CO2 reforming," *ADVANCES IN CATALYSIS, VOL 47*, vol. 47, pp. 65-139, 2002.

[29] J. R. Rostrup-Nielsen, "Chapter 1. Catalytic Steam Reforming," in *Catalysis: Science and Technology, Volume 5, 1984*, John R. Anderson and M. Boudart, Eds. Berlin;: Springer-Verlag, Berlin, West Ger, 1984, pp. 72-95.

[30] K. De Jong and J. Geus, "Carbon Nanofibers: Catalytic Synthesis and Applications," *Catalysis Reviews*, vol. 42, no. 4, pp. 481-510, Nov. 2000.

[31] S. Helveg, C. López-Cartes, J. Sehested, P. L. Hansen, B. S. Clausen, J. R. Rostrup-Nielsen, F. Abild-Pedersen, and J. K. Nørskov, "Atomic-scale imaging of carbon nanofibre growth.," *Nature*, vol. 427, no. 6973, pp. 426-9, Jan. 2004.

[32] M. a. Cullinan and M. L. Culpepper, "Control of carbon nanotube geometry via tunable process parameters," *Applied Physics Letters*, vol. 93, no. 10, p. 103106, 2008.

[33] K. Christensen, D. Chen, R. Lodeng, and a Holmen, "Effect of supports and Ni crystal size on carbon formation and sintering during steam methane reforming," *Applied Catalysis A: General*, vol. 314, no. 1, pp. 9-22, 2006.

[34] I. M. Kennedy, "Models of soot formation and oxidation," *Progress in Energy and Combustion Science*, vol. 23, no. 2, pp. 95-132, Jan. 1997.

[35] J. Appel, H. Bockhorn, and M. Frenklach, "Kinetic modeling of soot formation with detailed chemistry and physics: laminar premixed flames of C2 hydrocarbons," *Combustion and Flame*, vol. 121, no. 1–2, pp. 122-136, Apr. 2000.

[36] A. Kazakov and M. Frenklach, "Dynamic Modeling of Soot Particle Coagulation and Aggregation: Implementation With the Method of Moments and Application to High-Pressure Laminar Premixed Flames," *Combustion and Flame*, vol. 114, no. 3–4, pp. 484-501, Aug. 1998.

[37] V. M. Janardhanan and O. Deutschmann, "CFD analysis of a solid oxide fuel cell with internal reforming: Coupled interactions of transport, heterogeneous catalysis and electrochemical processes," *Journal of Power Sources*, vol. 162, no. 2, pp. 1192-1202, Nov. 2006.

[38] J. R. Rostrup-nielsen, "Equilibria of decomposition reactions of carbon monoxide and methane over nickel catalysts," *Journal of Catalysis*, vol. 27, no. 3, pp. 343-356, Dec. 1972.

[39] P. K. de Bokx, A. J. H. M. Kock, E. Boellaard, W. Klop, and J. W. Geus, "The formation of filamentous carbon on iron and nickel catalysts I. Thermodynamics," *Journal of Catalysis*, vol. 96, no. 2, pp. 454-467, Dec. 1985.

[40] I. Alstrup, "A new model explaining carbon filament growth on nickel, iron, and Ni$z.sbnd;Cu alloy catalysts," *Journal of Catalysis*, vol. 109, no. 2, pp. 241-251, Feb. 1988.

[41] Y. Jiang and A. V. Virkar, "A High Performance, Anode-Supported Solid Oxide Fuel Cell Operating on Direct Alcohol," *Journal of The Electrochemical Society*, vol. 148, no. 7, p. A706, 2001.

[42] H. Wang and M. Frenklach, "A detailed kinetic modeling study of aromatics formation in laminar premixed acetylene and ethylene flames," *Combustion and Flame*, vol. 110, no. 1–2, pp. 173-221, Jul. 1997.

[43] J. R. Rostrup-Nielsen and J. Sehested, "Whisker carbon revisited," in *Studies in Surface Science and Catalysis: Volume 139*, vol. 139, Elsevier, 2001, pp. 1–12.

[44] S. Yoon, I. Kang, and J. Bae, "Suppression of ethylene-induced carbon deposition in diesel autothermal reforming," *International Journal of Hydrogen Energy*, vol. 34, no. 4, pp. 1844-1851, Feb. 2009.

[45] S. Yoon, I. Kang, and J. Bae, "Effects of ethylene on carbon formation in diesel

autothermal reforming," *International Journal of Hydrogen Energy*, vol. 33, no. 18, pp. 4780-4788, Sep. 2008.

[46] S. Yoon, Y. Kim, S. Kim, and J. Bae, "Effects of low hydrocarbons on the solid oxide fuel cell anode," *Journal of Solid State Electrochemistry*, vol. 14, no. 10, pp. 1793-1800, Apr. 2010.

[47] D. L. Trimm, "Fundamental aspects of the formation and gasification of coke," in *Pyrolysis: Theory and Industrial Practice*, L. F. Albright, B. L. Crynes, and W. H. Corcoran., Eds. New York: Academic Press, 1983, pp. 203-232.

[48] D. L. Trimm, "The formation and removal of coke from nickel catalyst," *Catalysis Reviews Science and Engineering*, vol. 16, no. 1, pp. 155–189, 1977.

[49] D. Trimm, "Coke formation and minimisation during steam reforming reactions," *Catalysis Today*, vol. 37, no. 3, pp. 233-238, Aug. 1997.

[50] D. Chen, K. Christensen, E. Ochoafernandez, Z. Yu, B. Totdal, N. Latorre, a Monzon, and a Holmen, "Synthesis of carbon nanofibers: effects of Ni crystal size during methane decomposition," *Journal of Catalysis*, vol. 229, no. 1, pp. 82-96, Jan. 2005.

[51] M. Toebes, "Impact of the structure and reactivity of nickel particles on the catalytic growth of carbon nanofibers," *Catalysis Today*, vol. 76, no. 1, pp. 33-42, Nov. 2002.

[52] L. Aparicio, "Transient Isotopic Studies and Microkinetic Modeling of Methane Reforming over Nickel Catalysts," *Journal of Catalysis*, vol. 165, no. 2, pp. 262-274, Jan. 1997.

[53] D. Chen, R. Lødeng, K. Omdahl, A. Anundsks, O. Olsvik, and A. Holmen, "A Model for Reforming on Ni Catalyst with Carbon Formation and Deactivation," in *Studies in Surface Science and Catalysis; Volume 139*, vol. 139, Elsevier, 2001, pp. 93-100.

[54] D. Chen, "Deactivation during carbon dioxide reforming of methane over Ni catalyst: microkinetic analysis," *Chemical Engineering Science*, vol. 56, no. 4, pp. 1371-1379, Feb. 2001.

[55] G. Tibbetts, "Why are carbon filaments tubular?," *Journal of Crystal Growth*, vol. 66, no. 3, pp. 632-638, May 1984.

[56] P. E. Nolan, D. C. Lynch, and A. H. Cutler, "Carbon Deposition and Hydrocarbon Formation on Group VIII Metal Catalysts," *The Journal of Physical Chemistry B*, vol. 102, no. 21, pp. 4165-4175, May 1998.

[57] M. P. Manning, J. E. Garmirian, and R. C. Reid, "Carbon deposition studies using nickel and cobalt catalysts," *Industrial & Engineering Chemistry Process Design and Development*, vol. 21, no. 3, pp. 404-409, Jul. 1982.

[58] J. N. Armor, "The multiple roles for catalysis in the production of H2," *Applied Catalysis A: General*, vol. 176, no. 2, pp. 159-176, Jan. 1999.

[59] G. K. Gupta, E. S. Hecht, H. Zhu, A. M. Dean, and R. J. Kee, "Gas-phase reactions of methane and natural-gas with air and steam in non-catalytic regions of a solid-oxide fuel cell," *Journal of Power Sources*, vol. 156, no. 2, pp. 434-447, Jun. 2006.

[60] W. R. Smith and R. W. Missen, *Chemical reaction equilibrium analysis : theory and algorithms*. New York: Wiley-Interscience, 1982, p. 364 p.

[61] W. R. Smith and R. W. Missen, "Strategies for solving the chemical equilibrium problem and an efficient microcomputer-based algorithm," *The Canadian Journal of Chemical*, vol. 66, no. Cl, pp. 591-598, 1988.

[62] W. R. Smith and R. W. Missen, "Calculating complex chemical equilibria by an improved reaction-adjustment method," *The Canadian Journal of Chemical Engineering*, vol. 46, no. 4, pp. 269-272, Aug. 1968.

[63] B. J. Mcbride, M. J. Zehe, and S. Gordon, "NASA Glenn Coefficients for Calculating Thermodynamic Properties of Individual Species: NASA/TP—2002-211556," 2002.

Page left intentionally blank

Chapter 3

Analysis of multi-step CO electrochemistry on Ni pattern anode of SOFCs

Abstract

We propose a new multi-step CO electrochemistry model in which CO is directly involved in the charge-transfer steps. The model structure, with a single set of kinetic parameters at each temperature, succeeds in reproducing the characteristics of the EIS data of patterned anodes including: (1) the two suppressed semi-circles and (2) the drop in polarization resistance as the activation overpotential increases. At high activation overpotentials, our model predicts the experimentally reported inductive behavior. Using the same set of parameters, our model prediction of the steady-state Tafel plots agrees well with the reported data including the asymmetry of the anodic and cathodic currents. Our model can also explain the positive dependence of the exchange current density on p_{CO_2}.

Nomenclature

Symbol	Meaning	Common Units
A	Pre-exponential factor	[mol, m, sec, Pa]
A_{YSZ}	YSZ electrolyte surface area	[mm^2]
A_{Ni}	Ni surface area	[mm^2]
c_k	Concentration of gas species k	[mol/m^3]
C	Capacitance	[F]
D_i	Surface diffusion diffusion coefficients of species i	[m^2/s]
E	Electric potential difference	[V]
E	Activation energy	[kJ/mol]
F	Faraday Constant	96,485 [C/mol]
I	Current	[A]
I^0	Exchange current	[A]
j	Imaginary unit	Dimensionless
J_k	Molar flux of gas species k	[$mol/m^2 \cdot sec$]
k_B	Boltzmann constant	[eV/K]
k	Reaction rate constant	[mol, m, sec, Pa]
$k_{i,f}$	Forward reaction constant of reaction i	[mol, m, sec, Pa]
$k_{i,b}$	Bckward reaction constant of reaction i	[mol, m, sec, Pa]
K_i	Equilibrium constant for reaction i	[mol, m, sec, Pa]
l_{TPB}	TPB length	[mm]
n_{CPE}	Empirical exponent of CPE	Dimensionless
p	Pressure	[N/m^2]
Q	Constant phase element	[$F/(1/s)^{1-n}$]
R	Universal gas constant	8.314 [J/mol·K]
R	Resistance	[Ω]
T	Temperature	[K]
Y	Admittance	[1/ Ω]
z	Valence of the charge carrier	Dimensionless
Z	Impedance	[Ω]

Greek Symbol	Meaning	Common Units
β_i	Cathodic charge-transfer coefficient in reaction i	Dimensionless
η	Anode activation overpotential	[V]
δ_{Ni}	Ni width	[μm]
δ_{YSZ}	YSZ width	[μm]
Γ	Surface site density	[mol/cm^2]
γ_{CO}	Sticking probability of CO	Dimensionless
θ_i	Coverage of species i	Dimensionless

ρ	Charge density	[C/m^3]
ε	Dielectric constant	Dimensionless
ε_0	Vacuum permittivity	[F/m]
Φ	Electric potential	[V]
ω	Frequency	[1/sec]

Subscript	**Meaning**
b	Backward
CPE	Constant Phase Element
dl	Double layer
el	Electrolyte
eq	Equilibrium
f	Forward or faradaic
i	Species or reaction i
ss	Steady-state
ohm	Ohmic

Superscript	**Meaning**
eff	Effective
0	Exchange current density

3.1. Introduction

Solid oxide fuel cells (SOFCs) can operate on various fuels, including hydrogen, carbon monoxide, methane and other hydrocarbons [1–7]. However, there is no consensus on which species are electrochemically oxidized at the anode triple-phase boundary (TPB) when carbon-containing fuels are used. Because hydrocarbon (HC) fuels are partially or completely reformed to other species, such as hydrogen and carbon monoxide, while flowing through a porous nickel anode, determining the composition of the fuel when it is electrochemically oxidized is a challenge.

Fast direct electrochemical oxidation of hydrocarbons in SOFCs has been suggested by two groups, Barnett group [1] at Northwestern University, and Gorte group [2,8,9] at the University of Pennsylvania. Both groups used dry hydrocarbons to exclude possible reforming reactions. However, Mogensen and Kammer [10] suspect that hydrocarbon conversion proceeds by pathways other than direct oxidation, e.g., by cracking and reforming followed by electrochemical oxidation of the fuel fragments and reforming products. This is because the measured open circuit voltages (OCVs) are much lower than those predicted by the Nernst equations. It is still being debated whether hydrocarbon fuels directly participate in charge-transfer reactions without being reformed to H_2 and/or CO which are subsequently involved in the electrochemical reactions.

Carbon monoxide almost always exists when a hydrocarbon fuel is supplied because the fuel is reformed or pyrolyzed internally or externally. Much research has been conducted on CO electrochemistry using Ni patterned anodes [11], Ni point anodes [12,13] and Ni/YSZ porous anodes [14–16]. When pure CO is supplied to a porous anode, the maximum power density is reported to reach about 40% of that obtained using pure H_2 [14]. According to the experimental

results on a patterned anode [11], the maximum power density using pure CO is about 50% of that using pure H_2. Matsuzaki and Yasuda reported that the electrochemical oxidation rate of H_2 was 2-3 times faster than that of CO [16]. Even though the CO electrochemical oxidation rate is slower than H_2, it is not negligible.

Based on the following two arguments, CO electrochemistry has been ignored in many MEA models [17,18]:

(i) CO electrochemical oxidation rate is slower than that of H_2,

(ii) CO is reformed to H_2 via the water-gas shift reaction at the anode prior to reaching the TPB.

However, as shown above, CO electrochemistry is not negligible and the degree of shifting of CO to H_2 depends on the operating conditions. When 97% CH_4 and 3% H_2O is fed to the anode, CO and H_2 have comparable concentrations at the TPB even after reforming in the anode [18]. Therefore, one needs to include, at least, the CO electrochemistry in models of HC electrochemical oxidation. While numerous studies have tried to unravel the details of H_2 electrochemistry on Ni/YSZ electrodes, very limited studies have been published on CO electrochemical oxidation.

In this chapter, based on the literature review in Section 3.2, a new multi-step charge-transfer reaction mechanism of CO electrochemistry is proposed. A pattern anode model is derived in Section 3.3 in which the electrochemistry model is coupled with surface diffusion and reactions in the neighborhood of the TPB. Analytical solutions of the model are obtained under equilibrium, steady-state conditions, as well as under sinusoidal small perturbation conditions used in electrochemical impedance spectroscopy (EIS) measurements. Unknown parameters in the kinetics model are obtained by fitting the model to Habibzadeh's EIS measurements [19] in

Section 3.4. The results of the proposed mechanism are then compared to the steady-state and equilibrium measurements of Habibzadeh [19]. The inductive behavior of the impedance observed by Lauvstad et al. [13] are discussed in Section 3.6. The results are summarized in Section 3.8.

3.2. Literature Review

Previous studies on CO electrochemistry have reported a number of reaction mechanisms. Based on a proposed mechanism, expressions for experimentally measurable quantities, such as the exchange current density and the polarization resistance, are derived and their values are compared with experimental results to examine the validity of the structure of the proposed mechanism and obtain the unknown parameters in the mechanism. Electrochemical Impedance Spectroscopy (EIS) has also been used in the literature and its measurements have been interpreted using equivalent circuits models. Both the interpretation and the comparison with the models lead to qualitative conclusions on the CO mechanisms. In this section, several mechanisms are reviewed. We select a mechanism for further development in the next section.

Etsell and Flengas [20] investigated the anodic reactions of several porous Pt electrodes and proposed the following two mechanisms:

Mechanism I.

$$O_O^x(YSZ)+(YSZ \text{ or } Ni) \leftrightarrow O(YSZ \text{ or } Ni)+2e^- + V_O^{\bullet\bullet}(YSZ)$$
$$CO(g)+O(YSZ \text{ or } Ni) \leftrightarrow CO_2(g)$$

where O(Ni or YSZ) is a neutral oxygen atom on Ni or YSZ surface, and O_O^x is an oxygen ion(O^{2-}) occupying an oxygen ion site in the YSZ bulk structure. In this chapter, a bulk species in the YSZ crystal is described using the Kröger-Vink notation. In Kröger-Vink notation, the

electric charge is defined relative to the site occupied by a species, rather than its absolute charge. Accordingly, a vacancy at an oxygen site has two positive charges relative to the oxygen ion and is represented as $V_O^{\bullet\bullet}$. (YSZ) and (Ni) represent an empty site on YSZ and Ni surface, respectively.

Mechanism II

$$CO(g) + O_O^{\times}(YSZ) \leftrightarrow CO_2(g) + V_O^{\bullet\bullet}(YSZ) + 2e^{-}(Ni)$$

Mechanism I postulates that neutral oxygen is formed via the electrochemical charge-transfer reaction and subsequently oxidize CO producing CO_2 via a thermochemical reaction. In other words, CO does not participate in the charge-transfer reaction directly. On the other hand, in Mechanism II CO_2 and CO are directly involved in the electrochemical reaction. Based on Mechanism II, the exchange current density, i_0, was expressed as

$$i_0 = k(1-\theta_{CO})\, p_{CO}^{1/2}\, p_{CO_2}^{1/2} \tag{3.1}$$

where θ_{CO} is the surface coverage of CO, and p_{CO} and p_{CO_2} are partial pressures of CO and CO_2.

Equation (3.1) indicates that the maximum exchange current density should occur below 50% CO in CO-CO_2 mixture. Etsell and Flengas [20] experimental results show that the exchange current density should be the maximum around 50% CO + 50% CO_2. The same dependence of the exchange current density on CO partial pressure could also be explained by assuming that CO is in the adsorbed form. Therefore, Etsell and Flengas [20] concluded that gaseous or adsorbed CO and gaseous CO_2 participate directly in the electrochemical steps of the electrode reaction.

Setoguchi et al. [21] investigated the effect of the fuel on the anodic reactions on Ni/YSZ

cermet electrode. Their experimental results show that the anode electrochemistry exhibited the same characteristics at a fixed oxygen partial pressure for three different fuel mixtures such as H_2-H_2O, CO-CO_2, and CH_4-H_2O. However, when the measured oxygen partial pressures are different, the anode electrochemistry showed different characteristics. Setoguchi et al. [21] concluded that anodic polarization depends strongly on the oxygen partial pressure in the fuel mixture, but is independent of the fuel type (H_2, CO, or CH_4).

Mizusaki et al. [22] studied the reaction kinetics of CO on porous Pt. They investigated a mechanism in which O_2 is produced at the TPB as a result of the reverse reaction of the oxygen reduction reaction at the cathode as shown below

$$2O_O^x(YSZ) \leftrightarrow O_2(g) + 4e^- + 2V_O^{\bullet\bullet}(YSZ)$$

Next the produced O_2 gas reacts with CO to produce CO_2. In other words, the mechanism assumed that the electrochemistry at the anode and at the cathode are fundamentally the same but occur in the reverse direction. If this was the case, the anodic and cathodic polarization should have similar characteristics. However, Mizusaki et al. [22] found that the anodic polarization conductivity has different characteristics from that of the cathode reactions and rejected the mechanism. Instead, Mizusaki et al. [22] suggested that the electrochemical reaction in a CO-CO_2 atmosphere proceeded directly with CO and CO_2. To explain the 1/2 dependence of p_{CO} on the anodic current, they used the following rate-limiting reaction between the adsorbed CO and CO_2 on the Pt surface and the adsorbed oxygen on the YSZ surface, without any further discussion of a full detailed mechanism.

$$CO(Pt) + O(YSZ) \leftrightarrow CO_2(Pt)$$

Aagerg et al [23] compared CO and H_2 electrochemistry in more detail and concluded that

CO polarization resistance is 2-5 times higher than H_2. They reported that the measured exchange current density had a maximum around 45% CO and 55% CO_2 rather than increasing monotonically with p_{CO} and that the anodic charge-transfer coefficients for H_2 and CO were 1 and 1/2, respectively. They concluded that their experimental data corresponded, to some extent, to the Etsell and Flengas Mechanism II [20] where CO and CO_2 were directly involved in the charge-transfer step.

Holtappels et al. [24] examined the CO/CO_2 electrochemistry on Ni/YSZ as a function of the electrode potential and the partial pressure of the reactants at 1273K. They reported highly unstable electrode reactivity, fluctuating between an active and a passive mode as shown in Figure 3-1.

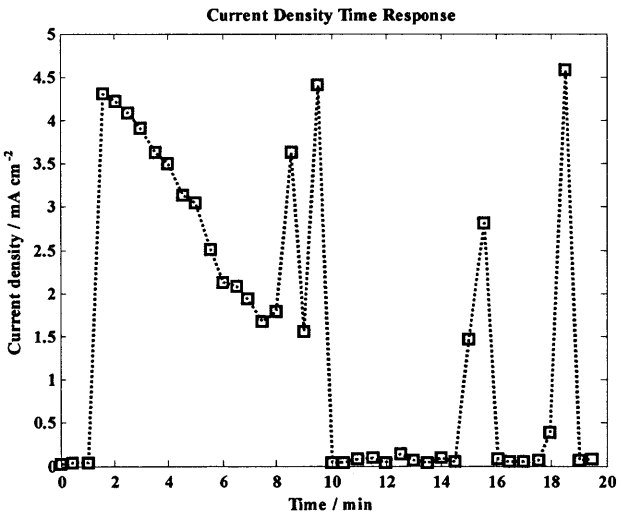

Figure 3-1. Current density- time response of a Ni-YSZ cermet electrode with the total overpotential of 40 mV(including the Ohmic overpotential). p_{CO}= 0.1 bar and p_{CO_2} = 0.02 bar, T=1000 °C. Reproduced from Hotalppels [24]

They tried to explain this observation qualitatively using a "modified reconstruction model" in which the Ni surface is modified depending on the degree of carbon coverage which changes the reaction rate. They acknowledged that Aarberg et al. [23] reported no instabilities and that

this discrepancy, compared to their work, was tentatively attributed to differences in the sample preparation, leading to different properties of the electrode surfaces. It is noted that, in the active state, the CO oxidation reaction is more than one order of magnitude slower than the hydrogen oxidation reaction on these Ni-YSZ cermet electrodes. These results show clear differences in the kinetics of the CO and H_2 oxidation reaction.

Matsuzaki and Yasuda [16] designed experiments to explore the effects of p_{O_2} and the water-gas shift (WGS) reaction on the H_2 and CO electrochemistry on a Ni-YSZ cermet electrode. Even under constant p_{CO_2}, CO electrochemistry was 2-3 times slower than H_2 electrochemistry. This contradicted Setoguchi et al.'s finding reported above [21] that the electrochemical reaction at the anode is independent of the fuel. From the EIS analysis using Randle-type circuit, they concluded that CO electrochemistry is slower than H_2 because of the higher surface diffusion resistance of CO at 1023K, and because of the higher surface diffusion resistance and charge-transfer resistance at 1273K. They also showed that the WGS is fast and reaches equilibrium based on the observation that different fuels produced the same results when their expected equilibrium composition were the same.

Boulenouar et al. [25] applied Ni grid electrode to exclude the complex gas transport effects in the porous electrode. To examine the effects of p_{CO} and p_{CO_2}, they varied one of these two partial pressures while keeping the other constant. They showed that the pressure dependence of the anode polarization conductivity is proportional to $\left(p_{CO}\right)^{1/4}$ and $\left(p_{CO_2}\right)^{1/2}$ on average. They also showed that the anode polarization in not a function of the oxygen partial pressure, contrary to Setoguchi et al.'s finding reported above. From the EIS analysis, Boulenouar et al. [25] suggest that CO, O, and CO_2 participate in the reaction mechanism, CO and O being in the

adsorbed form.

Based on the previous models, Lauvstad et al. [12] examined four possible mechanisms for CO electrochemical oxidation. These models are:

(a) Model 1

Oxidation of gaseous CO via adsorbed atomic oxygen, which is the same as Etsell and Flengas [20] Model I. There is only one adsorbate, O(YSZ)

$$O_O^x(YSZ)+(YSZ)\leftrightarrow O(YSZ)+V_O^{\bullet\bullet}(YSZ)+2e^-(Ni)$$
$$CO(g)+O(YSZ)\leftrightarrow CO_2(g)+(YSZ)$$

(b) Model 2

Oxidation of adsorbed CO via adsorbed atomic oxygen, which is the Boulenouar mechanism where there are two adsorbates, CO(Ni) and O(YSZ) [25].

$$CO(g)+(Ni)\leftrightarrow CO(Ni)$$
$$O_O^x(YSZ)+(YSZ)\leftrightarrow O(YSZ)+V_O^{\bullet\bullet}(YSZ)+2e^-(Ni)$$
$$CO(Ni)+O(YSZ)\leftrightarrow CO_2(g)+(Ni)+(YSZ)$$

(c) Model 3

The lifetime of adsorbed atomic oxygen on the YSZ surface is sufficiently short so that charge-transfer proceeds directly between $CO(Ni)$ and $O_O^x(YSZ)$ in the region close to the TPB.

$$CO(g)+(Ni)\leftrightarrow CO(Ni)$$
$$O_O^x(YSZ)+CO(Ni)\leftrightarrow CO_2(g)+V_O^{\bullet\bullet}(YSZ)+(Ni)+2e^-(Ni)$$

(d) Model 4

Assuming the rates of the diffusion process and the charge-transfer reaction to be of the same order of magnitude, both must be included in the mass balance performed on the adsorbed species. This is the same as Mechanism 3 except that the adsorbed CO diffusion toward the TPB

is included.

These four mechanisms led to different exchange current density expressions and equivalent circuits. Lauvstad et al. [13] conducted experiments using a Ni point electrode in contact with YSZ and showed that only Model 2, which includes two adsorbed intermediates, can reproduce the low frequency inductive behavior as well as the overall shape of their EIS measurements.

Costa-Nunes et al. [26] compared the performance of Cu-CeO2-YSZ and Ni-YSZ anodes using H_2, CO and syngas. Cells with Cu–CeO_2–YSZ anodes exhibited similar performance when operating on H_2 or CO fuels, while cells with Ni–YSZ anodes exhibited substantially lower performance when operating on CO compared with H_2. They qualitatively explained the slow CO electrochemistry based on the argument that the strong adsorption of CO on Ni surface prevents CO spillover to the electrolyte while adsorbed H easily moves to the electrolyte.

Ehn et al. [27] pointed out the disagreements among previous measurements using Ni point and Ni-YSZ porous anodes. In porous anodes, the TPB length is hard to determine because of its complex structure. In a point electrode, the TPB length is still difficult to vary in a controlled manner. Instead, Ni pattern anodes were used for the electrochemical measurements in CO/CO_2 and H_2/H_2O atmospheres. Two Ni pattern anodes (Sample A and B) were prepared by varying the Ni purity (99.999% and 99.995%) and thickness (0.5 and 1 μm) as listed in Table 3-1. Even though the two pattern anodes shared the same TPB length, they showed significantly different results. In Sample A, the polarization resistance in CO/CO_2 was about 50 times larger than in H_2/H_2O. On the other hand, Sample B showed less difference; the polarization resistance in CO/CO_2 was about six times larger than in H_2/H_2O. Holes were formed in Sample A during the test because it was not thick enough while only bubbles appeared in Sample B. The formation of holes increased the TPB length and produced lower polarization resistance in Sample A than in

Sample B. The segregation of impurity in Sample B led to an insulating layer formation, thereby affecting the electrode reactions. They concluded that H_2 and CO electrode reaction rates are on the same order of magnitude and it is hard to obtain a well-defined TPB even in the patterned anode.

Table 3-1. Sample data including purity of the nickel that was used in processing, thickness of the nickel layer, processed triple phase boundary length, L_{TPB}, and the effect of testing on the appearance nickel electrode. * is the observation after testing.

Sample	Ni-purity	Ni-thickness	L_{TPB}	Nickel surface*	Pattern*
A	99.999%	0.5 μm	41 cm	Holes	intact
B	99.995%	1 μm	41 cm	Bubbles	loosen

Even though Sukeshini et al. [11] adopted the same method of Ni patterned anode, a 100-nm thin Ni pattern broke up into interconnected region, and they failed to get a relationship between the TPB length and the electrochemistry. They found that

(i) the H_2 electrochemistry rate was significantly faster than the CO electrochemistry rate

(ii) the H_2 electrochemistry was dominant during the oxidation of H_2/CO mixture

(iii) H_2O inhibits CO electrochemistry and there was negligible water-gas shift.

They noted that there was a lack of a quantitative multi-step mechanism to interpret their kinetic measurements.

Habibzadeh et al. [28] continued to use Sukeshini's work in the same group but with a thicker (1 micron) patterned anode, which enables the investigation of the effect of the TPB length. Four different patterns with the same TPB length and different Ni area showed different performance. This suggested that processes related to adsorption, surface diffusion, and desorption might impact the availability of a TPB surface site fractions and thus charge-transfer steps. Moreover, the dry CO electrochemical oxidation rates were found to be no more than 2-4 times less than the

H_2 electrochemical oxidation rate at comparable conditions. It was also reported that the addition of 3% H_2O to CO increased the performance by as much as 40-50 %, likely due to the water-gas shift reaction on the Ni surface, which is directly opposite to Sukeshini et al. [11]. However, there was no further discussion on this point. Habibzadeh [19] also developed the following CO electrochemical oxidation.

(a) Adsorption/desorption

$$CO(g) + (Ni) \leftrightarrow CO(Ni)$$

$$CO_2(g) + (Ni) \leftrightarrow CO_2(Ni)$$

$$O_2(g) + (Ni) \leftrightarrow 2O(Ni)$$

(b) Surface reaction

$$CO(Ni) + O(Ni) \leftrightarrow CO_2(Ni)$$

(c) One step Electrochemistry

$$CO(Ni) + O^{2-}(YSZ) \leftrightarrow CO_2(Ni) + (YSZ) + 2e^-(Ni)$$

(d) CO surface diffusion

He added CO surface diffusion on the Ni surface to the mechanism. However, instead of solving a differential reaction-diffusion equation to get the spatial distribution of surface species on Ni and YSZ, he assumed a linear profile for the surface species along an effective diffusion length, which was not defined quantitatively. His EIS experimental measurements and simulation results, shown in Figure 3-2 and 3-10, show the following.

(1) While the simulation using the proposed model showed a large high frequency semi-circle and a small low frequency semi-circle, the measurements showed two comparable size suppressed semi-circles.

(2) The polarization resistance, which is defined as the impedance when the frequency is zero and corresponds to the higher value of the two real axis intercepts of the EIS plot in Figure 3-2 and 3-3, decreased as the applied anode activation overpotential increased in both experiments and simulations. However, a large discrepancy was noticeable. Especially at OCV, the simulation result was more than 40% off from measurements.

He suggested that using a constant phase element (CPE) instead of a pure capacitor to model the double layer can resolve the disagreement in the shape of the EIS results, that is the perfect semi-circles vs. the suppressed semi-circles. He concluded that the proposed model failed to capture the surface diffusion and adsorption/desorption of the species that accounts for the low frequency semi-circle.

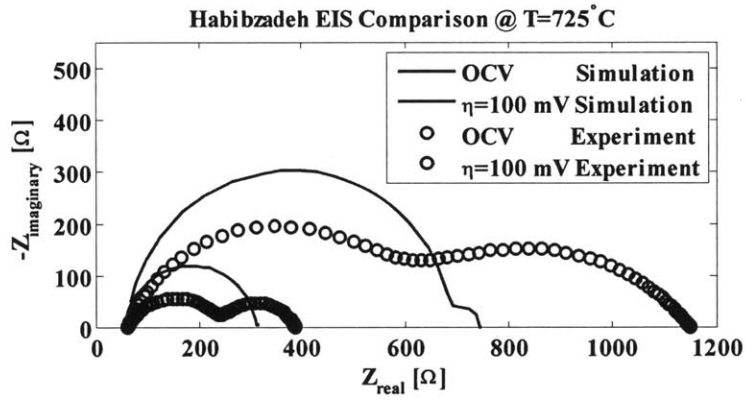

Figure 3-2. Habibzadeh EIS simulation and his experimental measures at OCV and η=100 mV when T=725 °C. Solid lines are for the simulation results and open circles are for experimental measurements.

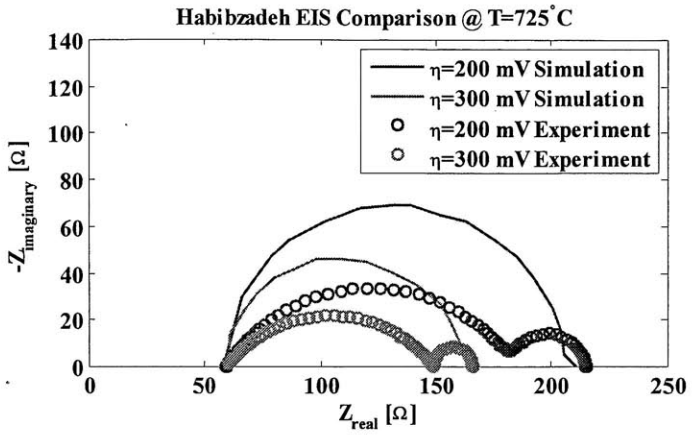

Figure 3-3. . Habibzadeh EIS simulation and his experimental measures at η=200 mV and η=300 mV when T=725 °C. Solid lines are for the simulation results and open circles are for experimental measurements. .

Recently, Yurkiv et al. [29] examined an elementary kinetic mechanism of the electrochemical CO oxidation mechanism. The mechanism consisted of three gas species (CO, CO2, O2), four Ni surface species ((Ni), CO(Ni), CO_2(Ni), O(Ni)), four YSZ surface species ((YSZ), CO(YSZ), O^-(YSZ), O^{2-}(YSZ)), and two bulk species ($O_O^{\times}$ and $V_O^{\bullet\bullet}$). The one dimensional reaction-diffusion model was applied on the Ni and YSZ surfaces. They compared the three different charge-transfer pathways in the CO electrochemistry mechanisms. All the three pathways are based on the oxygen-spillover mechanism [21][12]. In other words, CO does not participate in the charge-transfer reaction but reacts with oxygen atoms on Ni producing CO_2. The three mechanisms are:

(1) O1 + O2

$$O^{2-}(YSZ) \leftrightarrow O^{-}(YSZ) + e^{-}(Ni)$$
$$O^{-}(YSZ) + (Ni) \leftrightarrow O(Ni) + (YSZ) + e^{-}(Ni)$$

(2) O3 + O4

$$O^{2-}(YSZ)+(Ni)\leftrightarrow O^{-}(Ni)+(YSZ)+e^{-}(Ni)$$
$$O^{-}(Ni)\leftrightarrow O(Ni)+e^{-}(Ni)$$

(3) O5 (Single-step)

$$O^{2-}(YSZ)+(Ni)\leftrightarrow O(Ni)+(YSZ)+2e^{-}(Ni)$$

As far as we know, this is the first work including two-step charge-transfer reactions. However, the calculation domain and corresponding boundary conditions were not specified in their work. They fitted their model to the point anode measurements by Lauvstad et al. [13] and the O1+O2 reaction pathway showed the best agreement in the Tafel plots and the impedance plots. However, it failed to reproduce the low frequency inductive loop. Note that the low frequency inductive loop was the single determining factor in choosing a possible reaction pathway in Lauvstad et at. [13] as reported above.

There are some consistent and some contradictory experimental observations in the literatures and they are summarized as follows.

(i) The dependence of the exchange current density, i_0, on p_{CO} and p_{CO_2} was studied. Etsell and Flengas [20] compared the measured exchange current densities at several CO compositions in CO-CO_2 mixtures, and reported that i_0 should peak near 50% of CO. Aaberg et al. [23] also observed that i_0 reached a maximum near 45% CO. They supported Etsell and Flengas's Mechanism II where both CO and CO_2 are directly involved in the electrochemical step because i_0 based on the Mechanism II was expected to reach a maximum below 50% of CO. Because p_{CO} and p_{CO_2} were varied simultaneously in both studies, the reaction order with respect to CO and CO_2 could not be obtained experimentally. However, Etsell and Flengas's Mechanism II predicted the reaction order of ½ for both CO and CO_2. Boulenouar et al. [25] measured the

reaction order with respect to CO and CO_2 by changing p_{CO} or p_{CO_2} while keeping the other constant. The measured reactions orders were ¼ and ½ with respect to CO and CO_2, respectively. To sum, there was positive dependence of the CO electrochemistry on p_{CO} and p_{CO_2} even though the reaction orders with respect to CO were different.

(ii) Aaberg et al. [23] measured the apparent charge-transfer coefficient, which is the slope of the anodic branch when the activation overpotential is high in the Tafel plots. They reported that the apparent charge-transfer coefficient was unity. Sukeshini et al. [11] also measured the apparent charge-transfer coefficient from the Tafel plots and reported that it was between 0.25-0.45. One-half of the apparent charge-transfer coefficient value is considered the anodic charge-transfer coefficient because two electrons are involved in the overall CO electrochemical oxidation. The values reported for the anodic charge-transfer coefficient in different experiments were different.

(iii) Which partial pressures among p_{O_2}, p_{CO} and p_{CO_2} affect the overall CO electrochemical oxidation has also been discussed. If the CO electrochemical oxidation depends only on p_{O_2}, it can be concluded that CO and CO_2 do not directly participate in the electrochemistry step. In other words, the anodic reaction is the reverse of the oxygen reduction reaction (ORR) in the cathode. Setoguchi et al. [21] measured the equilibrium p_{O_2} for different fuel compositions and reported that the anode electrochemical oxidation reactions depended strongly on the oxygen partial pressure and was independent of the fuel type such as H_2, CO, or CH_4. On the other hand, Matsuzaki and Yasuda [16] reported that the electrochemical oxidation in the anode depended on the partial pressures of the fuel even when the equilibrium p_{O_2} was the same. Boulenour et al. [25] also showed that the CO electrochemical oxidation reaction depended on the pressures of

CO and CO_2, but not on the equilibrium O_2 partial pressure.

(iv) The role of water in the CO electrochemistry was studied. The addition of water to the fuel promoted the overall CO electrode kinetics in Habibzadeh et al. [28] experiments, while the opposite results were also reported by the same group in Sukeshini et al. [11].

Previous researchers proposed a number of CO electrochemistry mechanisms. The charge-transfer reaction models can be divided into two groups;

(i) In the first group, CO does not participate in the charge-transfer reactions. In this case, the overall charge-transfer reaction is referred to as an oxygen-spillover mechanism [12,21,29].

$$O_O^{\times}(YSZ) \leftrightarrow O(Ni) + 2e^{-}(Ni)$$

(ii) In the second group, CO participates in a charge-transfer reaction directly, either in the adsorbed form (Langmuir-Hinshelwood mechanism, $CO(Ni) + O_O^{\times} \leftrightarrow CO_2(g) + 2e^{-}(Ni)$) or in the gaseous phase (Eley-Rideal mechanism, $CO(g) + O_O^{\times} \leftrightarrow CO_2(g) + 2e^{-}(Ni)$) [11,19,20,23].

A similar development of charge-transfer reaction mechanisms can be found in H_2 electrochemistry. Two most frequently mentioned pathways in H_2 electrochemistry are the hydrogen-spillover mechanism and the oxygen-spillover mechanism. Vogler et al. [30] examined seven possible H_2 charge-transfer pathways including the hydrogen and oxygen-spillover mechanisms and concluded that only the hydrogen-spillover mechanism yielded agreement with the complete experimental data set on Ni pattern anode by Bieberle et al. [31]. Goodwin et al. [32] also compared simulation results based on the hydrogen and oxygen-spillover mechanisms with Ni pattern anode measurements by Mizusaki et al. [33]. The hydrogen-spillover mechanism provided a good quantitative representation of the measured polarization behavior over a wide range of gas-phase composition and with both anode and cathode biases. The hydrogen-spillover

mechanism has been more widely accepted and seems more probable than the oxygen-spillover mechanism in H_2 electrochemical oxidation mechanisms.

In conclusion, the CO electrochemistry mechanism is still unclear. Moreover, there has been no multi-step mechanism in which CO is directly involved in the charge-transfer reaction. In the following section, we propose a detailed CO electrochemistry mechanism in which CO directly participates in two one-electron charge-transfer reactions and use Habibzadeh pattern anode experimental measurements [19] to obtain unknown kinetic parameters.

3.3. CO Electrochemistry Model Development

The overall electrochemical oxidation reaction for CO can be written in the form

$$CO(g) + O^{2-}(YSZ) \leftrightarrow CO_2(g) + 2e^{-}(Ni)$$

Three species are associated with this reaction: gaseous CO and CO2, and oxygen ions O^{2-}, which is generally assumed to exist in the bulk lattice of the electrolyte (in Kröger-Vink notation, an oxygen ion is written as $O_O^{\times}$ having neutral charge because the oxygen ion occupies its site in the lattice). In the following section, possible intermediate species on Ni and YSZ are examined and a new multi-step CO oxidation mechanism with two-step charge-transfer reactions and with CO participating in the charge-transfer reactions is proposed.

3.3.1. Possible intermediate surface species on Ni and YSZ

3.3.1.1. Ni surface

It is known that CO is strongly chemisorbed on Pt and Ni catalysts [20,34]. Costa-Nunes et al. [26] used the strong adsorption of CO on Ni to explain the poor performance of a cell

fueled by CO with an Ni-YSZ anode compared to one fueled by H_2. In the hydrogen charge-transfer reaction, hydrogen dissociatively adsorbs on Ni, and the H atoms spillover onto YSZ reacting with O ions on the YSZ and shedding an electron to the Ni. However, the strong adsorption of CO on Ni inhibits this kind of spillover process, which can lead to the observed poor performance of the CO electrochemistry. Adsorption of CO_2 on platinum group metals has not been observed [34]. Lauvstad et al [12] and Etsell and Flengas [20] both neglected the possibility of nondissociative adsorption of CO_2 in their CO electrochemical oxidation mechanism because CO_2 adsorption was not observed on Pt in the range 25-1400 °C. It was therefore assumed that CO_2 desorbs immediately after its formation. Because the anode-side oxygen partial pressure is on the order of 10^{-14} (0.7V @ 800°C) to 10^{-20} bar (1V @ 800°C), we assume that it is unlikely that gaseous O_2 is formed or dissociatively adsorbs on Ni. Hence, in our proposed mechanism, only CO species can exist on the Ni surface.

3.3.1.2. YSZ surface

Recently, Yurkiv et al. [29] measured CO and CO_2 adsorption on YSZ surface. They found that no CO is adsorbed at $T > 600K$. It was concluded that CO oxidation to CO_2 on YSZ occurs via Eley-Rideal mechanism where gaseous CO directly reacts with oxygen on YSZ surface to yield gas-phase CO_2. Hence, CO and CO_2 adsorption on YSZ will not be considered in our mechanism.

Oxygen incorporation reaction has been studied extensively on mixed ionic and electronic conductor $SrTiO_3$ [35–37]. Based on experiments, the following oxygen incorporation mechanism has been proposed [34,35,38] .

$$O_2(g) \leftrightarrow O_2(ad)$$
$$O_2(ad) + e^- \leftrightarrow O_2^-(ad)$$
$$O_2^-(ad) + e^- \leftrightarrow O_2^{2-}(ad)$$
$$O_2^{2-}(ad) \leftrightarrow 2O^-(ad)$$
$$O^-(ad) + e^- + V_o \leftrightarrow O_o^{2-}(YSZ)$$

Because the formation of neutral atomic O on a wide band gap oxide surface is expected to be energetically unfavorable, reactions with neutral O atom were neglected. Also, $2O^{2-}$ surface species was not considered because it was found to be stable only inside the crystal lattice [38]. From the oxygen incorporation mechanism, the possible surface species are O_2, O_2^-, O_2^{2-} and O^-. While the formation of O_2^- superoxide ions by oxygen adsorption has been frequently observed on wide bandgap oxides, the existence of adsorbed O_2^{2-} is more controversial. Note that the material studied is mixed ionic and electronic conductor (MIEC) where electrons are readily involved in the reactions. Also the oxygen partial pressures in oxygen incorporation studies are 0.0001-0.3bar [35], which is significantly higher than the anode-side oxygen partial pressures, 10^{-14} (0.7V @ 800°C) to 10^{-20} bar (1V @ 800°C). Considering that the oxygen partial pressure at the anode is significantly lower that at the cathode and the electrons are only available at the TPB rather than on the entire surface, the oxygen molecules, O_2, O_2^{2-} and O_2^- are neglected in our mechanism. Yurkiv et al. [29] also only considered O^- species on the YSZ surface even though there was no discussion on other possible oxygen species on YSZ. Therefore, in the proposed mechanism, there is only O^- species on the YSZ surface.

3.3.2. Proposed mechanism

Based on the analysis of the most likely species on the surfaces of the anode and

electrolyte, a mechanism that includes three elementary reactions in the Ni-YSZ TPB region is proposed. The reactions are:

1. Adsorption/desorption on the Ni surface

$$CO(g)+V(Ni)\leftrightarrow CO(Ni) \qquad \text{(R. 1)}$$

2. Two-step charge-transfer reactions at the TPB

$$O_O^x(YSZ)+(YSZ)\leftrightarrow O^-(YSZ)+V_O^{\bullet\bullet}(YSZ)+e^-(Ni) \qquad \text{(R. 2)}$$

$$O^-(YSZ)+CO(Ni)\leftrightarrow CO_2(g)+(YSZ)+(Ni)+e^-(Ni) \qquad \text{(R. 3)}$$

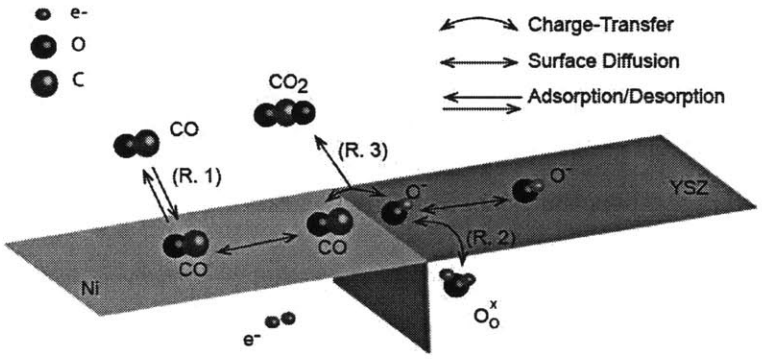

Figure 3-4. Schematics of CO electrochemical oxidation at TPB

On the Ni anode surface, CO(Ni) is an adsorbed CO molecule, (Ni) is an empty surface site, and e-(Ni) is an electron within the Ni anode. Within the YSZ electrolyte, $O_O^x(YSZ)$ is a lattice oxygen and $V_O^{\bullet\bullet}(YSZ)$ is an oxygen vacancy. It is often reasonable to assume that the concentrations of $V_O^{\bullet\bullet}(YSZ)$ and $O_O^x(YSZ)$ in the bulk of the electrolyte are constant and mainly determined by the doping level [39]. On the YSZ surface there is a single species, O^- (YSZ), and empty sites (YSZ). The net anode half-cell electrochemical oxidation reaction of

carbon monoxide can be written in Kröger-Vink notation as,

$$CO(g) + O_O^x(YSZ) \leftrightarrow CO_2(g) + V_O^{\bullet\bullet}(YSZ) + 2e^-(Ni) \qquad \text{(R. 4)}$$

The three step reaction mechanism is composed of two charge-transfer reactions (i.e., R. 2 and R. 3) and one adsorption/desorption reaction (i.e., R. 1). The three reaction steps involve two surface species, CO(Ni) and O^-(YSZ), and two gas-phase species. (R. 2) produces O^-(YSZ) at the TPB. (R. 3) consumes O^-(YSZ) at the TPB. If the rates of (R. 2) and (R. 3) are not the same, O^-(YSZ) can accumulate in the neighborhood of the TPB and diffuse away on YSZ. This is the first two-step charge-transfer mechanism where CO directly participates in the charge-transfer reactions. The only other two-step charge-transfer mechanism for CO was proposed recently by Yurkiv et al. [29] , which was based on an oxygen-spillover mechanism where CO is involved only through thermochemical reactions. As mentioned earlier, H_2 electrochemistry mechanism show that better agreement could be reached with hydrogen-spillover mechanism than oxygen-spillover mechanism.

3.3.3. Anode geometry

A typical SOFC anode is made of porous Ni/YSZ cermet(a composite of a ceramic and a metal). Although the porous structure yields high electrochemical performance, it is not well-suited for studying the processes at the TPB itself. This is because the active regions are deep inside the porous structure and are therefore not easily accessible using microscopic or spectroscopic techniques. Also, the exact microstructural properties and the TPB length are usually not known. Electrochemical experiments with a well-defined model anode such as patterned or point anodes are more suitable for detailed examination of actual interfacial electrochemistry [40].

Among CO electrochemistry experimental data, the most complete and extensive results on Ni patterned anode were reported by Habibzadeh [19]. He reported pattern-anode measurements that provide a great deal of information which can be used to examine the fundamental mechanism of CO electrochemical oxidation. In his experiment, electrochemical impedance measurements were performed for four overpotnetials, 0, 100, 200, and 300 mV at four different temperatures, 700°C, 725°C, 750°C, and 775°C with fixed gas compositions. Steady-state Tafel plots were also reported at these temperatures. The partial pressure of CO_2 was varied independently by using mixtures of CO and CO_2 diluted in Ar.

Because of the availability of these data, we chose to develop a reaction-diffusion model based on the same pattern anode geometry (see top panel of Figure 3-5) used by Habibzadeh. The nickel-pattern width and thickness are δ_{Ni} and h_{Ni}, respectively, and the catalyst area A_{Ni} is the total surface area of the exposed Ni. The electrolyte gap width δ_{YSZ} defines the pattern spacing and h_{YSZ} is the electrolyte thickness. Each pattern has a three-phase boundary length L_{TPB} defined by the intersection of the Ni, YSZ, and the gas. Because of the periodicity of the pattern, the model can be formulated using only the section highlighted in the bottom panel of Figure 3-5 (shown in cross-section). This geometry consists of one half of one strip of the Ni and YSZ, with symmetry conditions applied at the left and right boundaries. The x and y coordinates are measured from the TPB toward the center of the Ni and YSZ strips, respectively. The parameters $L_{Ni} = \delta_{Ni}/2$ and $L_{YSZ} = \delta_{YSZ}/2$ are the half-widths of the pattern.

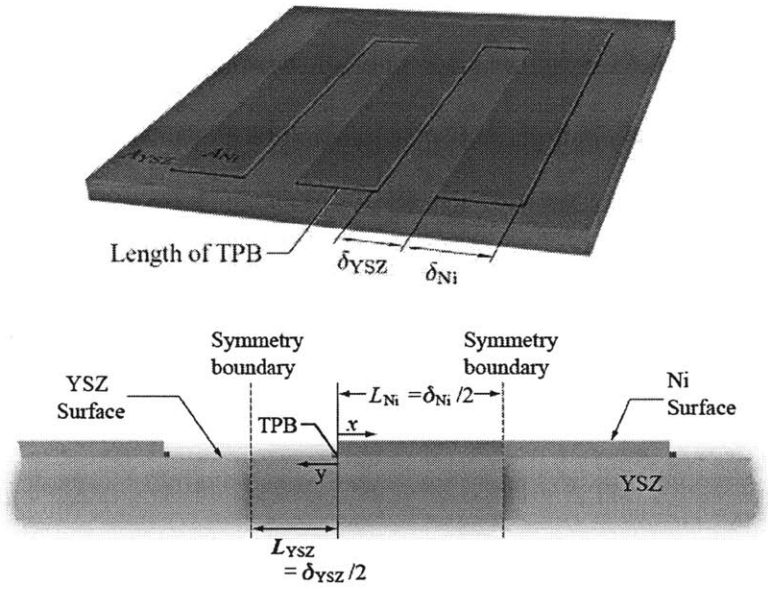

Figure 3-5. (Top panel) Schematic drawing shows the geometry of the Ni patterns used by Habibzadeh [19]. The same geometry is used here as a basis for our mathematical models. Parameter definitions are given in the text. Image and description are modified from the given reference (Bottom panel) Simplified geometry used for modeling purposes as based on prepared Ni-patterned-anodes.

Table 3-2 Geometric parameters of Ni patterned anode used by Habibzadeh [19].

Parameters	Values	Units
Ni Width (δ_{Ni})	100	μm
YSZ width (δ_{YSZ})	111	μm
Electrolyte Area (A_{YSZ})	20	mm^2
Ni Area (A_{Ni})	3.16	mm^2
TPB length (l_{TPB})	64.2	mm

3.3.4. The anode model

In this section, the governing equations for the two surface species, CO(Ni) and O^-(YSZ), are

formulated based on the proposed CO electrochemical oxidation mechanism. We assume that the charge-transfer reactions (R. 2 and R. 3) occur only at the TPB. Habibzadeh et al. [28] reported that the Ni surface area impacts the electrochemistry of CO, which implies that the surface diffusion of the adsorbed CO species play a role in CO electrochemistry. Therefore, the surface diffusion of CO on the Ni surface is included in our analysis. On the YSZ free surface, only the surface diffusion of O^-(YSZ) is considered because there is no surface reaction other than the charge-transfer reactions at the TPB. Because the Ni pattern width (100μm) and YSZ gap (111μm) between the Ni patterns are small compared with the length of the Ni pattern (3mm), the Ni and YSZ surfaces are modeled as one-dimensional domains along the Ni pattern width and the YSZ gap. The governing equations are formulated as one-dimensional reaction-diffusion equations with their boundary conditions determined by the charge-transfer steps (R. 2 and R. 3) at the TPB. The formulation of the governing equations is similar to that used by Habibzadeh [19] except that:

(1) the CO surface diffusion on Ni is formulated without using arbitrary assumptions with regard to the effective diffusion length. Instead of assuming a linear concentration profile along the effective diffusion length, the profile is obtained from the solution of the governing equations..

(2) the charge-transfer reactions are modeled as two consecutive single-electron transfer steps (R. 2 and R. 3).

(3) A conservation equation of the new intermediate species, O^-(YSZ), is introduced. The distribution of O^-(YSZ) is governed by its surface diffusion on YSZ and the charge-transfer reactions at the TPB.

3.3.4.1. Diffusion of CO along the Ni surface

The coverage of CO(Ni) can be described using a one-dimensional reaction-diffusion equation such that

$$\frac{\partial \Gamma_{Ni}\theta_{CO}(x,t)}{\partial t} = D_{CO}\frac{\partial^2 \Gamma_{Ni}\theta_{CO}(x,t)}{\partial x^2} + k_{1,f}p_{CO}\left(1-\theta_{CO}(x,t)\right) - k_{1,b}\Gamma_{Ni}\theta_{CO}(x,t) \quad (3.2)$$

θ_{CO} is the surface coverage [unitless] of the adsorbed carbon monoxide on the anode CO(Ni). Here, $\theta_{CO}(x,t)$ is the surface coverage at coordinate x measured from the TPB along the Ni surface. Accordingly, $\theta_{CO}(0,t)$ is the surface coverage at the TPB. For simplicity, and to keep the notations consistent with the case in which surface diffusion is neglected, θ_{CO}^0 (i.e., with no parenthesis) refers to $\theta_{CO}(0,t)$. The surface site density Γ_{Ni} (mol/cm^2) and surface diffusion coefficient D_{CO} (cm^2/s) are assumed to be constant. The forward and backward rate constants $k_{1,f}$ and $k_{1,b}$ of reaction (R. 1) are associated with the adsorption and desorption of CO on nickel. The partial pressure of gaseous CO is p_{CO} and is taken to be constant. Note that the surface molar concentration (mol/cm^2) is given by $\Gamma_{Ni}\theta_{CO}(x,t)$.

While the current from a porous electrode is usually normalized with respect to the nominal electrolyte area, the current from a patterned anode can be normalized by: (1) the TPB length; (2) the Ni catalyst area; or (3) the YSZ electrolyte area. In the formulation, we use the current instead of the current density in order to avoid any confusion from normalization and validate it using the raw data from Habibzadeh [19].

The 1-D governing equation (3.2) for the coverage of CO(Ni) is a second-order linear partial differential equation requiring two boundary conditions on the single spatial variable x. The first of these is applied at the TPB and relates the surface diffusion flux of CO to the

generation rate of CO by the charge transfer reaction (R. 3). Mathematically, this is written as

$$-D_{CO}\left.\frac{\partial \Gamma_{Ni}\theta_{CO}(x,t)}{\partial x}\right|_{x=0} = -\frac{I_3}{FL_{TPB}} \tag{3.3}$$

where F=96485 [C/mol] is the Faraday constant, L_{TPB} is the TPB length, and I_3 is the current [A] associated with the reaction (R. 3), in which the adsorbed CO(Ni) appears as a reactant.

The second boundary condition relates the geometry of the physical domain on which a solution is sought. Under the 1-D approximation along the spatial coordinate x, a symmetry boundary condition is applied at the pattern centerline as

$$D_{CO}\left.\frac{\partial \Gamma_{Ni}\theta_{CO}(x,t)}{\partial x}\right|_{x=L_{Ni}} = 0 \tag{3.4}$$

where L_{Ni} is half of the Ni pattern width as shown in Figure 3-5.

In the governing equations of CO(Ni), all the kinetic parameters, corresponding to the adsorption/desorption reactions of CO, and the surface diffusion coefficient, D_{CO}, are known. The rates of CO adsorption and desorption on Ni can be taken from the reaction mechanism describing the heterogeneous reforming of CH_4 over a Ni catalyst [41]. The adsorption rate parameter, $k_{1,f}$, can be written simply in terms of a sticking probability γ_{CO}=0.5 from Hecht et al [41] as

$$k_{1,f} = \frac{\gamma_{CO}}{\sqrt{2\pi M_{CO} RT}} = \left[\frac{mole}{N\sec}\right] \tag{3.5}$$

The desorption rate parameter of CO on Ni is obtained from detailed balance and is written as

$$k_{1,b} = A_{des,CO} \exp\left(-\frac{E_{des,CO}}{RT}\right) = \left[\frac{1}{\text{sec}}\right] \tag{3.6}$$

Where $A_{des,CO} = 4.041 \times 10^{11} s^{-1}$ and the activation energy $E_{des,CO} = 112.85\ kJ/mol$ taken from Hecht et al [41]. For simplicity, the dependence of the activation energy on CO surface coverage is not considered.

The diffusivity can be written in an Arrhenius form as follows

$$D = D_0 \exp\left(-\frac{E_{act}}{RT}\right) \tag{3.7}$$

where D_0 is the pre-exponential factor and E_{act} is the activation energy.

The CO surface diffusion coefficients on Ni surface were measured more than 35 years [42,43]. However, the reported values vary by orders of magnitude, depending on the experimental methods, surface coverage and surface directions (e.g., (001) or (111)). The activation energy in Equation (3.7) is 2605 - 28945 J/ mol. Moreover, there is a wide range of values for D_0 (the pre-exponential coefficient): varying between 10^{-8} and 1 [m^2/s]. At T~750 °C, the surface diffusion coefficient of adsorbed CO on Ni, computed from the reported values, is in the range of 2.5×10^{-6} to 4.95×10^{-13} [m^2/s]. For our simulation, we chose Lawrence Berkeley Lab data [44] where the pre-exponential coefficient is 4.5×10^{-6} [m^2/sec] and the activation energy is 14,602 J.

3.3.4.2. Diffusion of O^- along the YSZ surface

(1) Governing equations

The transport of charged species is often modeled by the Nernst-Planck equation describing the flux of charge species under the influence of a concentration gradient and the electric field gradient. In one dimension, for a species i this equation can be written as follows

$$J_i = -D_i \frac{\partial c_i}{\partial y} - \frac{z_i F}{RT} D_i c_i \frac{\partial \phi}{\partial y} \tag{3.8}$$

where J is the flux [mol/m^{2}s] along coordinate y, D_i is the diffusion coefficient [m^2/s], ϕ is the electric potential, c is the concentration [mole/m^3], and z is the valence of the charge carrier, T is the temperature [K] and R=8.314 [J/mol K] is the universal gas constant.

The electric potential ϕ is unknown and is described by the Possion equation of electrostatics (Gauss's law for the electric field) as follows.

$$\frac{\partial^2 \phi}{\partial y^2} = -\frac{\rho}{\varepsilon \varepsilon_0} = -\frac{F}{\varepsilon \varepsilon_0}\left[\sum_i z_i c_i\right] \tag{3.9}$$

Where ρ is the charge density, ε is the dielectric constant, and $\varepsilon_0 = 8.854 \times 10^{-12}$ [F/m] is the vacuum permittivity. Because $F/\varepsilon_0 = O\left(10^{16}\right)$ [cm V/mol] is large, very high electric fields result from very small deviations from electroneutrality. It is, therefore, often reasonable to assume that $\sum_i z_i c_i = 0$ except at the charge-transfer interface where a large potential difference is expected to develop. The electroneutrality requires a charged species to move in a pair with an oppositely charged species. It can be shown that the transport of this pair can be described by Fick's law of a neutral component while adjusting the diffusion coefficient to the ambipolar diffusion coefficient. Let's assume that there are two monovalent species, a positively charged species and a negatively charged species.

$$\frac{\partial c_-}{\partial t} = -\frac{\partial}{\partial y}\left(-D_- \frac{\partial c_-}{\partial y} + \frac{F}{RT} D_- c_- \frac{\partial \phi}{\partial y}\right) \tag{3.10}$$

$$\frac{\partial c_+}{\partial t} = -\frac{\partial}{\partial y}\left(-D_+ \frac{\partial c_+}{\partial y} - \frac{F}{RT} D_{O^-} c_+ \frac{\partial \phi}{\partial y}\right) \tag{3.11}$$

where their concentrations and diffusivities are given as c_+ and c_-, D_+ and D_-, espectively.

When we apply the electroneutrality condition $c_- = c_+$ and combine Equations (3.10) and (3.11), they reduce to an equation describing the diffusion of a neutral species according to Fick's law as follows.

$$\frac{\partial c_-}{\partial t} = D_{eff} \frac{\partial^2 c_-}{\partial y^2} \tag{3.12}$$

$$\text{where } D_{eff} = 2\left(\frac{1}{D_-} + \frac{1}{D_+}\right)^{-1} \tag{3.13}$$

Thus, the effective diffusivity is determined by the species with the lower diffusivity.

The one-dimensional approximation and charge neutrality assumption can be applied inside a uniform bulk (usually inside an electrolyte), but not necessarily on a surface. On a surface, the Possion-Nernst-Planck (PNP) equation, the combination of Equations (3.8) and (3.9), needs to be solved in a multi-dimensional space. Because it is a very challenging task in itself, previous researchers have assumed that the charged species transport on a surface follows Fick's law of a neutral species [29,32,45] and we follow the same approach. Thus, the simple Fickian approach is taken for the diffusion of O^- on the YSZ surface.

In our model, the governing equation is a diffusion equation of O^-(YSZ) along the YSZ surface because, in the proposed CO electrochemical oxidation, there is no surface reaction on the YSZ except at the TPB. The governing equation reduces to

$$\frac{\partial \Gamma_{YSZ}\theta_{O^-}(y,t)}{\partial t} = D_{O^-} \frac{\partial^2 \Gamma_{YSZ}\theta_{O^-}(y,t)}{\partial y^2} \tag{3.14}$$

where θ_{O^-} is a site fraction of adsorbed O^- on the YSZ surface. The surface site density Γ_{YSZ} (mol/cm^2) and surface diffusion coefficient D_{O^-} (cm^2/s) are assumed constant. As adopted in the description of CO coverage on Ni, $\theta_{O^-}(x,t)$ is the surface coverage at coordinate y

measured from the TPB along the YSZ surface as shown in Figure 3-5. Accordingly, $\theta_{O^-}(0,t)$ is the surface coverage at the TPB. For simplicity, and to keep the notations consistent with the case in which surface diffusion is neglected, $\theta^0_{O^-}$ (i.e., with no parenthesis) refers to $\theta_{O^-}(0,t)$.

(2) Boundary conditions

The 1-D governing equation (3.14) for the coverage of O^-(YSZ) is a second-order linear partial differential equation requiring two boundary conditions on the single spatial variable y. The first of these is applied at the TPB and relates the surface diffusion flux of O^- to the generation rate of O^- by the charge-transfer reactions (R. 2) and (R. 3). Mathematically, this is written as

$$-D_{O^-}\frac{\partial\theta_{O^-}(0,t)}{\partial y}=\frac{I_2-I_3}{\Gamma_{YSZ}FL_{TPB}} \tag{3.15}$$

where I_2 and I_3 are the current [A] associated with (R. 2) and (R. 3), respectively.

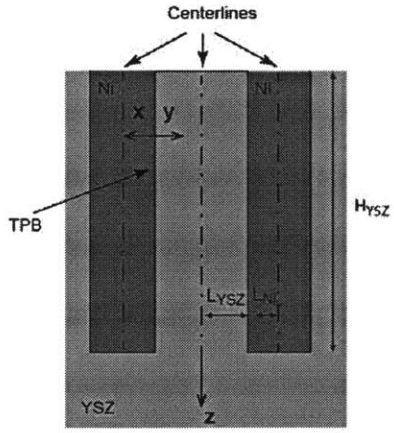

Figure 3-6. A schematic of the 1-D YSZ Domain

The second boundary condition relates to the geometry of the physical domain on which a solution is sought. Under the 1-D approximation along the spatial coordinate y, a symmetry boundary condition is applied at the centerline as

$$D_{O^-} \frac{\partial \theta_{O^-}(L_{YSZ}, t)}{\partial y} = 0 \tag{3.16}$$

where L_{YSZ} is the half width of the YSZ gap between Ni patterns strips as shown in Figure 3-6. This boundary condition will always hold if the 1-D approximation is valid.

If the diffusion coefficient D_{O^-} is very high, the 1-D approximation may not be valid since O^- will continue to increase on the YSZ strip until its concentration is much higher than the concentration of O^- outside of the 1-D domain. Under these conditions, diffusion of O^- along the z-coordinate direction (parallel to the pattern strips instead of transverse to them) is expected to be non-negligible. In essence, when D_{O^-} is large, the problem becomes 2-D in nature. An effective D_{O^-} above which the 1-D approximation is no longer justified can be estimated from

$$D_{O^-}^{eff} \sim O(H_{YSZ}^2 / \tau_{ch}) \tag{3.17}$$

where H_{YSZ} is the length of the YSZ strip between the Ni patterns (see Figure 3-6) and τ_{ch} is a characteristic time scale. For the patterned anodes used by Habibzadeh, $H_{YSZ} = 3\times10^{-3}$ m. Further, the frequencies associated with CO electrochemical oxidation process on the pattern anode are reported by Habibzadeh [19] to range between 10^{-1} to 10^{3} [Hz]. Therefore, the corresponding shortest characteristic time is 10^{-3} [sec]. Using these values, $D_{O^-}^{eff} \sim O(1\times10^{-2}\ m^2 / \sec)$.

When $D_{O^-} > 1\times10^{-2}$ [m^2/sec], it is reasonable to assume that O^- species will diffuse along the length of the YSZ strip and spill over onto the YSZ surface supporting the pattern anode for meaningful timescales associated with the CO electrochemical process. Despite this 2-D behavior, extension of the 1-D YSZ domain along which O^-(YSZ) can diffuse will still allow the problem to be solved using a 1-D formulation. That is, because the entire YSZ surface is much

larger than the 1-D YSZ domain (the entire YSZ surface is 25.4mm and 25.4mm and the width of YSZ gap is 0.111 mm), the following boundary condition can be applied in a 1-D setting to account for 2-D behavior if $D_{O^-} > 1\times10^{-2}$ [m^2/sec],

$$\frac{\partial\theta_{O^-}(\infty,t)}{\partial y}=0 \tag{3.18}$$

To summarize, the second boundary condition depends on the value of D_{O^-}. There are two cases:

(1) If $D_{O^-} < 1\times10^{-2}$ [m^2/sec], the symmetry boundary condition is applied at the centerline as

$$D_{O^-}\frac{\partial\theta_{O^-}(L_{YSZ},t)}{\partial y}=0 \tag{3.16}$$

(2) If $D_{O^-} > 1\times10^{-2}$ [m^2/sec], the following boundary condition is applied to account for the 2-D nature of the problem by effectively extending the 1-D domain,

$$\frac{\partial\theta_{O^-}(\infty,t)}{\partial y}=0 \tag{3.18}$$

In the governing equation of O^- on the YSZ surface, D_{O^-} is an unknown parameter, and the boundary condition, (3.16) or (3.18), is chosen according to the value of D_{O^-}. The other boundary condition is applied at the TPB according to (3.15) and is independent of the value of D_{O^-}.

3.3.4.3. Electrochemistry governing equations

The expressions for the currents produced by (R. 2) and (R. 3) can be formulated using

the Butler-Volmer equations for the two reactions:

$$I_2 = FL_{TPB}\left\{k_{2,f}\left(1-\theta_{O^-}\right)\exp\left(\frac{(1-\beta_2)FE}{RT}\right)-k_{2,b}\theta_{O^-}\exp\left(\frac{-\beta_2 FE}{RT}\right)\right\} \quad (3.19)$$

$$I_3 = FL_{TPB}\left\{k_{3,f}\theta_{O^-}\theta_{CO}\exp\left(\frac{(1-\beta_3)FE}{RT}\right)-k_{3,b}\left(1-\theta_{O^-}\right)\left(1-\theta_{CO}\right)p_{CO_2}\exp\left(\frac{-\beta_3 FE}{RT}\right)\right\} \quad (3.20)$$

where E is electric potential difference $E=\phi_a-\phi_{e,a}$ across the anode-electrolyte double layer. The ϕ_a is the electric potential in the metal anode, and $\phi_{e,a}$ is the electric potential in the electrolyte immediately outside the double layer on the anode side. The physical anode potential difference, E, has a single value, independent of how many charge-transfer pathways are active [32]. β_i is a cathodic charge-transfer coefficient of (R. i). $k_{i,f}$ and $k_{i,b}$ are the forward and backward reaction rate constants of (R. i). The charge-transfer reactions depend only on the concentrations of CO and O^- at the TPB where the reactions occur. For simplicity, θ_{CO}^0 and $\theta_{O^-}^0$ refer to the surface coverage at TPB in the following sections.

The total current is the sum of the two currents from (R. 2) and (R. 3) as follows.

$$I = I_2 + I_3 = f_1\left(E,\theta_{CO}^0,\theta_{O^-}^0\right) \quad (3.21)$$

We will reference the electrical potential to the equilibrium potential and derive an expression in terms of the overpotential, $\eta = E - E_{eq}$, which is usually measured and reported.

For the current density equation for I_2,

$$I_2 = \hat{k}_{2,f}\left(1-\theta_{O^-}^0\right)\exp\left((1-\beta_2)f\eta\right)-\hat{k}_{2,b}\theta_{O^-}^0\exp\left(-\beta_2 f\eta\right) \quad (3.22)$$

where $f=\frac{F}{RT}$, $\hat{k}_{2,f}=FL_{TPB}k_{2,f}\exp\left((1-\beta_2)fE_{eq}\right)$, and $\hat{k}_{2,b}=FL_{TPB}k_{2,b}\exp\left(-\beta_2 fE_{eq}\right)$.

I_2 in Equation (3.22) can be expresses in terms of the exchange current density I_2^0,

instead of E_{eq} as follows.

$$I_2 = I_2^0 \left\{ \frac{\left(1-\theta_{O^-}^0\right)}{\left(1-\theta_{O^-}^{0\,*}\right)} \exp\left(\frac{(1-\beta_2)F\eta}{RT}\right) - \frac{\theta_{O^-}^0}{\theta_{O^-}^{0\,*}} \exp\left(\frac{-\beta_2 F\eta}{RT}\right) \right\} \tag{3.23}$$

where $I_2^0 = FL_{TPB}\left(k_{2,f}\left(1-\theta_{O^-}^{0\,*}\right)\right)^{\beta_2}\left(k_{2,b}\theta_{O^-}^{0\,*}\right)^{(1-\beta_2)}$ and the star means the properties are determined at equilibrium to differentiate them from those at out of equilibrium condition.

For the current density equation for I3,

$$I_3 = \hat{k}_{3,f}\theta_{O^-}^0\theta_{CO}^0 \exp\left((1-\beta_3)f\eta\right) - \hat{k}_{3,b}\left(1-\theta_{O^-}^0\right)\left(1-\theta_{CO}^0\right)p_{CO_2}\exp\left(-\beta_3 f\eta\right) \tag{3.24}$$

where $\hat{k}_{3,f} = FL_{TPB}k_{3,f}\exp\left((1-\beta_3)fE_{eq}\right)$, and $\hat{k}_{3,b} = FL_{TPB}k_{3,b}\exp\left(-\beta_3 fE_{eq}\right)$.

I_3 in Equation (3.24) can be expresses in terms of the exchange current density I_3^0, instead of E_{eq} as follows.

$$I_3 = I_3^0 \left\{ \frac{\theta_{O^-}^0\theta_{CO}^0}{\theta_{O^-}^{0\,*}\theta_{CO}^{0\,*}} \exp\left(\frac{(1-\beta_3)F\eta}{RT}\right) - \frac{\left(1-\theta_{O^-}^0\right)\left(1-\theta_{CO}^0\right)p_{CO_2}}{\left(1-\theta_{O^-}^{0\,*}\right)\left(1-\theta_{CO}^{0\,*}\right)p_{CO_2}^*} \exp\left(\frac{-\beta_2 F\eta}{RT}\right) \right\} \tag{3.25}$$

where $I_3^0 = FL_{TPB}\left(k_{3,f}\theta_{O^-}^{0\,*}\theta_{CO}^{0\,*}\right)^{\beta_3}\left(k_{3,b}\left(1-\theta_{O^-}^{0\,*}\right)\left(1-\theta_{CO}^{0\,*}\right)p_{CO_2}^*\right)^{1-\beta_3}$.

The forward and backward reaction constants, $k_{i,f}$ and $k_{i,b}$ are unknown. These values will be determined by fitting the model prediction to experimental data. The two charge-transfer coefficients are taken to be ½ because (R. 2) and (R. 3) are elementary reactions [47].

3.3.4.4. Constant Phase Element

The interface where the ionic conductor YSZ and the electronic conductor Ni meet is known to behave as a capacitor, in which a charging and discharging current is generated when the voltage changes [46]. The impedance of the double-layer capacitance is written as

$$Z_{C_{dl}} = \frac{1}{j\omega C_{dl}} \tag{3.26}$$

where $j = \sqrt{-1}$, ω is the frequency, and C_{dl} is the double-layer capacitance. Note that the impedance consists of a real and an imaginary part. The real part describes the resistive contribution, whereas the imaginary part describes the capacitive contribution. A negative imaginary part indicates a capacitive behavior, whereas a positive imaginary part indicates an inductive behavior.

In the equivalent circuit modeling of the EIS, instead of a simple capacitor as in Equation (3.26), a constant phase element (CPE) is often introduced to better fit the data. This is because a CPE can simulate the depressed semi-circle often observed in EIS data while a pure capacitor can reproduce only a perfect semi-circle. The impedance of CPE is defined as

$$Z_{CPE} = \frac{1}{Q(j\omega)^{n_{CPE}}} \tag{3.27}$$

where Q denotes the constant phase element $[F/(1/s)^{1-n}]$ and n_{CPE} is an empirical exponent.

The appearance of a CPE, i.e. the observation of a frequency dispersion, is often attributed to the distributed microscopic material properties, for instance inhomogeneities in the electrode material or its surface. For the impedance simulation in this thesis, the CPE is used to model the capacitor-like behavior of the interface. The parameters Q and n_{CPE} will be used as fitting parameters. The exponent n_{CPE} takes a value between 0 and 1. If n_{CPE} =1, the CPE behaves like an ideal capacitor. Therefore, it is expected that Q will have a similar value to that of the double-layer capacitance, C_{dl}. Bieberle [48] studied various Ni-based SOFC anodes such as Ni pattern, Ni gauze, Ni pate, screen-printed Ni-YSZ, sputtered Ni-YSZ and sprayed Ni-YSZ. It

was shown that C_{dl} depended on the structure of the anode. For the Ni patterned anode, the C_{dl} ranges from 9.3×10^{-5}- 7.3×10^{-4} [F/cm^2] (based on the Ni pattern area) depending on the overpotential applied. Hendriks[49] measured C_{dl} between gold (current blocking electrode) and YSZ to exclude the faradaic effects. Their measurement agreed well with the estimate using Gouy-Chapman theory. At 900K, their measured capacitance was ~ 2.0×10^{4} F/cm^2. As a first estimate in the fitting procedure used in our work, this value is used for Q in the CPE.

There are seven unknown parameters, among which four ($k_{2,f}$, $k_{2,b}$, $k_{3,f}$, and $k_{3,b}$) are from the charge-transfer reactions, two Q and n_{CPE} are from the constant phase element, and D_{O^-}, the O^- diffusion coefficient. These unknown parameters are obtained by fitting the anode model to experimental measurements.

3.3.5. Analysis

Two approaches have been used to examine multi-step CO electrochemical oxidation using the governing equations described in Section 3.3.4:

(1) An analytical approach, which was used by Lauvstad et al. [12]. In this approach, the steady-state solutions of the mass balance equations of the participating species and the electrochemical impedance response expressions were derived. The electrochemical impedance response expressions were simplified by lumping unknown parameters, and the corresponding equivalent circuits were suggested. Attempts to obtain fundamental kinetic parameters were not made. Since the work of Lauvstad et al [12], efforts to use the analytical solution approach to examine CO electrochemistry have gone by the wayside.

(2) The more popular approach involves numerical simulations of the mass balance governing equations of species while incorporating the proposed electrochemistry mechanism

[19,30,32] where there are often more unknown parameters than the analytical approach. The larger the number of fitting parameters, the more difficult it is to find a unique set of values for the unknown parameters. In other words, different sets of parameter values may give the same current-overpotential behavior, thereby limiting the ability to draw conclusions regarding the electrochemistry.

We will use the analytical solution approach to develop the simplest kinetic mechanism which includes a single species on each of the Ni and YSZ surface. The conservation equations are first transformed to ordinary differential equations (ODEs), which are solved analytically, and the resulting expressions are used to fit the experimental results.

In the following subsections, the partial differential equations are transformed to ODEs, which are solved to obtain expressions under the following operating conditions: (1) equilibrium, (2) steady-state conditions and (3) sinusoidal small perturbation applied to measure the impedance. These expressions are used to obtain the unknown kinetic parameters using EIS measurements and to validate the proposed mechanism against equilibrium and steady-state data.

3.3.5.1. Solution at equilibrium or OCV

At equilibrium, I_2=0 and I_3=0 and all the unsteady terms are zero. For the Ni surface, θ_{CO} is constant and uniform. Thus, $\frac{\partial \theta_{CO}(x,t)}{\partial t} = 0$ and $\frac{\partial^2 \theta_{CO}(x,t)}{\partial x^2} = 0$ in Equation (3.2). The equilibrium CO coverage is

$$\theta_{CO}^{*} = \frac{k_{1,f} p_{CO}^{*}}{k_{1,f} p_{CO}^{*} + k_{1,b}\Gamma_{Ni}} = \frac{K_1 p_{CO}^{*}}{\Gamma_{Ni} + K_1 p_{CO}^{*}} \tag{3.28}$$

where $K_1 = \frac{k_{1,f}}{k_{1,b}}$.

The YSZ surface should have a uniform concentration profile because, according to our model, there is no reaction on the YSZ.

From I_2=0 and I_3=0 in Equations (3.19) and (3.20),

$$\exp\left(\frac{FE^{eq}}{RT}\right)=\frac{k_{2,b}\theta_{O^-}^{0\,*}}{k_{2,f}\left(1-\theta_{O^-}^{0\,*}\right)}=\frac{\theta_{O^-}^{0\,*}}{K_2\left(1-\theta_{O^-}^{0\,*}\right)} \tag{3.29}$$

$$\exp\left(\frac{FE^{eq}}{RT}\right)=\frac{k_{3,b}\left(1-\theta_{O^-}^{0\,*}\right)\left(1-\theta_{CO}^{0\,*}\right)p_{CO_2}^{*}}{k_{3,f}\theta_{O^-}^{0\,*}\theta_{CO}^{0\,*}}=\frac{\left(1-\theta_{O^-}^{0\,*}\right)\left(1-\theta_{CO}^{0\,*}\right)p_{CO_2}^{*}}{K_3\theta_{O^-}^{0\,*}\theta_{CO}^{0\,*}} \tag{3.30}$$

where $K_2=\frac{k_{2,f}}{k_{2,b}}$ and $K_3=\frac{k_{3,f}}{k_{3,b}}$

From the three equations, (3.28), (3.29) and (3.30), θ_{CO}^{*}, $\theta_{O^-}^{*}$ and E^{eq} can be determined.

An exchange current density has been used to characterize the electrochemical reactions along with the charge-transfer coefficients. Previous experiments extracted the exchange current density information from the Tafel plots and reported how it changed depending on the concentrations of the reactants and products. In our case, these are the partial pressures of CO and CO_2. These expressions can be used later for determining the rate-limiting step.

From Equations (3.28), (3.29), and (3.30), θ_{CO}^{*} and $\theta_{O^-}^{*}$ are expressed in terms of the partial pressures of CO and CO_2. Substituting these in the coverages in Equations (3.23) and(3.25), the exchange current densities are described in terms of p_{CO} and p_{CO_2}. The expressions are simplified under the assumption that the YSZ surface is nearly vacant because of the very limited coverage of O^-(YSZ) (i.e., $1-\theta_{O^-}^{*}\approx 1$).

$$I_2^0=\frac{FL_{TPB}\left(\Gamma_{Ni}\right)^{1/4}K_2^{1/4}\sqrt{k_{2,b}}\sqrt{k_{2,f}}\left(P_{CO_2}\right)^{1/4}}{K_1^{1/4}K_3^{1/4}\left(P_{CO}\right)^{1/4}} \tag{3.31}$$

$$I_3^0 = \frac{FL_{TPB}\left(\Gamma_{Ni}\right)^{3/4} K_1^{1/4} K_2^{1/4} \sqrt{k_{3,b}} \sqrt{k_{3,f}} \left(P_{CO}\right)^{1/4} \left(P_{CO_2}\right)^{3/4}}{K_3^{1/4}\left(\Gamma_{Ni} + K_1 P_{CO}\right)} \tag{3.32}$$

where I_2^0 and I_3^0 are the exchange current for (R. 2) and (R. 3).

3.3.5.2. Steady state analysis

At steady state, $\frac{\partial \theta_{CO}(x,t)}{\partial t} = 0$ and Equation (3.2) becomes an ODE. The steady state CO coverage is computed by solving the ODE using boundary conditions (3.3) and (3.4). The solution is as follows.

$$\theta_{CO}(x) = \frac{N}{M^2} + \frac{e^{ML_{Ni}} e^{-Mx}}{M\left(e^{-ML_{Ni}} - e^{ML_{Ni}}\right)} \frac{I_3}{D_{CO}\Gamma_{Ni} FL_{TPB}} + \frac{e^{-ML_{Ni}} e^{Mx}}{M\left(e^{-ML_{Ni}} - e^{ML_{Ni}}\right)} \frac{I_3}{D_{CO}\Gamma_{Ni} FL_{TPB}} \tag{3.33}$$

where $M^2 = \frac{k_{1,f} p_{CO} + \Gamma_{Ni} k_{1,b}}{\Gamma_{Ni} D_{CO}}$ and $N = \frac{k_{1,f} p_{CO}}{\Gamma_{Ni} D_{CO}}$.

The value of the surface coverage relevant to the electrochemistry model is the value of θ_{CO} at TPB (x=0)

$$\theta_{CO}^0 = \theta_{CO}(0) = \frac{N}{M^2} - \frac{I_3}{D_{CO}\Gamma_{Ni} FL_{TPB} M \tanh\left(ML_{Ni}\right)} \tag{3.34}$$

The steady-state solution of Equation (3.14) satisfying the boundary condition (3.16) shows that O^- coverage should be uniform on the YSZ surface. Then, the boundary condition (3.15) reduces to

$$I_2 = I_3 \tag{3.35}$$

Given the activation overpotential, the corresponding values of $\theta_{O^-}^0$, θ_{CO}^0, and I_3 are calculated from the two Butler-Volmer Equations (3.22) and (3.24), and Equations (3.34), and

(3.35) above.

3.3.5.3. EIS simulation

Besides the steady-state data, that is the Tafel plots, the impedance spectra can give additional information regarding the physicochemical processes and are therefore particularly suited for model development/validation. The calculation of the electrochemical impedance is based on the assumption that a sinusoidal small-amplitude perturbation of the overpotential, $\Delta\eta$, around the steady-state value, η_{ss}, leads to a similar sinusoidal perturbation of all other outputs including ΔI, $\Delta\theta^0_{CO}$, and $\Delta\theta^0_{O^-}$. The activation overpotential can be written as

$$\eta = \eta_{ss} + \Delta\eta \exp(j\omega t) \tag{3.36}$$

where $j = \sqrt{-1}$, $\Delta\eta$ and ω are the complex amplitude and the angular frequency ($\omega = 2\pi f$, f=frequency) of the perturbation.

The resulting faradaic current and surface coverages of the adsorbed species can be represented as follows.

$$I_f = I_{f,ss} + \Delta I_f \exp(j\omega t) \tag{3.37}$$

$$\theta^0_{CO,f} = \theta^0_{COf,ss} + \Delta\theta^0_{CO,f} \exp(j\omega t) \tag{3.38}$$

$$\theta^0_{O^-,f} = \theta^0_{O^-,f,ss} + \Delta\theta^0_{O^-,f} \exp(j\omega t) \tag{3.39}$$

The faradaic admittance (Y_f) and impedance(Z_f) are defined as follows.

$$Z_f = \frac{1}{Y_f} = \frac{\Delta\eta}{\Delta I_f} \tag{3.40}$$

The most detailed analytical EIS calculation of CO electrochemistry was performed by Lauvstad et al. [12] in which the derivation was straightforward because their mechanisms included only a single step charge-transfer reaction. In their analysis, Lauvstad et al. [12] lumped

unknown parameters to obtain the corresponding equivalent circuit models. In order to relate multiple currents to a single overpotential applied at the electrode in the analysis of a multi-step charge-transfer mechanism, matrix algebra has been employed [50–52].

To relate the imposed overpotential perturbation amplitude, $\Delta\eta$, to the amplitude of the response faradaic current ΔI_f, the two faradaic current Equations (3.22) and (3.24) are Taylor-expanded to the linear term around the steady state value as follows.

$$\Delta I_2 = I_{2,\eta}\Delta\eta + I_{2,CO}\Delta\theta^0_{CO} + I_{2,O^-}\Delta\theta^0_{O^-} \tag{3.41}$$

$$\Delta I_3 = I_{3,\eta}\Delta\eta + I_{3,CO}\Delta\theta^0_{CO} + I_{3,O^-}\Delta\theta^0_{O^-} \tag{3.42}$$

where $I_{m,\eta} = \partial I_m / \partial\eta$, $I_{m,CO} = \partial I_m / \partial\theta^0_{CO}$, $I_{m,O^-} = \partial I_m / \partial\theta^0_{O^-}$, and m indicates the reaction number of (R. 2) and (R. 3). The partial derivatives are evaluated from Equations (3.22) and (3.24) as follows.

$$I_{2,\eta} = \hat{k}_{2,f}\left(1-\theta^0_{O^-}\right)\left(1-\beta_2\right)f\exp\left(\left(1-\beta_2\right)f\eta\right) + \hat{k}_{2,b}\theta^0_{O^-}\beta_2 f\exp\left(-\beta_2 f\eta\right) \tag{3.43}$$

$$I_{2,CO} = 0 \tag{3.44}$$

$$I_{2,O^-} = -\hat{k}_{2,f}\exp\left(\left(1-\beta_2\right)f\eta\right) - \hat{k}_{2,b}\exp\left(-\beta_2 f\eta\right) \tag{3.45}$$

$$I_{3,\eta} = \hat{k}_{3,f}\theta^0_{O^-}\theta^0_{CO}\left(1-\beta_3\right)f\exp\left(\left(1-\beta_3\right)f\eta\right) + \hat{k}_{3,b}\left(1-\theta^0_{O^-}\right)\left(1-\theta^0_{CO}\right)P_{CO_2}\beta_3 f\exp\left(-\beta_3 f\eta\right) \tag{3.46}$$

$$I_{3,CO} = \hat{k}_{3,f}\theta^0_{O^-}\exp\left(\left(1-\beta_3\right)f\eta\right) + \hat{k}_{3,b}\left(1-\theta^0_{O^-}\right)P_{CO_2}\exp\left(-\beta_3 f\eta\right) \tag{3.47}$$

$$I_{3,O^-} = \hat{k}_{3,f}\theta^0_{CO}\exp\left(\left(1-\beta_3\right)f\eta\right) + \hat{k}_{3,b}\left(1-\theta^0_{CO}\right)P_{CO_2}\exp\left(-\beta_3 f\eta\right) \tag{3.48}$$

To obtain an impedance, we need to relate $\Delta\theta_{O^-}$ and $\Delta\theta_{CO}$ to either $\Delta\eta$ or ΔI.

First for the CO species. Substituting Equation (3.38) to Equation (3.2) and the boundary conditions (3.3) and (3.4), the governing equation and the boundary conditions of $\Delta\theta_{CO}$ become

$$\frac{\partial\theta_{CO}}{\partial t} = j\omega\Delta\theta_{CO} = D_{CO}\frac{\partial^2\Delta\theta_{CO}(x,t)}{\partial x^2} - \left(k_{1,f}P_{CO}\Delta\theta_{CO}(x,t) + k_{1,b}\Gamma_{Ni}\Delta\theta_{CO}(x,t)\right) \tag{3.49}$$

$$-D_{CO}\frac{\partial \Delta\theta_{CO}(0,t)}{\partial x} = -\frac{\Delta I_3}{\Gamma_{Ni} FL_{TPB}} \tag{3.50}$$

$$D_{CO}\frac{\partial \Delta\theta_{CO}(L_{Ni},t)}{\partial x} = 0 \tag{3.51}$$

The solution of the ODE yields

$$\Delta\theta_{CO}(x,\omega) = \frac{\Delta I_3}{D_{CO}\Gamma_{Ni} FL_{TPB}}\left(\frac{e^{\hat{M}L}e^{-\hat{M}x}}{\hat{M}\left(e^{-\hat{M}L_{Ni}} - e^{\hat{M}L_{Ni}}\right)} + \frac{e^{-\hat{M}L_{Ni}}e^{\hat{M}x}}{\hat{M}\left(e^{-\hat{M}L_{Ni}} - e^{\hat{M}L_{Ni}}\right)}\right) \tag{3.52}$$

$$\Delta\theta_{CO} = \Delta\theta_{CO}(0,\omega) = -\frac{\Delta I_3}{D_{CO}\Gamma_{Ni} FL_{TPB}\hat{M}\tanh\left(\hat{M}L_{Ni}\right)} \tag{3.53}$$

where $\hat{M}^2 = \dfrac{k_{1,f}P_{CO} + \Gamma_{Ni}k_{1,b} + \Gamma_{Ni}j\omega}{D_{CO}\Gamma_{Ni}}$.

Similarly, substituting Equation (3.39) into the Equation (3.14) and boundary conditions (3.15) and (3.16), the governing equation and boundary conditions of $\Delta\theta_{O^-}$ become

$$\frac{\partial\theta_{O^-}}{\partial t} = j\omega\Delta\theta_{O^-} = D_{O^-}\frac{\partial^2\Delta\theta_{O^-}(y,t)}{\partial y^2} \tag{3.54}$$

$$-D_{O^-}\frac{\partial\Delta\theta_{O^-}(0,t)}{\partial y} = \frac{\Delta I_2 - \Delta I_3}{\Gamma_{YSZ} FL_{TPB}} \tag{3.55}$$

$$D_{O^-}\frac{\partial\Delta\theta_{O^-}(L_{YSZ},t)}{\partial y} = 0 \tag{3.56}$$

The solution to the ODE yields

$$\Delta\theta_{O^-}(y,\omega) = -\frac{\Delta I_2 - \Delta I_3}{\Gamma_{YSZ} FL_{TPB}}\left(\frac{e^{\hat{U}L_{YSZ}}e^{-\hat{U}y}}{\hat{M}\left(e^{-\hat{U}L_{YSZ}} - e^{\hat{U}L_{YSZ}}\right)} + \frac{e^{-\hat{U}L_{YSZ}}e^{\hat{U}y}}{M\left(e^{-\hat{U}L_{YSZ}} - e^{\hat{U}L_{YSZ}}\right)}\right) \tag{3.57}$$

$$\Delta\theta_{O^-} = \Delta\theta_{O^-}(0,\omega) = \frac{\Delta I_2 - \Delta I_3}{D_{O^-}\Gamma_{YSZ} FL_{TPB}\hat{U}\tanh\left(\hat{U}L_{YSZ}\right)} \tag{3.58}$$

where $\hat{U}^2 = \dfrac{j\omega}{D_{O^-}}$.

In the case of high O^- diffusion coefficient, $\tanh\left(\hat{U}L_{YSZ}\right)=1$ is substituted in Equation(3.58) according to the boundary condition Equation (3.18).

The four Equations (3.41), (3.42), (3.53), and (3.58) can be cast in a matrix form as follows.

$$\begin{pmatrix}\Delta\eta\\ \Delta\eta\\ 0\\ 0\end{pmatrix}=G\begin{pmatrix}\Delta I_2\\ \Delta I_3\\ \Delta\theta^0_{CO}\\ \Delta\theta^0_{O^-}\end{pmatrix} \tag{3.59}$$

Where G is defined by

$$G=\begin{pmatrix}\frac{1}{I_{2,\eta}} & 0 & 0 & -\frac{I_{2,O^-}}{I_{2,1}}\\ 0 & \frac{1}{I_{3,\eta}} & -\frac{I_{3,CO}}{I_{3,\eta}} & -\frac{I_{3,O^-}}{I_{3,\eta}}\\ -\frac{1}{D_{O^-}\Gamma_{YSZ}FL_{TPB}\hat{U}\tanh\left(\hat{U}L_{YSZ}\right)} & \frac{1}{D_{O^-}\Gamma_{YSZ}FL_{TPB}\hat{U}\tanh\left(\hat{U}L_{YSZ}\right)} & 0 & 1\\ 0 & \frac{1}{D_{CO}\Gamma_{Ni}FL_{TPB}\hat{M}\tanh\left(\hat{M}L_{Ni}\right)} & 1 & 0\end{pmatrix} \tag{3.60}$$

Multiplying both sides of (3.59) by G^{-1}, ΔI_2 and ΔI_3 are expressed in terms of $\Delta\eta$ only.

$$\begin{pmatrix}\Delta I_2\\ \Delta I_3\\ \Delta\theta^0_{CO}\\ \Delta\theta^0_{O^-}\end{pmatrix}=G^{-1}\begin{pmatrix}\Delta\eta\\ \Delta\eta\\ 0\\ 0\end{pmatrix} \tag{3.61}$$

Or,

$$\Delta I_2=\left(G^{-1}{}_{1,1}+G^{-1}{}_{1,2}\right)\Delta\eta \tag{3.62}$$

$$\Delta I_3 = \left(G^{-1}{}_{2,1} + G^{-1}{}_{2,2}\right)\Delta\eta \tag{3.63}$$

where $G^{-1}_{i,j}$ is the (i,j) element of the matrix G^{-1}

Therefore, the faradaic impedance is

$$Z_f = \frac{\Delta\eta}{\Delta I_f} = \frac{\Delta\eta}{\Delta I_2 + \Delta I_3} = \frac{1}{G^{-1}{}_{1,1} + G^{-1}{}_{1,2} + G^{-1}{}_{2,1} + G^{-1}{}_{2,2}} \tag{3.64}$$

The double layer charging/discharging current

There are two kinds of currents in the impedance measurements, the faradaic current and the double layer-charging current:

$$\Delta I_{total} = \Delta I_{dl} + \Delta I_f = \left(\frac{1}{Z_{dl}} + \frac{1}{Z_f}\right)\Delta\eta = \frac{\Delta\eta}{Z_{total}} \tag{3.65}$$

Hence, the total impedance is the sum of the faradaic impedance and double layer impedance arranged in parallel:

$$Z_{total} = \frac{Z_f Z_{CPE}}{Z_{CPE} + Z_f} \tag{3.66}$$

where Z_{CPE} is given by Equation (3.27).

In this section, we derived analytical expressions for the equilibrium solution, steady-state solution, and the EIS solution, and identified seven unknown parameters, among which four are from the charge-transfer reactions, $k_{2,f}$, $k_{2,b}$, $k_{3,f}$, and $k_{3,b}$, and two are from the constant phase element, Q and n_{CPE}, and D_{O^-}, the O^- diffusion coefficient. In the next section, the unknown parameters are obtained by fitting the solution to the experimental measurements.

3.4. Parameter fitting

The seven unknown parameters, $k_{2,f}$, $k_{2,b}$, $k_{3,f}$, $k_{3,b}$, Q, n_{CPE}, and D_{O^-}, identified in the previous section are obtained by fitting the anode model to the experimental EIS measurements. The model with the parameters obtained from EIS results will be validated in the next section by comparing the prediction to the measured Tafel plots.

3.4.1. Experimental data for parameter fitting

The most extensive experimental measurements for CO/ CO_2 mixtures were conducted by Habibzadeh [19]. EIS measurements were performed for each applied overpotential, 0, 100, 200 and 300 mV at four different temperatures, 700°C, 725°C, 750°C, and 775°C with fixed p_{CO} = 0.323 bar and p_{CO_2} = 0.0323 bar, as shown in Table 3-3. These EIS measurements will be used to obtain the seven unknown parameters.

Table 3-3. Operating parameters in Habibzadeh EIS measurements (taken from [19])

Parameters	Values	Units
Temperature (T)	700, 725, 750 and 775	°C
p_{CO}	0.323	Bar
p_{CO_2}	0.032	Bar
P_{Ar}(diluent)	0.0.645	Bar
η	0, 100, 200, 300	mV

EIS measurements have often been reported in the form of Nyquist plots where the real part of the impedance is plotted on the X-axis and the imaginary part on the Y-axis. Because the

imaginary part of the EIS data is often negative, the Y-axis is defined as (-) of its imaginary value. A Nyquist plot does not provide frequency information at which the impedance is measured. EIS measurements presented in the form of an equivalent circuit are more useful because an equivalent circuit is sufficient to reproduce the EIS measurement for later use. Habibzadeh [19] used an equivalent circuit format to report his EIS measurements. The equivalent circuit parameters were obtained by fitting the resulting impedance based on the equivalent circuit to the EIS measurements

Habibzadeh [19] observed two suppressed semicircles in the anodic impedance as shown in Figure 3-7. To fit the EIS data, he used the equivalent circuit shown in Figure 3-8 where two sets of a CPE and a resistor connected in parallel are connected in series. This was done because one set of a CPE and a resistor connected in parallel can reproduce only one suppressed semi-circle in the Nyquist plot. Habibzadeh [19] showed that the EIS measurements and his fitted results using the equivalent circuits agreed well at OCV and η=100 mV, as shown in Figure 3-7. An equivalent circuit can also be used to interpret the EIS data and explain the observed trends. However, this does not allow for clear physical interpretation of the equivalent circuit elements. Thus, Habibzadeh [19] used the equivalent circuit not to interpret the data, but to report the measurements in a compact form. The values of all the elements corresponding to Habibzadeh's operating conditions [19] are listed in Table 3-4. In addition to the values of the elements, Table 3-4 includes two characteristic frequencies each of which is defined when the imaginary part of the impedance, corresponding to each set of a CPE and a resistance connected in parallel, reaches its maximum absolute value. The high and low characteristic frequencies are mostly on the order of $O(10^2$ Hz) and $O(10^{-1}$ Hz). As discussed above, any attempt to relate the frequencies to any physical processes was not made.

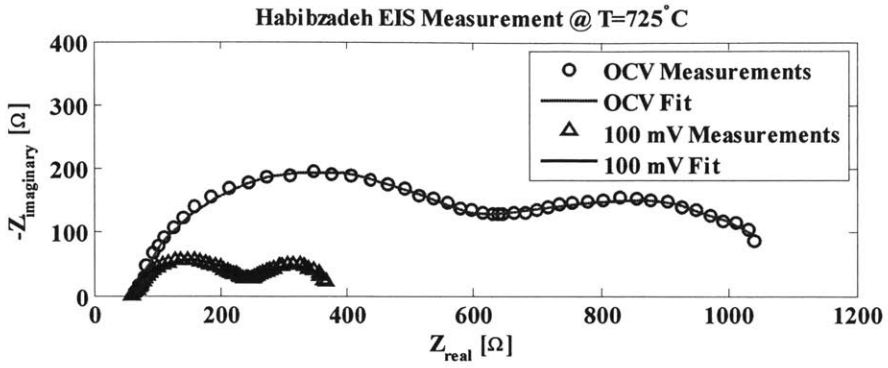

Figure 3-7. Anodic impedance measurement by Habibzadeh [19] at T=725 °C, the applied anodic activation overpotential is zero and 100 mV. Open circles and triangles are measurements and red and black solid lines are his fitting results using the equivalent circuits (taken from [19])

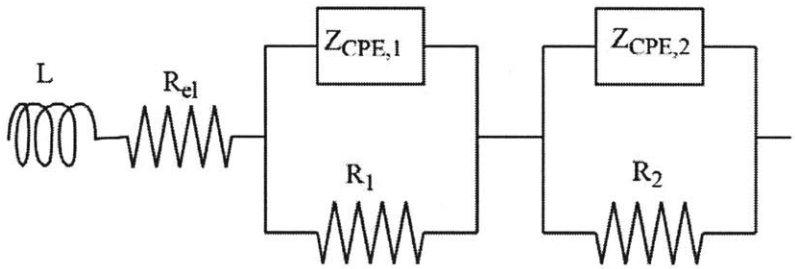

Figure 3-8. The equivalent circuit used by Habibzadeh to model the anodic impedance for CO electrochemistry. R_{el} stands for the electrolyte resistance. Z_{CPE} is the constant phase element. R_1 and R_2 are resistance to fit the suppressed semi-circles in conjunction with CPEs.

Table 3-4. The equivalent circuit parameters obtained by fitting the impedance data of the patterned anode to the equivalent circuit shown in Figure 3-8. Q_1 and Q_2 are the constant phase elements $[F/(1/s)^{1-n}]$, n_1 and n_2 are the empirical exponents of CPE [unitless]. The electrolyte resistance, R_{el}, and R_1 and R_2 are in units of [Ω]. The characteristic frequency (Hz) for each set of a CPE and a resistor are defined when the imaginary part of the impedance based on each set reaches its maximum absolute value and are denoted as ω_1 and ω_2. (Taken from Table 5.6 in [19])

T(°C)	η (mV)	L	R_{el}	R_1	$Q_1 \times 100$	$n_{CPE,1}$	ω_1	R_2	Q_2	$n_{CPE,2}$	ω_1
700	0	0	75.53	830.43	0.0017	0.649	35.98	950.42	0.0806	0.76	0.295
	100	0	75.05	285.66	0.003	0.698	143.26	162.4	0.0044	0.779	0.241
	200	0	73.25	150.6	0.0066	0.618	279.52	23.57	0.0168	0.816	0.496
	300	0	73.44	109.65	0.0088	0.598	366.86	18.61	0.0886	0.966	0.094

725	0	0	59.27	508.18	0.0018	0.77	68.41	581.04	0.0011	0.584	0.322
	100	0	57.89	183.31	0.0036	0.691	223.85	145.92	0.0046	0.718	0.278
	200	0	68.48	124.98	0.0061	0.629	374.8	31.19	0.0316	0.901	0.162
	300	0	67.34	89.86	0.0001	0.575	498.95	16.8	0.06	1	0.158
750	0	0	47.61	389.39	0.0027	0.733	79.88	524.65	0.0016	0.648	0.219
	100	0	45.66	137.07	0.007	0.63	255.77	102.17	0.0051	0.8	0.362
	200	0	44.7	91.29	0.0002	0.536	316.03	14.56	0.0186	0.951	0.627
	300	0	45.3	54.62	0.0001	0.612	589.31	196.32	0.0532	0.191	0
775	0	0	36.04	235.74	0.0045	0.691	113.98	489.95	0.0019	0.707	0.18
	100	0	32.76	94.01	0.0003	0.485	209.15	39.08	0.0056	1	0.729
	200	0	35.17	66.3	0.0003	0.53	283.04	5.6	0.0466	1	0.609
	300	0	35.43	46.74	0.0002	0.554	661.83	79.82	2.4648	0.42	0

Note that the reported experimental results are not the raw data, but the fitted values for the equivalent circuit elements. The agreement between Habibzadeh's measurements and his fitting data was shown only at OCV and η=100 mV when T=725°C, as shown in Figure 3-7. Therefore, at other operating conditions, there could be an inherent error in the reported "experimental data" resulting from the fitting procedures.

We reproduce the EIS measurements using the equivalent circuit in Figure 3-8 with the values in Table 3-4, at 10 equally-spaced frequencies on a logarithmic scale in each decade of frequency from 10^{-10} Hz to 10^{10} Hz. In other words, the EIS measurements are reproduced at 201 frequencies for 20 decades of frequency between 10^{-10} Hz and 10^{10} Hz at each overpotential. Because the unknown parameters in our model are assumed to be functions of temperature only, the same values of these parameters apply to all anode activation overpotentials, 0, 100mV, 200mV and 300 mV, at the same temperature. Therefore, a total of 804 EIS measurements are used to obtain the seven fitting parameters at a given temperature.

3.4.2. Procedure for parameter fitting

In our model, the four kinetics parameters, $k_{2,f}$, $k_{2,b}$, $k_{3,f}$, and $k_{3,b}$, and O^- diffusion coefficient, D_{O^-}, are functions of temperature only, as expressed in the Arrhenius equation. It is assumed that Q and n_{CPE} are functions of temperature only as well. These unknown parameters are obtained by fitting our model to Habibzadeh EIS measurements [19] at each temperature where the measurements were made, while being kept constant for different activation overpotentials at the same temperature.

In order to simulate the EIS at a given η_{act}, a steady-state solution is computed around which the voltage perturbation, $\Delta\eta$, is applied. For a given anode activation overpotential, η_{act}, the steady state $\theta_{O^-}^0$, θ_{CO}^0, and $I_{total} = 2I_2 = 2I_3$ can be found from the equations below using the Matlab nonlinear solver 'fsolve'.

$$\theta_{CO}^0 = \theta_{CO}(0) = \frac{N}{M^2} - \frac{I_3}{D_{CO}\Gamma_{Ni} F L_{TPB} M \tanh(ML_{Ni})} \tag{3.34}$$

$$I_2 = \hat{k}_{2,f}\left(1-\theta_{O^-}^0\right)\exp\left((1-\beta_2) f\eta\right) - \hat{k}_{2,b}\theta_{O^-}^0 \exp\left(-\beta_2 f\eta\right) \tag{3.22}$$

$$I_3 = \hat{k}_{3,f}\theta_{O^-}^0\theta_{CO}^0 \exp\left((1-\beta_3) f\eta\right) - \hat{k}_{3,b}\left(1-\theta_{O^-}^0\right)\left(1-\theta_{CO}^0\right) p_{CO_2} \exp\left(-\beta_3 f\eta\right) \tag{3.24}$$

The EIS can be obtained using the steady-state θ_{O^-} and θ_{CO} and the following equations.

$$Z_f = \frac{\Delta\eta}{\Delta I_f} = \frac{\Delta\eta}{\Delta I_2 + \Delta I_3} = \frac{1}{G^{-1}_{1,1} + G^{-1}_{1,2} + G^{-1}_{2,1} + G^{-1}_{2,2}} \tag{3.64}$$

where matrix G is given in Equation (3.60), and

$$Z_{CPE} = \frac{1}{Q(j\omega)^{n_{CPE}}} \tag{3.27}$$

$$Z_{total} = \frac{Z_f Z_{CPE}}{Z_{CPE} + Z_f} \tag{3.66}$$

Once the impedances at the 804 frequencies at a given temperature are computed, the magnitude of the error between the complex values of the simulated impedance and the EIS measurements is minimized using the non-linear least square method in Matlab function, 'lsqnonlin'. During the fitting procedure, each point is equally weighted. The limitation of 'lsqnonlin' function is that it can be trapped in a local minimum, instead of a global minimum. Therefore, we also applied global optimization functions, 'GlobalSearch' and 'patternsearch'. These functions failed to produce a different set of parameter values with which our model can show a better agreement with the impedance measurements.

As shown in Figure 3-9 and 3-10, the magnitude of the EIS data becomes smaller as the applied activation overpotential increases. For example, the polarization impedance at OCV is almost 10 times larger than that at η_{act} = 300 mV. Because we perform a least square fit using the data at all the overpotentials with equal weight, the fitting error can be more noticeable at higher activation overpotentials where the absolute impedance is small.

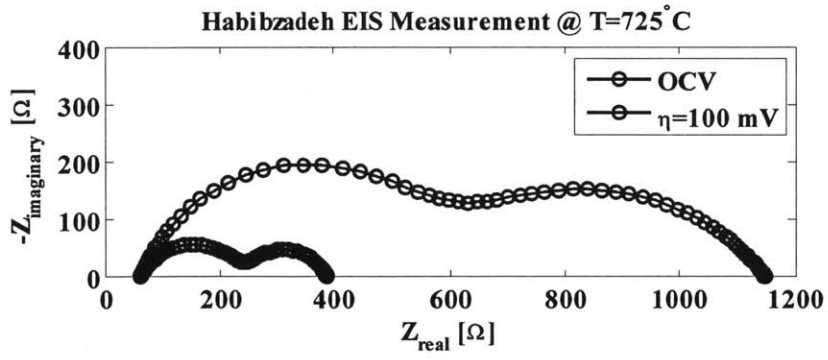

Figure 3-9. The anodic impedance data calculated using Habibzadeh [19] equivalent circuit model and the element parameters in Table 3-4 when T=725 °C and the applied anodic activation overpotential is zero and 100 mV. (Reproduced from [19])

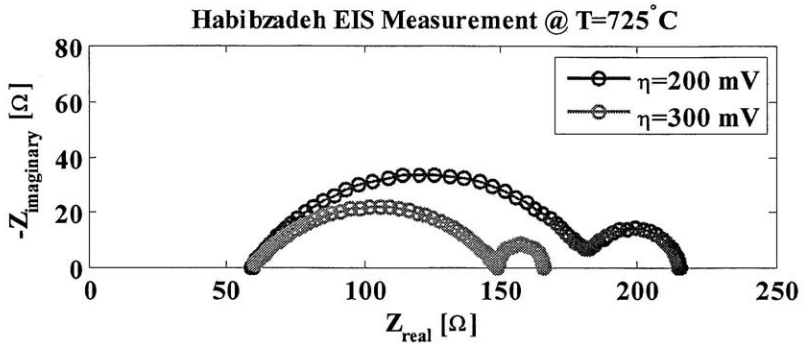

Figure 3-10. The anodic impedance data calculated using Habibzadeh [19] equivalent circuit model and the element parameters in Table 3-4 when T=725 °C and the anodic activation overpotential applied is 200 mV and 300 mV. (Reproduced from [19])

The parameters obtained from the least square fit using Habibzadeh EIS measurements are given in Table 3-5.

Table 3-5. The RGD model parameters are obtained using the EIS measurements by Habibzadeh [19].

T (^{0}C)	775	750	725	700	Units
$k_{2,f}$	9.99E-09	3.65E-09	1.70E-09	1.00E-09	mole/(sec m)
$k_{2,b}$	6.36E-03	3.36 E-03	2.29 E-03	1.09E-04	mole/(sec m)
$k_{3,f}$	8.18E-07	7.93E-07	7.97E-07	2.99E-08	mole/(sec m)
$k_{3,b}$	5.63E-10	6.88E-10	8.84E-10	7.96E-10	mole/(sec m Pa)
Q	4.96E-05	5.96E-06	1.33E-05	6.44E-06	$[F/(1/s)^{1-n}]$
n_{CPE}	0.417	0.8543	0.7836	0.8097	unitless
D_{O^-}	1	1	1	1	m^2/sec

Our model results show that the faradaic impedance is responsible for the low frequency semi-circle, as shown in Figure 3-11. The high frequency semi-circle is attributed to the CPE. Among Habibzadeh fitting elements, Q_1 and $n_{CPE,1}$ appear to correspond to the double layer charging impedance in our model. Both Q_1 in the Habibzadeh elements and Q in our model are

of the same order of magnitude, $O(10^{-5}\text{-}10^{-6})$.

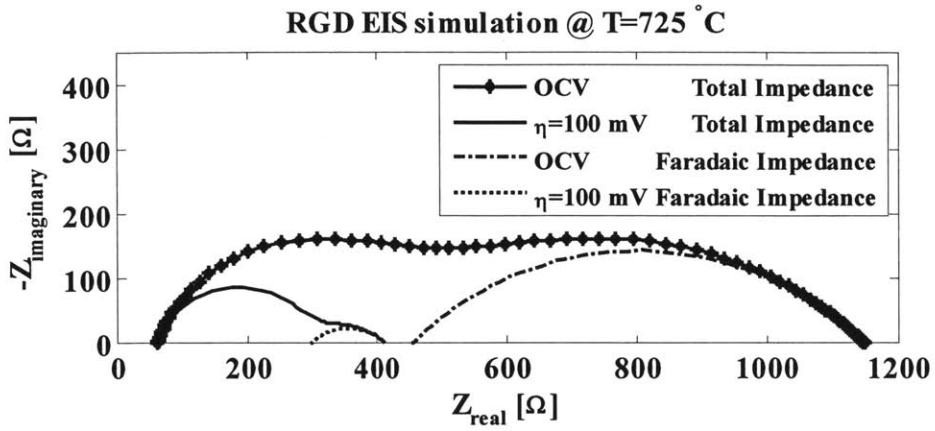

Figure 3-11. Contribution of the faradaic impedance to the total impedance at T=725°C when the anodic activation overpotential is 0 and 100 mV.

3.4.3. Results

The Nyquist plot is the most widely used form for reporting EIS measurements and for showing agreement between measurements and simulations using either an equivalent circuit or a fundamental formulation of the physics and chemistry in the fuel cell. However, the Nyquist plot does not include frequency information and the same Nyquist plot can be generated with different characteristic frequencies. Hence, besides the Nyquist plot, the Bode plot will be used to compare the experimental results and the model results.

In the Bode plot, the characteristic frequencies are defined at the peaks of the phase angle of the impedance. The phase angle is the difference in the phase between the voltage perturbation and current response. When the frequency of the voltage perturbation is much higher than the rates of the faradaic processes, the faradic current fails to respond, and the current response is from the double layer charging/discharging. This is because as the frequency increases, Z_{CPE} approaches zero and the corresponding phase angle is zero. When the frequency of the voltage

perturbation is lower than that of the physical processes related to current production, the current can successfully follow the voltage perturbation without phase delay. Therefore, the characteristic frequencies correspond to prevailing physical processes.

3.4.3.1. T=700 °C

Figure 3-12 shows the Nyquist plot at T=700 °C. As the applied activation potential increases, the polarization impedances decrease and the suppressed semi-circle at the lower frequency (the right semi-circle in the Nyuist plot) shrinks. The model with the parameters obtained as described above captures these two observations well. The discrepancy between the experimental data and the model results is more noticeable at higher activation overpotentials, 300 mV and 400 mV, because fitting the data is done using equal weight at all frequencies while the absolute value of the EIS at these overpotentials are small. It is worth nothing that in the model results, at higher η and low frequency, a small circle appears in the fourth quadrant, which is called the inductive effect.

The Bode plots are shown in Figure 3-13 and 3-14 at T=700 °C. The characteristic frequencies (the frequencies where the phase angle of the complex impedances are at their peaks) remain at 10^4 for the high frequency region in the measurement and simulations. In the low frequency region, the measured characteristic frequency changes from 10^{-3} to 10^0 as the applied activation overpotential increases from the OCV to η=100 mV. However, the characteristic frequencies in the simulation results remain at 10^{-3}.

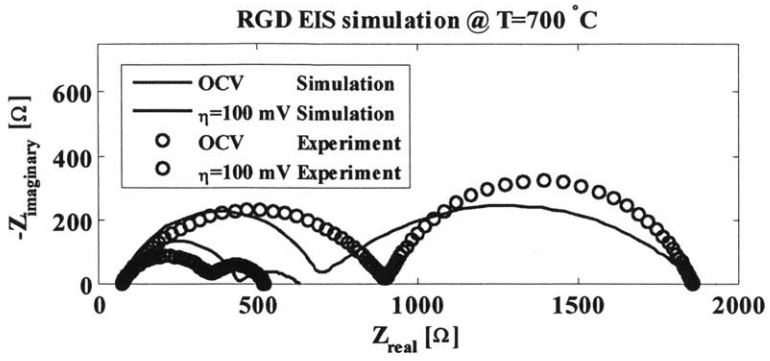

(a)

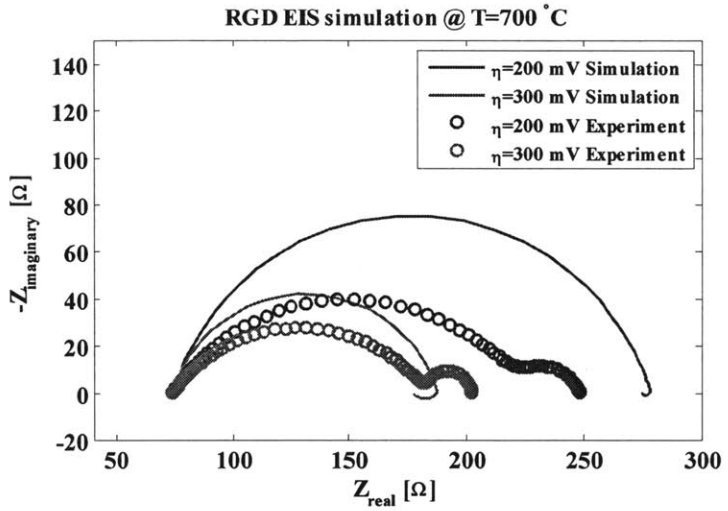

(b)

Figure 3-12. RGD EIS simulation: the Nyquist Plot @ T=700°C and the comparison with Habibzadeh experimental measurements. Simulation results are plotted as lines while the experimental results are shown with open circles. (a) η= 0 mV and η = 100 mV, (b) η= 200 and η= 300 mV

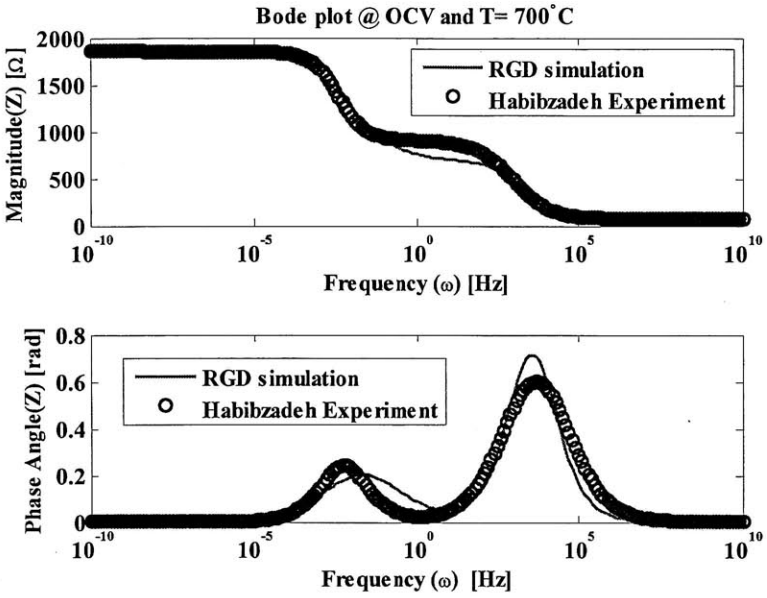

(a)

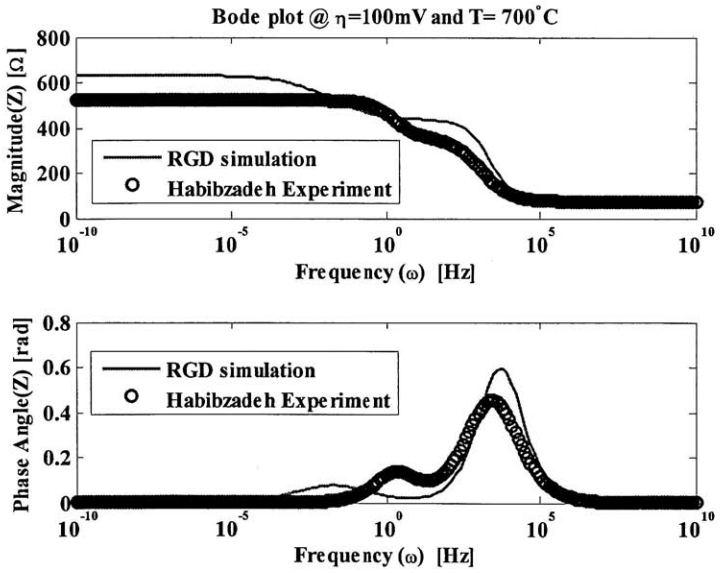

(b)

Figure 3-13. RGD EIS simulation: the Bode Plot @ T=700°C and the comparison with Habibzadeh experimental measurements. Simulation results are plotted as lines while the experimental results are shown with open circles. (a) OCV and (b) η=100mV

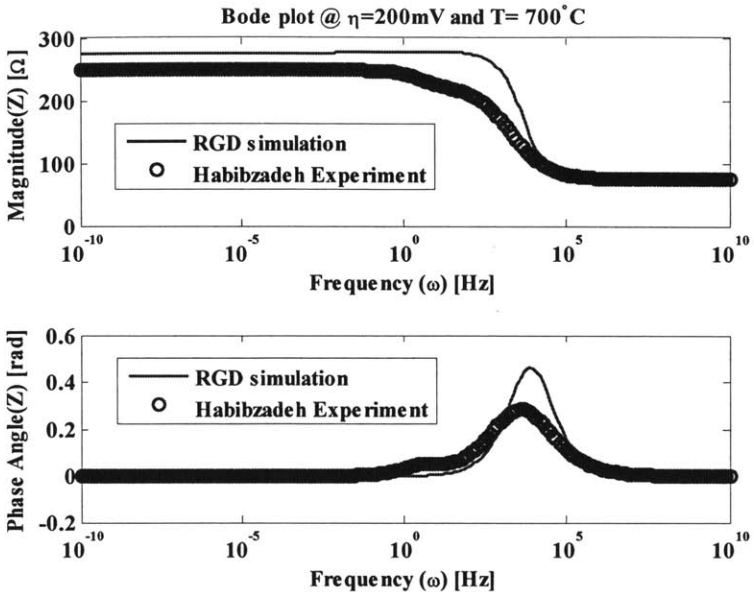

(a)

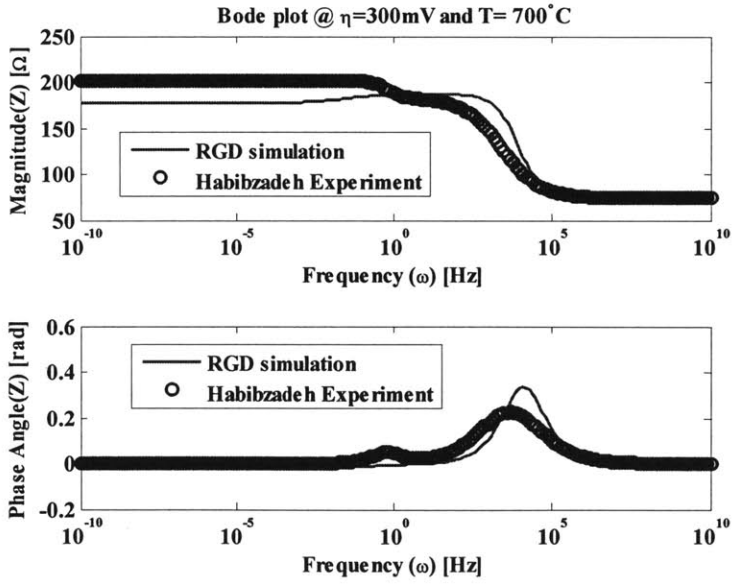

(b)

Figure 3-14. RGD EIS simulation: the Bode Plot @ T=700°C and the comparison with Habibzadeh experimental measurements. Simulation results are plotted as lines while the experimental results are shown with open circles. (a) η=200mV (b) η=300mV

3.4.3.2. T=725 °C

The Nyquist plot at T=725°C is shown in Figure 3-15. Similar trends are observed in the measurements and in the model results: as the activation overpotential increases (1) the polarization impedance reduces and (2) the low frequency semi-circle shrinks. The discrepancy between the experimental measurements and the model results is more noticeable at the higher activation overpotential 200 mV and 300 mV when the magnitude of the impedance is low. The same inductive effect appears at higher activation overpotential.

The Bode plots at T=725°C are shown in Figure 3-16 and 3-17. The characteristic frequencies are at 10^0 and 10^4 in both measurements and the model results except when η=300mV where the measured high characteristic frequency surged from 10^4 to 10^8.

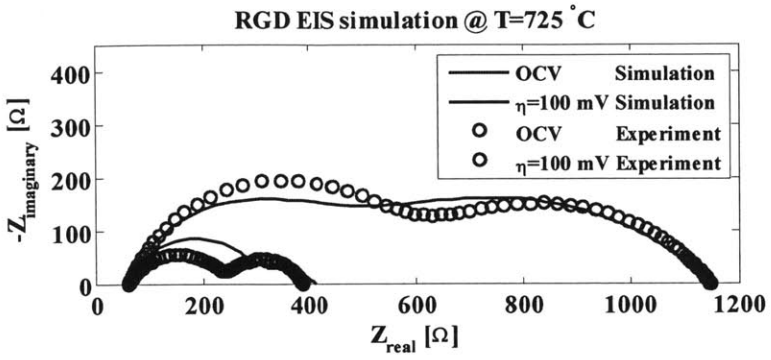

(a)

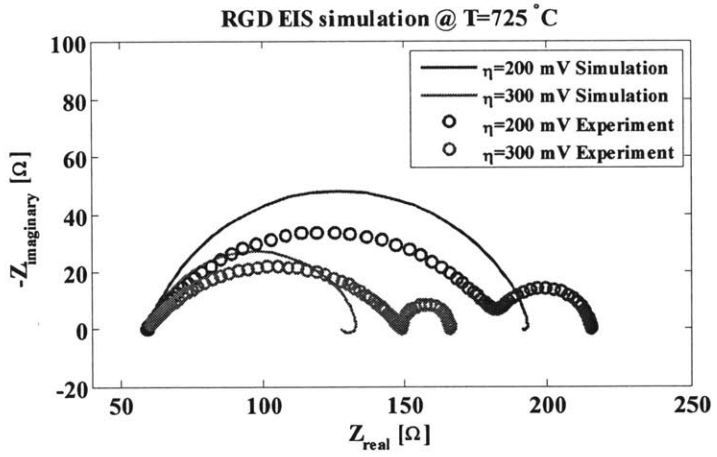

(b)

Figure 3-15. RGD EIS simulation: the Nyquist Plot @ T=725°C and the comparison with Habibzadeh experimental measurements. Simulation results are plotted as lines while the experimental results are shown with open circles. (a) η= 0 mV and η = 100 mV, (b) η= 200 and η= 300 mV

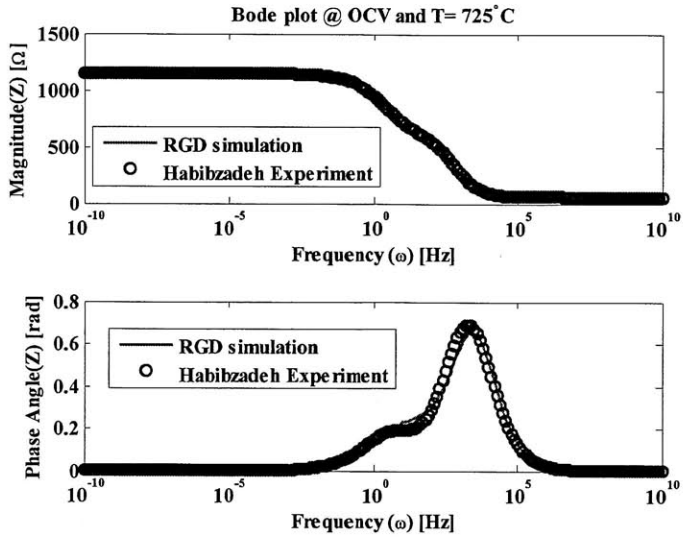

(a)

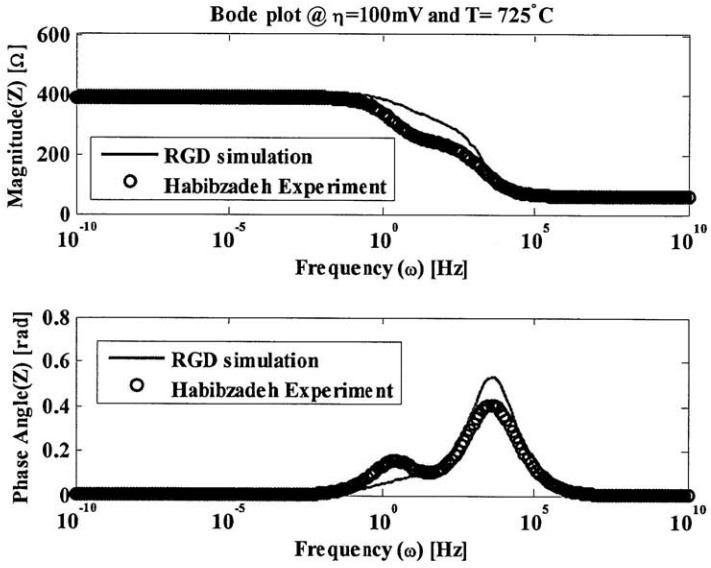

(b)

Figure 3-16. RGD EIS simulation: the Bode Plot @ T=725°C and the comparison with Habibzadeh experimental measurements. Simulation results are plotted as lines while the experimental results are shown with open circles. (a) OCV and (b) η=100mV

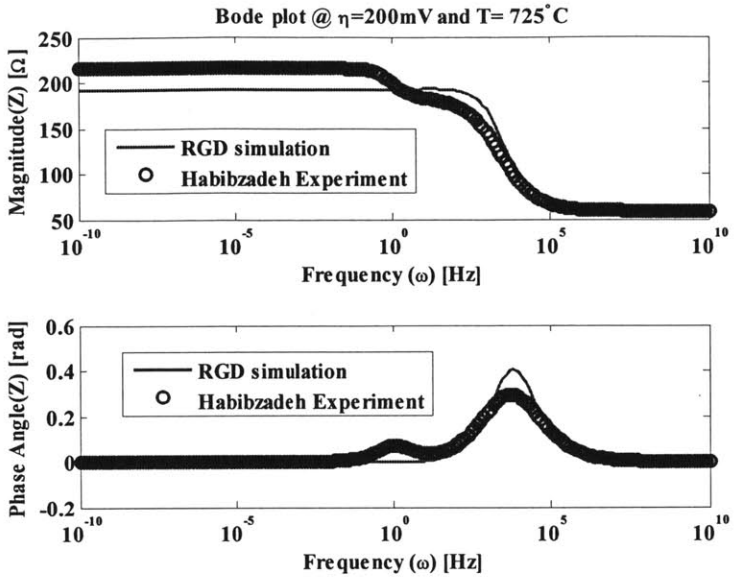

(a)

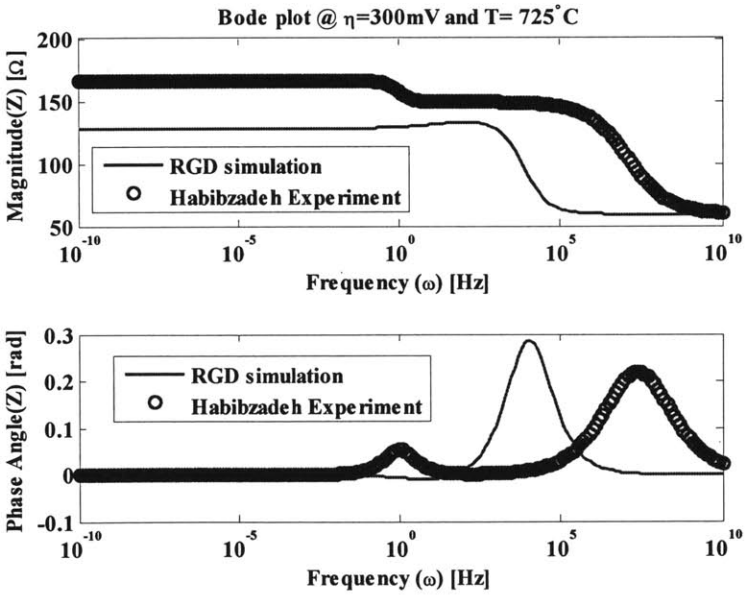

(b)

Figure 3-17. RGD EIS simulation: Bode Plot @ T=725°C and the comparison with Habibzadeh experimental measurements. Simulation results are plotted as lines while the experimental results are shown with open circles. (a) η=200mV (b) η=300mV

3.4.3.3. T=750 °C & T=775 °C

Nyquist plots at T=750°C and T=775°C are shown in Figure 3-18 and 3-19. The polarization impedance ($\Delta\eta/\Delta i$) can be interpreted as the inverse of the instantaneous slope in i-η curve. Because the current has an exponential dependency on the activation overpotential, according to the Butler-Volmer expression, the polarization impedance decreases as the actvation overpotential increases. As the activation overpotential increases to η=300mV, the measured polarization impedance decreases according to the same trend observed in T=700°C and T=725°C. However, at η=300mV, the measured polarization impedance suddenly increased at both temperatures. This abnormal behavior was neither noted or discussed in Habibzadeh's thesis [19]. It is suspected that another process not captured in the kinetics mechanism may be at work at 300 mV.

In the same experimental setting, Habibzadeh [19] reported that green color NiO formed when the Ni patterned anode was exposed to Ar at an activation overpotential of 400 mV. He concluded that the applied overpotential of 400 mV forced the bulk oxygen inside the YSZ to move toward the anode and react with the Ni to form NiO. We suspect that the abnormal increase of the polarization impedance might be related to the insulating effect of NiO, and exclude the impedance measurements at 300mV in the fitting at both T=750°C and T=775°C. Therefore, we expected the fitted results to show a large discrepancy at η=300mV.

The Bode plots at T=750°C are shown in Figure 3-20 and 3-21. The characteristic frequencies stay the same at 10^0 and 10^4 in the simulations, whereas the characteristic frequencies in the measured impedance change from 10^0 to 10^{-4} in the low frequency region and from 10^4 to 10^8 in the high frequency region as the activation overpotential increases above 100

mV.

The Bode plots at T= 775°C are shown in Figure 3-22 and 3-23. In the measured impedance, the low characteristic frequencies are at O(1) except when η=300 mV, while the high characteristic frequencies are at 10^8 Hz except when η=0 mV. The simulation results show that the low and high characteristic frequencies remain at 10^1 and 10^7 Hz at all activation overpotentials.

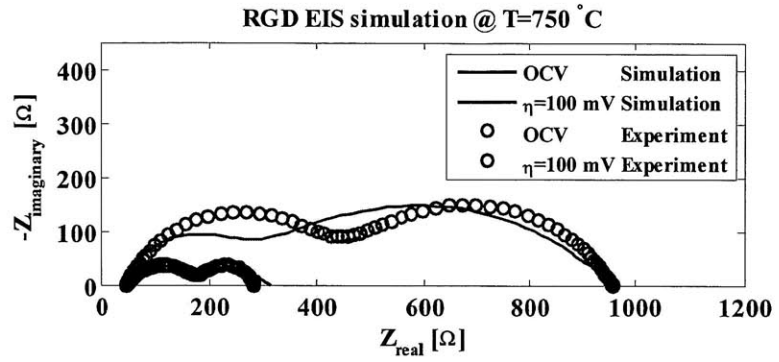

(a)

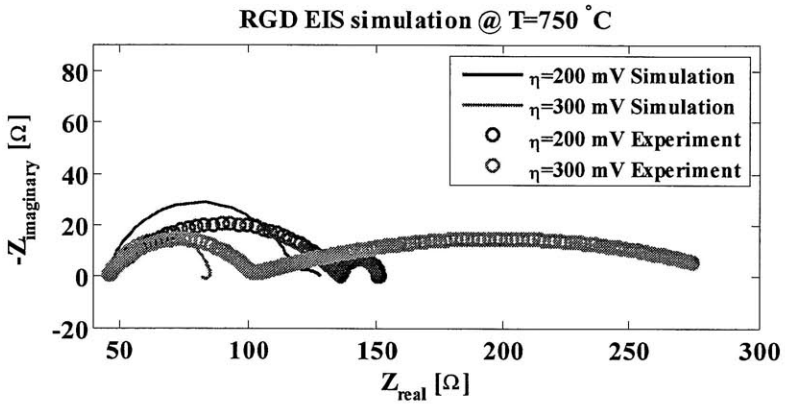

(b)

Figure 3-18. RGD EIS simulation: the Nyquist Plot @ T=750°C and the comparison with Habibzadeh experimental measurements. Simulation results are plotted as lines while the experimental results are shown with open circles. (a) η= 0 mV and η = 100 mV, (b) η= 200 and η= 300 mV

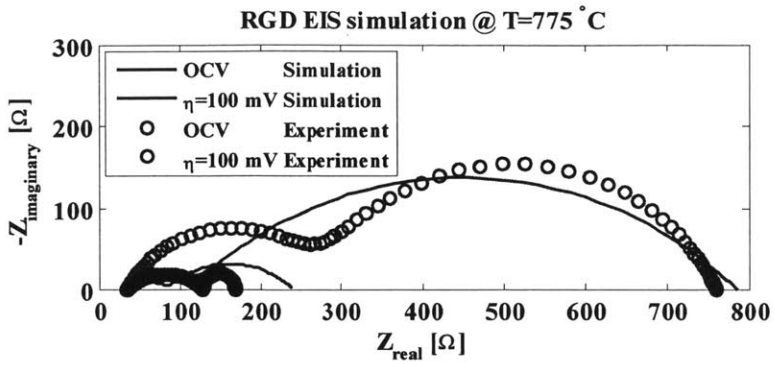

(a)

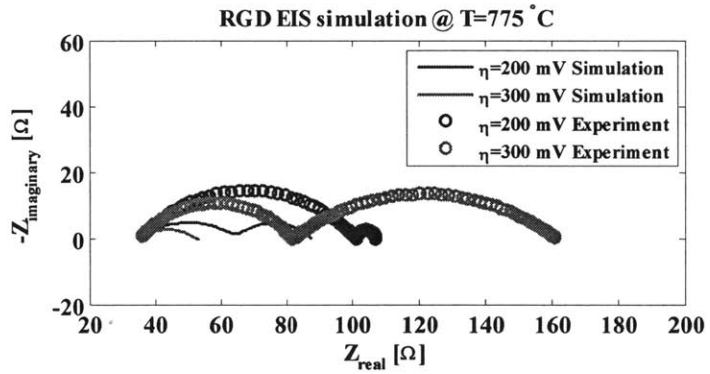

(b)

Figure 3-19. RGD EIS simulation: the Nyquist Plot @ T=775°C and the comparison with Habibzadeh experimental measurements. Simulation results are plotted as lines while the experimental results are shown with open circles(a) η= 0 mV and η = 100 mV, (b) η= 200 and η= 300 mV

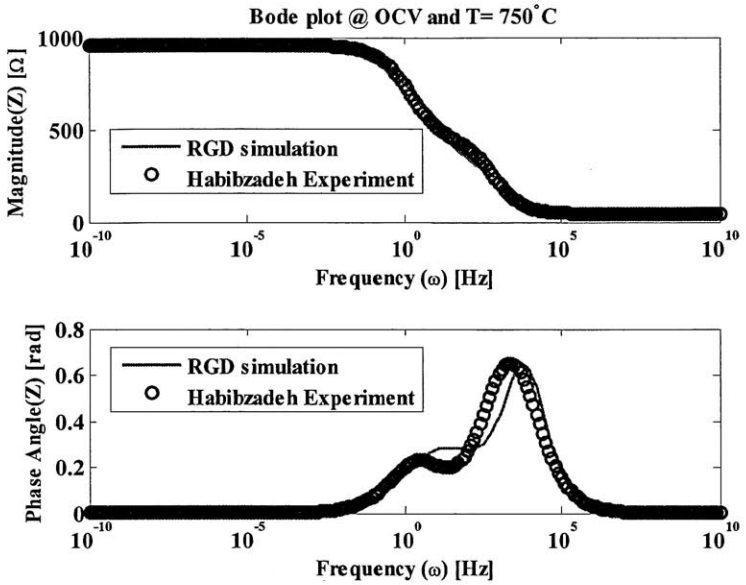

(a)

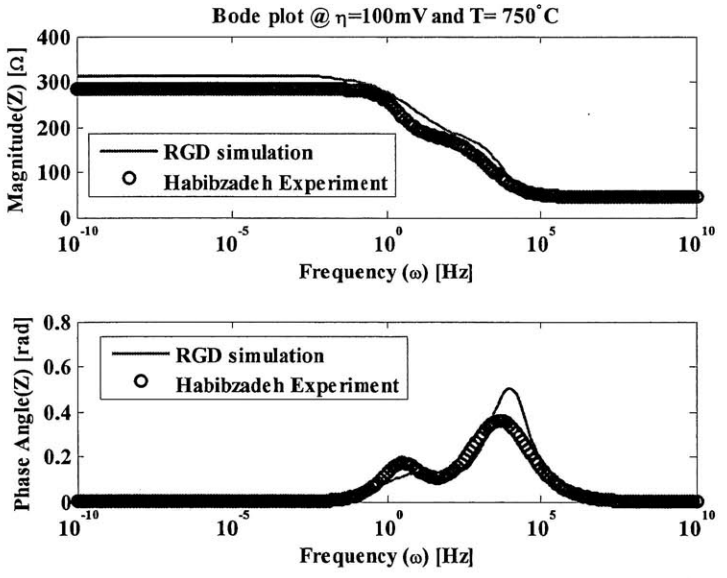

(b)

Figure 3-20. RGD EIS simulation: the Bode Plot @ T=750°C and the comparison with Habibzadeh experimental measurements. Simulation results are plotted as lines while the experimental results are shown with open circles. (a) OCV and (b) η=100mV

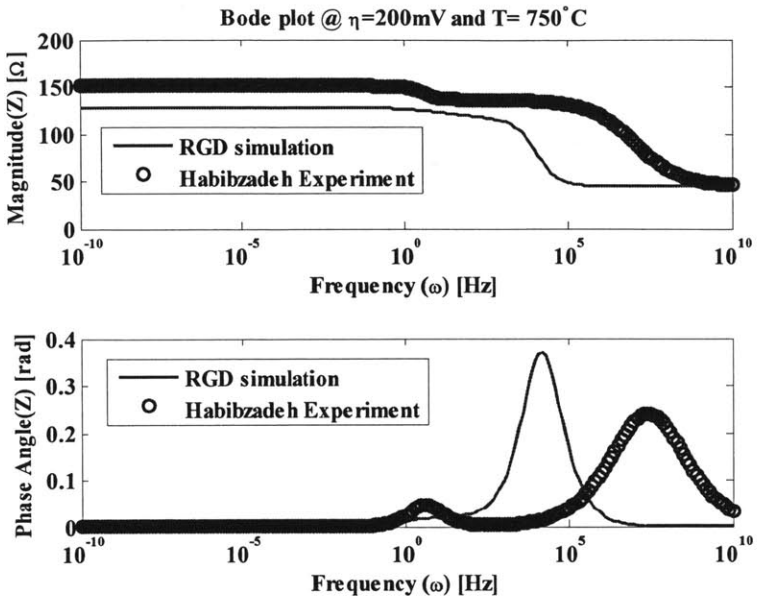

(a)

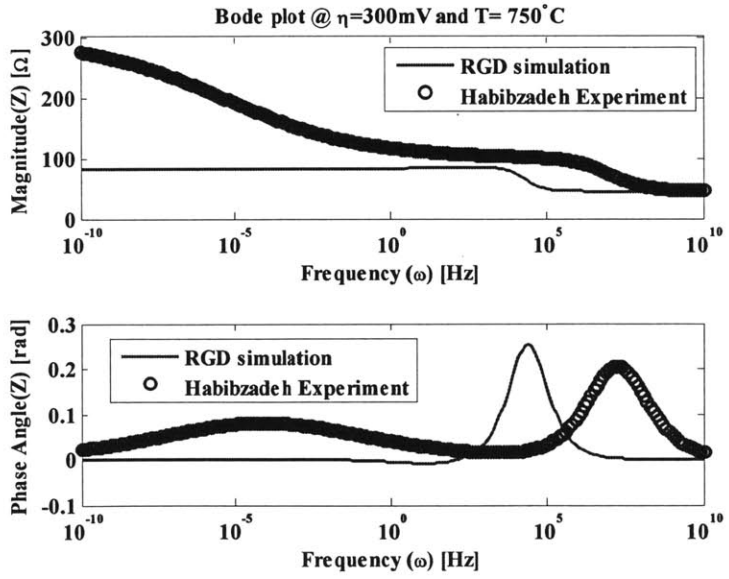

(b)

Figure 3-21. RGD EIS simulation: the Bode Plot @ T=750°C and the comparison with Habibzadeh experimental measurements. Simulation results are plotted as lines while the experimental results are shown with open circles. (a) η=200mV (b) η=300mV

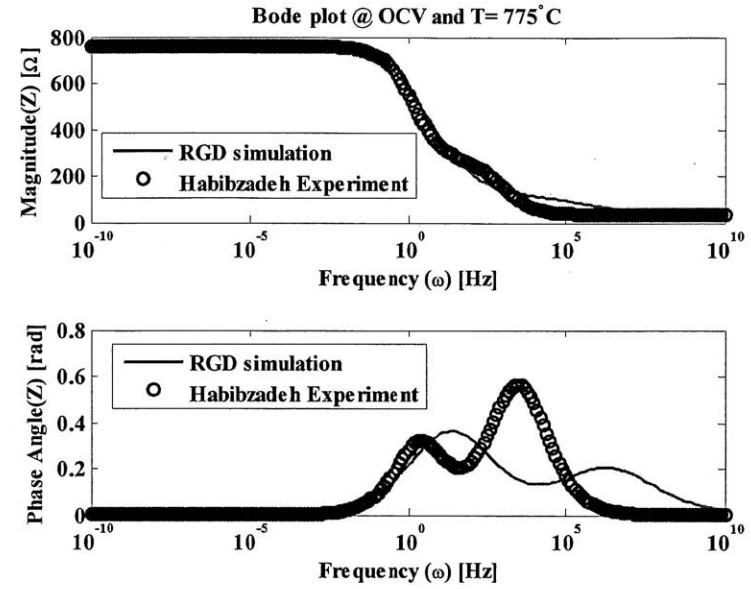

(a)

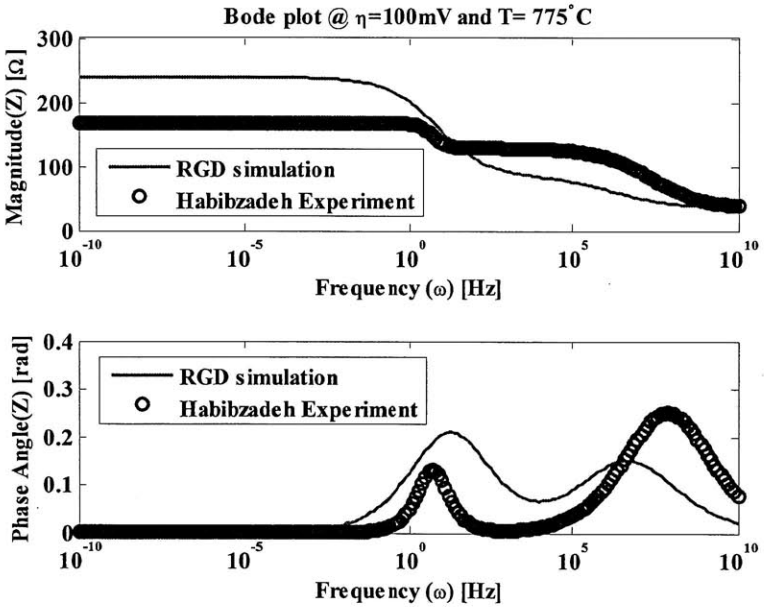

(b)

Figure 3-22. RGD EIS simulation: the Bode Plot @ T=775°C and the comparison with Habibzadeh experimental measurements. Simulation results are plotted as lines while the experimental results are shown with open circles. (a) OCV and (b) η=100mV

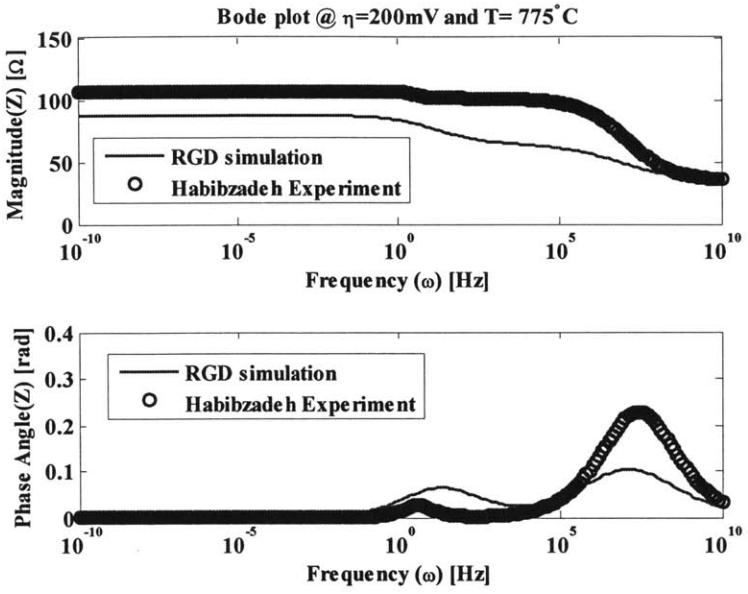

(a)

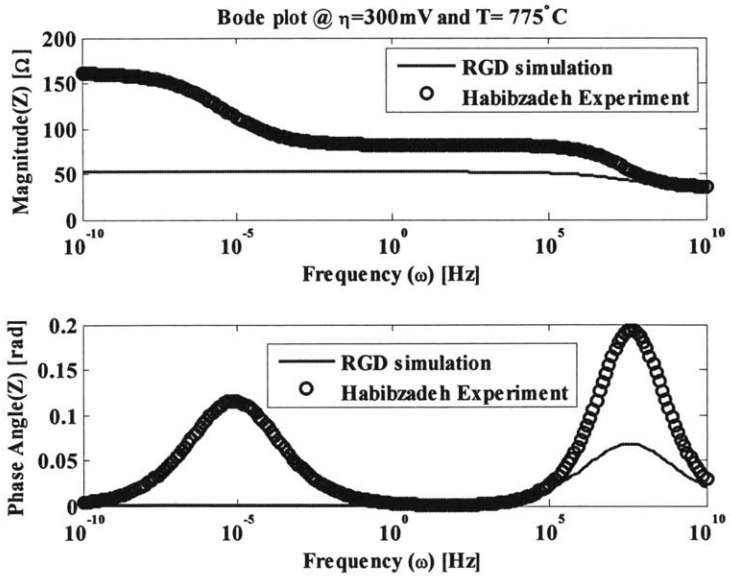

(b)

Figure 3-23. RGD EIS simulation: the Bode Plot @ T=775°C and the comparison with Habibzadeh experimental measurements. Simulation results are plotted as lines while the experimental results are shown with open circles. (a) η=200mV (b) η=300mV

3.4.4. Discussion

After measuring the impedance and reporting the data using an equivalent circuit model, Habibzadeh [19] proceeded to fit his measurements using his proposed electrochemistry mechanism presented in Section 3.2. However, his modeling results showed two perfect semi-circles. The polarization impedances were off by more than 40% and 25% from the measurements at the OCV and 100 mV, respectively, as shown in Figure 3-2.

Overall, our modeling results showed better agreements in the polarization impedance at all activation overpotentials than the Habibzadeh model [19]. At OCV and 100 mV, the two suppressed semi-circles were well reproduced. The low frequency suppressed semi-circle shrinks as the activation overpotential increases. In the model results, the characteristic frequencies remain the same regardless of the applied activation overpotentials. On the other hand, the measured characteristic frequencies in the impedance sometimes changed by $O(10^3\text{-}10^4)$. Because the adsorption/desorption and diffusion are not affected by the activation overpotential, and the CPE is assumed to be a function of temperature only, the characteristic frequencies are not expected to change by several orders of magnitude with the activation overpotential. The most frequently observed characteristic frequencies in both the model and measured impedance are 10^0 and 10^4 for the low and high frequency regions, respectively.

Table 3-6 summarizes the conditions where the measured characteristic frequencies are different from the most frequently observed values. The measurements at η=300 mV at both 750°C and 775°C were excluded from the data used to produce the model parameter because NiO formation is suspected. The only discrepancy observed at the low characteristic frequencies is at T=700°C and η=0 mV. Because the high characteristic frequency is mainly determined by

the CPE, fitting the data can be improved by changing the values to be dependent on the activation overpotential. Whether an error was incurred while the equivalent circuit was fitted to the experimental measurement by Habibzadeh [19] should also be investigated.

Table 3-6. Measurement conditions when the measured characteristic frequencies differ from the most frequently observed values of $O(10^0)$ and $O(10^4)$ in the low and high frequency regions, respectively.

Temperatures (°C)	Activation Overpential η (mV)	Characteristic Frequencies	
		Low	High
700	0	**10^{-2}**	10^4
725	300	10^0	**10^8**
750	200	10^0	**10^8**
	300	**10^{-4}**	**10^8**
775	100	10^0	**10^8**
	200	10^0	**10^8**
	300	**10^{-5}**	**10^8**

Surface diffusion of O^-

The values obtained for the O^- surface diffusion coefficients while fitting the model to the EIS data are $O(1\ m^2/sec)$ for all cases. This is several orders of magnitude higher than those for all known charged mobile species diffusion coefficient in the bulk YSZ, as shown in Table 3-7. The surface diffusion coefficient of O^- has never been measured because its existence on the surface itself is not easy to detect. Note that surface diffusion coefficients can be higher than those in the bulk due to the reduction in activation energy on the surface.

Table 3-7. O^{2-} ion, electron and hole diffusion coefficients @ 900C in the YSZ bulk [53]

Species	Diffusivity (cm^2/sec)

Oxygen ion	$D_h = 1.6\times10^{-4}\times\exp\left(-\frac{0.1\ eV}{k_BT}\right)$
Electron	$D_e = 5.4\times10^{-1}\times\exp\left(-\frac{0.55\ eV}{k_BT}\right)$
Hole	$D_{V_O^{\cdot\cdot}} = 1.9\times10^{-2}\times\exp\left(-\frac{0.83\ eV}{k_BT}\right)$

Where $k_B = 8.618\times10^{-5}\left(eVK^{-1}\right)$

Even for the CO surface diffusion coefficients on Ni surface, which has been studied for more than 35 years, the experimentally measured values vary by several orders of magnitude depending on the measurement method, the coverage and the surface directions as discussed in 3.3.4.1.

When Volger et al [30] investigated seven possible reaction pathways of H_2 electrochemistry, it was not possible to reproduce the Tafel data with any of the assumed charge-transfer mechanism. Only after the surface diffusion coefficients of H_2O and OH^- on YSZ had been adjusted was agreement achieved between the simulation and the experiments. More than five orders of magnitude higher diffusivities for H_2O and OH^- on YSZ than the reported values were required to fit experimental data for their H1 mechanism:

$$H(Ni) + OH^-(YSZ) \leftrightarrow H_2O(YSZ) + (Ni) + e^-(Ni).$$

By adding another step, $H(Ni) + O^{2-}(YSZ) \leftrightarrow OH^-(YSZ) + (Ni) + e^-(Ni)$, to the H1 mechanism, the H_2O diffusivity could be reduced from 6.3×10^3 cm^2/s to 1.3×10^{-3} cm^2/s, which was close to the reported 1.5×10^{-5} cm^2/s at 973K [30]. The same approach could be applied in our model to reduce the high O^- diffusion coefficient, by adding the following additional charge-transfer reaction on the YSZ to our existing two-step charge-transfer reactions (which is part of mechanism proposed by Yurkiv et al. [29]):

$$O^{-}(YSZ)+(Ni)\leftrightarrow O(Ni)+(YSZ)+e^{-}(Ni) \quad \text{(R. 5)}$$

We have shown that the current model structure itself can reproduce the two suppressed semi-circles. However, the optimization of the fitting parameters might have been stuck in a local minimum near the initial guess. Actually, the solution from the nonlinear least square fit function from Matlab depends on the initial guesses. We applied other global optimization algorithms provided in Matlab such as; (1) the global search algorithm: Gradient-based minimization algorithm using multiple initial guesses randomly generated, and (2) the pattern search algorithm: Derivative-free minimization using complete poll options on. It was not possible to find parameters with lower O^{-} surface diffusivity to fit all the overpotentials by global minimization solvers in Matlab. The global optimization solvers were implemented with the default options. It is possible that another set of fitting parameters can be found by thorough global optimization scheme.

Another solution to this issue of O^{-} surface diffusivity may be to reformulate the governing equation for the charge species O^{-} on the YSZ surface, or to relax the electroneutrality assumption. The diffusion equation for the O^{-} was converted to a neutral diffusion equation by assuming charge neutrality. This one dimensional approximation and charge neutrality assumption can be applied inside a uniform bulk, but not necessarily on a surface. If this assumption is relaxed, the Poisson-Nernst-Planck (PNP) equations may need to be solved in multi-dimensional space as discussed in 3.3.4.2.

3.5. Validation

In the previous section, the unknown parameters in the kinetic model are obtained by fitting the model of the EIS to the measured EIS data at constant p_{CO}=0.32 bar and p_{CO_2}=0.032 .

In this section, the proposed mechanism with the kinetic parameters obtained so far is validated against the steady-state measurements, the Tafel plots, and the exchange current density measurements. Note that there is no additional fitting in this section.

3.5.1. Tafel plots

In order to compute the electrochemical impedance, the steady-state information, θ_{O^-}, θ_{CO}, and $I_{total} = 2I_2 = 2I_3$, had to be found first, followed by solving the equations governing the perturbation and matching these solutions to the measured EIS data. However, the good match with the EIS data does not guarantee good agreement in steady-state Tafel measurement (i-η curve). Because the impedance is defined as Δη/Δi, a good agreement in the polarization impedances (when ω=0) can lead to the correct slope only, not the absolute value in the Tafel plots. Habibzadeh [19] provided measurements of the steady-state Tafel plots against which our proposed mechanism will be compared using the same kinetic parameters obtained in the previous section.

For a given activation overpotential, the corresponding steady-state currents can be obtained from the equations below using the Matlab nonlinear solver 'fsolve'.

$$\theta_{CO}^0 = \theta_{CO}(0) = \frac{N}{M^2} - \frac{I_3}{D_{CO}\Gamma_{Ni}FL_{TPB}M\tanh(ML_{Ni})} \tag{3.34}$$

$$I_2 = \hat{k}_{2,f}\left(1-\theta_{O^-}^0\right)\exp\left(\left(1-\beta_2\right)f\eta\right) - \hat{k}_{2,b}\theta_{O^-}^0\exp\left(-\beta_2 f\eta\right) \tag{3.22}$$

$$I_3 = \hat{k}_{3,f}\theta_{O^-}^0\theta_{CO}^0\exp\left(\left(1-\beta_3\right)f\eta\right) - \hat{k}_{3,b}\left(1-\theta_{O^-}^0\right)\left(1-\theta_{CO}^0\right)p_{CO_2}\exp\left(-\beta_3 f\eta\right) \tag{3.24}$$

The steady-state solution depends only on the unknown parameters, $k_{2,f}$, $k_{2,b}$, $k_{3,f}$, and $k_{3,b}$. The computed Tafel plots are shown in Figure 3-24. As expected, the slope decreases as the activation overpotential increases at all temperatures. Also, the electrochemical kinetics

improves with temperatures, leading to larger current densities. The anodic slope is steeper than the cathodic slope, which translates to a larger anodic charger transfer coefficient than a cathodic charge-transfer coefficient. This asymmetry is reproduced because of the utilization of a multi-step charge-transfer reaction mechanism even when the charge-transfer coefficients are assumed to be ½ for the two charge-transfer step, Equations (3.19) and (3.20).

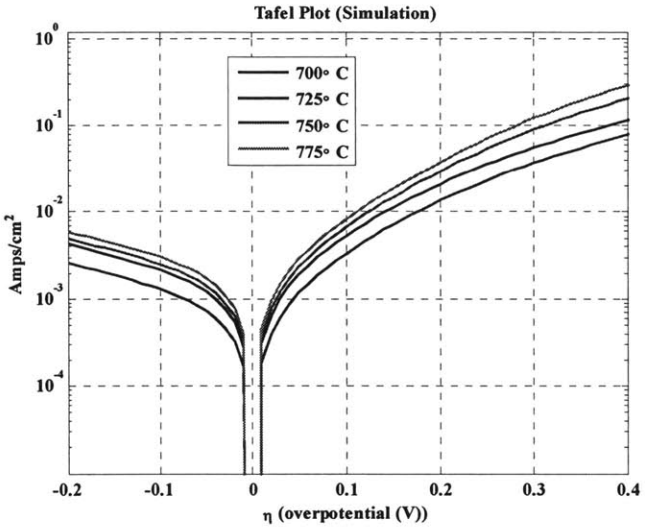

Figure 3-24. Tafel Plot simulation using the kinetic parameters obtained from the EIS measurement

Figure 3-25 shows a detailed comparison of the Tafel plots obtained from our simulation with the kinetic parameters identified using the EIS and Habibzadeh[19] experimental measurements. Overall, our simulation successfully predicts the steady state i-η characteristics. However, discrepancies develop as the applied activation overpotential increases. In particular, the disagreement is noticeable at T=750 °C and 775 °C, and as the activation overpotenial exceeds 300 mV. In other words, the measured steady state resistance is larger than that predicted by our simulation. This is consistent with the abnormal behavior observed in the EIS in that the polarization resistance increases when the activation overpotential changes from 200mV to 300 mV.

As mentioned before, this abnormal behavior and the associated discrepancies between the measurement and the predictions can be attributed to the NiO formation which is not modeled in our analysis. It is known from the experimental observations that applying significant anode overpotential (0.5V) for a lengthy period of time can have a similar effect as oxygen leakage. When oxygen is leaked to an Ni anode, it forms NiO, raising the polarization resistance. Lauvstad et al. [13] suspected the formation of an insulating NiO layer at high anodic overpotentials based on his experimental measurements. Habibzadeh [19] reported that NiO actually forms when an overpotential of 400mV is applied to an anode with inert argon.

In conclusion, the proposed CO electrochemistry whose kinetic parameters are obtained using the EIS data is successful in predicting the Tafel plots until the activation overpotential ~ 300mV. Beyond that, it is possible that NiO forms and disagreement is observed.

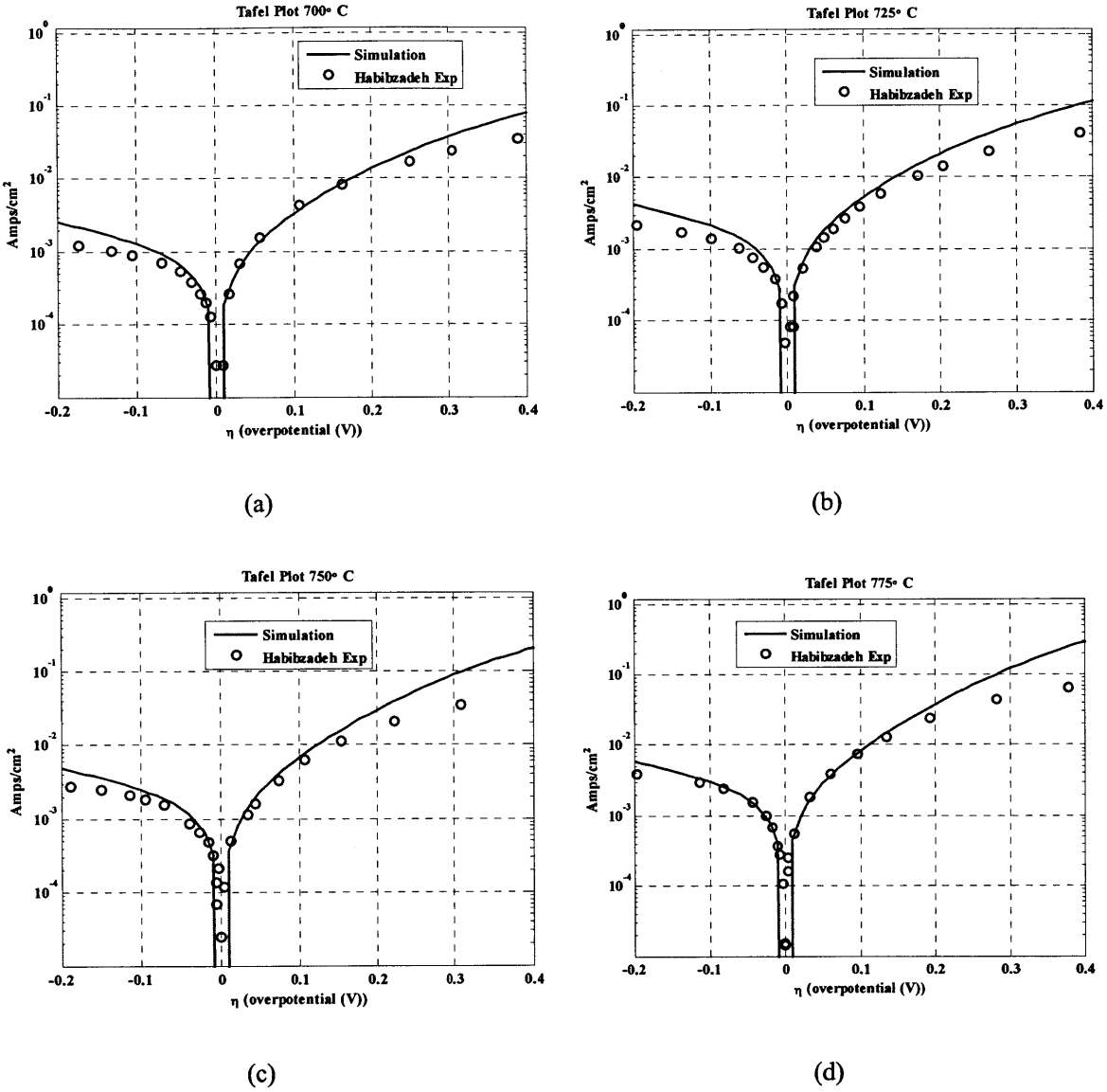

Figure 3-25. Detailed Tafel plots comparison with Habibzadeh experiments: (a) T=700 °C, (b) T=725 °C, (c) T=750 °C, (d) T=775 °C

3.5.2. Effect of p_{CO} and p_{CO_2}

When Habibzadeh [19] measured the EIS, p_{CO}=0.32 bar and p_{CO_2}=0.032 bar were kept constant while T and η were varied, as mentioned in 3.4.1. He also reported the measured exchange current density for different partial pressures of CO_2 from 0.0017 to 0.0833 bar

keeping p_{CO} constant at 0.33bar while adding Ar as a diluent. It was reported that the exchange current density (I_0) depended weakly and positively on p_{CO_2}. This is opposite to what would be expected from the global reaction perspective because CO_2 is the product of the reaction. According to the Le Chatelier principle, increasing the product concentration should decease the reaction rate; but the reported experiments show the opposite. However, the Le Chatelier principle in this simple form is only true for a purely chemical system where reaction rates are indeed only influenced by concentration. In an electrochemical system, such as an SOFC electrode, reaction rates are influenced by the electrode potential as well as the concentrations. A variation in the gas-phase composition changes both the concentrations of the adsorbed intermediates participating in the charge-transfer reaction and the electrode potential. The combined concentration and potential change leads to the observed counter-intuitive change in the macroscopic electrode response [40]. These effects can only be captured by applying detailed elementary electrochemical reactions.

When either of the two charge-transfer reactions is assumed to be rate-limiting, a modified Bulter-Volmer expression can be obtained with its corresponding exchange current density. The exchange current density expressions in Equation (3.31) and (3.32) show positive dependence on p_{CO_2}. A similar analysis was performed on a multi-step H_2 electrochemistry, which showed positive dependence of the exchange current density on H_2O partial pressure, known as the water catalytic effect [54].

The parameters obtained from fitting the model to the EIS data are assumed to be functions of temperature only. The exchange current densities can be expressed in terms of the same kinetic parameters. Figure 3-26 shows a comparison between the experimentally measured

exchange current density and our simulations. The exchange current densities for both cases exhibit positive dependence on p_{CO_2}. The measured exchange current densities have similar slope to I_2^0 while their values are close to I_3^0 when p_{CO} and p_{CO_2} have comparable values. We conclude that the current is more likely to be limited by (R. 3) when p_{CO_2} / p_{CO} is between 0.05 and 0.3 if either of the two charge-transfer reactions is rate-limiting. When $p_{CO_2} / p_{CO} < 0.04$, it is difficult to claim that either of the two is a rate-limiting step.

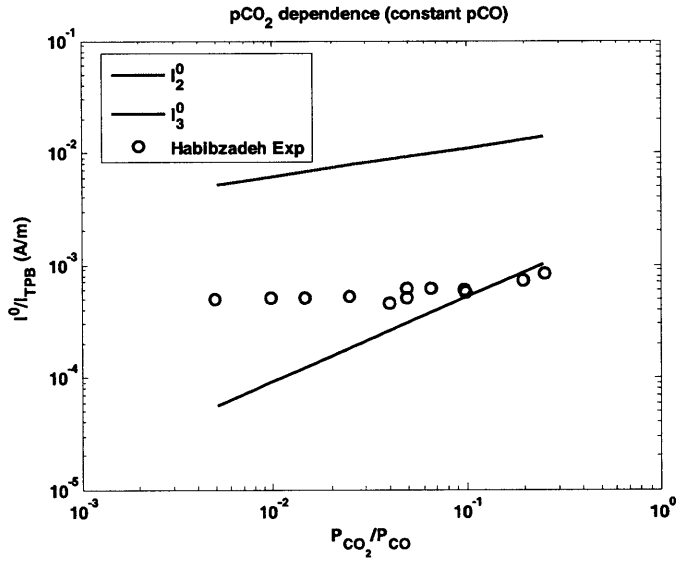

Figure 3-26. The dependence of the exchange current density on p_{CO_2} at constant p_{CO} at T=775°C: Experimental measurements from Habibzadeh Thesis is marked as open circles, two exchange current densities from (R. 2) and (R. 3) are denoted as I_2^0 and I_3^0.

To summarize, in the steady-state measurements, some of the kinetics phenomena observed in the EIS are no longer present, such as the double-layer charging/discharging current observed in the high frequency region (~10^5) and the O^- diffusion on YSZ in the low frequency region (~10^0). At steady-state, only two charge-transfer reactions, CO adsorption/desorption and

CO diffusion on Ni play roles in the proposed mechanism. The proposed mechanism with the four kinetic parameters, $k_{2,f}$, $k_{2,b}$, $k_{3,f}$, and $k_{3,b}$, obtained by fitting the model to the EIS data can successfully predict the Tafel plots except when the activation overpotential exceeds 300 mV where NiO formation is suspected. The proposed mechanism is also successful in explaining the positive dependence of the exchange current density on p_{CO_2}.

3.6. The low frequency inductive loop

The structure of the proposed multi-step charge-transfer mechanism successfully reproduces the EIS data. With the kinetic parameters obtained by fitting the model to the EIS data, the Tafel plots and the exchange current density measured by Habibzadeh [19] can also be reproduced reasonably well. We will now investigate the inductive behavior reported by Lauvstad et al. [13]. Lauvstad et al. [13] measured the electrochemical impedance using Ni point electrode. Most of their Nyquist plots had a single suppressed semi-circle. They observed a loop in the fourth quadrant in the impedance Nyquist plot at lower frequency when a high activation overpotential was applied, as shown in Figure 3-27. Because this behavior can be reproduced by adding an inductor to the equivalent circuit, this is often called a low-frequency inductive loop [55].

Using an analysis similar to that described in 3.3.5, Lauvstad et al. [13] derived expressions for the impedance according to four possible electrochemistry models that are described in Section 3.2. Only one mechanism involving two adsorbed intermediates was successful in reproducing the low frequency inductive behavior [12,13]. This low frequency inductive behavior was used as the single most important factor in selecting a probable electrochemical pathway among the four proposed mechanisms because all of them were

successful in producing reasonable agreement with the single suppressed semi-circle shape of the experimental data. Yurkiv et al [29] proposed a two-step charge-transfer reaction for CO based on an oxygen-spillover mechanism and fitted the model to the Lauvstad et al.'s data [13]. Yurkiv et al.'s mechanism showed an overall good agreement with the Tafel and EIS measurements [29]. However, it failed to reproduce the low frequency inductive loop.

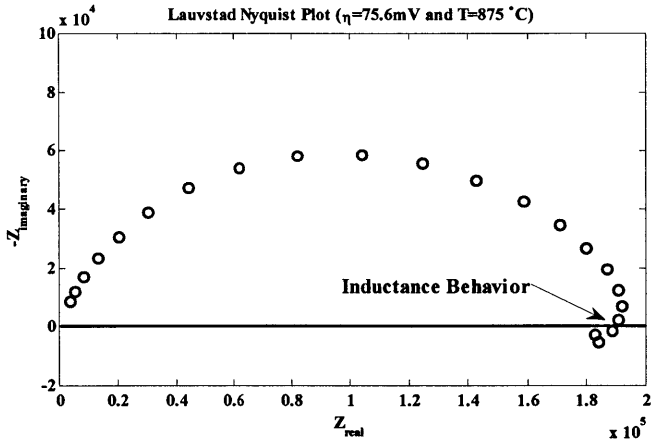

Figure 3-27. Impedance spectrum recorded on Ni point electrode at the activation overpotential=75.6 mV, T=875°C, and p_{CO}= 0.333 atm and p_{CO_2} = 0.667 atm.

Figure 3-28 and 3-29 show the Nyquist plots at T=725°C and T=750°C, respectively, obtained using our model. The applied activation overpotential changes from the OCV up to 300 mV. First, we observe that the overall impedance decreases as the temperature rises from 725°C to 750°C. Moreover, the two semi-circles transition to a single semi-circle and develops an inductance loop at an anodic overpotential=300 mV. This inductive behavior was not reported in Habibzadeh [19], which could be accounted for by the NiO formation in the experiments, as discussed earlier. Habibzadeh reported NiO formation at high anodic overpotential, which resulted in the abnormal behavior of increasing the polarization resistance at 300 mV. This insulating NiO layer might obscure the small inductive loop.

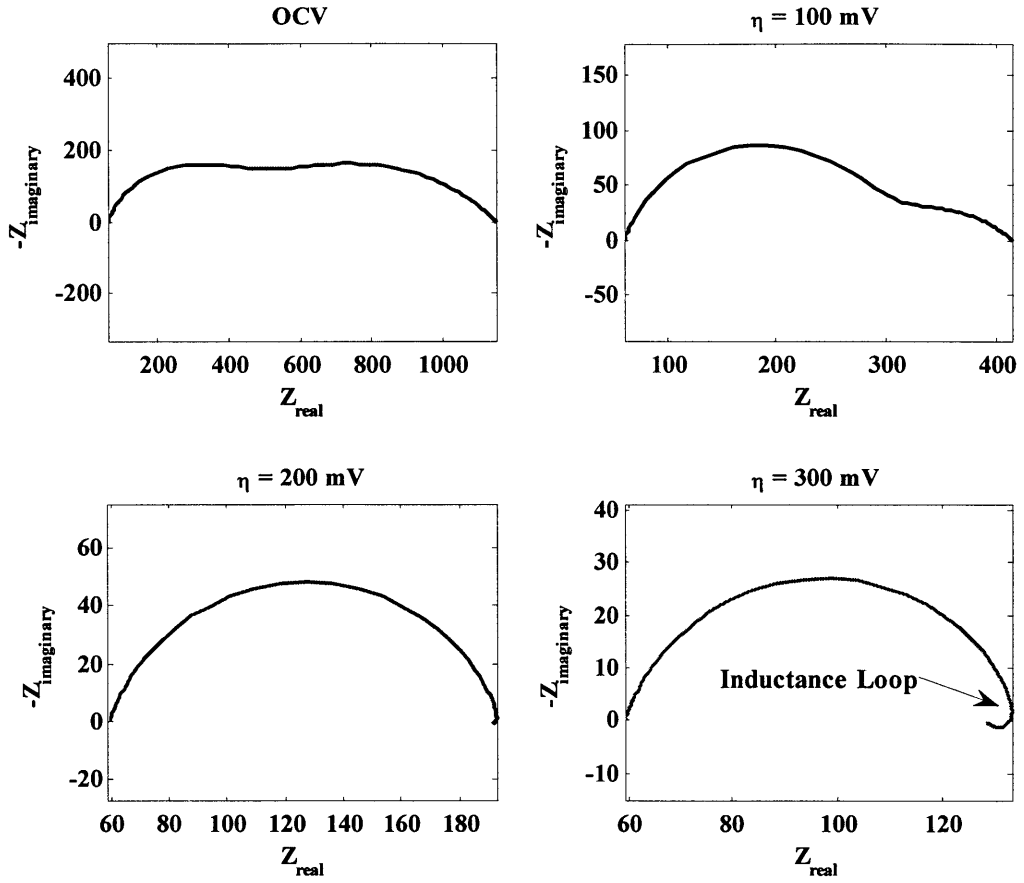

Figure 3-28. Simulated impedance Nyquist Plots at T=725°C at different activation overpotentials from OCV to 300 mV., same as Figure 3-15 but with expanded axis.

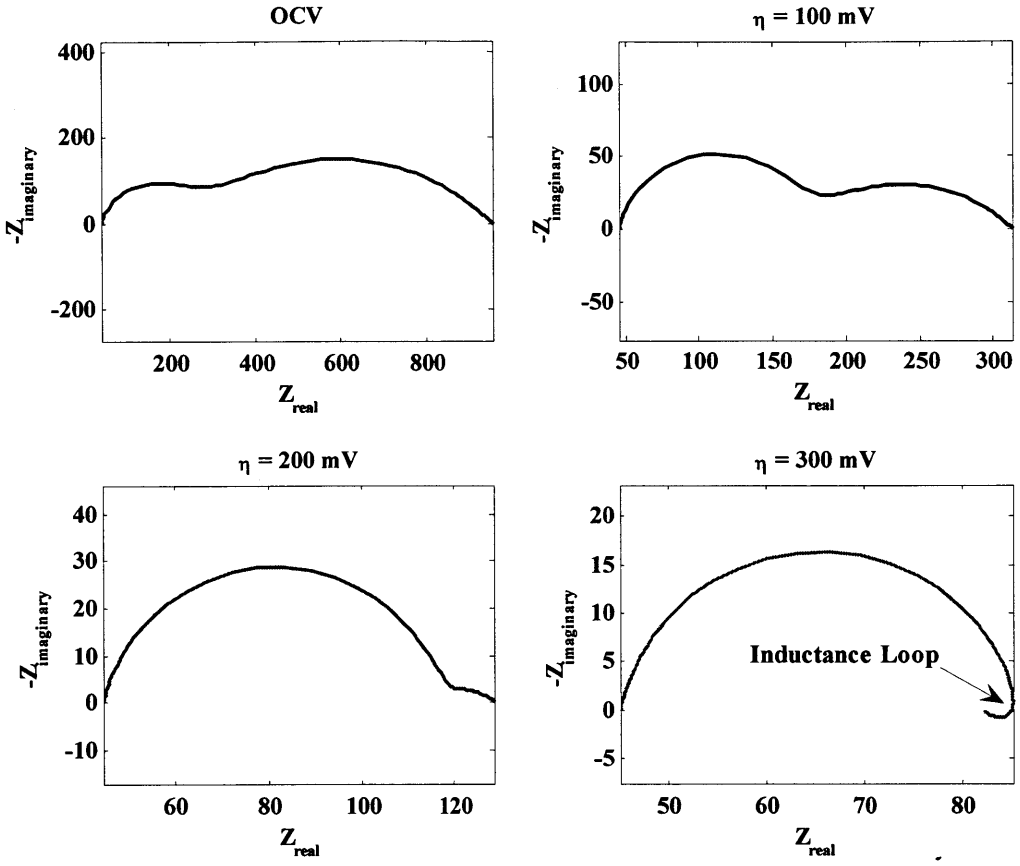

Figure 3-29. Simulated impedance Nyquist Plots at T=750°C at different activation overpotentials from OCV to 300 mV, same as Figure 3-18 but with expanded axis

To explain the origin of the inductive behavior, let's define the faradaic impedances $Z_{f,2}$ and $Z_{f,3}$ for each charge-transfer step of (R. 2) and (R. 3) as follows.

$$Z_{f,2} = \frac{\Delta\eta}{\Delta I_2} \tag{3.67}$$

$$Z_{f,3} = \frac{\Delta\eta}{\Delta I_3} \tag{3.68}$$

The total impedance was defined as in 3.3.5

$$Z_f = \frac{\Delta\eta}{\Delta I_2 + \Delta I_3} = \frac{1}{1/Z_{f,2} + 1/Z_{f,3}} \tag{3.69}$$

The impedance corresponding to the faradaic currents from (R. 2) and (R. 3) are shown in Figure 3-30 and 3-31. The current from (R. 2) grows as the perturbation voltage increases in time behaving like a capacitor. As the steady-state activation overpotential increases, the (-) phase angle of $Z_{f,2}$ decreases monotonically. The current from (R. 3) decreases as the perturbation voltage increases in time behaving like an inductor. The total faradaic impedance, Z_f shown in Equation (3.69), behaves like a capacitor overall until the steady-state activation overpotential reaches 300 mV where the inductive behavior appears as shown in Figure 3-32. Because of the complex interplay among the adsorption/desorption of CO, the surface diffusion of CO and O^-, and the two charge-transfer reactions, it is not obvious how to explain the resulting faradaic impedances. However, the opposite behavior of $Z_{f,2}$ and $Z_{f,3}$ lead to either a capacitive or an inductive appearance in the total faradaic impedance, Z_f, depending on their relative magnitude. The two-step charge-transfer mechanism leads to the transition from two semi-circles to one semi-circle with the inductive loop.

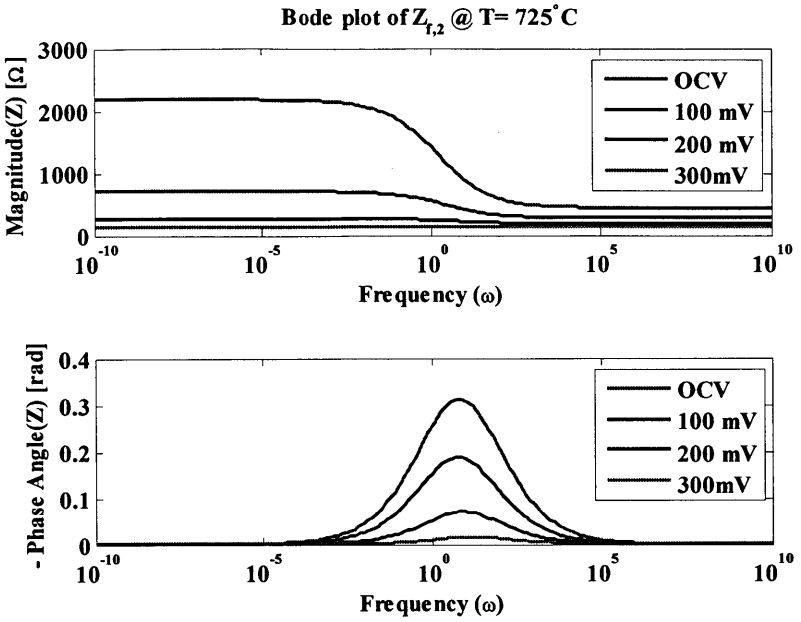

Figure 3-30. The impedance of the faradaic current from (R. 2) at T=725 °C.

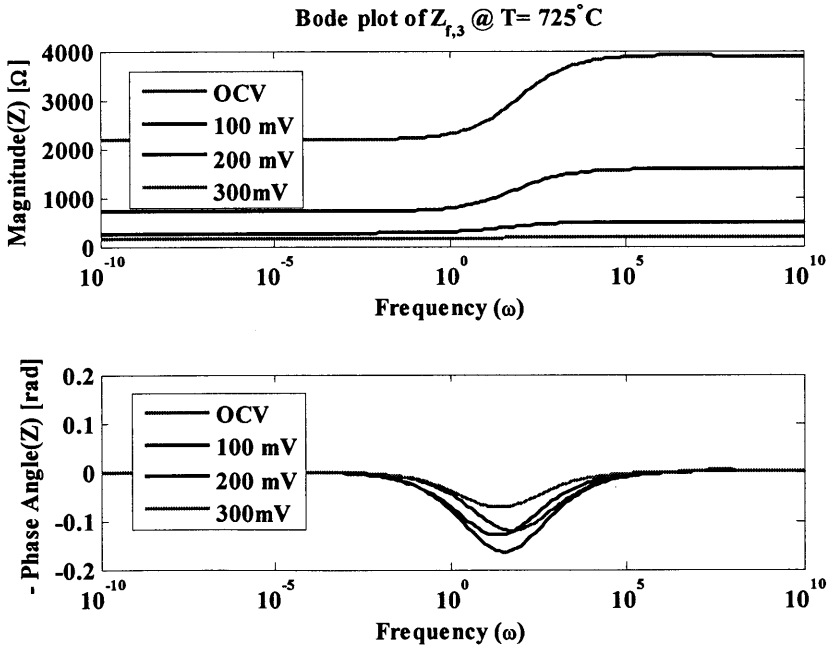

Figure 3-31. The impedance of the faradaic current from (R. 3) at T=725 °C.

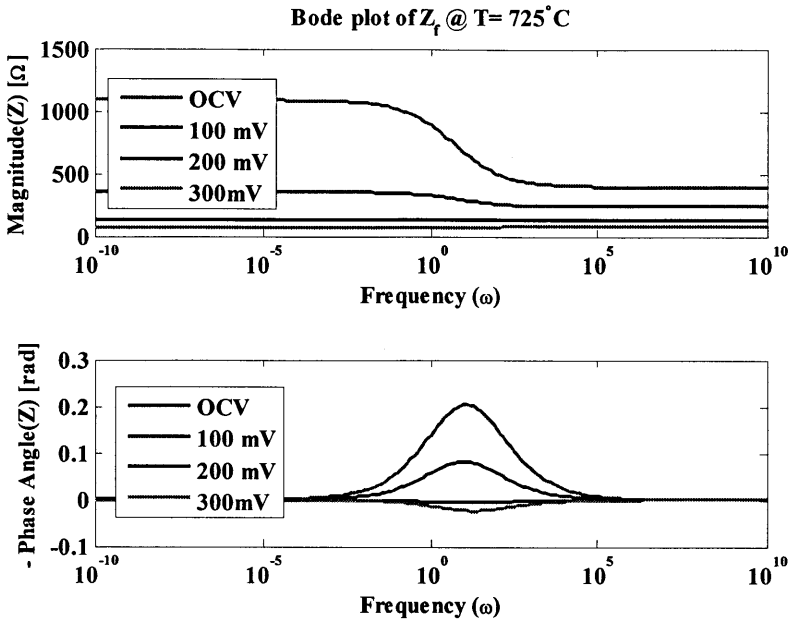

Figure 3-32. The total faradaic impedance at T=725 °C.

3.7. Application of the CO electrochemistry mechanism to MEA

Of more interest is the application of the proposed CO electrochemistry model to a typical porous electrode structure to predict the performance of a fuel cell. In principle, the proposed CO electrochemistry mechanism can be applied to the porous structure once the necessary geometric information, including the TPB length and the equivalent Ni pattern width, is found for the porous structure. However, the TPB length itself is hard to determine. Even for the patterned anode, the seemingly straight TPB line is no longer straight at higher resolution images. Bessler et al. [40] reviewed the experimental data for patterned and point anodes used to examine hydrogen electrochemistry and found that there is large scatter of 2.5 orders of magnitude in the TPB-length-specific resistance because of the following reasons:

(1) Patterned anodes experience morphology changes by grain growth, delamination from

a support, rounding off of the originally sharp corners, becoming island-like Ni agglomerates.

(2) an "Impure" (99.8%) Ni electrode can result in a big difference in the measurements from a "pure" (99.995%) Ni electrode by forming a second phase impurity ridges at the TPB.

(3) The relaxation time is reported to be on the order of hours. Depending on the measurement history, the experimental data can be affected by dynamic effects.

(4) The electrochemical performance strongly depends on the gas phase composition in a non-intuitive way.

The TPB length per unit volume increased by 5-6 orders of magnitude when going from point to patterned to cermet anodes [40]. However, the reported performance was not improved as much by these structural changes. Further research needs to be done to link the performance improvement to the structural change. Until then, the two geometric parameters, the TPB length and the equivalent Ni catalyst width, may be used as a fitting parameter

3.8. Conclusion

We proposed a new multi-step CO electrochemistry model where CO is directly involved in the charge-transfer steps, which is different from the Yurkiv et al.'s mechanism [29]. One set of parameters at each temperature succeeded in reproducing the following characteristics of the impedances at all activation overpotentials: (1) the two suppressed semi-circles in the impedance, and (2) the polarization resistance reduces as the activation overpotential increases. The same parameters successfully predicted the following features in the steady-state Tafel plots: (1) the asymmetry of the anodic and cathodic currents, and (2) the reduction in the slope as overpotential increases. The electrochemistry mechanism can explain the positive dependency of the exchange current density on p_{CO_2} as well. Furthermore, at high activation overpotentials, the

inductive behavior, reported from Lauvstad et al. [13], is predicted from our model.

Even though the high O^- diffusion coefficient remains to be resolved, this model can reproduce a wide range of experimental measurements with one set of fitting parameters. At steady-state, the concentration of O^- is uniform on the YSZ surface. Hence, only four kinetic parameters, $k_{2,f}$, $k_{2,b}$, $k_{3,f}$, and $k_{3,b}$, are used to compute the current at a given activation overpotential. Because the analytical approach is employed, the overall computation time is short enough to allow the current model to be implemented in more complex models such as MEA and cell stack models.

3.9. References

[1] E. P. Murray, T. Tsai, and S. A. Barnett, "A direct-methane fuel cell with a ceria-based anode," *Nature*, vol. 400, no. 6745, pp. 649–651, 1999.

[2] S. Park, J. Vohs, and R. J. Gorte, "Direct oxidation of hydrocarbons in a solid-oxide fuel cell," *Nature*, vol. 404, no. 6775, pp. 265-7, Mar. 2000.

[3] Z. Zhan, J. Liu, and S. A. Barnett, "Operation of anode-supported solid oxide fuel cells on propane–air fuel mixtures," *Applied Catalysis A: General*, vol. 262, no. 2, pp. 255-259, May 2004.

[4] Z. Zhan and S. A. Barnett, "Solid oxide fuel cells operated by internal partial oxidation reforming of iso-octane," *Journal of Power Sources*, vol. 155, no. 2, pp. 353-357, 2006.

[5] J. Liu and S. A. Barnett, "Operation of anode-supported solid oxide fuel cells on methane and natural gas," *Solid State Ionics*, vol. 158, no. 1, pp. 11–16, Feb. 2003.

[6] Y. Lin, Z. Zhan, J. Liu, and S. A. Barnett, "Direct operation of solid oxide fuel cells with methane fuel," *Solid State Ionics*, vol. 176, no. 23–24, pp. 1827-1835, Jul. 2005.

[7] Z. Zhan and S. A. Barnett, "Operation of ceria-electrolyte solid oxide fuel cells on iso-octane–air fuel mixtures," *Journal of Power Sources*, vol. 157, no. 1, pp. 422-429, 2006.

[8] S. Park, R. Craciun, J. M. Vohs, and R. J. Gorte, "Direct oxidation of hydrocarbons in a solid oxide fuel cell. I. Methane oxidation," *Journal of the Electrochemical Society*, vol. vol, pp. 146pp3603-3605, 1999.

[9] R. J. Gorte, S. Park, J. M. Vohs, and C. Wang, "Anodes for direct oxidation of dry hydrocarbons in a solid-oxide fuel cell," *Advanced Materials*, vol. 12, no. 19, pp. 1465-1469, 2000.

[10] M. Mogensen and K. Kammer, "Conversion of Hydrocarbons in Solid Oxide Fuel Cells," *Annual Review of Materials Research*, no. 13, 2003.

[11] A. M. Sukeshini, B. Habibzadeh, B. P. Becker, C. A. Stoltz, B. W. Eichhorn, and G. S. Jackson, "Electrochemical Oxidation of H2, CO, and CO/H2 Mixtures on Patterned Ni Anodes on YSZ Electrolytes," *Journal of The Electrochemical Society*, vol. 153, no. 4, p. A705, 2006.

[12] G. O. Lauvstad, R. Tunold, and S. Sunde, "Electrochemical Oxidation of CO on Pt and Ni Point Electrodes in Contact with an Yttria-Stabilized Zirconia Electrolyte: I. Modeling of Steady-State and Impedance Behavior," *Journal of The Electrochemical Society*, vol. 149, no. 12, pp. 497-505, Dec. 2002.

[13] G. O. Lauvstad, R. Tunold, and S. Sunde, "Electrochemical oxidation of CO on Pt and Ni point electrodes in contact with an yttria-stabilized zirconia electrolyte: II. Steady-State and Impedance Measurements," *Journal of the Electrochemical Society*, vol. 149, no. 12, pp. 506-514, Dec. 2002.

[14] Y. Jiang and A. V. Virkar, "Fuel composition and diluent effect on gas transport and performance of anode-supported SOFCs," *Journal of the Electrochemical Society*, vol. 150, no. 7, pp. 942-951, 2003.

[15] W. Andre, S. Bastian, C. Axel, and D. Herbstritt, "Oxidation of H2, CO and methane in SOFCs with Ni/YSZ-cermet anodes," *Solid State Ionics*, vol. 152, pp. 543–550, 2002.

[16] Y. Matsuzaki and I. Yasuda, "Electrochemical oxidation of H2 and CO in a H2-H2O-CO-CO2 system at the interface of a Ni-YSZ cermet electrode and YSZ electrolyte," *Journal of the Electrochemical Society*, vol. 147, no. 5, pp. 1630-1635, 2000.

[17] H. Zhu, R. J. Kee, V. M. Janardhanan, O. Deutschmann, and D. G. Goodwin, "Modeling elementary heterogeneous chemistry and electrochemistry in solid-oxide fuel cells," *Journal of the Electrochemical Society*, vol. 152, no. 12, p. A2427-A2440, 2005.

[18] V. M. Janardhanan and O. Deutschmann, "Numerical study of mass and heat transport in solid-oxide fuel cells running on humidified methane," *Chemical Engineering Science*, vol. 62, no. 18–20, pp. 5473-5486, Sep. 2007.

[19] B. Habibzadeh, "Understanding CO oxidation in SOFC's using nickel patterned anode," University of Maryland, 2007.

[20] T. H. Etsell and S. N. Flengas, "Overpotential Behavior of Stabilized Zirconia Solid Electrolyte Fuel Cells," *Journal of The Electrochemical Society*, vol. 118, no. 12, p. 1890, 1971.

[21] T. Setoguchi, K. Okamoto, K. Eguchi, and H. Arai, "Effects of anode material and fuel on anodic reaction of solid oxide fuel cells," *Journal of The Electrochemical Society*, vol. 139, no. 10, pp. 2875-2880, 1992.

[22] J. Mizusaki, H. Tagawa, Y. Miyaki, S. Yamauchi, K. Fueki, I. Koshiro, and K. Hirano, "Kinetics of the electrode reaction at the CO-CO2, porous Pt/stabilized zirconia interface," *Solid state ionics*, vol. 53, pp. 126–134, 1992.

[23] R. J. Aaberg, R. Tunold, S. Tjelle, and R. Odegard, "Oxidation of CO and H-2 on Ni/YSZ cermet electrodes," in *Proceedings of the 17th Riso International Symposium: High Temperature Electrochemistry: Ceramics and Metals*, 1996, pp. 511-518.

[24] P. Holtappels, L. G. J. De Haart, U. Stimming, I. C. Vinke, and M. Mogensen, "Reaction of CO/CO2 gas mixtures on Ni-YSZ cermet electrodes," *Journal of Applied*

Electrochemistry, vol. 29, no. 5, pp. 561-568, 1999.

[25] Boulenouar FZ, Yashiro K, Oishi M, Kaimai A, Nigara Y, Kawada T, and Mizusaki J, "Electrochemical oxidation of CO in a CO-CO2 system at the interface of Ni grid electrode/YSZ electrolyte," *SOLID OXIDE FUEL CELLS VII (SOFC VII)*, vol. 2001, no. 16, pp. 759-768, 2001.

[26] O. Costa-Nunes, R. J. Gorte, and J. M. Vohs, "Comparison of the performance of Cu-CeO2-YSZ and Ni-YSZ composite SOFC anodes with H2, CO, and syngas," *Journal of power sources*, vol. 141, no. 2, pp. 241–249, 2005.

[27] A. Ehn, J. Hogh, M. Graczyk, K. Norrman, L. Montelius, M. Linne, and M. Mogensen, "Electrochemical measurements made in dry CO/CO2 and H2/H2O atmospheres on single crystal YSZ using pattern electrodes," in *Proceedings of the 26th Risø International Symposium on Materials Science: Solid State Electrochemistry*, 2005, pp. 177-183.

[28] B. Habibzadeh, A. M. Sukeshini, B. Becker, and G. S. Jackson, "CO Electrochemical Oxidation on Ni Patterned Anodes for Assessing Solid Oxide Fuel Cell Kinetics," in *ECS Transactions*, 2008, vol. 11, no. 33, pp. 53-61.

[29] V. Yurkiv, D. Starukhin, H.-R. Volpp, and W. G. Bessler, "Elementary Reaction Kinetics of the CO/CO2/Ni/YSZ Electrode," *Journal of The Electrochemical Society*, vol. 158, no. 1, p. B5, 2011.

[30] M. Vogler, A. Bieberle-Hütter, L. Gauckler, J. Warnatz, and W. G. Bessler, "Modelling Study of Surface Reactions, Diffusion, and Spillover at a Ni/YSZ Patterned Anode," *Journal of The Electrochemical Society*, vol. 156, no. 5, p. B663, 2009.

[31] A. Bieberle, L. P. Meier, and L. J. Gauckler, "The Electrochemistry of Ni Pattern Anodes Used as Solid Oxide Fuel Cell Model Electrodes," *Journal of The Electrochemical Society*, vol. 148, no. 6, p. A646, 2001.

[32] D. G. Goodwin, H. Zhu, A. M. Colclasure, and R. J. Kee, "Modeling Electrochemical Oxidation of Hydrogen on Ni–YSZ Pattern Anodes," *Journal of The Electrochemical Society*, vol. 156, no. 9, p. B1004, Sep. 2009.

[33] J. Mizusaki, H. Tagawa, T. Saito, T. Yamamura, K. Kamitani, K. Hirano, S. Ehara, T. Takagi, T. Hikita, and M. Ippommatsu, "Kinetic studies of the reaction at the nickel pattern electrode on YSZ in H2/H2O atmospheres," *Solid State Ionics*, vol. 70–71, pp. 52-58, May 1994.

[34] A. Bielański and J. Haber, *Oxygen in catalysis*. New York: M. Dekker, 1991.

[35] R. Merkle and J. Maier, "Oxygen incorporation into Fe-doped SrTiO3: Mechanistic interpretation of the surface reaction," *Physical Chemistry Chemical Physics*, vol. 4, no.

17, pp. 4140-4148, Aug. 2002.

[36] J. Fleig, R. Merkle, and J. Maier, "The p(O2) dependence of oxygen surface coverage and exchange current density of mixed conducting oxide electrodes: model considerations.," *Physical chemistry chemical physics : PCCP*, vol. 9, no. 21, pp. 2713-23, Jun. 2007.

[37] M. Leonhardt, R. a. De Souza, J. Claus, and J. Maier, "Surface Kinetics of Oxygen Incorporation into SrTiO[sub 3]," *Journal of The Electrochemical Society*, vol. 149, no. 2, p. J19, 2002.

[38] R. a De Souza, "A universal empirical expression for the isotope surface exchange coefficients (k*) of acceptor-doped perovskite and fluorite oxides.," *Physical chemistry chemical physics : PCCP*, vol. 8, no. 7, pp. 890-7, Feb. 2006.

[39] A. Mitterdorfer, "Identification of the reaction mechanism of the Pt, O2(g)|yttria-stabilized zirconia system Part I: General framework, modelling, and structural investigation," *Solid State Ionics*, vol. 117, no. 3–4, pp. 187-202, Feb. 1999.

[40] W. G. Bessler, M. Vogler, H. Störmer, D. Gerthsen, A. Utz, A. Weber, and E. Ivers-Tiffée, "Model anodes and anode models for understanding the mechanism of hydrogen oxidation in solid oxide fuel cells.," *Physical chemistry chemical physics : PCCP*, vol. 12, no. 42, pp. 13888-903, Nov. 2010.

[41] E. S. Hecht, G. K. Gupta, H. Zhu, A. M. Dean, R. J. Kee, L. Maier, and O. Deutschmann, "Methane reforming kinetics within a Ni–YSZ SOFC anode support," *Applied Catalysis A: General*, vol. 295, no. 1, pp. 40-51, Oct. 2005.

[42] E. Seebauer and C. E. Allen, "Estimating surface diffusion coefficients," *Progress in Surface Science*, vol. 49, no. 3, pp. 265-330, Jul. 1995.

[43] R. Gomer, "Diffusion of adsorbates on metal surfaces," *Reports on Progress in Physics*, vol. 53, no. 7, pp. 917-1002, Jul. 1990.

[44] X.-D. Xiao, Y. Xie, and Y. Shen, "Coverage dependence of anisotropic surface diffusion: CO/Ni(110)," *Physical Review B*, vol. 48, no. 23, pp. 17452-17462, Dec. 1993.

[45] W. G. Bessler, S. Gewies, and M. Vogler, "A new framework for physically based modeling of solid oxide fuel cells," *Electrochimica Acta*, vol. 53, no. 4, pp. 1782-1800, Dec. 2007.

[46] E. Barsoukov and J. Ross Macdonald, *Impedance spectroscopy : theory, experiment, and applications.*, 2nd ed. /. Hoboken N.J.: Wiley-Interscience, 2005.

[47] A. J. Bard and L. R. Faulkner, *Electrochemical methods : Fundamentals and applications*, 2nd ed. New York: John Wiley & Sons, Inc, 2001.

[48] A. Bieberle, "The Electrochemistry of Solid Oxide Fuel Cell Anodes: Experiments, Modeling, and Simulations," Technische Wissenschaften ETH Zürich, 2000.

[49] M. Hendriks, "The electrochemical double-layer capacitance of yttria-stabilised zirconia," *Solid State Ionics*, vol. 146, no. 3–4, pp. 211-217, Feb. 2002.

[50] A. Lasia, "Applications of Electrochemical Impedance Spectroscopy to Hydrogen Adsorption, Evolution and Absorption into Metals," in *Modern Aspects of Electrochemistry*, vol. 35, B. E. Conway and R. E. White, Eds. Springer US, 2002, pp. 1-49.

[51] D. A. Harrington, "Electrochemical impedance of multistep mechanisms: mechanisms with diffusing species," *Journal of Electroanalytical Chemistry*, vol. 403, no. 1–2, pp. 11-24, Feb. 1996.

[52] D. A. Harrington, "Electrochemical impedance of multistep mechanisms : a general theory," *Journal of electroanalytical chemistry*, vol. 449, no. 1–2, pp. 9-28.

[53] K. Sasaki and J. Maier, "Re-analysis of defect equilibria and transport parameters in Y2O3-stabilized ZrO2 using EPR and optical relaxation," *Solid State Ionics*, vol. 134, no. 3–4, pp. 303-321, 2000.

[54] W. Y. Lee, D. Wee, and A. Ghoniem, "An improved one-dimensional membrane-electrode assembly model to predict the performance of solid oxide fuel cell including the limiting current density," *Journal of Power Sources*, vol. 186, no. 2, pp. 417-427, 2009.

[55] M. E. Orazem and B. Tribollet, *Electrochemical Impedance Spectroscopy (The ECS Series of Texts and Monographs)*. Wiley-Interscience, 2008, p. 560.

Page left intentionally blank

Chapter 4

Membrane-electrode assembly model of SOFCs using syngas with detailed H_2 and CO electrochemistry

Abstract

We develop a membrane-electrode-assembly (MEA) model incorporating multi-species transport through the porous structure, detailed elementary heterogeneous reactions on the Ni surface, and for the first time, detailed electrochemistry models for H_2 and CO. The model successfully reproduces the performance of SOFCs using pure H_2 or CO. The MEA model can isolate/distinguish between the roles/contributions of the reforming chemistry and CO electrochemistry in SOFCs using syngas. Adding reforming thermochemistry improves the agreement with experiments at lower current densities, and raises the limiting current density by providing more H_2 via the water-gas shift reaction. Adding CO electrochemistry improves the prediction at high current densities by the additional current generated by the CO electrochemical oxidation. The current from CO becomes comparable to that from H_2 as the CO content at the TPB increases.

Nomenclature

Symbol	Meaning	Common Units
A	Pre-exponential factor	[mol, m, sec, Pa]
A_s	Specific catalyst area per unit volume of electrode	[1/m]
B_o	Permeability	[m^2]
c_k	Concentration of gas species k	[mol/m^3]
$c_{surf,k}$	Concentration of surface species k	[mol/m^2]
D_i	Surface diffusion diffusion coefficients of species i	[m^2/s]
c_t	Total molar concentration.	[mol/m^3]
d_0	Characteristic pore diameter	[m]
d_m	Diameter of molecules	[m]
d_p	Diameter of matrix particle	[m]
D_{ij}	Ordinary binary diffusion coefficients	[m^2/s]
D_{co}	CO Surface diffusion diffusion coefficients	[m^2/s]
D_{iM}^e	Effective Knudsen diffusion coefficient of species i	[m^2/s]
E	Electric potential difference	[V]
E	Activation energy	[kJ/mol]
F	Faraday Constant	96,485 [C/mol]
i	Current density	[A/cm^2]
i_0	Exchange current density	[A/cm^2]
J_k	Molar flux of gas species k	[$mol/m^2 \cdot sec$]
k_B	Boltzmann constant	[eV/K]
k	Reaction rate constant	[mol, m, sec, Pa]
$k_{i,f}$	Forward reaction constant of reaction i	[mol, m, sec, Pa]
$k_{i,b}$	Bckward reaction constant of reaction i	[mol, m, sec, Pa]
K_g	Number of gas species	Dimensionless
K_s	Number of surface species	Dimensionless
l_{TPB}	TPB length per nominal electrolyte area	[m/cm^2]
L_{Ni}	Half of the Ni pattern width	[μm]
M_i	Molar mass of species i	[kg/mol]
p	Pressure	[N/m^2]
R_{ohm}	Ohmic resistance	[Ω]
$R_{gas,i}$	Rate of homogeneous reaction i	[mol/m^3]
$R_{surface,i}$	Rate of heterogeneous reaction i	[mol/m^2]
$\Re$	Universal gas constant	8.314 [J/mol·K]
S_i^e	Local adsorption probability of gas species i	Dimensionless
S_i^0	Sticking coefficient	Dimensionless
$\dot{s}_{gas,k}$	Production rates of the species i by homogeneous reactions	[$mol/m^3 \cdot sec$]
$\dot{s}_{surface,k}$	Production rates of the species i by heterogeneous reactions	[$mol/m^2 \cdot sec$]

T	Temperature	[K]
V	Convection velocity	[m/sec]
V^D	Diffusion velocity	[m/sec]
X_i	Mole fraction of species i	Dimensionless
z	Valence of the charge carrier	Dimensionless

Greek Symbol	**Meaning**	**Common Units**
β_i	Cathodic charge transfer coefficient in reaction i	Dimensionless
γ_{CO}	Sticking probability of CO	Dimensionless
Γ	Surface site density	[mol/cm^2]
ε	Porosity	Dimensionless
$\varepsilon_{CO(s)}$	CO(s) coverage dependent activation energy	[kJ/mol]
$\eta_{a.a}$	Activation overpotential at the anode	[V]
$\eta_{a.c}$	Activation overpotential at the cathode	[V]
$\eta_{conc.a}$	Concentration overpotential at the anode	[V]
$\eta_{conc.c}$	Concentrattion overpotential at the cathode	[V]
η_{ohm}	Ohmic overpotential	[V]
θ_i	Coverage of species i	Dimensionless
μ^v	Viscosity	[kg·m/sec]
μ^v_{mix}	Mixture viscosity	[kg·m/sec]
v_i	Stoichiometric coefficient of species i	Dimensionless
$v_{i,k}$	Stoichiometric coefficient of the species k in reaction i	Dimensionless
v_v	Stoichiometric coefficient of vacancies	Dimensionless
ϕ	Electric potential	[V]

Subscript	**Meaning**
a	Activation or anode
b	Backward
c	Cathode
conc	Concentration
el	Electrolyte
eq	Equilibrium
f	Forward or faradaic
i,j,k	Species
ohm	Ohmic
rev	reversible
ss	Steady-state
s	Surface species

t	Total

Superscript	**Meaning**
e	Effective
0	Exchange current density

4.1. Introduction

One of the advantages of SOFCs is its fuel flexibility. It has been shown that SOFCs can run on various hydrocarbon (HC) fuels including methane [1,2], propane [3], butane [4], and iso-octane [5,6] as well as hydrogen. When a HC fuel is fed into a SOFC, it undergoes reforming to syngas because of the high operating temperature, typically >600C, the abundance of Ni catalyst in a typical Ni/YSZ anodes, and the presence of water or other products of the electrochemical reactions. When H_2 and CO reach the triple phase boundary between the metal, electrolyte, and the gas phase, they are electrochemically oxidized using oxygen ion transported through the electrolyte from the cathode. Because of the complex coupling of the multiphysics processes, including porous-media transport, thermochemical reforming reactions, and electrochemical reactions, Membrane-Electrode-Assembly (MEA) models should incorporate all of these processes to be useful for performance prediction.

Transport through the porous structure is usually modeled using the Dusty-Gas-Model (DGM), which is known to capture the physics of transport in this medium better than the Fick's law [7]. The reforming reactions are analyzed via either global reactions such as the water-gas-shift(WGS) reaction and methane reforming reactions [8], or through a fully detailed set of elementary reactions [9,10]. Among all the physical processes in the fuel cell, electrochemistry is the least understood. The most pronounced difference among MEA models is in the electrochemistry model. Besides H_2, it has been shown experimentally that CO can be electrochemically oxidized directly [11–13]. However, a reliable CO electrochemistry model has not been developed until recently, and as a result, previous MEA models often assumed that CO electrochemistry is negligible. The purpose of this chapter is to apply a detailed CO

electrochemistry model recently developed by our group, along with a previously developed detailed H_2 electrochemistry, to evaluate how it affects the overall performance of a SOFC operating on syngas. In Section II, previous MEA models for syngas fuel, especially regarding their electrochemistry models, are reviewed. In Section III, the physical processes such as transport, thermochemical reactions, and multiple electrochemical reactions, are formulated. In Section III the simulation procedures are described. Results are discussed in Section IV.

4.2. Literature Review

Because a detailed syngas electrochemistry mechanism is not yet available, there is no MEA model that incorporates detailed multiple reaction pathways via CO and H_2. Approaches taken by previous researchers can be classified as (1) no electrochemistry in the analysis [8], (2) a global reaction approach [14,15], (3) assuming that H_2 electrochemistry is dominant [10,16–20], or (4) O_2 electrochemistry models [21]. Each of these is discussed in some detail below.

4.2.1. No electrochemistry in the analysis

Gemmen and Tembly [8] presented a model for the transport of gases through the anode, as well as gas species reactions within the anode consisting of methane reforming and water-gas shift. They assumed that there are two electrochemistry pathways via CO and H_2 and the total current is assumed to be the sum of the two. However, they found that there is no consistency regarding the treatment of the combined CO and H_2 electrochemistry. For instance, Matsuzaki and Yasuda [22] suggested that the ratio of H_2:CO electrochemistry rates is 2:1, while Aguiar et al [23] chose to ignore CO electrochemistry altogether. For their analysis, Gemmen and Trembly [8] chose to assume that the current from H_2 electrochemistry is four times larger than that from

CO electrochemistry. For a given total current, the mole fluxes of H_2, H_2O, CO and CO_2 are then specified accordingly as boundary conditions for the chemically reacting flow analysis in the anode. Because there is no further consideration of the electrochemistry, the overall voltage was not analyzed, and only the transport and chemistry in the anode were investigated.

4.2.2. The global reaction approach

In the absence of detailed elementary reactions, the global reaction approach is usually taken. Vakouftsi et al [14] assumed a global reaction form for the charge-transfer reaction and derived an expression for the exchange current density using the reaction order based on the following global reaction:

$$H_2 + CO + 2O^{2-} \leftrightarrow H_2O + CO_2 + 4e^-$$

However, the global reaction rate cannot represent the case when either H_2 or CO is non-existent because the overall rate tends to be zero. In another study, Vakouftsi et al [15] assumed that H_2 and CO were electrochemically oxidized at the TPB according to the following individual global reactions,

$$H_2 + O^{2-} \leftrightarrow H_2O + 2e^-$$

$$CO + O^{2-} \leftrightarrow CO_2 + 2e^-$$

They applied a general Butler-Volmer equation to relate the current to the anodic activation overpotential. However, there was no dependency of the exchange current density on the concentrations of the reactants (H_2 and CO) or the products (H_2O and CO_2), which were assumed to be constant and obtained from another paper. Hence, the applicability of that approach is quite restricted. In principle, an expression for the exchange current density can be derived for each of the two electrochemical reactions to extend the applicability of the model.

However, this approach cannot reflect some unexpected subtle dependencies in the electrochemical reactions such as; (1) increasing p_{H_2O} strongly promotes the electrode kinetics [24,25], and (2) increasing p_{CO_2} also strongly enhances the electrode kinetics [26].

Because H_2O and CO_2 are reaction products, the Le Chatelier principle suggests that the reaction rate should decrease with increasing p_{H_2O} and p_{CO_2}. However, experimental observations indicate the reverse trend. Note that the Le Chatelier principle in this simple form is only true for a purely chemical system where reaction rates are indeed only influenced by concentration. In an electrochemical system, such as an SOFC electrode, reaction rates are additionally influenced by the electrode potential. A variation in gas-phase composition changes both the concentrations of the adsorbed intermediates participating in the charge-transfer reaction and the electrode potential. The combined variations in concentration and potential lead to the observed unexpected change [27]. These effects can only be captured by applying detailed elementary electrochemical reactions.

4.2.3. The H_2 electrochemistry dominant approach

Many researchers [10,16–20] assumed that H_2 is the only electrochemically active species and neglected the contribution of CO because (1) the rate at which CO is converted in the water-gas-shift reaction far exceeds the rate of electrochemical oxidation of CO [18,22], and (2) when both CO and H_2 are present in the system, H_2 appears to dominate over CO in the charge-transfer chemistry [11]. However, the water-gas-shift reaction can convert CO to H_2 only when there is sufficient H_2O. Depending on the types of fuels and the technologies of gasification or reforming, the composition of syngas varies widely. Generally, methane-derived syngas via

reforming is H_2-rich while coal-derived syngas via gasification is CO-rich. To illustrate this point, Table 4-1 shows syngas compositions from different gasifiers using two kinds of coal. In particular, syngas from the Shell dry-feed gasifier consists of a minimal amount of H_2O, thereby experiencing negligible water-gas-shift reaction. From the syngas, approximately three times the amount of CO as compared to H_2 will be found at the TPB.

Gasifier	Coal	Syngas compositions (vol%)								
		H_2	H_2O	CO	CO_2	CH_4	Ar	N_2	H_2S	COS
Texaco	Illinois 6	30.28	16.45	39.58	10.78	0.08	0.91	0.73	1.00	0.03
Shell	Illinois 6	26.74	2.01	63.05	1.49	0.03	1.1	4.08	1.3	0.14
	Texas lignite	27.57	3.2	60.63	2.77	0.03	1.03	4.34	0.32	0.04
Destec	Texas lignite	24.6	34.64	21.81	17.15	0.03	0.78	0.54	0.25	0.01

Table 4-1. Syngas compositions of typical entrained-flow coal gasifier [21]

When CO is the dominant species in the fuel composition, the assumption that H_2 electrochemistry is still dominant and CO electrochemistry can be safely neglected must be revisited. The extreme and obvious case is pure stream of CO, which would produce zero current under the usual assumption. Habibzadeh et al [28] supported the suggestion that CO electrochemistry should not be ignored in simulations of SOFCs when using syngas or coal-gas.

4.2.4. O_2 electrochemistry approach

Bieberle [29] proposed an oxygen spillover mechanism to describe H_2 electrochemistry. In this mechanism, oxygen in the YSZ bulk spills over to the Ni surface forming O adsorbate, O(Ni), while producing two electrons. The adsorbed oxygen reacts with H(Ni) producing

OH(Ni), which subsequently reacts with another H(Ni) generating H_2O(Ni). H(Ni) is involved only in the surface reaction, and not in the charge-transfer reactions. Because the charge-transfer reaction is independent of the fuel type, it can be applied not only to H_2 fuel , but also to CO and syngas.

Charge-transfer reaction

$$O_O^x + (Ni) \leftrightarrow O(Ni) + V_O^{\bullet\bullet} + 2e^-(Ni)$$

Adsorption/desorption

$$H_2(g) + 2(Ni) \leftrightarrow 2H(Ni)$$

$$H_2O(g) + (Ni) \leftrightarrow H_2O(Ni)$$

Surface reactions

$$O(Ni) + H(Ni) \leftrightarrow OH(Ni) + (Ni)$$

$$2OH(Ni) \leftrightarrow H_2O(Ni) + H(Ni)$$

$$H(Ni) + OH(Ni) \leftrightarrow H_2O(Ni) + (Ni)$$

Li et al [21] applied the Bieberle's mechanism in which the effects of H_2 and CO on the SOFC performance are reflected only through heterogeneous reactions. However, it is questionable whether the oxygen spillover mechanism can correctly capture even the H_2 electrochemistry. Vogler et al [30] compared seven possible H_2 electrochemical pathways including the oxygen spillover mechanism of Bieberle and a hydrogen spillover mechanism proposed by Goodwin [16,31]. After validating against the experimental anode data from Bieberle [25], only the hydrogen spillover mechanism by Goodwin yielded agreement with the complete experimental data set. Similarly, Goodwin et al. [32] compared model results using the

hydrogen spillover and the oxygen spillover mechanisms to the patterned anode experimental data from Mizusaki et al. [24] and reached the same conclusion, i.e., that the hydrogen spillover mechanism provides good quantitative representation of the measured polarization behavior over a wide range of gas-phase compositions and with both anode and cathode biases.

An MEA model that incorporates a detailed H_2 and CO electrochemistry mechanisms, which is validated against experimental results, is needed.

4.3. Formulation

In this section, the formulation of an MEA model is described in which the multiphysics processes including the transport through porous electrodes, thermochemical reactions, and H_2 and CO electrochemical reactions as well as the ionic transport through the electrolyte are included.

4.3.1. Conservation equations

Consider reactive porous-media transport in an electrode such as that illustrated in Figure 4-1.

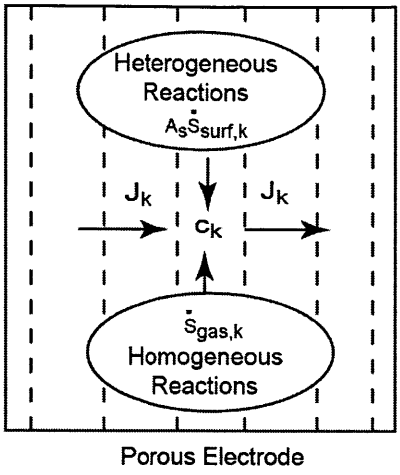

Figure 4-1 Mass conservation in the electrode

The conservation equation for the gas-phase species is

$$\varepsilon \frac{\partial c_k}{\partial t} = A_s \dot{s}_{surf,k} + \dot{s}_{gas,k} - \nabla \cdot J_k \quad (k = 1, \ldots, K_g) \tag{4.1}$$

where ε is the porosity, c_k is the concentration of gas species k [mol/m^3], J_k is the molar flux of species k [mol/m^2·sec], $\dot{s}_{surf,k}$ is the production rate of the gas species k on the surface by heterogeneous reactions [mol/m^2·sec], A_s is the specific catalyst area [1/m], $\dot{s}_{gas,k}$ is the production rate of the gas species k by homogenous reactions [mol/m^3·sec], and K_g is the total number of gas species. The molar fluxes are determined using the Dusty-Gas-Model (DGM). The production rates of the gas species are obtained from the thermo-chemistry model.

The surface species conservation equation is

$$\frac{\partial c_{surf,k}}{\partial t} = \dot{s}_{surf,k} \quad (k = 1, \ldots, K_s) \tag{4.2}$$

where $c_{surf,k}$ is the concentration of surface species k [mol/m^2], $\dot{s}_{surf,k}$ is the production rate of the surface species k by heterogeneous reactions [mol/m^2·sec], and K_s is the total number

of surface species.

Unlike the gaseous species, the surface species are effectively immobile on length scales larger than an individual catalyst particle. Hence, the surface species transport over macroscopic distance is assumed negligible [33].

4.3.2. Transport in porous media

The flux J_k is computed using the Dusty-Gas-Model (DGM) [34], which is a straight-forward application of the Stefan-Maxwell diffusion equations, where the solid phase is represented using giant immobile molecules ('dust') uniformly distributed in space. It is generally agreed that the DGM is a convenient approach to modeling combined bulk and Knudsen diffusion. Moreover, the DGM can explain physical phenomena which cannot be explained by the Fick's model, such as osmotic diffusion (diffusion that occurs in the absence of the concentration gradient), reverse diffusion (diffusion that occurs counter to the concentration gradient), and diffusion barrier (there is no flux when there is a large concentration gradient) [7].

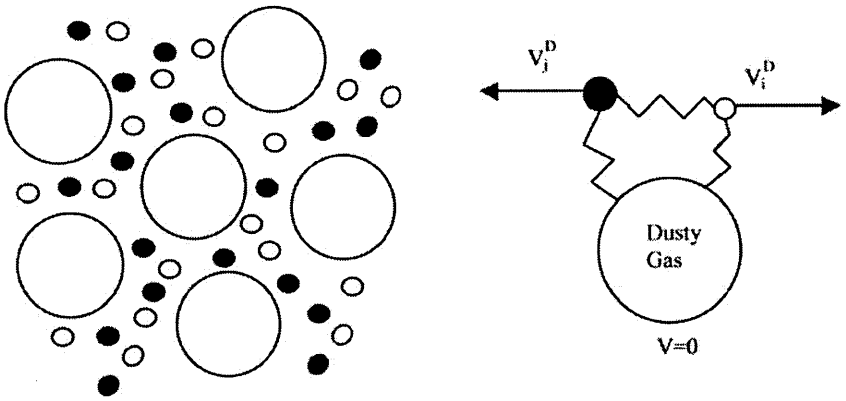

Figure 4-2 Dusty Gas Model

The DGM can be written as an implicit relationship among the molar concentratinos, molar fluxes, concentration gradients, and the pressure gradient

$$-\nabla c_i = \sum_{j(\neq i)} \frac{1}{c_t D_{ij}^e}(c_j J_i - c_i J_j) + \frac{J_i}{D_{iM}^e} + \frac{B_0}{\mu_{mix}^v}\frac{c_i}{D_{iM}^e}\nabla p \qquad (4.3)$$

where $c_t = \frac{p}{RT}$ is total molar concentration [mol/m^3], D_{ij}^e is the effective binary diffusion coefficient in the porous medium [m^2/sec], μ_{mix}^v is the mixture viscosity [kg·m/sec], B_o is the permeability [m^2], and p is the pressure [Pa], and D_{iM}^e is the effective Knudsen diffusion coefficient [m^2/sec].

The transport of gaseous species through porous electrodes is affected by the microstructure of the electrodes, particularly, the porosity (ε), permeability (B_0), pore size, and tortuosity factor.

4.3.3. Thermochemistry

Because of the relatively high operating temperatures and the presence of catalytic surfaces in the anode structure, various thermochemical reactions occur within the anode, such as steam reforming, water-gas shift, partial oxidation, and carbon formation. A substantial impediment to the direct use of hydrocarbon fuels in SOFCs is carbon formation in the anodes [35–38]. Thermo-chemistry has usually been handled using significant simplifying assumptions, such as local equilibration of reforming and water-gas-shift chemistry [13,39], or global reaction kinetics [40]. Recently, detailed kinetics models based on the knowledge of the elementary reactions have been established and validated over a wide range of conditions [9,10]. Because nickel is the most common anode metal, being a cost-effective catalyst, the reactions of methane on *Ni* have been extensively studied.

- Homogeneous thermo-chemistry

Gas-phase chemistry in the anode may be neglected because the heterogeneous thermo-chemical reactions are considerably faster than homogeneous thermo-chemistry and the probability for gas-gas collisions is low when the pore spaces are comparable to the mean free-path length [16]. Under this assumption,

$$\dot{s}_{gas,k} = 0 \qquad (k = 1, \ldots, K_g) \tag{4.4}$$

- Heterogeneous thermo-chemistry

The surface mechanism for methane reforming and oxidation over nickel is detailed by Hecht et al [9], which was evaluated only at 800°C. This mechanism is extended by Janardhanan and Deutschmann [10] and evaluated for temperatures between 200 and 1700°C. The reaction mechanism (shown in Table 4-2) consists of 6 pairs for adsorption/ desorption of 6 gas species, and 15 pairs of forward and backward surface reactions among 12 adsorbed species. In total, there are 42 reactions. The use of microkinetic mechanisms for reforming and/or catalytic partial oxidation, given the difficulty of obtaining accurate thermodynamic data for surface species, has a potential problem that the individual reactions might not satisfy microscopic reversibility. Moreover, the predicted gas-phase concentrations might not be consistent with the equilibrium values. To avoid this problem, the kinetics data of the backward reactions are calculated from thermodynamics using mass-action kinetics.

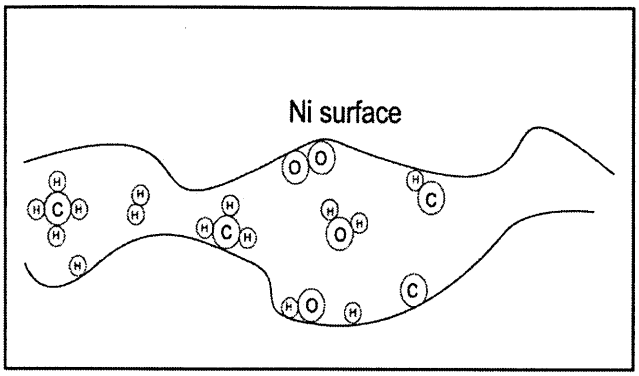

Figure 4-3 The Schematics of Elementary Heterogeneous Chemistry

The net production rate of any gas or surface species k on the surface by heterogeneous reactions is given by

$$\dot{s}_{surf,k} = \sum_i R_{surf,i} v_{i,k} \tag{4.5}$$

where $R_{surf,i}$ is the rate of heterogeneous reaction i $[mol/(m^2\,\mathrm{sec})]$ and $v_{i,k}$ is the stoichiometric coefficient of the species k in reaction i, which is positive for products and negative for reactants.

For the adsorption reactions (reactions 1, 3, 5, 7, 9 and 11 in Table 4-2), the reaction rate can be computed using the kinetic theory of gases by [41]

$$R_{surf,k} = S_i^e \sqrt{\frac{\Re T}{2\pi M_i}} c_i \quad (\mathrm{k} = 1, 3, 5, 7, 9 \text{ and } 11) \tag{4.6}$$

where S_i^e is a local adsorption probability of gas species i.

This equation assumes a Boltzmann distribution of molecular velocities near the surface.

The local adsorption probability is defined as [41]

$$S_i^e = S_i^0 \theta_v^{\nu_v} \tag{4.7}$$

where S_i^0 is a sticking coefficient, which determines the probability that a particle hitting the surface is adsorbed, θ_v is the vacancy coverage, and v_v is the stoichiometric coefficient of vacancies.

For the desorption and surface reactions between surface species, where only surface species are involved, the reaction rates can be expressed using mass-action kinetics as

$$R_{surf,k} = k_k(T)\prod_{react} c_{surf,i}^{v_i} \tag{4.8}$$

where k_i is the reaction rate constant of the reaction i.

The reaction rate constants are represented in the Arrhenius form

$$k = AT^n \exp\left(-\frac{E_a}{\Re T}\right) \tag{4.9}$$

where A is a pre-exponential factor and E_a is the activation energy.

In principle, the activation energy can vary with coverage because of multiple binding states and attractive and repulsive lateral interactions between adsorbed particles. The activation energy for desorption usually decreases with increasing the coverage because a repulsive adsorbate-adsorbate interaction results in the weakening of the bonding of the molecules to the surface [42,43]. Adsorption of CO on a metal shows a delicate interplay between the repulsive inter-adsorbate forces and structural changes within the adsorbed layer. This interplay results in modifications in the CO-substrate bonding strength and geometry. Therefore, the activation energy dependency on CO coverage is included in the reactions of 12, 20, 21 and 23. The net activation energies depend on the adsorbed CO(s) coverage, $\theta_{CO(s)}$, in the form

$$k = AT^n \exp\left(-\frac{E_a}{\Re T}\right)\exp\left(-\frac{\varepsilon_{CO(s)}\theta_{CO(s)}}{\Re T}\right) \tag{4.10}$$

in which $\varepsilon_{CO(s)}$ is the CO*(s)* coverage-dependent activation energy.

Table 4-2 Detailed heterogeneous elementary chemical reactions for CH_4 reforming on Ni by Janardhanan and Deutschmann [10]

	Reaction	A^a	n	E_a
	Adsorption/Desorption			
1	$H_2+(Ni)+(Ni)\rightarrow H(Ni)+H(Ni)$	1.000×10^{-02b}	0.0	0.00
2	$H(Ni)+H(Ni)\rightarrow H_2+(Ni)+(Ni)$	$2.545\times10^{+19}$	0.0	81.21
3	$O_2+(Ni)+(Ni)\rightarrow O(Ni)+O(Ni)$	1.000×10^{-02b}	0.0	0.00
4	$O(Ni)+O(Ni)\rightarrow O_2+(Ni)+(Ni)$	$4.283\times10^{+23}$	0.0	474.95
5	$CH_4+(Ni)\rightarrow CH_4(Ni)$	8.000×10^{-03b}	0.0	0.00
6	$CH_4(Ni)\rightarrow CH_4+(Ni)$	$8.705\times10^{+15}$	0.0	37.55
7	$H_2O+(Ni)\rightarrow H_2O\ (Ni)$	1.000×10^{-01b}	0.0	0.00
8	$H_2O\ (Ni)\rightarrow H_2O+(Ni)$	$3.732\times10^{+12}$	0.0	60.79
9	$CO_2+(Ni)\rightarrow CO_2\ (Ni)$	1.000×10^{-05b}	0.0	0.00
10	$CO_2\ (Ni)\rightarrow CO_2+(Ni)$	$6.447\times10^{+07}$	0.0	25.98
11	$CO+(Ni)\rightarrow CO\ (Ni)$	5.000×10^{-01b}	0.0	0.00
12	$CO\ (Ni)\rightarrow CO+(Ni)$	$3.563\times10^{+11}$	0.0	111.27
		$\varepsilon_{CO(s)}$		-50.0_c
	Surface reactions			
13	$O(Ni)+H(Ni)\rightarrow OH(Ni)+(Ni)$	$5.000\times10^{+22}$	0.0	97.9
14	$OH(Ni)+(Ni)\rightarrow O(Ni)+H(Ni)$	$1.781\times10^{+21}$	0.0	36.09
15	$OH(Ni)+H(Ni)\rightarrow H_2O\ (Ni)+(Ni)$	$3.000\times10^{+20}$	0.0	42.7
16	$H_2O\ (Ni)+(Ni)\rightarrow OH(Ni)+H(Ni)$	$2.271\times10^{+21}$	0.0	91.76
17	$OH(Ni)+OH(Ni)\rightarrow H_2O\ (Ni)+O(Ni)$	$3.000\times10^{+21}$	0.0	100.0
18	$H_2O(Ni)+O(Ni)\rightarrow OH(Ni)+OH(Ni)$	$6.373\times10^{+23}$	0.0	210.86
19	$O(Ni)+C(Ni)\rightarrow CO(Ni)+(Ni)$	$5.200\times10^{+23}$	0.0	148.1
20	$CO(Ni)+(Ni)\rightarrow O(Ni)+C(Ni)$	$1.354\times10^{+22}$	− 3.0	116.12
		$\varepsilon_{CO(s)}$		-50.0_c
21	$O(Ni)+CO(Ni)\rightarrow CO_2(Ni)+(Ni)$	$2.000\times10^{+19}$	0.0	123.6
		$\varepsilon_{CO(s)}$		-50.0_c
22	$CO_2(Ni)+(Ni)\rightarrow O(Ni)+CO(Ni)$	$4.653\times10^{+23}$	− 1.0	89.32
23	$HCO(Ni)+(Ni)\rightarrow CO(Ni)+H(Ni)$	$3.700\times10^{+21}$	0.0	0.0
		$\varepsilon_{CO(s)}$		50.0_c
24	$CO(Ni)+H(Ni)\rightarrow HCO(Ni)+(Ni)$	$4.019\times10^{+20}$	− 1.0	132.23
25	$HCO(Ni)+(Ni)\rightarrow O(Ni)+CH(Ni)$	$3.700\times10^{+24}$	− 3.0	95.8
26	$O(Ni)+CH(Ni)\rightarrow HCO(Ni)+(Ni)$	$4.604\times10^{+20}$	0.0	109.97
27	$CH_4(Ni)+(Ni)\rightarrow CH_3(Ni)+H(Ni)$	$3.700\times10^{+21}$	0.0	57.7
28	$CH_3(Ni)+H(Ni)\rightarrow CH_4(Ni)+(Ni)$	$6.034\times10^{+21}$	0.0	61.58
29	$CH_3(Ni)+(Ni)\rightarrow CH_2(Ni)+H(Ni)$	$3.700\times10^{+24}$	0.0	100.0
30	$CH_2(Ni)+H(Ni)\rightarrow CH_3(Ni)+(Ni)$	$1.293\times10^{+22}$	0.0	55.33
31	$CH_2(Ni)+(Ni)\rightarrow CH(Ni)+H(Ni)$	$3.700\times10^{+24}$	0.0	97.1
32	$CH(Ni)+H(Ni)\rightarrow CH_2(Ni)+(Ni)$	$4.089\times10^{+24}$	0.0	79.18
33	$CH(Ni)+(Ni)\rightarrow C(Ni)+H(Ni)$	$3.700\times10^{+21}$	0.0	18.8

34	$C(Ni)+H(Ni) \rightarrow CH(Ni)+(Ni)$	$4.562\times10^{+22}$	0.0	161.11	
35	$O(Ni)+CH_4(Ni) \rightarrow CH_3(Ni)+OH(Ni)$	$1.700\times10^{+24}$	0.0	88.3	
36	$CH_3(Ni)+OH(Ni) \rightarrow O(Ni)+CH_4(Ni)$	$9.876\times10^{+22}$	0.0	30.37	
37	$O(Ni)+CH_3(Ni) \rightarrow CH_2(Ni)+OH(Ni)$	$3.700\times10^{+24}$	0.0		130.1
38	$CH_2(Ni)+OH(Ni) \rightarrow O(Ni)+CH_3(Ni)$	$4.607\times10^{+21}$	0.0		23.62
39	$O(Ni)+CH_2(Ni) \rightarrow CH(Ni)+OH(Ni)$	$3.700\times10^{+24}$	0.0		126.8
40	$CH(Ni)+OH(Ni) \rightarrow O(Ni)+CH_2(Ni)$	$1.457\times10^{+23}$	0.0		47.07
41	$O(Ni)+CH(Ni) \rightarrow C(Ni)+OH(Ni)$	$3.700\times10^{+21}$	0.0		48.1
42	$C(Ni)+OH(Ni) \rightarrow O(Ni)+CH(Ni)$	$1.625\times10^{+21}$	0.0		128.61

a The units of A are given in terms of moles, centimeters, and seconds. E is kJ/mol.
b Sticking coefficient.
c Coverage-dependent activation energy.
Total available surface site density is $\Gamma = 2.60\times10^{-9} mol/cm^2$

Because the reaction mechanism is based on elementary molecular processes, it represents all the global processes in a SOFC anode, including

(i) Steam reforming of methane

$$CH_4 + H_2O \leftrightarrow CO + 3H_2$$

(ii) Water-gas-shift processes

$$H_2O + CO \leftrightarrow H_2 + CO_2$$

(iii) Oxidation of methane

$$CH_4 + 2O_2 \leftrightarrow CO_2 + 2H_2O$$

However, the mechanisms for carbon formation and bulk phase nickel oxidation are not specified. Thus, the examples discussed in this chapter use operating conditions where coking and NiO formation are not primary concerns.

4.3.4. Electrochemistry

Because the electrodes are electronic conductors and the electrolyte is an ionic conductor, the charge cannot cross directly between the electrode and the electrolyte. Rather, an electrochemical charge-transfer reaction is needed. Since the electrodes and the electrolyte all have free-charge carriers, each one is, to a good approximation, internally charge-neutral, with any excess charge being distributed on its surface. The interface behaves as a capacitor, with excess charge on one side and equal but opposite charge on the other side. The very thin (nanometer scale) region at the interface where the charge is stored is called the electric double layer. The electric potential varies sharply across the double layer. As the electrons cross the double layer, the charge-transfer reactions must overcome the potential difference across the double layer. The difference between the equilibrium and non-equilibrium potential changes across the double layer is defined as an activation overpotential.

Charge-transfer processes are among the least understood aspects of fuel-cell chemistry. To calculate the activation overpotential, an experimental approach was explored using the concept of an effective charge-transfer resistance, which is defined in terms of micro-structural parameters of the electrode, the intrinsic charge-transfer resistance, the ionic conductivity of the electrolyte, and the electrode thickness [44]. As an alternative analytical approach, a single global charge-transfer reaction was often used to describe the electrochemical kinetics, leading to the Butler-Volmer equation [45–47]. Since these two approaches are semi-empirical, there have been some efforts to develop a detailed charge-transfer kinetics in terms of elementary reaction steps, in a manner that resembles the treatment of heterogeneous thermo-chemistry.

4.3.4.1. H_2 Electrochemistry

The state-of-the-art approach is to apply a model that includes all elementary reactions. However, a clear understanding of the electrode kinetics does not yet exist. According to the literature, for example, adsorption/desorption, surface diffusion, hydroxyl formation, and charge-transfer are feasible rate-limiting reaction steps in the anode of an SOFC. Furthermore, it is not even evident whether the chemical and electrochemical reactions take place only on the surfaces of the *Ni* and the YSZ, or whether the bulk material is also active.

Zhu et. al. [16] applied a detailed H_2 electrochemistry model and obtained a Butler-Volmer formalism by assuming one of the steps to be rate-limiting. This approach provides qualitative information regarding the important functional dependencies such as the reaction order in the exchange current density, and enables comparison with experimental results that have been interpreted using parameters in the Butler-Volmer equation.

In developing an expression for the anode activation overpotential in the Butler-Volmer form, it is useful to begin by considering the elementary steps by which hydrogen is electrochemically oxidized. Global electrochemical oxidation of hydrogen can be written in Kroger-Vink notation as [48]

$$H_2(g) + O_O^x(el) \leftrightarrow H_2O(g) + V_O^{\cdot\cdot}(el) + 2e^-(a)$$

where (g) means gas phase, e^- (a) is an electron on the anode, and the species in the electrolyte follow the Kröger-Vink notation in which the subscript describes the relevant lattice site and the superscript describes the charge. For example, $V_O^{\cdot\cdot}$ is the vacancy on the oxygen site, hence the charge is positive 2 relative to the oxygen site, which should have negative 2 ions. This electrochemical reaction involves species in the gas, electrolyte, and anode (metal) phases.

A modified mechanism that includes five elementary reactions is assumed here. The mechanism is similar to the one used by De Boer [49] and the same as that appearing in Zhu et al. [16] and Lee and Ghoniem [50]. In this five-step mechanism, hydrogen is adsorbed only on the nickel surface *(Ni)* and other surface species reside on the electrolyte surface. Other than the adsorbed atomic hydrogen, *H(Ni)*, the Ni surface contains empty surface sites, *(Ni)*, and electrons within the Ni anode, $e^-(Ni)$. Within the YSZ electrolyte, there is a lattice oxygen, O_O^x(YSZ), and oxygen vacancies, $V_O^{\cdot\cdot}$(YSZ). On the YSZ surface there are three species, $OH^-(YSZ)$, $H_2O(YSZ)$, $O^{2-}(YSZ)$, and empty sites *(YSZ)*.

- Adsorption on the Ni surface

$$H_2(g)+2(Ni)\Leftrightarrow 2H(Ni) \tag{H. 1}$$

- Charge-transfer reactions at the TPB region

$$H(Ni)+O^{2-}(YSZ)\Leftrightarrow (Ni)+OH^-(YSZ)+e^-(Ni) \tag{H. 2}$$

$$H(Ni)+OH^-(YSZ)\Leftrightarrow (Ni)+H_2O(YSZ)+e^-(Ni) \tag{H. 3}$$

- Adsorption/desorption on the YSZ surface

$$H_2O(YSZ)\Leftrightarrow H_2O(g)+(YSZ) \tag{H. 4}$$

- Transfer of oxygen ion between the surface and the bulk YSZ

$$O_o^X(YSZ)+(YSZ)\Leftrightarrow O^{2-}(YSZ)+V_O^{\cdot\cdot}(YSZ) \tag{H. 5}$$

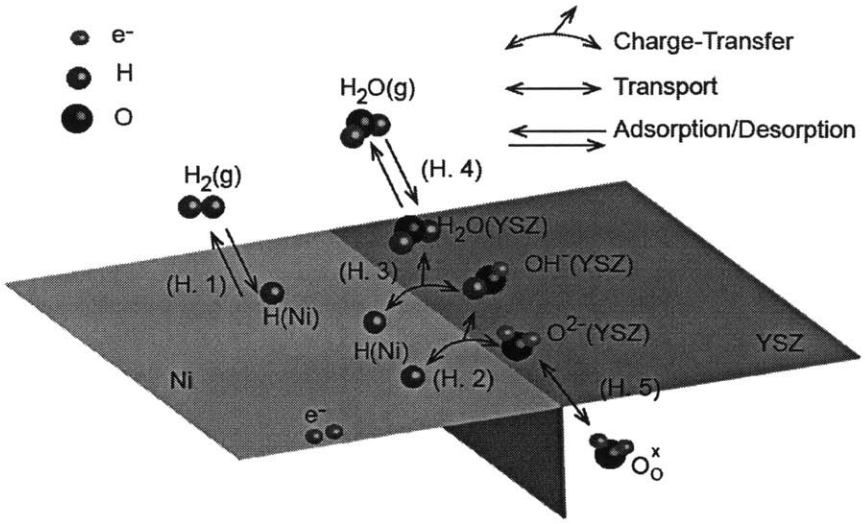

Figure 4-4. A schematic diagram of the H_2 electrochemical oxdiation mechanism

The residence time of adsorbed hydrogen is several nanoseconds and the corresponding diffusion length is several nanometers [51,52]. Therefore, it is reasonable to assume that surface diffusion of hydrogen is not important.

The surface species are related through reaction rate equations of the five steps (H. 1) to (H. 5). With the assumption that one reaction is rate-limiting, a relatively simple analytical expression between the activation overpotential and the current density can be derived from the forward and backward reaction rates of the rate-limiting reaction and the equilibrium constants of other reactions [50]. The analytical expression is cast into a general Butler-Volmer equation as

$$i_{H_2} = i_0 \left[\exp\left(\beta_a \frac{F\eta_{a,a}}{\Re T} \right) - \exp\left(-\beta_c \frac{F\eta_{a,a}}{\Re T} \right) \right] \tag{4.11}$$

where i_0 is the exchange current density [A/cm^2], β_a and β_c are the anodic and cathodic charge-transfer coefficients, and F is the Faraday constant.

Based on this type of analysis, the derived exchange current densities and charge-transfer

coefficients for different rate-limiting assumptions are summarized in Table 4-3. Note the expressions for the exchange current density and their dependence on the partial pressure of reactants and products as well as the charge-transfer coefficients.

Table 4-3 Butler-Volmer Form for Each Rate-limiting Reaction

Rate-limiting reaction	Exchange Current density	Anodic charge transfer coefficient	Cathodic charge transfer coefficient
1	$i_0 = i^*_{H_2}(p_{H_2})$	0	2
2	$i_0 = i^*_{H_2} \frac{p_{H_2O}^{1/4}\left(K_1 p_{H_2}\right)^{1/4}}{\left(1+\left(K_1 p_{H_2}\right)^{1/2}\right)}$	0.5	1.5
3	$i_0 = i^*_{H_2} \frac{(K_1 p_{H_2})^{1/4}(p_{H_2O})^{3/4}}{1+(K_1 p_{H_2})^{1/2}}$	1.5	0.5
4	$i_0 = i^*_{H_2}(p_{H_2O})$	2	0

4.3.4.2. CO Electrochemistry

The overall oxidation reaction for CO can be written in the form

$$CO(g) + O^{2-}(YSZ) \leftrightarrow CO_2(g) + 2e^-(Ni)$$

There are three species associated with this reaction: gaseous CO and CO_2, and oxygen ions O^{2-} that are generally assumed to exist in the bulk lattice of the electrolyte (in Kröger-Vink notation, this will be written as O_O^x having neutral charge because oxygen ion is sitting in its site).

A mechanism that includes three elementary reactions in the Ni-YSZ TPB region is proposed, fitted, and validated in the second part of this thesis, "Analysis of multi-step CO electrochemistry on Ni pattern anode of SOFCs". The reactions are:

1. Adsorption/desorption on the Ni surface

$$CO(g) + V(Ni) \leftrightarrow CO(Ni) \qquad \text{(CO. 1)}$$

2. Charge-transfer reactions at the TPB

$$O_O^x(YSZ) + (YSZ) \leftrightarrow O^-(YSZ) + V_O^{\bullet\bullet}(YSZ) + e^-(Ni) \quad \text{(CO. 2)}$$

$$O^-(YSZ) + CO(Ni) \leftrightarrow CO_2 + (YSZ) + (Ni) + e^-(Ni) \quad \text{(CO. 3)}$$

On the Ni anode surface, CO(Ni) is an adsorbed CO molecule, (Ni) is an empty surface site, and e-(Ni) is an electron within the Ni anode. Within the YSZ electrolyte, $O_O^x(YSZ)$ is a lattice oxygen and $V_O^{\bullet\bullet}(YSZ)$ is an oxygen vacancy. It is often reasonable to assume that the concentrations of $V_O^{\bullet\bullet}(YSZ)$ and $O_O^x(YSZ)$ in the bulk of the electrolyte are constant and mainly determined by the doping level [53]. On the YSZ surface there is a single species, O^- (YSZ), and empty sites (YSZ).

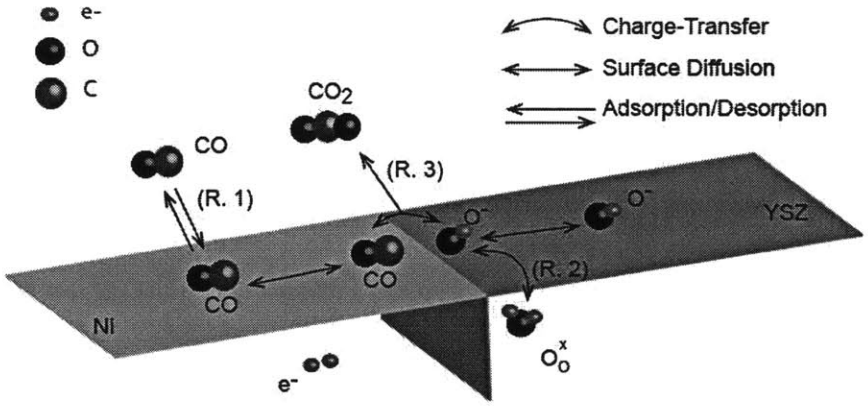

Figure 4-5. A schematic diagram of CO electrochemical oxidation at the TPB

The three step reaction mechanism is composed of two charge-transfer reactions (i.e., CO. 2 and CO. 3) and one heterogeneous chemical reaction (i.e., CO. 1). The three reaction steps involve two surface species, CO(Ni) and O^-(YSZ), and two gas-phase species. This is the first two-step charge transfer mechanism in which CO directly participates in the reaction. The only

other two-step charge transfer mechanism was proposed recently by Yurkiv et al. [54] , which is based on an oxygen spillover mechanism where CO is involved only through thermochemical reactions. Surface diffusion of adsorbed CO(Ni) and O^-(YSZ) are considered along the Ni and YSZ surface, respectively.

The expressions for currents from (CO. 2) and (CO. 3) can be formulated using Butler-Volmer equations as follows

$$i_2 = Fl_{TPB}\left\{k_{2,f}\left(1-\theta_{O^-}\right)\exp\left(\frac{\left(1-\beta_2\right)FE}{RT}\right)-k_{2,b}\theta_{O^-}\exp\left(\frac{-\beta_2 FE}{RT}\right)\right\} \quad (4.12)$$

$$i_3 = Fl_{TPB}\left\{k_{3,f}\theta_{O^-}\theta_{CO}\exp\left(\frac{\left(1-\beta_3\right)FE}{RT}\right)-k_{3,b}\left(1-\theta_{O^-}\right)\left(1-\theta_{CO}\right)p_{CO_2}\exp\left(\frac{-\beta_3 FE}{RT}\right)\right\} \quad (4.13)$$

where E is the electric potential difference $E=\phi_a-\phi_{e,a}$ across the anode-electrolyte double layer. The ϕ_a is the electric potential in the metal anode, and $\phi_{e,a}$ is the electric potential in the electrolyte immediately outside the double layer in the anode side. The physical anode potential has a single value, independent of how many charge-transfer pathways are operative [32]. β_i is a cathodic charge transfer coefficient of the charge-transfer reaction (CO. i). $k_{i,f}$ and $k_{i,b}$ are the forward and backward reaction rate constants of the charge-transfer reaction (CO. i). The charge-transfer reactions depend only on the concentrations of CO and O^- at the TPB where the reactions occur. θ_{CO} and θ_{O^-} in electrochemistry kinetics refer to the surface coverage at the TPB.

The total current is the sum of the two currents from (CO. 2) and (CO. 3) as

$$i_{CO} = i_2 + i_3 \quad (4.14)$$

At steady-state, the current from (CO. 2) and (CO. 3) should be same

$$i_2 = i_3 \tag{4.15}$$

The surface coverage of CO at the TPB, θ_{CO}, in a steady state is computed as

$$\theta_{CO} = \theta_{CO}(0) = \frac{N}{M^2} - \frac{i_3}{D_{CO}\Gamma_{Ni}FL_{TPB}M\tanh(ML_{Ni})} \tag{4.16}$$

where $M^2 = \frac{k_{1,f}p_{CO} + \Gamma_{Ni}k_{1,b}}{\Gamma_{Ni}D_{CO}}$ and $N = \frac{k_{1,f}p_{CO}}{\Gamma_{Ni}D_{CO}}$. The surface site density Γ_{Ni} (mol/cm^2) and surface diffusion coefficient D_{CO} (cm^2/s) are assumed constant. The forward and reverse rate constants $k_{1,f}$ and $k_{1,b}$ of reaction (R. 1) are associated with the adsorption and desorption of CO on nickel. The partial pressure of gaseous CO appears as p_{CO}. L_{Ni} is the distance between the TPB lines adjacent to each other along the Ni surface.

Given the anode activation overpotential, $E = E_{eq} + \eta_{a,a}$. The corresponding steady-state $\theta_{O^-}, \theta_{CO}$, i_2, and i_3 are calculated from two Butler-Volmer Equations (4.12) and (4.13), and Equations (4.15) and (4.16).

4.3.4.3. O_2 elecrochemistry

The overall oxygen reduction and incorporation at the electrode-electrolyte interface can be written as

$$\frac{1}{2}O_2(g) + V_O^{\cdot\cdot}(el) + 2e^-(c) \leftrightarrow O_O^{\times}(el)$$

where $V_O^{\cdot\cdot}(el)$ and $O_O^{\times}(el)$ denote the oxygen vacancies and lattice oxygen ions in the bulk of the electrolyte and $e^-(c)$ are the electrons within the cathode. As with oxidation at the anode,

the global reaction may be the result of several elementary steps.

Here, it is often assumed that oxygen reduction proceeds in two steps [16].

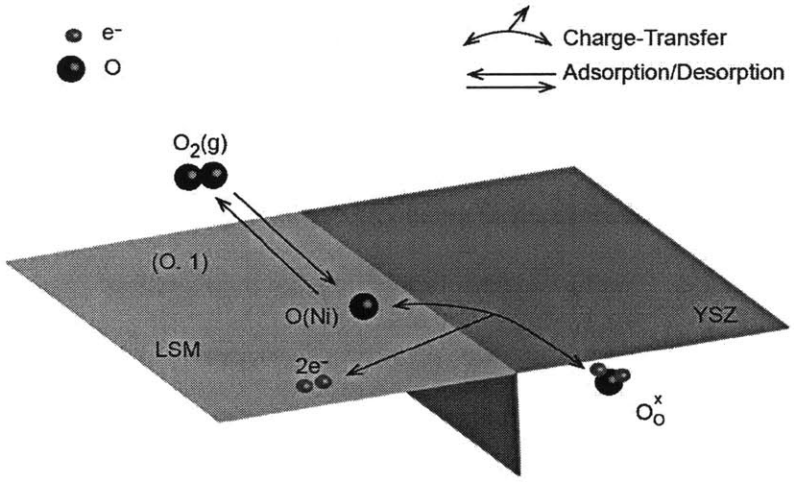

Figure 4-6. A schematic diagram of O_2 electrochemical reduction mechanism

- Adsorption/Desorption

$$O_2(g) + 2(c) \Leftrightarrow 2O_{ad}(c) \tag{6}$$

- Charge-transfer and incorporation at the TPB

$$O_{ad}(c) + V_o^{\bullet\bullet}(el) + 2e^-(c) \Leftrightarrow O_o^X(el) + (c) \tag{7}$$

In these reactions $O_{ad}(c)$ is adsorbed atomic oxygen on the cathode surface and (c) is an unoccupied cathode surface site.

The current density is determined by the charge-transfer reaction (7) and can be expressed using the electric potential difference between cathode and electrolyte, $\varepsilon_c[V]$, as follows

$$i_{O_2} = i_0 \left(\exp\left(\frac{F\eta_{a,c}}{2\Re T} \right) - \exp\left(-\frac{F\eta_{a,c}}{2\Re T} \right) \right) \tag{4.17}$$

where the exchange current density can be expressed as

$$i_0 = i_{O_2}^* \frac{\left(\frac{p_{O_2}}{K_6} \right)^{1/4}}{1 + \left(\frac{p_{O_2}}{K_6} \right)^{1/2}} \tag{4.18}$$

For an LSM-YSZ interface, K_6 can be represented in Arrhenius form as [55]

$$K_6 = A_{O_2} \exp\left(\frac{E_{O_2}}{\Re T} \right) \tag{4.19}$$

in which $A_{O_2} = 4.9 \times 10^8 \, atm$ and $E_{O_2} = 200 \, kJ / mol$.

Note that all the H_2, CO and O_2 electrochemistry models are developed based on the assumption that there is only single species on Ni or YSZ, namely, H(Ni), CO(Ni) or O(YSZ), respectively. The only necessary information for i-V relationship in the electrochemistry model is the gas species concentration at the TPB. On other hand, the CH_4 reforming reactions on Ni are developed based on 12 surface species on Ni. Therefore, only the gas species concentrations computed through the analysis of chemically reacting flow through porous electrode are coupled with the electrochemistry model.

4.4. Simulation Procedures

Where there is a single charge-transfer pathway, either a current density or an activation overpotential can be used as ia input parameter. In our previous MEA model [50], a current density was given as an input variable because the given current density can be directly utilized

as a boundary condition in the porous transport governing equations. When there are multiple charge-transfer pathways through H_2 and CO, the anode interface potential is a physical variable common to the multiple charge-transfer reactions and the current densities from H_2 and CO charge-transfer reactions are different and should be determined according to their electrochemistry model. Hence, in this model, the anode activation overpotential, $\eta_{a,a}$, is given as an input and the model is used to determine the cell voltage and total current. The total current density is the sum of the current densities from the two charge-transfer reactions:

$$i_{total} = i_{CO} + i_{H_2} \tag{4.20}$$

The cell potential can be expressed as the difference between the equilibrium potential E_{rev} and the sum of all the relevant overpotentials, which depend on the current density.

$$E_{cell} = E_{rev} - \eta_{conc,a} - \eta_{a,a} - \eta_{ohm} - \eta_{conc,c} - \eta_{a,c} \tag{4.21}$$

where $\eta_{conc,a}$ and $\eta_{conc,c}$ are the concentration overpotentials at the anode and cathode, respectively, η_{ohm} is the ohmic overpotential, and $\eta_{a,a}$ and $\eta_{a,c}$ are the activation overpotentail at the anode and the cathode, respectively.

The solution procedure follows several steps as outlined below:

(1) Calculate the equilibrium (reversible) potential

The equilibrium potential is computed either (1) using a global reaction based on assumed half-cell reactions at the anode and the cathode, or (2) using oxygen partial pressures at the anode and the cathode considering the fuel cell an oxygen concentration cell. If the gas species in the anode reach equilibrium, the results should be same either way regardless of the assumed half-cell reactions. It is assumed that the gas species in the anode are at equilibrium at

the open circuit voltage. The equilibrium potential is computed using the oxygen partial pressures at the anode and cathode as

$$E_{rev} = \frac{\Re T}{4F} \ln\left(\frac{p_{O_{2,c}}}{p_{O_{2,a}}}\right) \tag{4.22}$$

where $p_{O_{2,c}}$ and $p_{O_{2,a}}$ are the equilibrium oxygen partial pressures at the anode and cathode, respectively.

We used our in-house code [56] developed for multi-phase equilibrium calculation based on the Villar-Cruise-Smith method, adopted in both CHEMKIN and Cantera, for calculating the equilibrium concentrations of gas species.

(2) Calculate current densities from the electrochemistry models and determine the flux boundary conditions of species involved in each model for the transport governing equations through the porous electrodes.

For the given anode activation overpotential, i_{CO}, i_{H_2}, and i_{O_2} are computed from each electrochemical model. The boundary conditions for the reactants and the products in each electrochemistry model are determined depending on the number of electrons involved as

$$J_k = \nu_k \frac{i}{zF} \tag{4.23}$$

where ν_k is the stoichiometric coefficients in the electrochemical mechanism, z is the number of electrons involved in the mechanism, and F is the Faraday number.

For H_2 oxidation, the coefficients $\nu_{H_2} = 1$ and $\nu_{H_2O} = -1$, and z=2 according to the reaction $H_2 + O^{2-} \leftrightarrow H_2O + 2e^-$ and the current density is obtained from Equation (4.11). Similarly, for CO oxidation, $\nu_{CO} = 1$ and $\nu_{CO_2} = -1$, and z=2 according to the reaction,

$CO + O^{2-} \leftrightarrow CO_2 + 2e^-$ and the current density is obtained from Equations (4.12) and.(4.13) For the oxygen reduction reaction in the cathode, $\nu_{O_2} = 1$ and z=4 according to the reaction, $O_2 + 4e^- \leftrightarrow 2O^{2-}$ and the current density is obtained from Equation (4.17). In each, the species partial pressures are needed to evaluate the current densities at each time step. So, the flux boundary conditions are imposed function values.

(3) Calculate the concentration overpotentials

As a current density develops, the concentrations at the channel and at the TPB become different from each other. At this non-zero current, the reversible cell voltage needs to be adjusted using the concentrations of the species at the TPB that are actually participating in the electrochemical reactions. The reduction of the reversible cell voltage because of the transport and thermo-chemical reactions is defined as the concentration overpotential. The concentrations at the TPB are computed as follows.

The molar flux, J_k, are calculated using the concentrations at each time step from the DGM

$$-\nabla c_i - \frac{B_0}{\mu^v_{mix}} \frac{c_i}{D^e_{iM}} \nabla P = \sum_{j(\neq i)} \frac{1}{c_t D^e_{ij}} (c_j J_i - c_i J_j) + \frac{J_i}{D^e_{iM}} = [H][J] \tag{4.24}$$

where [H] is defined as

$$h_{kl} = \left[\frac{1}{D^e_{kM}} + \sum_{j \neq k} \frac{X_j}{D^e_{kj}} \right] \delta_{kl} + (\delta_{kl} - 1) \frac{X_k}{D^e_{kl}} \tag{4.25}$$

where X_j are mole fractions and δ_{kl} is the Kronecker delta.

The pressure gradient and concentration gradients are computed using the ideal gas law and a forward difference approximation, thereby determining the left hand side (LHS) of (4.24).

The molar flux, J_k, can be calculated as

$$[J] = [H]^{-1}[LHS] \tag{4.26}$$

The computed molar flux, J_k , is substituted into the conservation equations of the gas species.

$$\varepsilon \frac{\partial c_k}{\partial t} = A_s \dot{s}_{surf,k} - \nabla \cdot J_k \quad (k = 1, \ldots, K_g) \tag{4.27}$$

$$\frac{\partial c_{surf,k}}{\partial t} = \dot{s}_{surf,k} \quad (k = 1, \ldots, K_s) \tag{4.28}$$

The conservation equations above are reduced to a set of ordinary differential equation after applying the finite-volume method. The electrodes are approximated as continuous media with homogenized volume-averaged properties. Generation rates for each species, $\dot{s}_k$, are obtained from the elementary heterogeneous reaction model based on concentrations of gas and surface species at each time step. The ODEs for gas species and surface species are solved simultaneously using the function 'ode15s' in MATLAB® with the Gear's method option on.

The solutions are considered to reach steady-state when the maximum change in concentrations during the time integration is less than 0.1% of the total concentrations of the gas and surface species. The integration time span is continuously extended until the solutions reach steady-state. Once the solutions reach steady-state, the concentrations of the gas species at the TPB are used to calculate the equilibrium O_2 partial pressures using the in-house multi-phase equilibrium code [56]. The corresponding reversible cell voltage is computed using Equation (4.22). The difference between the reversible cell voltages based on the channel and at the TPB is defined as a concentration overpotential at each electrode, $\eta_{con,a}$ and $\eta_{con,c}$

$$\eta_{conc} = \left| \frac{\Re T}{4F} \ln\left(\frac{O_{2,TPB}}{O_{2,channel}} \right) \right| \tag{4.29}$$

(3) Calculate the activation overpotential for the cathode

For the cathode, the activation overpotential, $\eta_{a,c}$, can be computed using the following equation

$$i = i_{O_2}^{*} \frac{\left(\frac{p_{O_2}}{K_6} \right)^{1/4}}{1 + \left(\frac{p_{O_2}}{K_6} \right)^{1/2}} \left(\exp\left(\frac{F\eta_{a,c}}{2\Re T} \right) - \exp\left(-\frac{F\eta_{a,c}}{2\Re T} \right) \right) \tag{4.30}$$

$\eta_{a,c}$ is determined from the nonlinear solver, function 'fsolve' in MATLAB ®

(4) Calculate the ohmic overpotential

The ohmic overpotential, η_{ohm}, can be represented as

$$\eta_{ohm} = iR_{ohm} \tag{4.31}$$

where R_{ohm} is the ohmic resistance through the electrolyte and the electrodes. Because the ohmic resistance through the electrodes is negligible, the ohmic resistance is mainly determined by the electrolyte resistance (R_{el}). The electrolyte resistance, R_{el}, is expressed as

$$R_{ohm} = R_{el} = \frac{L_{el}}{\sigma_0 T^{-1} \exp\left(-\frac{E_{el}}{\Re T} \right)} \tag{4.32}$$

where E_{el} is the activation energy for ion transport and L_{el} is the electrolyte thickness, and σ_0 is the pre-exponential factor of the ionic conductivity.

(5) Calculate the cell voltage

The operating cell voltage is then calculated by subtracting all the activation

overpotentials as

$$E_{cell} = E_{rev,channel} - \eta_{conc,a} - \eta_{a,a} - \eta_{ohm} - \eta_{conc,c} - \eta_{a,c} \tag{4.33}$$

4.5. Simulation Results

The work by Jiang and Virkar [13] has the most complete data set available for anode-supported SOFC's with typical porous electrodes. The fuels investigated in that work include (1) H_2 diluted with He, N_2, H_2O and CO_2, (2) CO diluted with CO_2, and (3) mixtures of H_2 and CO. Table 4-4 lists the physical parameters used to describe the MEA structure.

Table 4-4 Table II. Parameters for an SOFC MEA structure. (Taken from [16])

Parameters	Value	Units
Anode		
Thickness (L_a)	1220	μm
Porosity (ε)	0.35	
Tortuosity (τ_g)	3.50	
Average pore radius (r_p)	0.50	μm
Average particle diameter (d_p)	2.50	μm
Specific catalyst area (A_s)	1080	cm^{-1}
Cathode		
Thickness (L_c)	30	μm
Porosity (ε)	0.35	
Tortuosity (τ_g)	3.50	
Average pore radius (r_p)	0.5	μm
Average particle diameter (d_p)	2.5	μm
Electrolyte:		
Thickness (Lel)	25	μm

Activation energy of O^{2-} (E_{el})	8.0×10^4	J/mol
Pre-factor of O^{2-} (σ_0)	3.6×10^5	S/cm

To match the model prediction to the experimental results, the hydrogen electrochemistry model described in the section 4.3.4.1 is first employed to fit Jiang and Virkar's data. For CO electrochemistry, two geometric parameters used in the patterned anode, the TPB length and the Ni Pattern width, are used as fitting parameters for the porous structure. Lastly, both H_2 and CO electrochemistry are incorporated together with the same fitting parameters obtained from the pure H_2 and pure CO fuel cases to predict SOFC performance with syngas.

4.5.1. Pure H_2 case

Without detailed knowledge of H_2 electrochemistry kinetics, a rate-limiting assumption is applied to lump unknown kinetic parameters into a single fitting parameter. Zhu et al [16] reported that reaction (H.3) is likely to be the rate-limiting reaction because it leads to a result that explains the experimental observations: (1) its exchange current density has positive dependence on H_2 and H_2O partial pressures and (2) the anodic charge-transfer coefficient is greater than the cathodic charge-transfer coefficient. This assumption has since been frequently accepted in MEA models [10,16–20]. We reproduce the current-voltage (i-V) curves using their fitting parameters.

Table 4-5. Fitting parameters for single rate-limiting from literatures

Parameters	Value	Units
$i^*_{H_2}$ (Fitting parameter)	8.5	A cm^{-2} $bar^{-3/4}$
$i^*_{O_2}$ (Fitting parameter)	2.8	A cm^{-2}

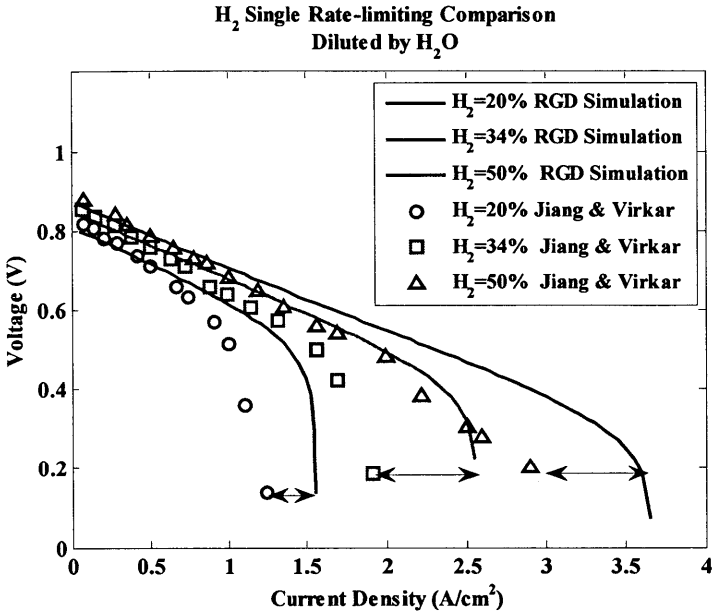

Figure 4-7. Comparison between the simulation results using a single-rate limiting reaction and experimental data from Jiang and Virkar.

Figure 4-7 shows good agreement at low current densities, but a discrepancy between the model and the experiment develops and grows as the current density increases. The simulation overestimates the limiting current density by 20-30%. As documented in the literature, predicting the limiting current density accurately has been challenging [39,46,57], and efforts to resolve this problem have focused on increasing the transport resistance by adding surface diffusion or adjusting the porosity or tortuosity to unphysical values. Lee et al. [50] proposed a rate-limiting switch-over mechanism so that the limiting current is determined not only by transport but also by kinetics. The switch-over model successfully and accurately predicts the limiting current densities, and as such, we adopt the rate-limiting switch-over mechanism to represent H_2 electrochemistry.

Table 4-6. The Butler-Volmer formulations when (H. 1) or (H.3) is assumed to be a rate-limiting step including the exchange current density expressions.

Rate-limiting Reaction	Activation Overpotential	Exchange Current density	$i^*_{H_2}$
1	$i = i_0\left[\exp\left(\frac{0F\eta_a}{\Re T}\right) - \exp\left(-\frac{2F\eta_a}{\Re T}\right)\right]$	$i_0 = i^*_{H_2}(p_{H_2})$	$i^*_{H_2} = 2Fa_{TPB}\frac{S^e_{H_2}}{\sqrt{2\pi M_{H_2}\Re T}}$
3	$i = i_0\left[\exp\left(\frac{3F\eta_a}{2\Re T}\right) - \exp\left(-\frac{F\eta_a}{2\Re T}\right)\right]$	$i_0 = i^*_{H_2}\frac{(K_1 p_{H_2})^{1/4}(p_{H_2O})^{3/4}}{1+(K_1 p_{H_2})^{1/2}}$	3.5

The switch-over model is based on the assumption that H_2 adsorption/desorption becomes the rate-limiting process at large current densities. The expression derived for the exchange current density i_0 physically represents the current density corresponding to the case when every hydrogen molecule adsorbed on empty Ni is electrochemically oxidized, producing two electrons. a_{TPB} is the TPB area per nominal electrolyte area, which is estimated as 0.013 from Lee et al. [50] based on 3-D reconstruction analysis of the porous anode by Wilson et al [58]. a_{TPB} is used as a fitting parameter because of its dependence on the manufacturing methods. a_{TPB} is 0.0086 for this simulation. Note that p_{H_2} is in unit of [Pa] in the exchange current density when reaction (H.1) is assumed to be rate-limiting.

Figure 4-8 depicts the comparison between the results of the simulation employing the rate-limiting switch-over mechanism and the experimental data from Jiang and Virkar [13]. The rate-limiting switch-over mechanism improved the overall accuracy, as well as the prediction of the limiting current density. Figure 4-9 shows the contributions of each overpotential in the rate-limiting switch-over mechanism when H_2=34% and H_2O=66%. The cathode activation

overpotential ($\eta_{act,c}$) and the ohmic overpotential (η_{ohm}) are comparable and dominant while anode activation overpotential ($\eta_{act,a}$) and anode concentration overpotential ($\eta_{conc,a}$) are almost half of $\eta_{act,c}$ and η_{ohm}. However, as the current density approaches its limiting value, $\eta_{act,a}$ grows rapidly and becomes dominant, therefore determining the limiting current value.

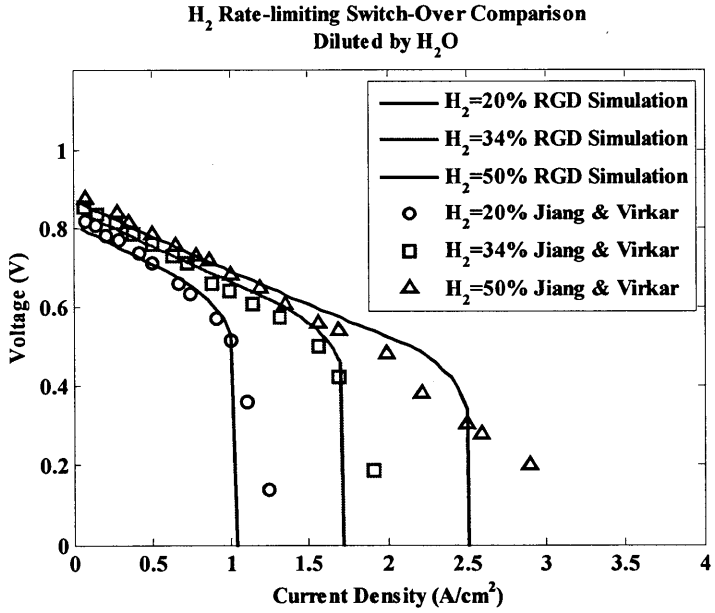

Figure 4-8. Comparison between simulation results using rate-limiting switch-over assumption and experimental data from Jiang and Virkar

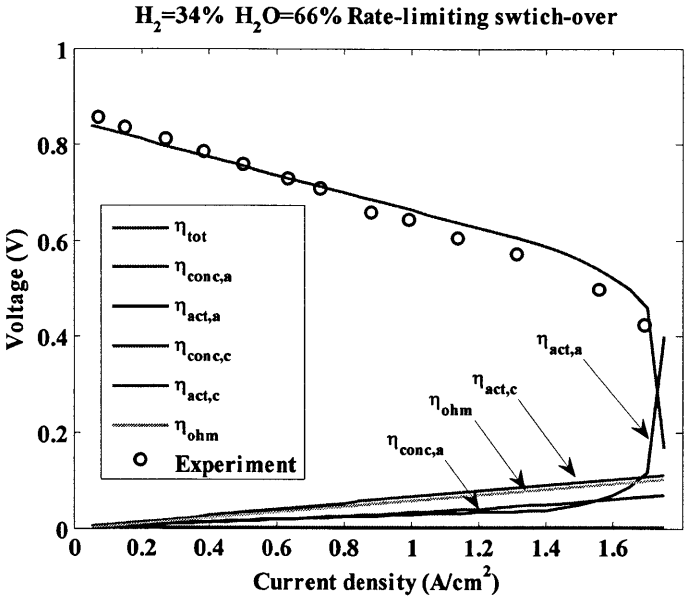

Figure 4-9. Contribution of each overpotential in rate-limiting switch-over mechanism when H_2=34% and H_2O=66%. Experiment represents the experimental measurements by Jiang and Virkar.

As shown in Figure 4-10, the limiting current density is determined by the concentration overpotential in the single rate-limiting mechanism. However, the activation overpotential dictates the limiting current density in the rate-limiting switch-over mechanism, which indicates that the electrochemical process is controlled not only by transport but also by kinetics.

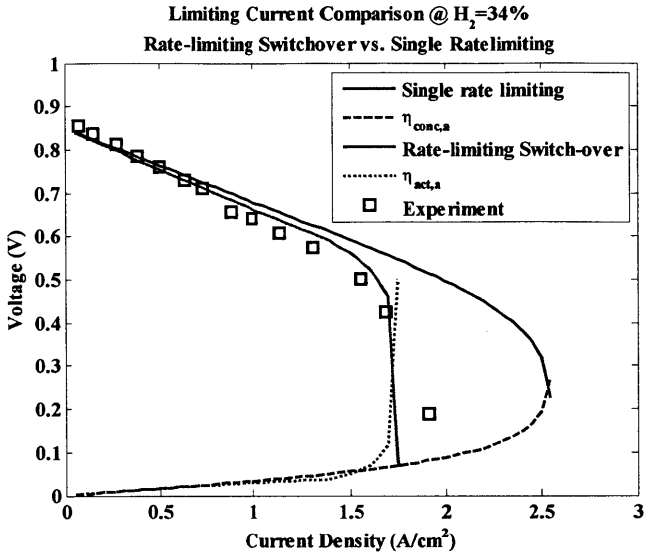

Figure 4-10. Limiting current density determination comparison between single rate-limiting and rate-limiting switch-over mechanism.

4.5.2. Pure CO case

In contrast to the H_2 electrochemistry where the rate-limiting assumptions need to be applied in the absence of detailed kinetic expressions, we will use the estimated kinetic parameters for the detailed multi-step CO electrochemistry on Ni pattern anode. When employing this mechanism, two parameters characterizing the geometry need to be defined. These parameters correspond to the TPB length and Ni pattern width. However, the performance of SOFC is not linearly proportional to the TPB length as formulated in the electrochemistry reaction rate because of the ambiguity of defining the TPB length even for model anodes such as patterned or point anodes. Bessler et al. [27] reviewed the experimental data for patterned and point anodes for hydrogen electrochemistry and found that there is a large scatter of 2.5 orders of magnitude in TPB-length-specific resistance. The following possible reasons are given to explain

this observation: (1) patterned anodes undergo morphology changes by grain growth, delamination from the support, rounding off of originally sharp corners, leading to island-like Ni agglomerates; (2) impurities in the 99.8% Ni electrodes can lead to the formation of ridges at the TPB in contrast to the 99.995% Ni electrodes; (3) the relaxation time is reported to be on the order of hours, and depending on the measurement history, the experimental data can be affected by dynamic effects; (4) the electrochemical performance strongly depends on gas phase composition in a non-intuitive way. To further this point, Bessler et al [27] also reported that the ratio of the TPB length over volume increased by 5-6 orders of magnitude when going from point to pattern to cermet anodes. However, the reported performance did not improve in proportion to this increase. Further research is needed to link the performance improvement to structural changes. For this analysis, the two geometric parameters, the TPB length and the equivalent Ni catalyst width, are used as fitting parameters.

The kinetic parameters for CO electrochemical oxidation are obtained from patterned anodes by fitting the CO electrochemistry model to Habibzadeh EIS measurements [12]. The same kinetic parameters obtained at T=775°C, closest to the operating temperature T=800°C, are adopted for this simulation as listed in Table 4-7.

Table 4-7 Kinetic parameters for CO electrochemistry from patterned Ni anodes

Parameters	Values	unit
$k_{2,f}$	6.29E-09	mole/(sec m)
$k_{2,b}$	3.86E-03	mole/(sec m)
$k_{3,f}$	8.09E-07	mole/(sec m)
$k_{3,b}$	5.78E-10	mole/(sec m Pa)

4.5.2.1. Fitting Results

Figure 4-11 compares the RGD fitting results to the experimental data by Jiang and Virkar [13]for a fuel composition of 18%, 32% and 44% of CO diluted with CO_2. Overall, the simulation agrees with the experimental data, but quantitative difference are observed especially at high currents and lower CO concentrations. The fitting parameter values are given as in Table 4-8. The performance of Jiang and Virkar's porous anode [13] is one order of magnitude better than that of Habibzadeh's patterned anode [12] at similar CO and CO_2 partial pressures and close to the OCV. Because both the porous and patterned anodes share the same dense YSZ electrolyte and the porous LSM/YSZ cathodes, the ohmic overpotential and cathode-related overpotentials are the same. The anode concentration overpotential is likely to be negligible for both porous and patterned anodes close to the OCV. The reported performance improvement can be accounted for by the increase in the TPB length from the pattern to the porous structure. In the CO electrochemistry simulation in the patterned anode, the l_{TPB} is assumed to be 0.32 m/cm^2 as measured by Habibzadeh [12]. Therefore, the l_{TPB} in the porous anode is expected to be larger by one order of magnitude, about 3.2 m/cm^2. The fitted value for l_{TPB} is 3 m/cm^2 as listed in Table 4-8.

Because half of the Ni pattern width, L_{Ni}, in the pattern anode is defined as the distance between the TPB lines where the symmetry boundary condition is applied, L_{Ni} in the porous anode corresponds to the distance between the TPB lines adjacent to each other. However, the 3D nature of the porous anode renders it hard to define the effective Ni pattern width in the porous anode. Based on the 3D reconstruction data of a Ni porous anode reported by Wilson et al [58], the TPB lines are a distance of 0.01-0.1 μm apart. The fitted L_{Ni} of 0.02 μm falls in this range.

Both the geometric fitting parameters are in a reasonable range.

Table 4-8 Fitting parameters for porous Ni anode

Parameters	Values	unit
l_{TPB}	3	(m/cm^2)
L_{Ni}	0.02	(μm)

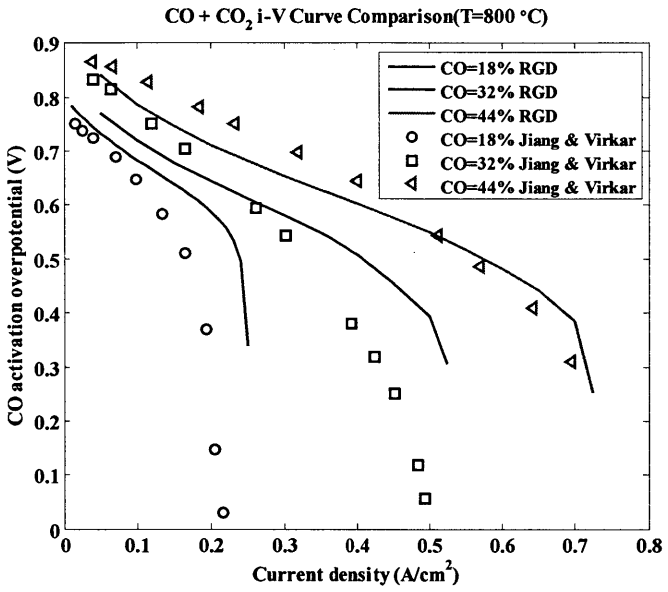

Figure 4-11. Comparison between the RGD model simulation and Jiang and Virkar experimental data on porous MEA with pure 18%, 32% and 44% of CO diluted with CO_2

Figure 4-12 illustrates the contribution of each overpotential and compares the i-V curve calculation with the experimental data from Jiang and Virkar [13]. While the cathode activation overpotential and ohmic overpotential are found to dominate when the fuel is H_2, sluggish CO electrochemistry leads to a dominant anode activation overpotential, and somewhat smaller anode concentration overpotential. The limiting current density is controlled by a combination of anode transport ($\eta_{conc,a}$) and CO electrochemistry kinetics ($\eta_{act,a}$).

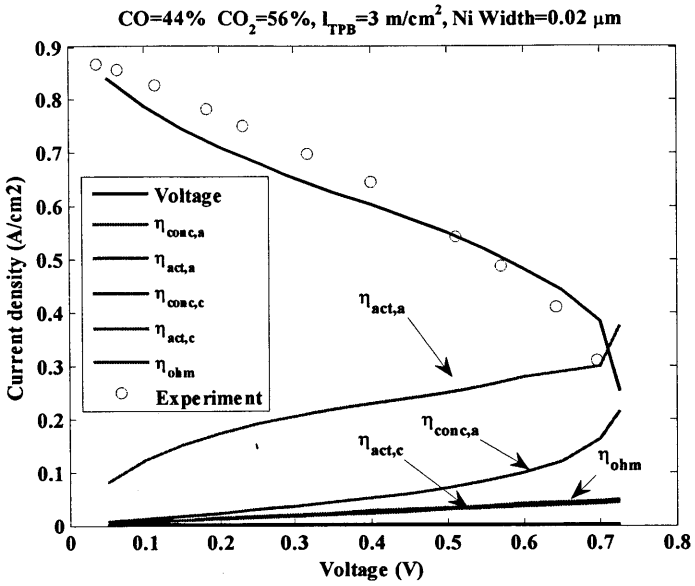

Figure 4-12. Contribution of each overpotential when CO=44% and CO_2=56%. Experiment represents the experimental measurements by Jiang and Virkar

Figure 4-13 shows the current contributions from reaction (CO. 2) and (CO. 3). The forward reaction rates (current generation) are plotted as dotted lines while the backward reaction rates (current consumption) are plotted as solid lines. The net current from each reaction is the difference between forward and backward rates. The total current is the sum of the two net currents. Because the calculation is at steady-state, the net currents from the two reactions should be equal. In addition, the overall magnitude of the reaction rates for (CO. 2) and (CO. 3) are comparable. Therefore, it is not obvious which, if either, of the two is rate-limiting at this operating condition.

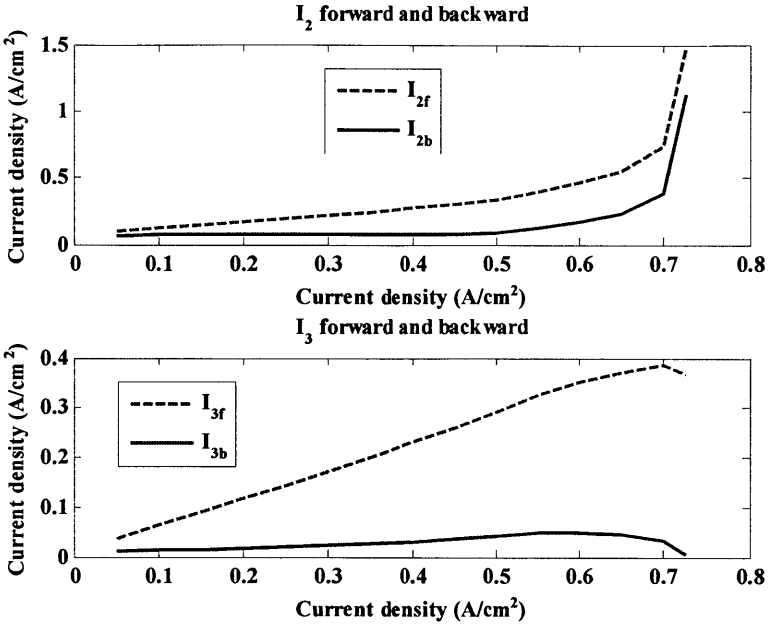

Figure 4-13. Current contribution from reactions (CO. 2) and (CO. 3). Dotted lines and solid lines represent the current generation and current consumptions, respectively, via forward and back reaction rate.

4.5.2.2. **Role of transport**

Figure 4-9 and 4-12 clearly indicate the relative role of the concentration overpotential for CO and H_2 electrochemistry, respectively. When the fuel compositions are comparable, e.g., H_2(34%)-H_2O(66%) and CO(32%)-CO_2(68%), the CO-CO_2 mixture is characterized by significantly higher concentration overpotential and reaches the limiting current density at a much lower value than the H_2-H_2O mixture. This is shown in Figure 4-14. Table 4-9 lists the binary diffusivities and Knudsen diffusion coefficients. The diffusivity for H_2-H_2O is 5.5 times higher than that for CO-CO_2. The Knudsen diffusion coefficient of H_2 is also 4 times higher than that of CO. Therefore, the transport of the heavier CO fuel molecules is slower than the lighter H_2 molecules, resulting in significantly largre anode concentration overpotential. The lower

performance for CO is attributed not only to the sluggish CO electrochemistry, but also to its slower transport compared with H_2.

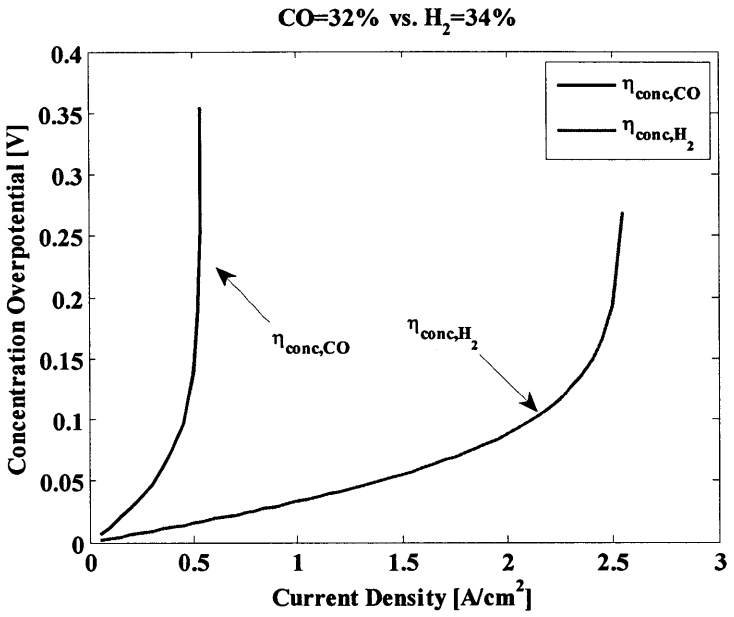

Figure 4-14. Comparison of concentration overpotentials when the fuels, H_2 and CO, have comparable concentrations. H_2 and CO are diluted by H_2O and CO_2, respectively, in this simulation.

Table 4-9. Binary and Knudsen diffusivities at 800C and 1 bar. Unit is [cm^2/sec]

	H_2	O_2	H_2O	CO	CO_2	CH_4	N_2	Knudsen Diffusion coefficient
H_2	0.0000	6.7869	**7.6604**	6.4360	5.5360	6.2076	6.3553	**1.1234**
O_2	6.7869	0.0000	2.2747	1.7983	1.4111	2.0032	1.7821	0.2809
H_2O	7.6604	2.2747	0.0000	2.2100	1.7196	2.3189	2.1969	0.3745
CO	6.4360	1.7983	2.2100	0.0000	**1.4027**	1.9550	1.7543	**0.3003**
CO_2	5.5360	1.4111	1.7196	1.4027	0.0000	1.5920	1.3941	0.2395
CH_4	6.2076	2.0032	2.3189	1.9550	1.5920	0.0000	1.9406	0.3972
N_2	6.3553	1.7821	2.1969	1.7543	1.3941	1.9406	0.0000	0.3003

4.5.2.3. Role of Ni surface area

In order to investigate the role of Ni surface area in the CO electrochemistry, the i-V

curves are computed with different Ni pattern widths from 0.005 μm to 0.2 μm as shown in Figure 4-15. Wider Ni patterns represent larger Ni surface areas. As the Ni pattern width increases, the performance improves, then saturates when the width reaches 0.1 μm. Further increasing the Ni pattern width above this limit shows little performance benefit, because the concentration of CO on the surface is close to the equilibrium balance between adsorption and desorption due to the fact that it is too far from the TPB to be affected by the electrochemistry. When the Ni pattern width is under this limit, the overall surface coverage of CO is less than the equilibrium value, thereby deteriorating the performance by reducing CO coverage at the TPB. Habibzadeh [12,28] reported the same saturation trend as the Ni pattern width increases approaching 0.05 μm. The exact limiting value depends on the TPB length and the operating conditions. Figure 4-16 and 4-17 illustrate how the limiting current density is determined depending on the Ni pattern widths of 0.005 μm and 0.2 μm, respectively, by showing the contribution of each overpotential. Slow adsorption kinetics control the limiting current when the Ni pattern width is 0.005 μm while gas transport limits the further increase of the current density at a pattern width of 0.2 μm. In regard to how these results translate to porous cermets, the size of the catalyst need to be chosen carefully. By manufacturing the anode with smaller Ni particles, the TPB length can be increased, thereby improving the overall performance. However, if the catalyst size is too small, there will be reduced available catalyst area for adsorption.

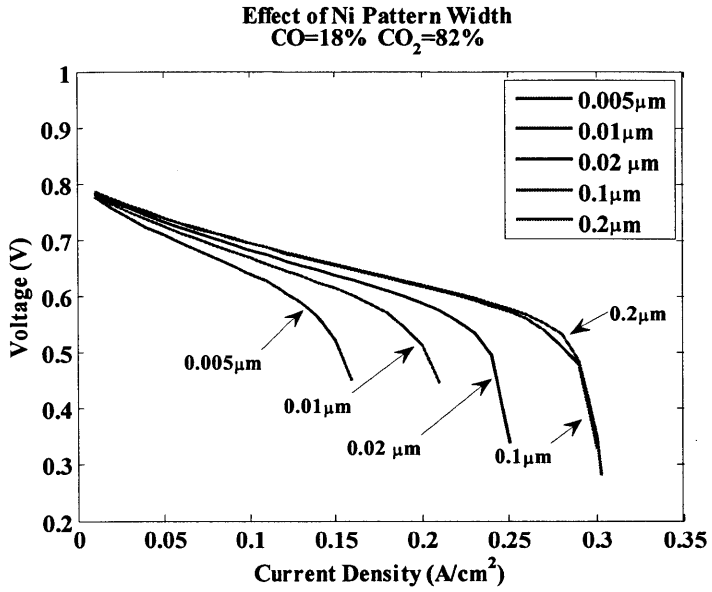

Figure 4-15. Effect of equivalent Ni pattern width in porous anode on the i-V curve when the fuel mixture is 18% CO and 82% CO_2.

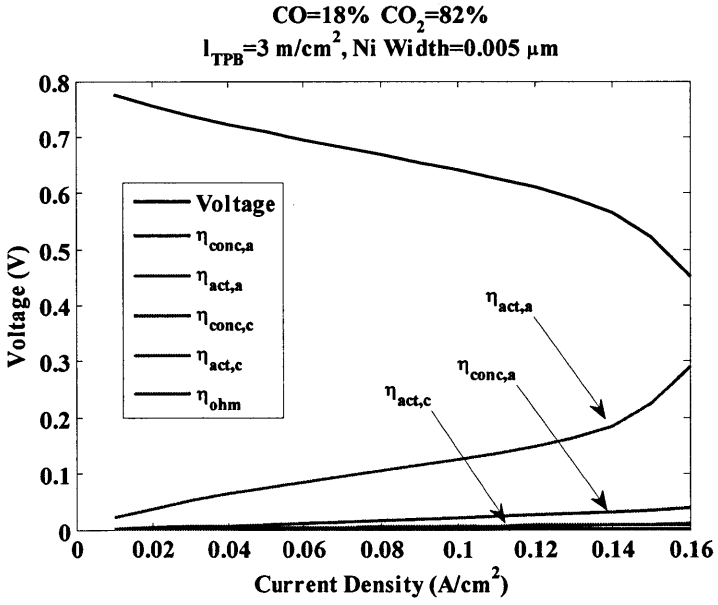

Figure 4-16. Contribution of each overpotential when Ni width=0.005 μm lTPB=3 m/cm2 for the fuel mixture of 18% CO and 82% CO_2.

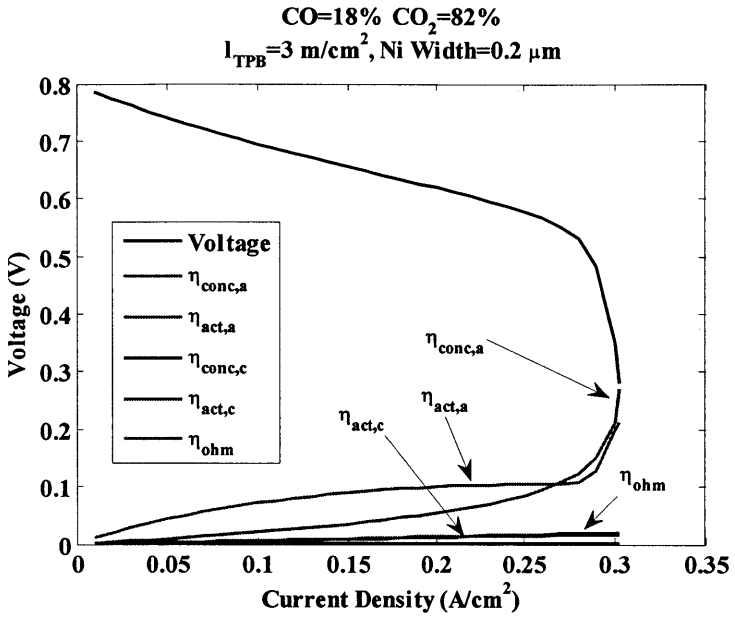

Figure 4-17. Contribution of each overpotential when Ni width=0.02 μm lTPB=3 m/cm2 for the fuel mixture of 18% CO and 82% CO_2.

4.5.3. H_2 + CO mixture

In the previous two sections, individual H_2 and CO electrochemistry mechanisms have been applied to predict the performance of an SOFC operating on either fuel individually, and results show reasonable agreement with corresponding experimental data by Jiang and Virkar [13]. Note that in the case of H_2, the electrochemical kinetic parameters are used as fitting parameters. On the other hand, in the case of CO, two geometric parameters are used as fitting parameters while keeping the electrochemical kinetic parameters obtained from the patterned anode studies as is.

We now further extend the application of both electrochemical reaction mechanisms to syngas mixture without any additional parameter fitting because all the data used for comparison is obtained from the same group. Accordingly, all parameters reported previously are used for the

syngas simulation. Thermochemical reactions can play a major role in syngas via the water-gas-shift reaction, contrary to pure H_2 and CO cases. In our calculations, the absence of H_2O and zero CO_2 lead to zero exchange current density (see Table 4-3 for H_2 electrochemistry and Equation (4.13) for CO electrochemistry), which is detrimental to steady-state calculations. To circumvent this problem, 1% H_2O and 1% CO_2 are assumed to exist in place of H_2 and CO, respectively. That is, for a nominal mixture of 86% H_2 and 14% CO, the actual simulated mixture is 85% H_2, 1% H_2O, 13% CO, and 1% CO_2.

4.5.3.1. **86% H_2 + 14% CO**

Figure 4-18 compares Jiang and Virkar's experimental data [13] for a nominal fuel mixture of 86% H_2 and 14% CO with the i-V curve calculations with three different models; (1) 'No reforming & only H_2' stands for a model with only H_2 electrochemistry on and with reforming chemistry off, (2) 'Reforming & Only H_2' is a model in which we turn on the reforming chemistry with still only H_2 electrochemistry on, (3) 'Reforming & Both CO and H_2' represents a model with all thermo- and electrochemistry involved active. By comparing them, the effect of reforming and additional CO electrochemistry can be examined. There is negligible difference among the three curves, implying that the effect of the reforming reactions and the additional CO current are not significant for this fuel mixture.

Figure 4-19 shows the concentration profiles along the anode near the limiting current density. The solid and dash-dash lines stand for the cases with the thermochemical reactions turned on and off, respectively. There are a large amounts of H_2O and H_2. The thermochemical reactions increased H_2 and CO_2 concentrations while reducing the amounts of H_2O and CO via

the water-gas shift reaction. This slight increase in the amount of H_2 leads to the increase in the limiting current density as shown in Figure 4-18. As shown in Figure 4-19, there is more H_2 than CO near the TPB, even at the limiting current density. For this composition, there is little contribution from CO to the electrochemistry because there is much more H_2 whose electrochemical oxidation rate is faster than that of CO. Besides, there is plenty of H_2O to reform CO.

Figure 4-20 compares the contribution of H_2 and CO electrochemistry to the total current density as a function of the applied activation overpotential. Note that the axes for the currents from H_2 and CO electrochemistry have different scale. As many previous researchers have assumed [10,16–20], the H_2 electrochemical reaction is dominant and the current from the CO electrochemistry is an order of magnitude smaller. The current from the H_2 electrochemistry is saturated at 4.1 A/cm^2 when the activation overpotential is around 0.1 V. The saturated H_2 current corresponds to the limiting current density in the i-V curve when the fuel is pure H_2.

Because H_2 electrochemistry is dominant throughout the range of current density, a good H_2 electrochemistry mechanism can lead to a good agreement with experimental data for the mixture of H_2 and CO. The good agreement shown in Figure 4-18 suggests that the adopted H_2 electrochemistry model is reasonably good. Figure 4-21 depicts the contribution of each overpotential. The three overpotentials, $\eta_{act,c}$, η_{ohm}, and $\eta_{conc,a}$, are comparable except near the limiting current density where there is rapid increase of $\eta_{act,a}$. The adopted rate-limiting switch-over mechanism predicts accurately the limiting current density, which is controlled by kinetics in this case.

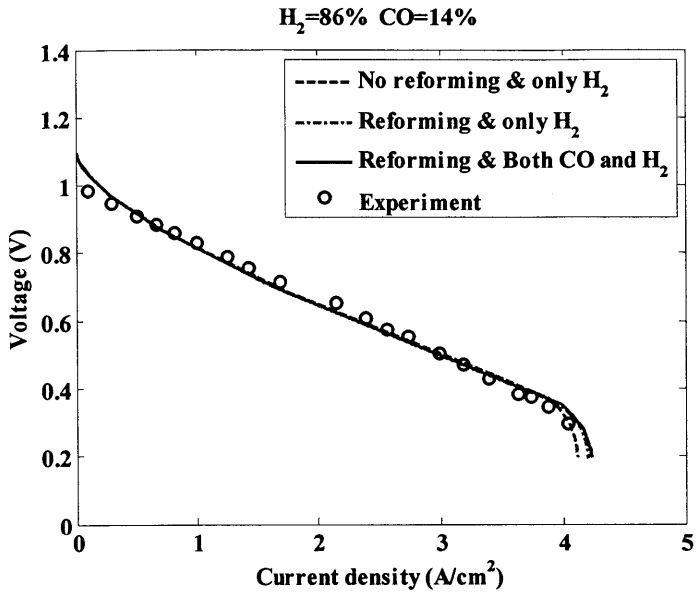

Figure 4-18. Comparison of i-V curves for the nominal fuel mixtures of 86% H_2 and 14% CO. Each curve shows the effects of each electrochemistry and reforming reactions. The dash-dash line stands for the case when there is no thermochemical reaction and only H_2 electrochemical reaction is assumed to occur. The dash-dot line stands for the case when thermochemical reactions are considered and only H_2 electrochemical reaction is assumed to occur. The solid line stands for the case when the thermochemical reactions are considered and both H_2 and CO electrochemical reactions are assumed to occur.

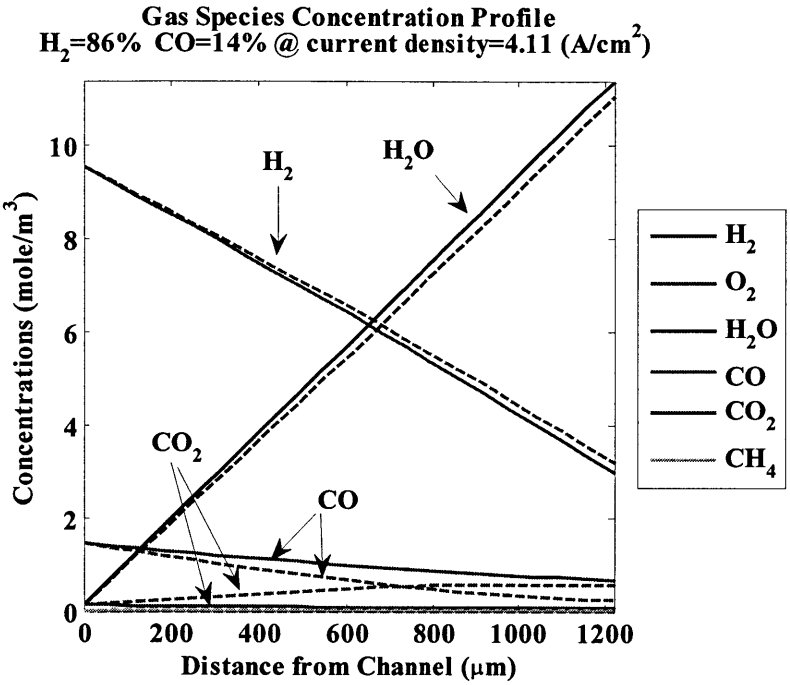

Figure 4-19. Gas species profiles along the anode from the fuel channel to the TPB for a nominal fuel mixture of 86% H_2 and 14% CO when the current density is 4.11 A/cm^2. The solid lines stand for the case when there is no reforming; the dash-dash lines represent for the case when the thermochemical reactions occur.

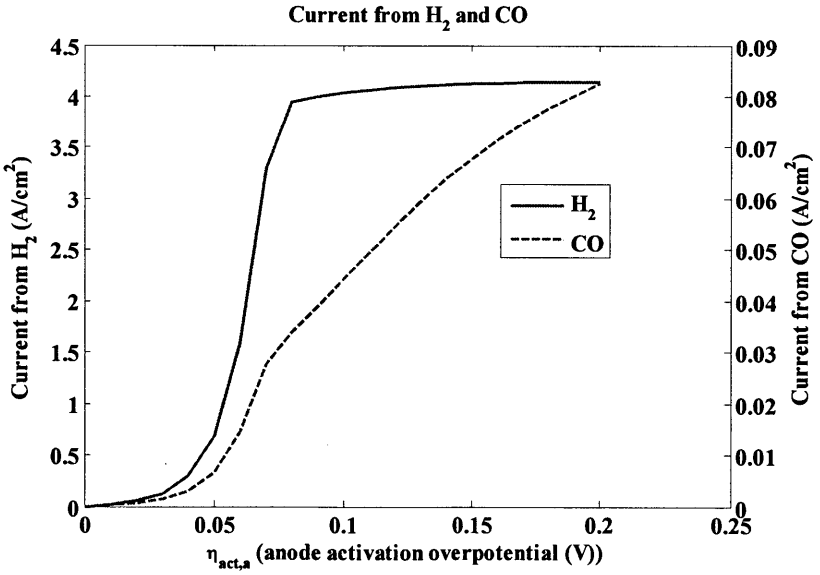

Figure 4-20. Contribution of H_2 and CO electrochemistry to current densities when the fuel is 86% H_2 and 14% CO, depending on the anode activation overpotential

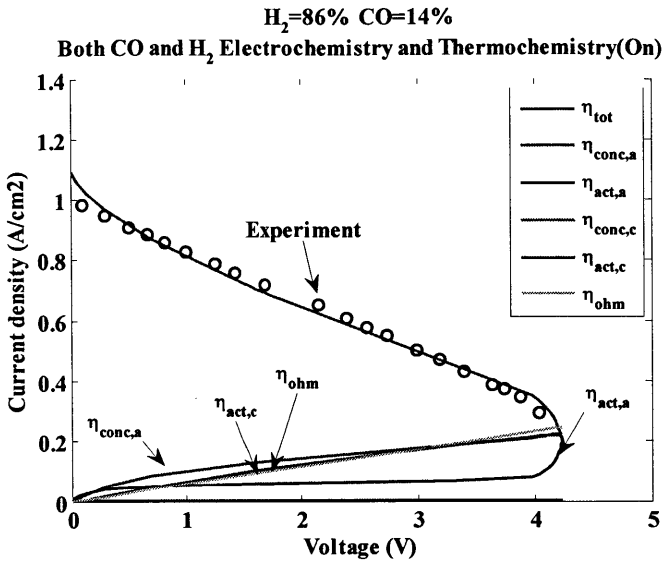

Figure 4-21. Contribution of each overpotential when the fuel is 86% H_2 and 14% CO.

4.5.3.2. 32% H_2 + 68% CO

Similar to the previous analysis, Figure 4-22 compares Jiang and Virkar's experimental data [13] for a nominal fuel mixture of 32% H_2 and 68% CO with the i-V calculations with three different models. In contrast to the case for the nominal fuel mixture of 86 H_2 and 14% CO, the reforming reactions and the additional CO current result in a significant change in the prediction of the i-V curves. Reforming reactions lead to the increase of the limiting current density from 1.5 A/cm^2 to 2 A/cm^2 and the agreement is improved at lower current densities. The additional CO electrochemistry further increases the limiting current density and improves the agreement. However, it cannot resolve the discrepancy at high current densities. This discrepancy will be discussed in section 4.5.3.4.

Figure 4-23 describes how the gas species concentrations changes by turning on the reforming chemistry with the given fuel mixture when the current density is 1.5A/cm^2 where the solid lines represent the case without reforming chemistry and the dotted lines stand for the cases with reforming chemistry. With the reforming chemistry, especially via water-gas-shift reaction $H_2O + CO \leftrightarrow H_2 + CO_2$, H_2O and CO are consumed producing CO_2 and H_2 as they approach the TPB where there is a large amount of H_2O product available from the H_2 electrochemistry. This additional H_2 could further increase the limiting current density up to 2 A/cm^2 as shown in Figure 4-22. Figure 4-24 shows the current density as a function of the anode activation overpotential when only H_2 electrochenmistry is allowed. The current is saturated at 2 A/cm^2 when the activation overpotential is 0.2 V.

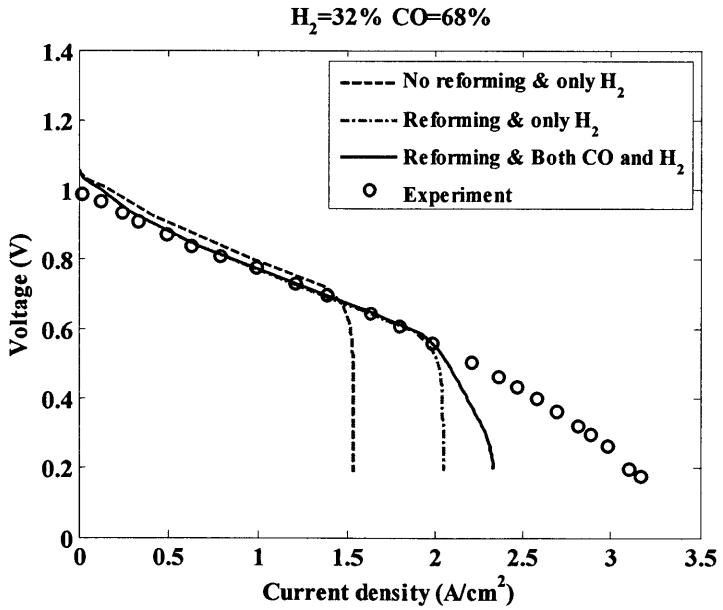

Figure 4-22. Comparison of i-V curves when the fuel is 32% H_2 and 68% CO. Each curve shows the effects of each electrochemistry and reforming reactions. The dash-dash line stands for the case when there is no thermochemical reaction and only H_2 electrochemical reaction is assumed to occur. The dash-dot line stands for the case when thermochemical reactions are considered and only H_2 electrochemical reaction is assumed to occur. The solid line stands for the case when the thermochemical reactions are

considered and both H_2 and CO electrochemical reactions are assumed to occur.

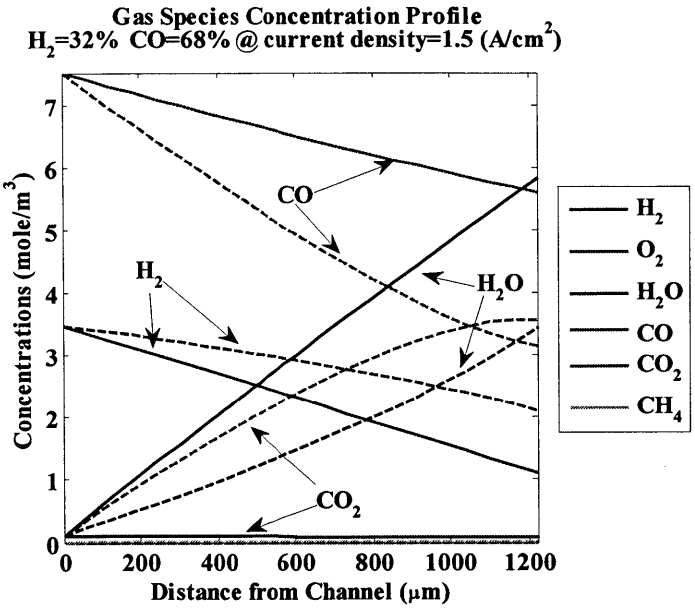

Figure 4-23. Gas species concentration change by turning on the reforming chemistry with the fuel mixture of 32% H_2 and 68% CO when the current density is 1.5 A/cm^2. The dotted lines stand for the case with reforming chemistry on while the solid lines are without the reforming chemistry.

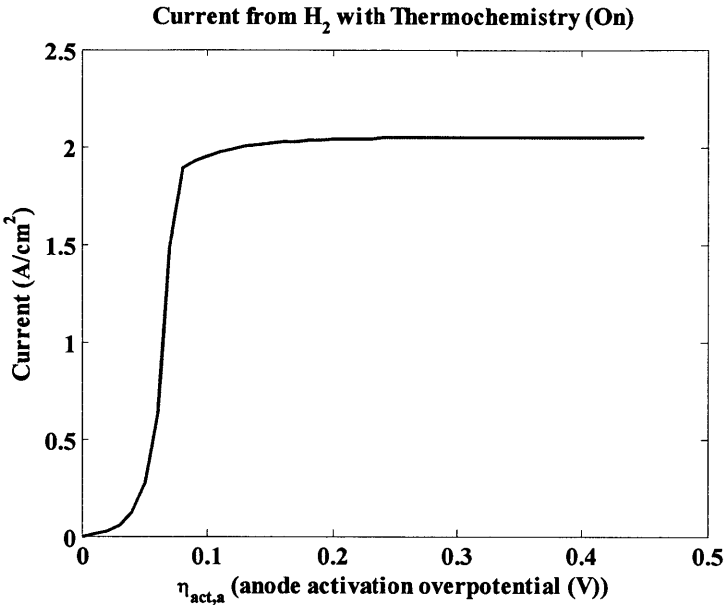

Figure 4-24. The current density from H_2 with the thermochemical reactions turned on when the fuel is 32% H_2 and 68% CO, as a function of the anode activation overpotential.

Finally, when the CO electrochemistry is employed in the simulation, there is an additional current from CO, accompanying the increase of the limiting current density to 2.4 A/cm^2. Figure 4-25 compares the current contribution from H_2 and CO electrochemistry as a function of the anode activation overpotential. For this fuel mixture, the current from CO grows to the same order of magnitude of the current from H_2, accounting for 25% of the total current near the limiting current density of 2.4 A/cm^2, in contrast to the fuel mixture of 86% H_2 and 14% CO where there is an order-of-magnitude difference between them. The current from H_2 electrochemistry stays the same with the case with no current from CO until the anode activation overpotential reaches 0.14 V. The further increase of the anode activation overpotential leads to the reduction of the current from H_2 and the increase of the current from CO.

Figure 4-26 shows the concentrations profiles for two anode activation overpotentials:

0.14 V and 0.39 V. The additional CO electrochemical reactions and the related thermochemical reactions result in the reduction of H_2 concentration at the TPB, thus the current from H_2 decreases. When the activation overpotential is 0.39 V, both the currents from H2 and CO are saturated and the total current is limited at 2.33 A/cm^2 as shown in Figure 4-22.

Figure 4-27 shows that all the overpoentials except the cathode concentration overpotential are comparable and the limiting current density is determined by the rapid increase of the anode activation overpotentials. Overall, the activation overpotential for 32% H_2 and 68% CO is larger than the previous case of 86% H_2 and 14% CO.

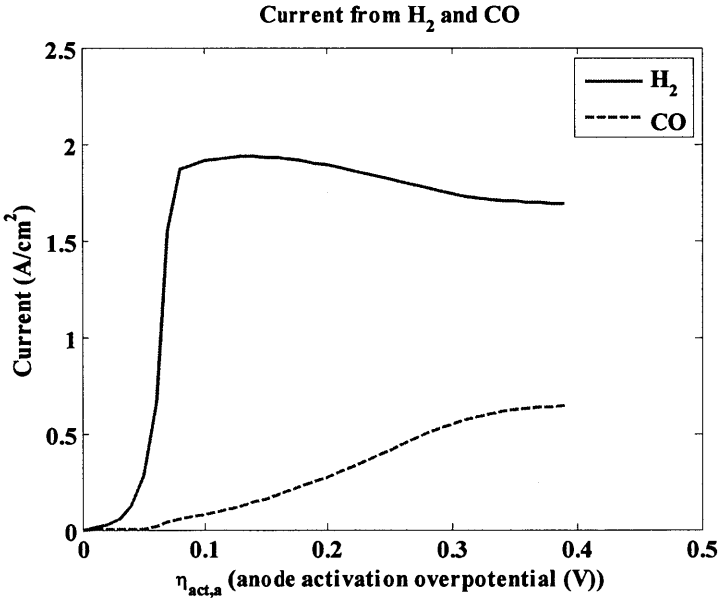

Figure 4-25. Contribution to the current density from H_2 and CO electrochemistry with the thermochemical reactions turned on when the fuel is 32% H_2 and 68% CO, as a function of the anode activation overpotential.

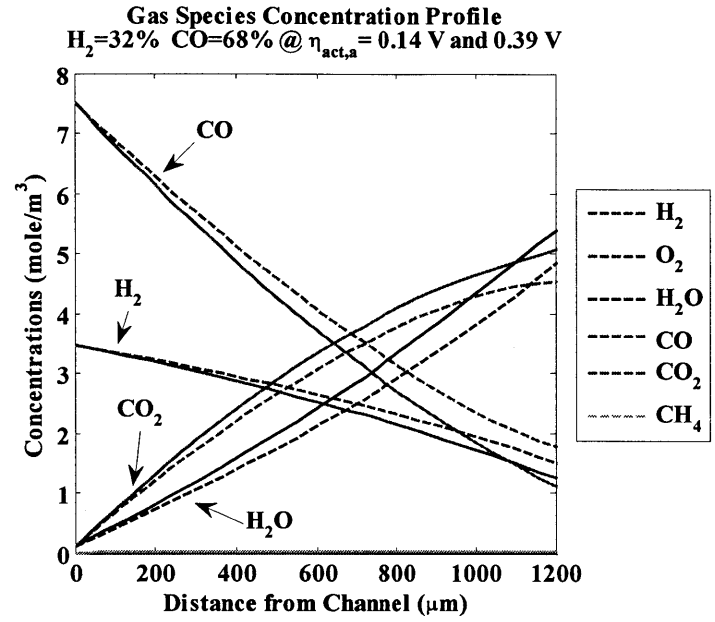

Figure 4-26. Gas species concentrations for the nominal fuel mixture of 32% H_2 and 68% CO. The dotted lines and the solid lines correspond to the case when the anode activation overpotential is 0.14 V and 0.39 V, respectively.

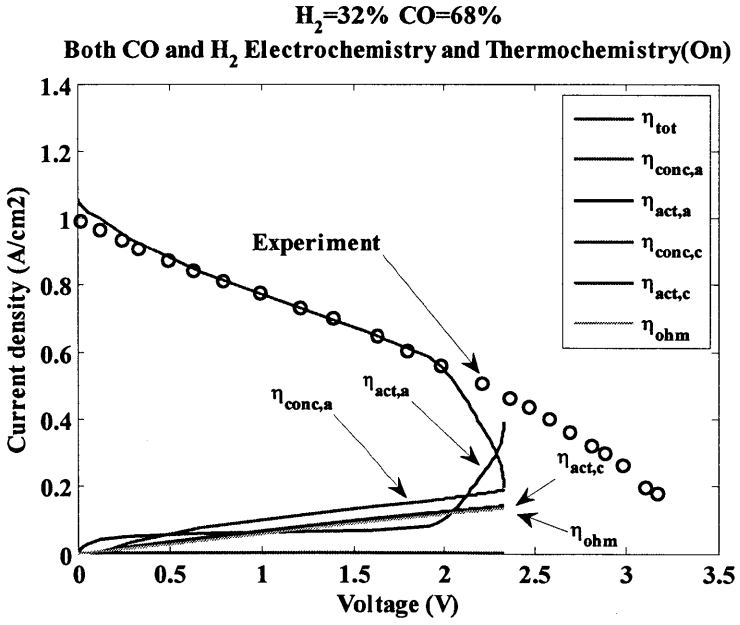

Figure 4-27. Contribution of each overpotential with the fuel mixture of 32% H_2 and 68% CO where reforming and both electrochemistry reactions are active.

4.5.3.3. 20% H_2 + 80% CO

The case with the nominal fuel mixture of 20% H_2 and 80% CO follows the same trend shown in the previous section as shown in Figure 4-28: (1) incorporating reforming reactions improves the agreement at lower current densities and increases the limiting current density; (2) The additional CO electrochemistry further increases the limiting current density. However, it cannot resolve the discrepancy at high current densities. This discrepancy will be discussed in section 4.5.3.4

When only H_2 electrochemistry is involved, the current is saturated at 1.5 A/cm2 when the activation overpotential is 0.2 V as shown in Figure 4-29. When both CO and H_2 electrochemistry are active, the current contribution from CO electrochemistry is responsible for around 50% of the total current density as shown in Figure 4-30. When the anode activation overpotential exceeds 0.15V, the active CO electrochemistry changes the compositions at the TPB as shown in Figure 4-31. The reduction in the H_2 concentration leads to the decrease of H_2 current. Even though the CO partial pressure is four times that of H_2 at the channel, the concentrations of H_2 and CO are comparable when the cell runs at the limiting current density. Therefore, the H_2 electrochemistry still plays a major role in this fuel composition.

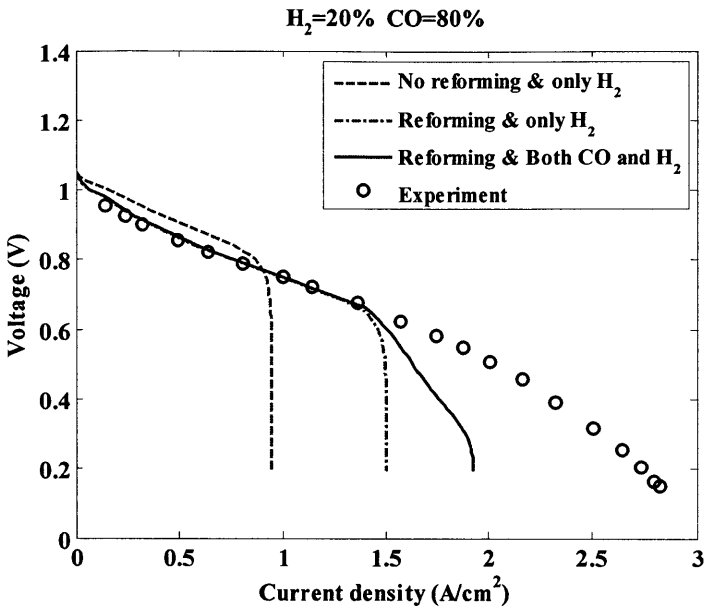

Figure 4-28. Comparison of i-V curves when the fuel is 20% H_2 and 80% CO. Each curve shows the effects of each electrochemistry and reforming reactions. The dash-dash line stands for the case when there is no thermochemical reaction and only H_2 electrochemical reaction is assumed to occur. The dash-dot line stands for the case when thermochemical reactions are considered and only H_2 electrochemical reaction is assumed to occur. The solid line stands for the case when the thermochemical reactions are considered and both H_2 and CO electrochemical reactions are assumed to occur.

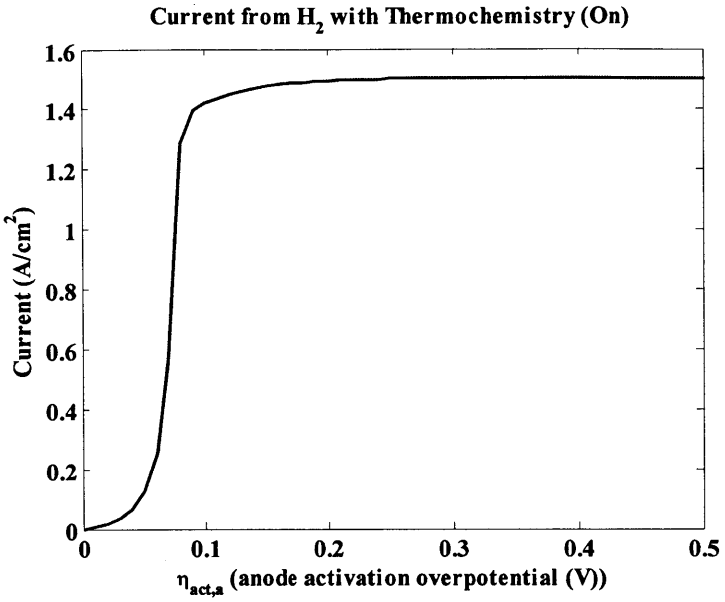

Figure 4-29. Contribution to the current density from H_2 with the thermochemical reactions turned on when the fuel is 20% H_2 and 80% CO, as a function of the anode activation overpotential. Only H_2 electrochemical reaction is turned on.

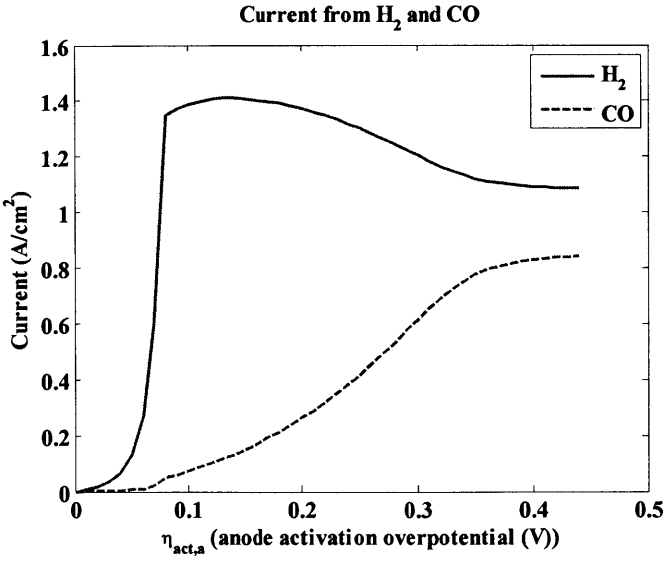

Figure 4-30. Contribution to the current density from H_2 and CO electrochemistry with the

thermochemical reactions turned on when the fuel is 20% H_2 and 80% CO, as a function of the anode activation overpotential.

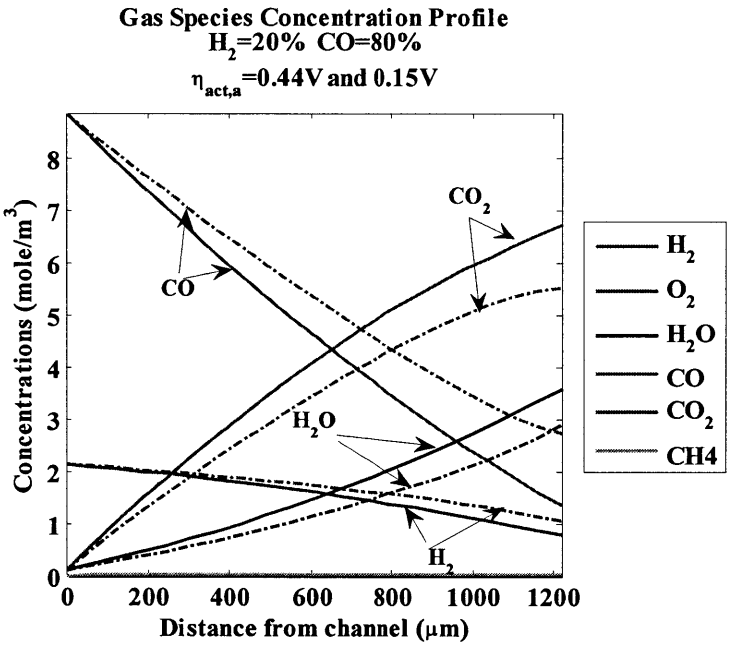

Figure 4-31. Gas species concentration profile along the anode with the fuel mixture of 20% H_2 and 80% CO. The dotted lines stand for the case when the activation overpotential is 0.15 V; the solid lines are when the activation overpotential is 0.44 V.

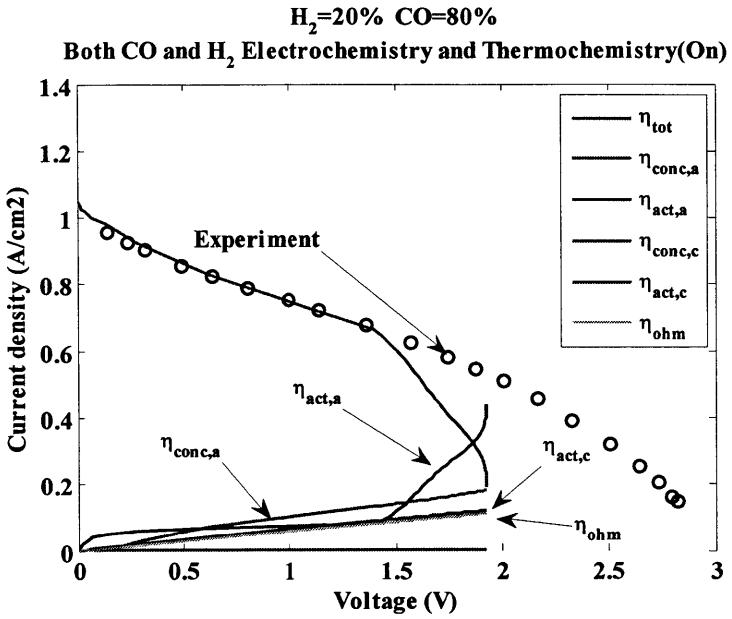

Figure 4-32. Contribution of each overpotential with the fuel mixture of 20% H_2 and 80% CO where reforming and both electrochemistry reactions are active.

4.5.3.4. Discussion

By adding the reforming thermochemistry and both the H_2 and CO electrochemistry, the current MEA model agrees better with the Jiang and Virkar's experimental data [13]. When the H_2 concentration is greater than the CO concentration, the overall performance is dominated by H_2 electrochemistry, resulting in almost perfect agreement with the experimental data, as shown for the fuel mixture of 86% H_2 and 14% CO. However, the discrepancy grows as the CO content in the fuel mixture rises. Habibzadeh et al. [28] reported that the addition of 3% H_2O to the CO/CO_2 anode fuel increases the patterned anode cell performance by as much as 40-50%. They suspected that the reforming chemistry via water-gas shift reaction may be responsible.

Sukeshini et al. [11] from the same group reported the opposite results that the addition of 4% H_2O to CO stream showed a strong deleterious effect on the electrochemistry. They argued that water-gas-shift reactions do not occur significantly near the TPB and the water may directly inhibit CO electrochemical oxidation processes. There is a need for further research on the effect of water on CO electrochemistry. At the predicted limiting current densities, there is plenty of H_2O at the TPB as shown in Figure 4-26 and 35. If water promotes CO electrochemistry at the TPB, the prediction of our MEA model can be improved by incorporating electrochemistry models that capture this effect, approaching Jiang and Virkar's experimental data [13].

Both H_2 and CO electrochemistry mechanisms are developed based on the assumption that H(Ni) and CO(Ni) are the only species on the Ni surface in each mechanism. And it was assumed that there is no interaction between the two charge-transfer electrochemistry. However, when the two electrochemical reactions proceed on the same Ni surface, it is likely that there is an interaction not only through the surface thermochemistry, but also between the two electrochemical steps. There is a need to develop a mechanism for syngas based on the proposed H_2 and CO electrochemistry steps in order to resolve the growing discrepancies in the computed i-V curves from the Jiang and Virkar's data [13].

4.6. Conclusion

We developed an SOFC MEA model using syngas incorporating multi-species transport, detailed elementary heterogeneous reactions on the Ni surface, and detailed electrochemistry models for H_2 and CO. For the chemically reacting flow in the porous electrodes, a detailed mechanism for heterogeneous CH_4 reforming on Ni is used, and transport is modeled using

Dusty-Gas-Model (DGM). Lack of a detailed CO electrochemical mechanism has traditionally been a bottleneck for syngas-based simulations. For the first time, we apply both detailed H_2 and CO electrochemistry to simulate SOFC using syngas fuel. Parameters of the MEA model are fitted to the Jiang and Virkar's experimental data [13] for pure H_2 and pure CO, and are validated against the Jiang and Virkar's experimental data [13] for syngas. For H_2 electrochemistry, the rate-limiting switch-over mechanism from Lee et al. [50] improves previous single-rate limiting assumptions and shows good agreement with the experimental data, especially near limiting current densities. For CO electrochemistry, a full three-reaction mechanism is employed and shows good agreement with experimental data. It is found that the lower performance of pure CO compared with H_2 can be attributed not only to the sluggish CO electrochemistry, but also to slow transport processes. Depending on the Ni porous structure, CO adsorption on Ni can be rate-determining near limiting current densities, which supports the H_2 rate-limiting switch-over assumption that H_2 adsorption can be rate-determining near the limiting current density. Hence, care should be taken when choosing the Ni catalyst size. For syngas, the MEA model can separate out the effects of reforming chemistry and the additional CO electrochemistry. The reforming chemistry improves the agreement at lower current densities and increases the limiting current density by providing more H_2 through H_2O produced at the TPB and water-gas shift reaction. CO electrochemistry is essentially negligible when the fuel is dominated by H_2. However, the current from CO electrochemistry becomes comparable to that from H_2 electrocehmistry as the CO content at the TPB increases. Nonetheless, there is some discrepancy between the MEA simulation and experimental data. This indicates a need to develop a new syngas mechanism based on the current H_2 and CO electrochemistry, which can explain the

effect of water on performance not only via thermochemistry but also via electrochemistry. It was mentioned in the section 4.3.4 that there is inconsistency in the underlying assumptions in the thermochemical model in the anode and the electrochemistry models at the TPB; the CH_4 reforming reactions on Ni assumed 12 surface species on Ni whereas only single species is assumed on Ni, H(Ni) or CO(Ni), in the H_2 and CO electrochemistry model, respectively. In the same fashion, the O_2 electrochemistry model assumed the single surface species, O(YSZ). In the analysis of H_2 and O_2 electrochemistry, unknown kinetics parameters are lumped together into a single fitting parameter with the single-species assumption. In order to couple the thermochemistry and the electrochemistry even in the surface species level, the H_2 thermochemistry mechanism needs to be improved to provide the fundamental kinetic parameters. The same level of detail of H_2 and CO electrochemistry models can enable to include the interaction between H_2 and CO electrochemistry on Ni.

4.7. References

[1] E. P. Murray, T. Tsai, and S. A. Barnett, "A direct-methane fuel cell with a ceria-based anode," *Nature*, vol. 400, no. 6745, pp. 649–651, 1999.

[2] J. Liu and S. A. Barnett, "Operation of anode-supported solid oxide fuel cells on methane and natural gas," *Solid State Ionics*, vol. 158, no. 1, pp. 11–16, Feb. 2003.

[3] Z. Zhan, J. Liu, and S. A. Barnett, "Operation of anode-supported solid oxide fuel cells on propane–air fuel mixtures," *Applied Catalysis A: General*, vol. 262, no. 2, pp. 255-259, May 2004.

[4] G. K. Gupta, A. M. Dean, K. Ahn, and R. J. Gorte, "Comparison of conversion and deposit formation of ethanol and butane under SOFC conditions," *Journal of Power Sources*, vol. 158, no. 1, pp. 497-503, Jul. 2006.

[5] Z. Zhan and S. A. Barnett, "Solid oxide fuel cells operated by internal partial oxidation reforming of iso-octane," *Journal of Power Sources*, vol. 155, no. 2, pp. 353-357, 2006.

[6] Z. Zhan and S. A. Barnett, "Operation of ceria-electrolyte solid oxide fuel cells on iso-octane–air fuel mixtures," *Journal of Power Sources*, vol. 157, no. 1, pp. 422-429, 2006.

[7] R. Krishna and J. Wesselingh, "The Maxwell-Stefan approach to mass transfer," *Chemical Engineering Science*, vol. 52, no. 6, pp. 861–911, 1997.

[8] R. Gemmen and J. Trembly, "On the mechanisms and behavior of coal syngas transport and reaction within the anode of a solid oxide fuel cell," *Journal of Power Sources*, vol. 161, no. 2, pp. 1084-1095, Oct. 2006.

[9] E. S. Hecht, G. K. Gupta, H. Zhu, A. M. Dean, R. J. Kee, L. Maier, and O. Deutschmann, "Methane reforming kinetics within a Ni–YSZ SOFC anode support," *Applied Catalysis A: General*, vol. 295, no. 1, pp. 40-51, Oct. 2005.

[10] V. M. Janardhanan and O. Deutschmann, "CFD analysis of a solid oxide fuel cell with internal reforming: Coupled interactions of transport, heterogeneous catalysis and electrochemical processes," *Journal of Power Sources*, vol. 162, no. 2, pp. 1192-1202, Nov. 2006.

[11] A. M. Sukeshini, B. Habibzadeh, B. P. Becker, C. A. Stoltz, B. W. Eichhorn, and G. S. Jackson, "Electrochemical Oxidation of H2, CO, and CO/H2 Mixtures on Patterned Ni Anodes on YSZ Electrolytes," *Journal of The Electrochemical Society*, vol. 153, no. 4, p. A705, 2006.

[12] B. Habibzadeh, "Understanding CO oxidation in SOFC's using nickel patterned anode," University of Maryland, 2007.

[13] Y. Jiang and A. V. Virkar, "Fuel composition and diluent effect on gas transport and performance of anode-supported SOFCs," *Journal of the Electrochemical Society*, vol. 150, no. 7, pp. 942-951, 2003.

[14] E. Vakouftsi, G. E. Marnellos, C. Athanasiou, and F. Coutelieris, "CFD modeling of a biogas fuelled SOFC," *Solid State Ionics*, vol. 192, no. 1, pp. 458-463, Jun. 2011.

[15] E. Vakouftsi, G. Marnellos, C. Athanasiou, and F. A. Coutelieris, "A detailed model for transport processes in a methane fed planar SOFC," *Chemical Engineering Research and Design*, vol. 89, no. 2, pp. 224-229, Feb. 2011.

[16] H. Zhu, R. J. Kee, V. M. Janardhanan, O. Deutschmann, and D. G. Goodwin, "Modeling elementary heterogeneous chemistry and electrochemistry in solid-oxide fuel cells," *Journal of the Electrochemical Society*, vol. 152, no. 12, p. A2427-A2440, 2005.

[17] H. Zhu and R. J. Kee, "Modeling Electrochemical Impedance Spectra in SOFC Button Cells with Internal Methane Reforming," *Journal of The Electrochemical Society*, vol. 153, no. 9, p. A1765, 2006.

[18] V. M. Janardhanan and O. Deutschmann, "Numerical study of mass and heat transport in solid-oxide fuel cells running on humidified methane," *Chemical Engineering Science*, vol. 62, no. 18–20, pp. 5473-5486, Sep. 2007.

[19] V. M. Janardhanan, V. Heuveline, and O. Deutschmann, "Performance analysis of a SOFC under direct internal reforming conditions," *Journal of Power Sources*, vol. 172, no. 1, pp. 296-307, Oct. 2007.

[20] G. M. Goldin, H. Zhu, R. J. Kee, D. Bierschenk, and S. A. Barnett, "Multidimensional flow, thermal, and chemical behavior in solid-oxide fuel cell button cells," *Journal of Power Sources*, vol. 187, no. 1, pp. 123-135, Feb. 2009.

[21] C. Li, Y. Shi, and N. Cai, "Elementary reaction kinetic model of an anode-supported solid oxide fuel cell fueled with syngas," *Journal of Power Sources*, vol. 195, no. 8, pp. 2266-2282, Apr. 2010.

[22] Y. Matsuzaki and I. Yasuda, "Electrochemical oxidation of H2 and CO in a H2-H2O-CO-CO2 system at the interface of a Ni-YSZ cermet electrode and YSZ electrolyte," *Journal of the Electrochemical Society*, vol. 147, no. 5, pp. 1630-1635, 2000.

[23] P. Aguiar, C. S. Adjiman, and N. P. Brandon, "Anode-supported intermediate temperature direct internal reforming solid oxide fuel cell. I: model-based steady-state performance," *Journal of Power Sources*, vol. 138, no. 1–2, pp. 120-136, Nov. 2004.

[24] J. Mizusaki, H. Tagawa, T. Saito, T. Yamamura, K. Kamitani, K. Hirano, S. Ehara, T. Takagi, T. Hikita, and M. Ippommatsu, "Kinetic studies of the reaction at the nickel pattern electrode on YSZ in H2/H2O atmospheres," *Solid State Ionics*, vol. 70–71, pp. 52-58, May 1994.

[25] A. Bieberle, L. P. Meier, and L. J. Gauckler, "The Electrochemistry of Ni Pattern Anodes Used as Solid Oxide Fuel Cell Model Electrodes," *Journal of The Electrochemical Society*, vol. 148, no. 6, p. A646, 2001.

[26] A. Utz, A. Leonide, A. Weber, and E. Ivers-Tiffée, "Studying the CO–CO2 characteristics of SOFC anodes by means of patterned Ni anodes," *Journal of Power Sources*, vol. 196, no. 17, pp. 7217-7224, Sep. 2011.

[27] W. G. Bessler, M. Vogler, H. Störmer, D. Gerthsen, A. Utz, A. Weber, and E. Ivers-Tiffée, "Model anodes and anode models for understanding the mechanism of hydrogen oxidation in solid oxide fuel cells.," *Physical chemistry chemical physics : PCCP*, vol. 12, no. 42, pp. 13888-903, Nov. 2010.

[28] B. Habibzadeh, A. M. Sukeshini, B. Becker, and G. S. Jackson, "CO Electrochemical Oxidation on Ni Patterned Anodes for Assessing Solid Oxide Fuel Cell Kinetics," in *ECS Transactions*, 2008, vol. 11, no. 33, pp. 53-61.

[29] A. Bieberle and L. J. Gauckler, "State-space modeling of the anodic SOFC system Ni, H2–H2O/YSZ," *Solid State Ionics*, vol. 146, no. 1–2, pp. 23-41, Jan. 2002.

[30] M. Vogler, A. Bieberle-Hütter, L. Gauckler, J. Warnatz, and W. G. Bessler, "Modelling Study of Surface Reactions, Diffusion, and Spillover at a Ni/YSZ Patterned Anode," *Journal of The Electrochemical Society*, vol. 156, no. 5, p. B663, 2009.

[31] D. G. Goodwin, "A patterned anode model with detailed chemisty," in *Solid Oxide Fuel Cells IX, SOFC IX: Cells, Stacks, and Systems - Proceedings of the International Symposium*, 2005, vol. PV 2005–07, pp. 699-707.

[32] D. G. Goodwin, H. Zhu, A. M. Colclasure, and R. J. Kee, "Modeling Electrochemical Oxidation of Hydrogen on Ni–YSZ Pattern Anodes," *Journal of The Electrochemical Society*, vol. 156, no. 9, p. B1004, Sep. 2009.

[33] R. J. Kee and M. E. Coltrin, *Chemically reacting flow : theory and practice* . New York : Wiley-Interscience, 2003.

[34] E. A. Mason and A. P. Malinauskas, *Gas transport in porous media : the dusty-gas model* . Amsterdam ; New York : Elsevier, 1983.

[35] R. J. Gorte, H. Kim, and J. M. Vohs, "Novel SOFC anodes for the direct electrochemical oxidation of hydrocarbon," *Journal of Power Sources*, vol. 106, pp. 10-15, 2002.

[36] C. Lu, S. An, W. Worrell, and J. Vohs, "Development of intermediate-temperature solid oxide fuel cells for direct utilization of hydrocarbon fuels," *Solid State Ionics*, pp. 47-50, 2004.

[37] R. Gorte, S. Park, and J. Vohs, "Anodes for Direct Oxidation of Dry Hydrocarbons in a Solid-Oxide Fuel Cell," *Advanced Materials*, vol. 12, no. 19, pp. 1465-1469, 2000.

[38] S. Park, R. Craciun, J. M. Vohs, and R. J. Gorte, "Direct oxidation of hydrocarbons in a solid oxide fuel cell. I. Methane oxidation," *Journal of the Electrochemical Society*, vol. vol, pp. 146pp3603-3605, 1999.

[39] R. E. Williford, L. A. Chick, G. D. Maupin, S. P. Simner, and J. W. Stevenson, "Diffusion limitations in the porous anodes of SOFCs," *Journal of the Electrochemical Society*, vol. 150, no. 8, pp. 1067-1072, 2003.

[40] W. Lehnert, J. Meusinger, and F. Thom, "Modelling of gas transport phenomena in SOFC anodes," *Journal of Power Sources*, vol. 87, pp. 57-63, 2000.

[41] O. Deutschmann, S. Tischer, and S. Kleditzsch, "DETCHEM User Manuel." Germany, 2005.

[42] E. Seebauer and C. E. Allen, "Estimating surface diffusion coefficients," *Progress in Surface Science*, vol. 49, no. 3, pp. 265-330, Jul. 1995.

[43] G. A. Somorjai, *Introduction to surface chemistry and catalysis*. New York: Wiley, 1994.

[44] A. V. Virkar, J. Chen, C. W. Tanner, and J.-W. Kim, "Role of electrode microstructure on activation and concentration polarizations in solid oxide fuel cells," *Solid State Ionics*, vol. 131, no. 1, pp. 189-198, 2000.

[45] R. E. Williford, L. a. Chick, G. D. Maupin, S. P. Simner, and J. W. Stevenson, "Diffusion Limitations in the Porous Anodes of SOFCs," *Journal of The Electrochemical Society*, vol. 150, no. 8, p. A1067, 2003.

[46] H. Zhu and R. J. Kee, "A general mathematical model for analyzing the performance of fuel-cell membrane-electrode assemblies," *Journal of Power Sources*, vol. 117, no. 1–2, pp. 61-74, 2003.

[47] S. H. Chan, K. A. Khor, and Z. T. Xia, "Complete Polarization Model of a Solid Oxide Fuel Cell and Its Sensitivity to the Change of Cell Component Thickness," *Journal of Power Sources*, vol. 93, pp. 130-140, 2001.

[48] D. V. Ragone, *Thermodynamics of materials*. New York: Wiley, 1995.

[49] B. de Boer, "SOFC Anode: Hydrogen oxidation at porous nickel and nickel/yttria-stabilized zirconia cermet electrodes," University of Twente, 1998.

[50] W. Y. Lee, D. Wee, and A. Ghoniem, "An improved one-dimensional membrane-electrode assembly model to predict the performance of solid oxide fuel cell including the limiting current density," *Journal of Power Sources*, vol. 186, no. 2, pp. 417-427, 2009.

[51] H. Z. Robert J. Kee David G. Goodwin, "Solid-oxide fuel cells with hydrocarbon fuels," in *Proceedings of the Combustion Institute*, 2005, vol. Proceeding, pp. 2379-2404.

[52] M. Mogensen and S. Skaarup, "Kinetic and geometric aspects of solid oxide fuel cell electrodes," *Solid State Ionics*, vol. 86–88, no. pt 2, pp. 1151-1160, 1996.

[53] A. Mitterdorfer, "Identification of the reaction mechanism of the Pt, O2(g)|yttria-stabilized zirconia system Part I: General framework, modelling, and structural investigation," *Solid State Ionics*, vol. 117, no. 3–4, pp. 187-202, Feb. 1999.

[54] V. Yurkiv, D. Starukhin, H.-R. Volpp, and W. G. Bessler, "Elementary Reaction Kinetics of the CO/CO2/Ni/YSZ Electrode," *Journal of The Electrochemical Society*, vol. 158, no. 1, p. B5, 2011.

[55] Y. Matsuzaki and I. Yasuda, "Relationship between the steady-state polarization of the SOFC air electrode, La0.6Sr0.4MnO3/YSZ, and its complex impedance measured at the equilibrium potential," *Solid State Ionics*, vol. 126, no. 3–4, pp. 307-313, 1999.

[56] W. Y. Lee and A. Ghoniem, "Thermodynamics Analysis of the Deposited Carbon on Ni anode of SOFCs," *In preparation*.

[57] J.-W. Kim, A. V. Virkar, K.-Z. Fung, K. Mehta, and S. C. Singhal, "Polarization effects in intermediate temperature, anode-supported solid oxide fuel cells," *Journal of the Electrochemical Society*, vol. 146, no. 1, pp. 69-78, 1999.

[58] J. R. Wilson, W. Kobsiriphat, R. Mendoza, H.-Y. Chen, J. M. Hiller, D. J. Miller, K. Thornton, P. W. Voorhees, S. B. Adler, and S. A. Barnett, "Three-dimensional reconstruction of a solid-oxide fuel-cell anode," *Nature Materials*, vol. 5, no. 7, pp. 541-544, 2006.

Page left intentionally blank

Chapter 5

General Conclusion

In this thesis, we examined three topics of research that are relevant to solid oxide fuel cells (SOFCs) operating on hydrocarbon fuels: (1) a thermodynamic analysis of the propensity for carbon formation in Ni-based anodes, (2) the development of a multi-step CO electrochemistry oxidation mechanism, and (3) the development of a membrane-electrode-assembly (MEA) model within which the CO electrochemistry mechanism is coupled to an existing and accepted mechanism for H_2 to predict the performance of the SOFC operating on syngas.

In regards to carbon formation, three kinds of deposited carbon have been observed: (1) encapsulating polymer, (2) carbon nano-fiber, and (3) soot consisting of polycyclic aromatic hydrocarbons (PAHs). Despite the differences in the chemical composition and the structure, all three types of carbon are referred to as deposited carbon. Likewise, all previous thermodynamic analyses were based on the assumption that the thermodynamic properties of graphite can represent those of the deposited carbon regardless of its formation mechanism. Our approach represents an effort to differentiate each type of the deposited carbon and improve the thermodynamic analysis considering each mechanism. Two dominant carbon deposition mechanisms have been identified: homogeneously formed soot and catalytically grown carbon fiber. The thermodynamic properties of these two types of carbon are different from graphite because of the different chemical composition and structure of soot and the carbon fiber. A new thermodynamic analysis approach is proposed in which we use: (1) experimentally measured

data for carbon fiber if the anode includes Ni catalysts, and (2) partial pressures of soot precursors, CH_3 and C_2H_2, instead of graphite, to predict soot formation. The new approach improves the prediction of carbon fibers and soot formation in the cases where previous thermodynamic analyses failed.

We note that the carbon fiber formed on Ni-YSZ has a different structure from that grown on a supported Ni catalyst on which the thermodynamic properties used for our study are based. Because of this, carbon fiber formed on Ni-YSZ may have different Gibbs free energy from that used here. A value for the Gibbs free energy of carbon fiber in a Ni-YSZ anode has never been reported. Knowledge of this value may be able to further improve the prediction of carbon deposition.

Rapid soot formation is observed when the partial pressures of CH_3 and C_2H_2, typical soot precursors, are $O(10^{-9})$ bar and $O(10^{-10})$ bar, respectively. These limits are set from only two cases. It is worthwhile to examine whether the same thresholds can be applied to more cases. If so, these threshold values can be used to determine whether a more detailed soot kinetic analysis should be performed.

Further, we propose a new multi-step CO electrochemistry model where CO is directly involved in the charge-transfer steps.

1. Adsorption/desorption on the Ni surface

$$CO(g) + V(Ni) \leftrightarrow CO(Ni) \qquad \text{(R. 1)}$$

2. Two-step charge-transfer reactions at the TPB

$$O_O^x(YSZ) + (YSZ) \leftrightarrow O^-(YSZ) + V_O^{\bullet\bullet}(YSZ) + e^-(Ni) \qquad \text{(R. 2)}$$

$$O^-(YSZ) + CO(Ni) \leftrightarrow CO_2(g) + (YSZ) + (Ni) + e^-(Ni) \qquad \text{(R. 3)}$$

One set of seven parameters, four ($k_{2,f}$, $k_{2,b}$, $k_{3,f}$, and $k_{3,b}$) from the charge-transfer reactions, two Q and n_{CPE} from the constant phase element, and D_{O^-}, the O^- diffusion coefficient, at each temperature succeeded in reproducing the following characteristics of the impedances at all activation overpotentials: (1) the two suppressed semi-circles in the impedance, and (2) the decrease in polarization resistance as the activation overpotential increases. The same parameters successfully predicted the following features in the steady-state Tafel plots: (1) the asymmetry of the anodic and cathodic currents, and (2) the reduction in the slope as overpotential increases. The electrochemistry mechanism can explain the experimentally reported positive dependency of the exchange current density on p_{CO_2} as well. Furthermore, at high activation overpotentials, the inductive behaviors are predicted from our model.

The most significant refinement that can be made to the proposed CO electrochemistry model would be to resolve the diffusion coefficient for O^-(YSZ), which is unreasonably high in our model. Two possible solutions are discussed: (1) modifying the governing equation for O^- (YSZ) diffusion and (2) adding another charge-transfer step to the existing two-step mechanism.

Lastly, we developed an MEA model of SOFC operating on syngas as fuel, which incorporates multi-species transport, detailed elementary heterogeneous reactions on the Ni surface, and detailed electrochemistry models for H_2 and CO. For the chemically reacting flow in the porous electrodes, a detailed mechanism for heterogeneous CH_4 reforming on Ni is used, and transport is modeled using Dusty-Gas-Model (DGM). Lack of a detailed CO electrochemical mechanism has traditionally been a bottleneck for syngas-based simulations. For the first time, we applied both detailed H_2 and CO electrochemistry to simulate a SOFC using syngas fuel. For H_2 electrochemistry, the rate-limiting switch-over mechanism improves previous single-rate

limiting assumptions and shows good agreement with the experimental data, especially near limiting current densities. For CO electrochemistry, a full three-reaction mechanism developed in Chapter 3 is employed and shows good agreement with experimental data. We found that the lower performance of a SOFC using pure CO compared with H_2 can be attributed not only to the sluggish CO electrochemistry, but also to slow transport processes. For syngas, the MEA model can separate out the effects of reforming chemistry and the additional CO electrochemistry. The reforming chemistry improves the agreement at lower current densities and increases the limiting current density by providing more H_2 through H_2O produced at the TPB and water-gas shift reaction. CO electrochemistry is essentially negligible when the fuel is dominated by H_2. However, the current from CO electrochemistry becomes comparable to that from H_2 electrocehmistry as the CO content at the TPB increases. Nonetheless, there is some discrepancy between the MEA simulation and experimental data. Because the current H_2 and CO electrochemistry model assumed only single species on Ni, H(Ni) or CO(Ni), respectively, the interaction between H and CO electrochemistry on Ni cannot be captured. The observed discrepancy can be improved by developing a new syngas mechanism that allows the interaction between H_2 and CO electrochemistry on Ni.